Multiphase Characteristics of Carbon Fiber-Reinforced Cementitious Materials Under Static and Freeze-Thaw Cyclic Loading Conditions

by

Maryam Monazami

B.Sc., Guilan University, 2013
M.Sc., Shahrood University of Technology, 2016

A Dissertation Submitted in Partial Fulfillment of
the Requirements for the Degree of

DOCTOR OF PHILOSOPHY

in the Department of Civil Engineering

We acknowledge and respect the lək̓ʷəŋən peoples on whose traditional territory the university stands and the Songhees, Esquimalt and W̱SÁNEĆ peoples whose historical relationships with the land continue to this day.

Multiphase Characteristics of Carbon Fiber-Reinforced Cementitious Materials under Static and Freeze-Thaw Cyclic Loading Conditions

by

Maryam Monazami
B.Sc., Guilan University, 2013
M.Sc., Shahrood University of Technology, 2016

Supervisory Committee

Dr. Rishi Gupta, Supervisor
Department of Civil Engineering

Dr. Cheng Lin, Departmental Member
Department of Civil Engineering

Dr. Dennis Hore, Outside Member
Department of Chemistry

Table of Contents

Supervisory Committee ii
Table of Contents iii
List of Tables viii
List of Figures ix
Abstract xii
Glossary xvi
Acknowledgment xviii
Chapter 1. Introduction 1
1.1. Overview 1
1.2. Carbon fibers 2
1.2.1. Polyacrylonitrile (PAN) 2
1.2.2. Pitch 2
1.2.3. Rayon 3
1.2.4. Bitumen 3
1.3. Carbon fiber application in construction industry 3
1.4. Dissertation Objectives 5
1.5. Research Outline 5
1.6. Research Contribution 8
1.7. Research Limitation 9
Chapter 2. Microstructural properties of carbon fibers 10
2.1. Introduction 10
2.2. Carbon fibers 11
2.2.1. Properties 11
2.2.1.1. PAN fibers 12
2.2.1.2. Pitch fibers 12
2.2.1.3. Morphology 12

2.2.2. Carbon fibers in concrete 13
2.2.3. Bitumen 15
2.3. Fiber characterization 16
2.3.1. Scanning electron microscopy 16
2.3.2. Energy dispersive x-ray 17
2.4. Alberta bitumen-based carbon fiber microstructural analysis 19
2.5. Conclusion 23
Chapter 3. Effect of curing age on pull-out response of carbon fibers 24
3.1. Introduction 24
3.2. Experimental investigation 27
3.2.1. Materials and cementitious mortar 27
3.2.2. Specimen preparation 28
3.2.3. Test setup and procedure 30
3.3. Experimental results and discussion 31
3.3.1. Effect of fiber type on fiber pull-out behavior 32
3.3.2. Effect of matrix age on fiber pull-out behavior 37
3.3.3. Interfacial strength 37
3.4. Conclusions 39
Chapter 4. Behavior of alkali treated and fly ash-alkali treated carbon fibers 41
4.1. Introduction 41
4.2. Experimental investigation 43
4.2.1. Materials 43
4.2.2. Preparation of samples 43
4.3. Results and discussion 46
4.3.1. Microstructure characterization of Carbon Fiber 46
4.3.2. Fiber pull-out behavior 47
4.3.3. Fiber contact angle 48
4.3.4. Fiber electrical resistivity 49
4.4. Conclusion 49

Chapter 5. Mechanical behavior and fracture energy of carbon fiber-reinforced concrete beams and panels 51
5.1. Introduction 51
5.2. Materials and methods 53
5.2.1. Raw materials 53
5.2.2. Design of FRCM 54
5.2.2.1. Tests on FRCMs 55
5.2.3. Design of FRC 56
5.2.3.1. Fresh properties 56
5.2.3.2. Compressive strength 57
5.2.4. Design of FRCP 58
5.2.4.1. Flexural behavior of FRCP 58
5.3. Results and discussions 59
5.3.1. Fresh properties 59
5.3.2. Compressive strength 62
5.3.2.1. Compressive strength of FRCM 62
5.3.2.2. Compressive strength of FRC 64
5.3.3. Flexural properties 64
5.3.3.1. Modulus of rupture and flexural toughness index (I5) 64
5.3.3.2. Fiber optimization through analysis of model 67
5.3.3.3. Flexural behavior of concrete 69
5.3.3.4. Prediction of flexural strength 70
5.3.4. Flexural behavior of round panels 73
5.3.5. Correlation between beams and panels flexural behavior 76
5.4. Conclusions 77
Chapter 6. Cement matrix deterioration after freeze-thaw exposure in electrically conductive carbon fiber-reinforced concrete 79
6.1. Introduction 79
6.2. Experimental investigation 81
6.2.1. Materials 81

6.3. Methods and equipment 82
6.3.1. Preliminary mechanical tests 82
6.3.2. Freeze-thaw cyclic test 82
6.3.3. Mass loss 83
6.3.4. Resonant frequency test 84
6.3.5. Ultrasonic pulse velocity test 84
6.3.6. Infrared (IR) thermography technique 85
6.3.7. Hammer percussion 86
6.4. Results and discussion 87
6.4.1. Compressive strength 87
6.4.2. Flexural properties 88
6.4.3. Mass loss 89
6.4.4. Dynamic modulus of elasticity 90
6.4.5. Ultrasonic pulse velocity 91
6.4.6. Resonant frequency 93
6.4.7. Hammer percussion 94
6.4.8. Infrared imaging 95
6.5. Result agreement 96
6.6. Conclusion 98
Chapter 7. Performance of carbon fiber-reinforced pavement with embedded sensors using destructive and non-destructive testing 100
7.1. Introduction 100
7.2. Materials and methodology 103
7.2.1. Selection of carbon fibers 103
7.2.2. Selection of site 103
7.2.2.1. Image analysis on pre-existing bus pads 104
7.2.3. Site development 105
7.2.3.1. Excavation of the existing bus pads 105
7.2.3.2. Installation of sensors 106
7.2.3.2.1. Temperature and relative humidity sensors 106
7.2.3.2.2. Strain gauges 107

7.2.3.2.3. Piezoelectric patches 108
7.2.4. Design mix and placing of concrete. 109
7.3. Results and discussions 110
7.3.1. Laboratory-based tests on concrete 110
7.3.1.1. Destructive tests 110
7.3.2. Structural health monitoring of bus pads 112
7.3.2.1. Visual monitoring of bus pads 113
7.3.2.2. Temperature and humidity monitoring of bus pads 115
7.3.2.3. Strain gauge measurements of bus pads 116
7.3.2.4. Health monitoring of bus pads at 28 days of casting 117
7.3.2.4.1. Schmidt hammer testing 118
7.3.2.4.2. Electrical resistivity 120
7.3.2.4.3. Ultrasonic pulse velocity testing 121
7.4. Conclusions 122
7.5. Authorship contribution statement 124
Chapter 8. Concluding remarks and key findings 125
Chapter 9. Recommendation for future work 130
References 133

List of Tables

Table 1. Classification of carbon fibers 12
Table 2. Carbon fiber properties in previous studies 13
Table 3. Properties of fibers 16
Table 4. Physical and mechanical properties of fibers 28
Table 5. Mixture proportion of mortar mix 28
Table 6. Summary of pull-out test results of fibers at different curing ages. 35
Table 7. Summary of fiber pull-out test results 48
Table 8. Electrical resistivity of untreated and treated carbon fibers 49
Table 9. Mixing proportions of cement mortar samples 55
Table 10. Flexural testing results of cement mortar samples 67
Table 11. Comparison of the predicted and experimental flexural strengths 72
Table 12. Summary of flexural behavior of round panels 75
Table 13. Minimum and maximum values of energy absorption in C1550 round panel specimens 75
Table 14. Mix designs of five different CFRC mixes 82
Table 15. Features and specifications of the FLIR camera 86
Table 16. Average compression and flexure properties of samples 89
Table 17. Crack analysis of existing bus pads 105
Table 18. Summary of flexural behavior of beams and round panels 111

List of Figures

Figure 1. Schematic description of the fracture process in uniaxial tension and the resulting stress-crack opening relationship 2
Figure 2. a) pitch-based carbon fibers b) bitumen-based carbon fibers c) PAN-based carbon fibers 16
Figure 3. SEM photos of a) pitch-based carbon fibers b) bitumen-based carbon fibers c) PAN-based carbon fibers 17
Figure 4. SEM photos of a) cross-section b) longitudinal view and c) bunch of bitumen-based carbon fibers ..... **Error! Bookmark not defined.**
Figure 5. EDX results of a) pitch-based b) bitumen-based c) PAN-based carbon fiber 19
Figure 6. SEM of BBCF 20
Figure 7. Elemental map of BBCF 21
Figure 8. Elemental point analysis of BBCF 21
Figure 9. Line scan profile of BBCF 22
Figure 10. Sieve analysis of a) fine aggregates b) coarse aggregates 27
Figure 11. a) steel fiber b) synthetic fiber c) PAN-based carbon fiber d) pitch-based carbon fiber 28
Figure 12. Optical microscope photos (division = 0.1 mm and D = diameter of bundle of fibers) a) D = 0.5 b) D = 0.8 c) D = 1 mm 29
Figure 13. Sample preparation steps a) 3D model of thin plastic plate b) 3D-printed plastic plates c) the plastic plate is placed inside the half-filled mortar d) samples ready to be demolded 30
Figure 14. Pull-out test set up a) pull-out test apparatus b) MTM testing machine c) CF being pulled out. 30
Figure 15. Fibers after pull-out test a) steel b) synthetic and c) carbon fiber 32
Figure 16. Different failure modes in carbon fibers a) fiber complete fracture b) fiber partial fracture c) fiber pull-out 33
Figure 17. Failure pattern in different types of fiber 34
Figure 18. Average tensile strength of different fibers at 28 days of curing 36
Figure 19. Pull-out behavior of fibers at different curing ages 37
Figure 20. Pull-out force-displacement behavior of different fibers: a) SF b) PAN-based CF c) SI d) pitch-based CF 38
Figure 21. Scanning electron microscopy images of CFs 43
Figure 22. Preparation of fibers a) Magnetic Stirrer with fly ash solution b) carbon fibers soaking in NaOH solution c) carbon fibers rinsed d) carbon fibers immersed in fly ash solution. 43
Figure 23. Fiber pull-out test set up 44
Figure 24. Fiber contact angle test set up 45
Figure 25. Electrical resistivity test set up 46
Figure 26. SEM of treated and untreated carbon fiber 47
Figure 27. Force-displacement behavior of treated and untreated carbon fibers 48
Figure 28. Contact angle of a) untreated carbon fiber b) NaOH treated carbon fiber c) NaOH+ fly ash treated carbon fiber. 49
Figure 29. Physical appearance of fibers a) Mitsubishi PAN-based CF b) Mitsubishi pitch-based CF c) Teijin PAN-based CF d) PP 54
Figure 30. Center-point flexural test on beams 57

Figure 31. Failure pattern in round panels according to ASTM C1550 58
Figure 32. Round panel test set up a) pre-cracking state b) the appearance of first crack c) complete failure state. 59
Figure 33. Flowability tests a) flow table results of cement mortar b) slump values of concrete (variation to CO shown over each bar) 61
Figure 34. Flow table test a) NC b) P6 62
Figure 35. Compressive strength results of a) cement mortar b) concrete 63
Figure 36. SEM of FRCM a) PPRM b) CFRM 63
Figure 37. Fracture behavior of different samples under compression 64
Figure 38. Load-Displacement curve in flexure 65
Figure 39. Pre-crack/post-crack energy absorption of cement mortar mixes 66
Figure 40. Flexural strength of mortar mixes 66
Figure 41. Surface quadratic polynomial fitting of a) flexural strength b) pre-crack absorbed energy c) post-crack absorbed energy. 69
Figure 42. Flexural strength of concrete mixes 70
Figure 43. Load-Displacement curve of concrete mixes under flexure 70
Figure 44. Variation of tensile strength vs flexural strength in a) PPRM b) CFRM 73
Figure 45. Fracture pattern of round panels a) CO b) 0.5PAT18 c) 1PAT18 74
Figure 46. Round panel test results a) representative load-displacement curves of round panels under bending b) energy absorption of panels at certain displacements 75
Figure 47. Analysis of variance on beams and round panels 76
Figure 48. Images of a) digital microscope, b & c) SEM of PAN-based carbon fibers 82
Figure 49. Freeze-thaw test setup 83
Figure 50. Resonant frequency test 84
Figure 51. Ultrasonic pulse velocity test 85
Figure 52. Hammer percussion test 87
Figure 53. Fracture pattern of concrete samples after compression test 88
Figure 54. Scaling of samples at different FT cycles 90
Figure 55. Mass loss of all samples at different FT cycles 90
Figure 56. Ultrasonic pulse velocity variations at different FT cycles 91
Figure 57. (a) DMOE variations at different FT cycles derived from UPV results (b) equation to predict DMOE for CF≤1% and (c) equation to predict DMOE for CF>1% 92
Figure 58. Dynamic properties at different FT cycles derived from RFT results 94
Figure 59. Dynamic properties of samples at different FT cycles derived from HP results 95
Figure 60. Infrared images of samples at 0 and 120 FT cycles 96
Figure 61. Summary of the DMOE derived from UPV, RF, and HP tests 98
Figure 62. Deterioration of pavement with time [230] 101
Figure 63. Details of the pavement and the construction site 103
Figure 64. Pre-exising condition of bus pads (a) B_{N-1} (b) B_{N-2S} (c) B_{CF-S} 104
Figure 65. Image analysis of pre-existing bus pad 104
Figure 66. Excavated bus pad site 105
Figure 67. The layout of bus pads and sensor location 106
Figure 68. Installed sensors and strain gauges 107

Figure 69. Installed piezoelectric patches 108
Figure 70. Finished bus pads 110
Figure 71. Load-displacement behavior of CO and CFRC under flexure a) beams b) round panel 112
Figure 72. NDTs used to assess pavement condition. 113
Figure 73. Condition assessment of bus pads at 28 days 114
Figure 74. Thermal photos of bus pads 114
Figure 75. Temperature variation from a) wireless sensors b) thermocouples 116
Figure 76. Strain gauge data after temperature corrections a) B_{N-2S} b) B_{CF-S} 117
Figure 77. NDT at 25 cm × 25 cm grids on bus pad 118
Figure 78. Variation of the Rebound number and compressive strength of bus pads a) B_{N-1} b) B_{N-2S} c) B_{CF-S} 119
Figure 79. Variation of the Electrical resistivity of concrete across the bus pad a) B_{N-1} b) B_{N-2S} c) B_{CF-S} 121
Figure 80. Variation of the UPV of concrete across the bus pad (a) B_{N-1} (b) B_{N-2S} (c) B_{CF-S} 122

Abstract

Aging concrete infrastructure, particularly in colder climates like Canada, demands urgent maintenance and renewal due to the severe temperature variations. These conditions lead to issues such as cracking, spalling, and overall deterioration. To ensure the longevity and functionality of infrastructures, it is crucial to use durable and high-performance materials. Adding fibers to the concrete mix can improve its toughness and resistance to cracking. Fiber-reinforced concrete (FRC) can withstand higher tensile stresses and distribute loads more effectively, increasing the overall durability.

Among various types of fibers, carbon fibers (CFs) have gained significant popularity due to their unique ability to confer self-deicing properties to cementitious materials. This characteristic holds particular importance in colder climates, where maintaining safe and accessible infrastructure, during harsh winter conditions is paramount. Carbon fiber-reinforced concrete (CFRC) has various advantages over normal concrete, including self-deicing, high strength, durability, and corrosion resistance. CFRC's self-deicing capability is achieved through the electrical conductivity of CFs, which allows an electric current to be applied to generate heat and melt ice or snow. This feature improves safety by preventing icy surface conditions and lowers maintenance costs for snow removal and deicing chemicals. CFRC is also highly durable and strong, making it suitable for infrastructure and architectural construction. Additionally, its resistance to corrosion ensures long-lasting performance and extends the lifespan of CFRC structures.

Integrating self-deicing CF reinforcement within concrete bus pads offers a practical approach to leverage their inherent self-deicing property, resulting in heightened passenger safety and convenience throughout the winter season. With CFs generating heat to melt accumulated ice and snow, the bus pads retain a snow-free surface, thereby mitigating the potential for slips and accidents among passengers and pedestrians. This endeavor directly fosters a transit environment that is safer and more accessible.

While numerous studies have studied self-deicing characteristics of CFRC in colder climates, a notable research gap exists in examining how CFRC responds to the rigorous challenges of freezing and thawing (FT) cycles. Despite the extensive exploration of CFRC's ability to melt ice and snow, the absence of investigations into its deterioration behavior under cyclic freezing and thawing conditions is a critical oversight. This dissertation aims to fill the existing knowledge gap and challenges related to the performance assessment of CFRC under cyclic freezing and thawing loading conditions, as well as introducing an optimized mix design for concrete suitable for colder

climates. The research methodology involves a comprehensive investigation that incorporates both destructive and non-destructive testing techniques.

It is clear that a multitude of pertinent factors, encompassing factors such as fiber and aggregate type, fiber length, cement paste composition, and different admixture can have significant impacts on the performance of cementitious composites. Within the context of this dissertation, however, the study has meticulously centered its investigative on carbon fiber's physical properties and its concentration. In the pursuit of refining the mix design to attain optimal outcomes, the research engaged in an array of destructive analyses, including compressive strength tests, splitting tensile strength tests, and flexural strength tests. These tests provide insights into the strength and structural behavior of CFRC under FT conditions, allowing for an evaluation of its performance.

In conjunction with conventional destructive tests, this research integrated non-destructive testing (NDT) methodologies to appraise the structural integrity and quality of the CFRC specimens. Employing advanced techniques including ultrasonic testing, rebound hammer analysis, and ground-penetrating radar, a comprehensive evaluation was systematically conducted on CFRC samples subjected to an extensive and rigorous regimen of 300 FT cycles. Throughout this demanding exposure, the samples underwent the complete array of non-destructive assessments at regular 30-cycle intervals. This approach was undertaken to meticulously discern and analyze the cumulative deteriorative effects that emanated from the repetitive FT cycles. These insights yielded a profound understanding of the durability performance of CFRC under the persistent challenge of FT conditions.

The synergistic integration of both destructive and non-destructive testing methodologies yields a holistic and nuanced comprehension of CFRC performance in areas with colder climate such as Canada. This assimilated knowledge stands as a pivotal cornerstone for the formulation of an intricately optimized mix design, one fortified to effectively withstand the challenges imposed by cyclic FT cycles. The research outcomes have the potential to contribute to the advancement of CFRC technology, enabling its effective use in regions with colder climates and facilitating the construction of durable and resilient infrastructure in such areas.

The dissertation is divided into three milestones, each with its own set of objectives and tasks, to systematically address the research questions and challenges related to CFRC.

Milestone 1 encompassed a comprehensive evaluation of mechanical properties and physical properties in different carbon fiber types, emphasizing a comparative analysis on commonly used CFs. The research extended to a novel bitumen-based carbon fiber (BBCF) from Alberta, seeking to understand its microstructure and potential for market adaptability. Techniques such as scanning

electron microscopy (SEM) and energy dispersive x-ray (EDX) spectroscopy, along with mechanical and electrical tests, were incorporated to assess the behavior of different types of CFs. Milestone 1 also presented a novel method using a supplementary cementitious materials (SCM) fiber coating technology. This breakthrough improved the interfacial transition zone (ITZ) between fibers and the cement matrix, resulting in improved composite performance. The goal of this milestone was to meticulously compare and establish correlations between the diverse properties exhibited by various fiber types. This systematic investigation attempted to identify the best fiber choice for incorporation into cementitious materials, thereby improving the cementitious composite's overall performance.

Milestone 2 shifted the focus to investigating the mechanical and fracture behavior of carbon fiber-reinforced cementitious composite (CFRCC) and the interrelationship between materials properties and mechanical performance. A systematic approach for Laboratory testing and structural analysis has been presented in this milestone.

Uniaxial tension tests were performed on dog bone-shaped Carbon Fiber Reinforced Mortar (CFRM) to analyze the behavior of samples subjected to axial tensile forces. Flexural characteristic of CFRC samples is key parameter that involves composite behavior under bending loads. While flexural testing often employs beams, it may not effectively represent the performance of fiber-reinforced concrete due to considerable differences in cracking behavior of FRC with normal concrete. This discrepancy is particularly noticeable in slab and pavement applications, owing to the substantial variability in flexural behavior observed in Fiber-Reinforced Concrete (FRC) beams. Additionally, the smaller fracture area resulting from a lower count of fibers further compounds this distinction.

During this milestone, a thorough and comprehensive analysis was conducted, focusing on the flexural strength of both round panels and beams. The flexural failure observed in round panels closely emulated the behavior seen in structural slabs, aligning with the principles of the yield line theory.

The characterization of flexural behavior involved toughness indices and key flexural strength parameters, including bending strength and modulus of elasticity. This analysis process ultimately led to the identification of an optimal mix design. This finding underscores the significance of fiber content in influencing the overall behavior and performance of CFRC composites.

Furthermore, to compare the experimental results of CFRC beam and panel flexure behavior, an analysis of variance was conducted. This statistical examination unveiled a notable 41% discrepancy in flexural properties between the two distinct sample geometries. This observation

highlights the importance of considering sample geometry when assessing the flexural behavior of CFRC materials.

Milestone 2 also involved a meticulous investigation into the FT behavior of the CFRC samples, evaluating their durability under the stress of 300 FT cycles. By studying the FT performance of the CFRC samples, the research aims to gain insights into the durability and resistance of CFRC to the effects of FT cycles, which can include cracking, spalling, and degradation. This information is valuable for assessing the suitability and long-term performance of CFRC in colder climates, where FT cycles are a significant concern.

In **Milestone 3**, a case study was conducted to evaluate the durability of an electrically conductive CFRC bus pad. The case study involved integrating sensors within the bus pad to monitor factors such as strain, temperature, and moisture content. The goal was to assess the performance and behavior of the CFRC bus pad in real-world conditions.

The research project aimed to gain insights into the structural integrity and durability of the CFRC bus pad by continuously monitoring its performance using embedded sensors. These sensors provided data on factors such as strain, temperature variations, and moisture content, allowing assessment the material's response to environmental influences. The study also focused on understanding how the CFRC bus pad performed under different operating conditions and evaluate its ability to withstand environmental factors.

The primary objective of the research project in this milestone was to conduct a comprehensive performance assessment of CFRC bus pads, encompassing both short-term and long-term evaluations. Through this assessment, the study sought to gain profound insights into the behavior and durability of CFRC bus pads. The findings derived from this significant milestone played an important role in enhancing the design and performance of CFRC materials, ensuring their suitability for practical applications such as bus pads. Moreover, these findings hold the potential to inform and shape future advancements in electrically conductive CFRC materials for various other purposes.

Glossary

Abbreviation or Symbol	Definition
A	cross-sectional area
A_f	cross-sectional area of fiber
ACI	American concrete institute
AEA	air entraining agent
ANOVA	analysis of variance
ASTM	American society for testing and materials
BBCF	bitumen-based carbon fibers
CF	carbon fiber
CFRC	carbon fiber-reinforced concrete
CFRCC	carbon fiber-reinforced cementitious composite
CFRCP	carbon fiber-reinforced concrete panels
CFRM	carbon fiber-reinforced mortar
CFRP	carbon fiber-reinforced polymer
CoV	coefficient of variance
CSA	the Canadian standards association
CT	composite theory
DMOE	dynamic modulus of elasticity
E_c	modulus of elasticity of concrete
E_f	modulus of elasticity of fiber
f_c	compressive strength
FRC	fiber-reinforced concrete
FRCM	fiber-reinforced cement mortar
FRCC	fiber-reinforced cement composites
FRCP	fiber-reinforced concrete panels
FT	freezing and thawing
GFRC	glass fiber-reinforced concrete
GU	general use
HP	hammer percussion
HWRA	high-range water reducing agent
ITZ	interfacial transition zone

LVDT	linear variable differential transformers
PAN	polyacrylonitrile
PP	polypropylene fiber
PFRC	polypropylene fiber-reinforced concrete
PPRM	polypropylene fiber-reinforced mortar
PRCP	polypropylene reinforced concrete pavement
RF	resonant frequency
SARA	saturate, aromatic, resin, asphaltene
SEM	scanning electron microscopy
SF	steel fiber
SFRC	steel fiber-reinforced concrete
TAIS	traffic accident information system
UPV	ultrasonic pulse velocity

Acknowledgment

First and foremost, I would like to sincerely thank my mentor and supervisor, ***Dr. Rishi Gupta****, for his guidance throughout my PhD journey. I am genuinely grateful to him for providing me the opportunity to work on this exciting project. I couldn't have finished this job without his advice, technical expertise, creative recommendations, and constant encouragement.*

I want to extend my deepest appreciation and recognition to my beloved parents, ***Soraya and Mahmoud.*** *Their unwavering prayers and blessings have been a constant source of support and inspiration throughout the journey of completing this thesis. Their guidance and encouragement have played a significant role in my achievements. While it is undeniably difficult to cope with the loss of my dearest father, his memory remains vivid and alive within me. I feel his presence, as his legacy continues to illuminate my path every single moment.*

I would like to thank our industry partners, Axel Meison and Dr. Paolo Bomben from Alberta Innovates for their involvement and guidance. I am very thankful for their technical and financial support.

I would like to express my gratitude to my defense committee, Dr. Cheng Lin and Dr. Dennis Hore, for their valuable intellectual contributions and technical expertise throughout the completion of this dissertation.

I would like to express my heartfelt appreciation for the contributions of my colleagues, as well as the visiting and co-op students who have played a significant role in this project. Their dedication and collaboration have been instrumental in the successful completion of this research.

I would also like to extend my gratitude to the technicians of the Civil Engineering Department, particularly Dr. Armando Tura, Bastien Lanusse and Arielle Garrett, for their technical support. The technical support received from Soliman is highly appreciated.

Finally, I would like to express my heartfelt gratitude to my husband, ***Dr. Navid Hooshyar.*** *His unwavering love, support and encouragement have been a constant source of strength, helping me overcome challenges and pushing me to reach my fullest potential. His belief in my abilities has been a driving force behind my success, and I am truly blessed to have him as my partner in life.*

Chapter 1. Introduction

1.1. Overview

Despite being the most popular and widely used construction material, concrete has a number of undesirable properties, including brittleness, the presence of microcracks, large drying shrinkage, low bonding strength in repair applications, low chemical resistance, and the inability to withstand tensile stresses [1–3]. These weaknesses reduce concrete's durability over time and, in some cases, result in catastrophic failures of haphazardly designed structures. Strong and ductile materials, such as steel bars, are commonly used in design to take advantage of high compressive strength and mitigate the frailty of concrete. These reinforcements are put in tensile stress zones, preventing concrete from failing in tension.
Under load, micro fractures appear throughout the paste in the interfacial transition zone (ITZ) between aggregates and cement paste. This process continues until the micro cracks collide with other micro cracks and merge to form macro-cracks [4]. A fully developed macro fracture reduces the load carrying capacity of concrete significantly. Concrete is predicted to collapse suddenly in the absence of steel support. However, even in the presence of tensile reinforcements such as standard steel rebars, the crack arrest mechanism remains ineffective. Along with the use of steel reinforcements, the tensile properties of concrete can be increased by randomly spreading discontinuous fibers into the mixture [3].

Fiber-reinforced concrete (FRC) refers to concrete that incorporates randomly distributed discontinuous fibers. FRC is a promising composite that effectively addresses the brittleness of traditional concrete and enhances its versatility. The primary objective of adding fibers is to control concrete cracking. The inclusion of fibers in FRC not only helps control crack formation but also extends to the post-cracking stage. The fibers act as bridging elements across cracks, slowing down the rate at which crack widths increase. This quality is often referred to as post-cracking ductility in FRC [5]. In some cases, fibers can be utilized for carrying load in non-structural applications. Figure 1 shows different phases of multiscale crack growth in fiber reinforced concrete [6].

Fibers can be classified into two major categories:1) macro fibers; 2) micro fibers. Macro fibers are long thick fibers that can help in load transfer as well as providing the macro crack bridging property to the mix. On the other hand, the micro fibers are short thin fibers and only participate providing the post-crack ductility. By virtue of their size, micro fibers can easily bridge the tensile stress across the ITZ’s, thereby preventing the micro cracks from taking place [7].

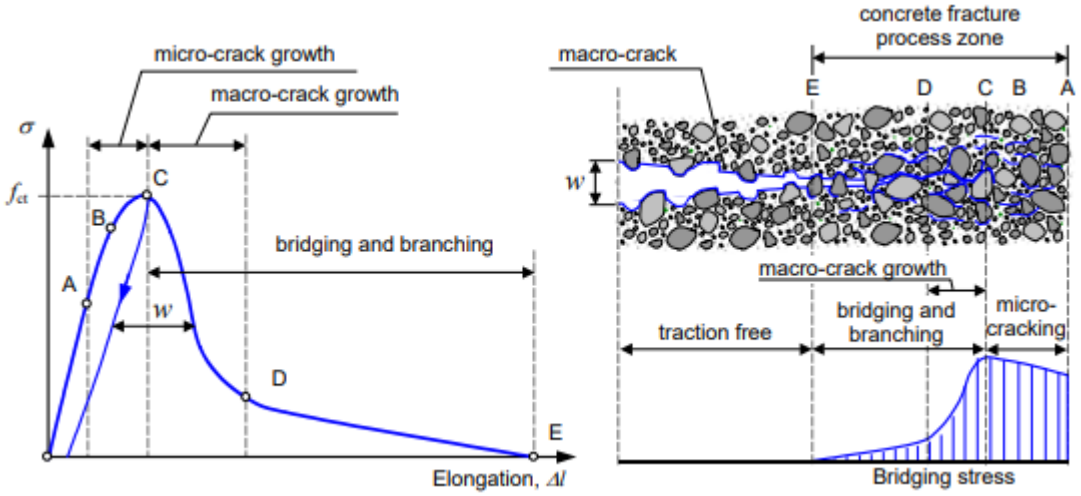

Figure 1. Schematic description of the fracture process in uniaxial tension and the resulting stress-crack opening relationship [6]

1.2. Carbon fibers

Among different types of fibers, carbon fiber (CF) has emerged as a game-changing material with exceptional properties, finding applications across diverse industries. CFs are manufactured using different precursors, each of which has unique features that influence the characteristics of the resulting CF. The three most used precursor materials are polyacrylonitrile (PAN), pitch and rayon [8].

1.2.1. Polyacrylonitrile (PAN)

Polyacrylonitrile is the most used precursor material in the manufacturing of CF due to its excellent mechanical properties, including high tensile strength and modulus [8] as well as resistant to chemical degradation and have good thermal stability [9]. During the carbonization process, PAN fibers have a relatively high carbon yield, resulting in CFs with a high carbon content. However, due to the high cost of PAN raw materials and the complexity of the manufacturing process, PAN-based CFs may be more expensive than alternative precursors [10].

1.2.2. Pitch

Pitch is a byproduct of the refining of petroleum or the distillation of coal tar. Pitch-based CFs have a high thermal conductivity, making them appropriate for applications requiring efficient heat transmission, such as those in the aerospace and energy sectors [11]. Pitch precursors provide a high carbon output, resulting in high CFs. Pitch-based CFs, on the other hand, have lower tensile strength and modulus than PAN-based fibers. Pitch-based CF manufacture is significantly more difficult and requires special machinery [8].

1.2.3. Rayon

Rayon is a synthetic fiber made from cellulose which is primarily derived from wood pulp. Rayon-based CFs have good mechanical properties, including tensile strength and modulus that are moderate [12]. Rayon CFs are often less expensive than PAN-based CFs. Rayon precursors have a lower carbon yield during carbonization, resulting in CFs with a lower carbon content. However, as compared to alternative precursors, rayon-based CFs are more flexible and easier to manufacture [13].

1.2.4. Bitumen

Bitumen, a dense and adhesive petroleum substance often known as asphalt, finds applications in road construction and industrial products due to its durability and weather resistance. Alberta, Canada, in particular, uses bitumen from oil sands, making it a valuable resource in a variety of applications. The utilization of Bitumen-based carbon fiber (BBCF) from Alberta represents an innovative response to the province's commitment to reduce oil sands usage for combustion purposes. In the pursuit of sustainable and high-performance solutions, this CF emerges as a promising alternative, bridging the gap between conventional materials and advanced technologies.

1.3. Carbon fiber application in construction industry

CF has shown great potential for various applications in the construction industry. The following contains some specific uses of CF in construction industry:

1. Concrete structure reinforcement: carbon fiber-reinforced polymer (CFRP) composites are used to reinforce and strengthen concrete structures such as beams, columns, slabs, and bridges [14]. CF reinforcement offers several advantages, including high tensile strength, excellent fatigue resistance, and corrosion resistance. CFRP composites are lightweight and have a high strength-to-weight ratio, making them an ideal choice for increasing the load-bearing capacity and extending the service life of structures [15].
2. Masonry structure Strengthening: CF sheets or strips can be attached to masonry elements such as brick or stone walls to increase their strength and seismic resistance. CF reinforcement increases flexural strength, enhances structural integrity, and helps in the prevention of cracking or failure under dynamic stresses [16,17] .
3. Structure repair and Rehabilitation: CF composite materials are often used to repair and rehabilitate damaged or deteriorated concrete structures. CF wraps or plates can be used to reinforce weak regions like columns, beams, or slabs [18,19].
4. Lightweight structures: CF composites are utilized in the manufacturing of lightweight

structures such as roofs, façade panels, and modular components. CF's light weight facilitates handling, transit, and assembly. Lightweight CF materials can contribute to energy-efficient construction and lower overall dead load on a building, allowing for new architectural concepts [20,21].

5. Seismic retrofitting: for seismic retrofitting of existing structures, CF reinforcing can be used. The ability of a structure to endure seismic stresses is considerably improved by adding CF composites to vulnerable or weak regions such as joints, connections, or shear walls. This contributes to the durability and safety of buildings in earthquake-prone areas [22,23].

CF electrically conductive pavements have gained popularity in recent years due to its capacity to alleviate snow and ice accumulation on road surfaces. These pavements create heat through the conductive characteristics of CF, effectively melting snow and ice and minimizing the requirement for manual snow removal or the usage of chemical deicers [24–27]. The CFs in the pavement form an electrically conductive network, allowing for the efficient flow of electrical current. When a current is provided, the resistance of the CFs generates heat, which is transported to the pavement surface, causing snow and ice to melt [28]. This technology has major benefits in cold climatic regions because it helps preserve clear and safe road surfaces, preventing accidents and promoting smooth driving.

While CF electrically conductive pavements, designed to melt snow and ice, are an innovative approach to winter road maintenance, the technology is still in its early stages, and comprehensive studies examining the long-term impact of snow and freezing and thawing (FT) cycle on the pavement's structural integrity are limited. Especially pavements in colder regions are prone to excessive FT cycles that can have more detrimental effects on the integrity of concrete structures. This deteriorative damage can be explained by two theories, hydrostatic pressure theory which suggests 9% expansion of water during freezing leading to microcracking [29,30] and osmotic theory which is about water vapor pressure difference between large and small pores that causes water to be forced into smaller pores [31]. There is indeed a lack of understanding when it comes to the deterioration of CFRC under FT conditions and comprehensive research is necessary to evaluate its behavior and durability in the specific intended environment.

1.4. Dissertation Objectives

The main objective of this dissertation is to study can be summarized in the following:

- Conduct a full physical characterization of the CFs, including microstructural analysis using SEM and EDX. (Goal: Understand the microstructure and composition of the fibers.)
- Investigate the microstructural characteristics of a new BBCF. (Goal: Assess the viability and unique properties of the new fiber.)
- Perform tensile strength testing, single fiber pull-out testing, and uniaxial dog bone testing on the fibers. (Goal: Determine the mechanical strength and bonding behavior of the fibers.)
- Measure the electrical resistivity of the CFs. (Goal: Evaluate the electrical conductivity of the fibers for potential applications.)
- Investigate the mechanical and fracture behavior of CFRM with various types and lengths of fibers. (Goal: Understand the performance and failure mechanisms of CFRM in order to select concrete mix designs for further analysis.
- Conduct tension and flexure testing on CFRC samples to assess their mechanical behavior, bending strength, and fracture resistance. (Goal: Evaluate the structural integrity and performance of CFRC under different loading conditions.)
- Study the freeze-thaw performance of CFRC samples to evaluate their durability and resistance to FT cyclic loading. (Goal: Assess the suitability and long-term performance of CFRC in cold climates.)
- Conduct a case study to evaluate the durability of an electrically conductive carbon fiber-reinforced composite bus pad and assess its performance and behavior in real-world conditions. (Goal: Assess the performance and behavior of the CFRC bus pad in real-world conditions.)

1.5. Research Outline

In **Chapter 1,** the background and importance of the study on CFRC in colder regions are established. It emphasizes the urgent need for maintenance and repairing of aged infrastructure, notably concrete bus pads, in colder temperature countries. To assure the lifetime and functioning of these structures, this chapter highlights the need of utilizing durable and high-performance materials. It recognizes the scarcity of thorough research on the performance of CFRC under cyclic FT loading circumstances and indicates the necessity to examine its application in snowy places. This chapter lays out the foundation for the succeeding research phases, which aim to design an effective CFRC mix, examine its bonding behavior, and evaluate its performance under FT conditions.

Chapter 2 which is a conference paper, entails a thorough investigation of the microstructure of BBCF. The goal of this phase is to get a thorough understanding of the physical and chemical characteristics of this particular form of CF. To examine and investigate the physical morphology of BBCF, several characterization techniques such as scanning electron microscopy (SEM) and energy dispersive x-ray (EDX) are used. Elemental composition analysis is also performed to determine the chemical elements of the fiber. This study assists in determining the composition and purity of the BBCF and allows for comparison with other commonly used CFs such as pitch-based and PAN-based fibers.

The results of microstructural investigation will provide essential knowledge into the distinctive features and characteristics of BBCF. These findings will serve as the foundation for future research and development.

Chapter 3 of the dissertation, which is a paper published in a peer-reviewed journal, mainly focuses on assessing the performance of CF and contrasting it with other types of fibers used in fiber-reinforced composites. The goal is to evaluate the bonding behavior and pull-out performance of CF using pull-out tests performed at various curing ages. Important parameters such as fiber tensile strength, average bond strength, equivalent bond strength, and average pull-out energy are investigated.

The findings of this chapter provide information into the performance of carbon fiber in FRC and its suitability for different applications. The study helps clarify fiber selection decisions for construction and engineering projects by comparing it to other fiber types.

Chapter 4 of the research, which is a presented conference paper, focuses on increasing the performance of CFs using surface coating methods. A comparative analysis is carried out to discover the most effective technique for enhancing ITZ and increasing mechanical characteristics of CFs. SEM is used to investigate the bonding between the CFs and the matrix, as well as to evaluate the impact of surface treatments on the fiber's surface. Sessile drop contact angle tests are also used to investigate the fiber's surface wettability, and four-probe electrical resistivity testing is used to assess the fiber's conductivity. Pull-out testing is used to assess the interfacial binding strength between the fiber and the matrix.

This knowledge will help the project team optimize surface coating procedures and improve the overall performance, durability, and application of CFRCC in following stages.

Chapter 5, which is a published paper in a peer-reviewed journal, focuses on the use of CFs as micro-reinforcement in round panels to avoid or retard crack development. This phase evaluates the yield-line theory for concrete pavements, as opposed to prior analyses that were confined to laboratory-scale samples. CF content and length are evaluated and compared to polypropylene fiber in terms of fresh properties and mechanical characteristics. A complete investigation of flexural strength using composite theory is included in the chapter, along with

predictions compared to experimental data. Concrete round panels are tested under center-point bending to determine the failure mechanism using yield-line theory. Overall, this chapter provides light on the practical application of CFRC in circular panels.

Chapter 6 of the thesis, which is a paper presently submitted in a peer-reviewed journal, focuses into the degradation of CFRC subjected to FT cycles. The use of CFs in concrete structures in snowy locations has grown in favor due to its self-deicing capabilities. However, there are uncertainties about how CFs affect the FT behavior, mass loss, and dynamic modulus of elasticity of concrete.

The study focuses at five different CFRC combinations with varied CF dosages (0.5%, 1%, 2%, and 3%). Every 30 FT cycles, non-destructive tests are performed to evaluate the quality of the concrete. The results offer experimental evidence of the effect of FT cycles on CFRC and emphasize the importance of fiber dosage.

Chapter 7 of the dissertation, which is a published peer-reviewed journal paper, presents the results of a case study comparing the performance of a CFRC bus pad with a normal concrete bus pad. The goal is to compare the real-time performance of the CFRC bus pad to that of a standard concrete bus pad. A variety of wireless sensors, including temperature and humidity sensors, thermocouples, and strain gauges, were placed in both pavements during construction. Data from both bus pads was collected on a regular basis, including visual inspections with a thermal imaging camera. Non-destructive testing (NDT) such as Schmidt Hammer (SH), Electrical Resistivity (ER), and Ultrasonic Pulse Velocity (UPV) were performed on both bus pads after 28 days of construction.

Overall, the case study provides valuable insight on the performance differences between CFRC and conventional concrete bus pads. These findings add to our understanding of how CFRC might improve the lifetime and durability of infrastructure.

1.6. Research Contribution

The research contribution of this dissertation can be summarized in the following:

- This dissertation provides a full grasp of the physical and chemical properties of BBCF through microstructural examination techniques such as SEM and EDX. The findings add to the body of knowledge by providing critical information on the distinguishing traits and characteristics of BBCF, allowing for further research and development of this newly developed CF.
- This dissertation compares CF's bonding behavior and pull-out behavior in fiber-reinforced composites to other types of fibers used in construction. The analysis of critical metrics such as fiber tensile strength, bond strength, and pull-out energy reveals information on the performance of CF.
- This dissertation investigates several surface coating strategies for improving the ITZ and mechanical properties of CFRCs. Using a novel fiber coating technique, this research contributes to optimizing surface coating procedures and improving the overall performance and durability of CFRCC by investigating the bonding between the CFs and the matrix, as well as evaluating the impact of surface treatments on the fiber's surface.
- Using the yield-line theory for concrete pavements, this dissertation investigates the use of CFs as micro-reinforcement in round panels to avoid fracture development. The investigation of flexural strength utilizing composite theory, as well as the evaluation of CF content and length, adds to practical insights into the application of CFRC in circular panels.
- The dissertation emphasizes the context and significance of exploring CFRC in colder regions, highlighting the critical need for long-lasting and high-performance materials for infrastructure maintenance and repair in colder climate countries. It acknowledges the scarcity of comprehensive research on the performance of CFRC under cyclic FT loading conditions and comprehensively investigate its applicability in snowy areas. The experimental evidence collected from evaluating concrete quality following FT cycles provides important insights into the impact of FT behavior and fiber dosage on CFRC.
- The dissertation includes a case study that compares the real-time performance of a CFRC bus pad to that of a typical concrete bus pad. The study provides useful insights into the performance differences and potential advantages of CFRC in terms of lifetime and durability for infrastructure applications by utilizing embedded sensors and conducting non-destructive testing.

1.7. Research Limitation

Several challenges have emerged throughout the research work that can be summarized as following:

1- The procurement of BBCF fiber was a challenge as only 7 grams were received, limiting the microstructure analysis.

2- The brittleness of BBCF resulted in difficulties in microstructural testing, and its tendency to transform into powder upon touch made mechanical testing nearly impossible.

3- The micrometer diameter of CF made performing electrical resistivity, pull-out, and contact angle tests on a single fiber unfeasible.

4- Monitoring the electrical resistivity of Fiber-Reinforced Concrete (FRC) samples during Freeze-Thaw (FT) testing could significantly contribute to investigating the self-deicing properties of the composite. However due to the FT concrete molds, it was not possible to insert any electrodes.

5- The non-destructive equipment and sensors used in this research were initially designed for non-conductive concrete. However, the incorporation of carbon fibers rendered some devices inapplicable, as the presence of carbon fibers interfered with the signals of these devices

6- The initially planned 225 mm 40 MPa concrete pavement deviated significantly from the design due to the project being handed over to a local contractor.

7- The concrete pavement, utilized as a daily bus stop, presented challenges for regular monitoring, thereby affecting the frequent assessment of its condition.

Chapter 2. Microstructural properties of carbon fibers

Paper Title: Microscale characteristics of new Bitumen-Based Carbon Fibers

Author(s): Maryam Monazami, Rishi Gupta

This paper was presented at the 2nd International Conference on New Horizons in Green Civil Engineering in Victoria, BC and has been subtly modified to ensure alignment with the dissertation's integrity and overall flow [29]. It focuses on the microscale characteristics of a new type of carbon fiber called bitumen based carbon fiber (BBCF). The chapter demonstrates the use of various microscale techniques to investigate different properties of this new precursor material, which is used in the production of carbon fiber. The research aims to provide insights into the microscale behavior and properties of BBCF, contributing to the development and understanding of carbon fiber characteristics.

2.1. Introduction

Industries have shown a growing interest in utilizing sustainable and renewable materials in the development of new composites. This interest stems from the desire to enhance specific properties of composites while ensuring their environmental sustainability. As a result, a wide range of shapes and materials, including both synthetic and natural materials, are being employed in various products. One approach to enhancing composite properties is through the incorporation of additional reinforcements, such as fibers. By adding fibers to composites, manufacturers can extend and improve their overall properties, aligning them with the requirements of diverse engineering applications. These improvements encompass both economic and functional aspects, making the composites more cost-effective and suitable for a broader range of applications. According to ACI 544 committee [30], there are four categories for FRC: SFRC (steel fiber reinforced concrete) GFRC (glass fiber reinforced concrete), SNFRC (synthetic fiber reinforced concrete) and NFRC (natural fiber reinforced concrete).

Among the many different types of fibers that are being used in concrete, CFs have been extensively exploited over the past few years due to their self-sensing ability. CFs can be classified as synthetic fibers. CFRC is highly suitable to maintain the longevity of infrastructure where corrosion of steel can shorten the useful service life of the structure. Therefore, this chapter presents an overview of the developments made in the area of carbon fiber cementitious composite (CFRCC) in terms of their types and properties, morphology, and application in concrete, and introduces a new type of BBCF for future applications that

underscores the roles of material scientists and manufacturing engineers for the future of this new CF through value addition to enhance its use.

Different industries, including aerospace, automobiles, construction, sports, and transportation, have embraced the use of CFs for distinct purposes. The concept of CFRC emerged in the 1980s, primarily by utilizing affordable pitch-based CFs [31]. One of the first studies on the incorporation of CFs in cement mortar was done by Ohama et al. [32], who reported that increasing the content of pitch CFs will improve the hardened properties of mortar. However, 3 mm CFs showed better results in comparison with 10 mm fibers. In the early 1990s, Banthia et al. [33] investigated the impact resistance of CFRM. A significant increase in fracture energy was observed in carbon fiber reinforced samples. A comprehensive study was done by Dr. Chung's research group about CFs [34–39,3]. The capability of concrete for detecting flaws [34] was studied and the new type of concrete was introduced as a new strain-stress sensor [35]. Traffic monitoring, fatigue damage self-monitoring and drying shrinkage of CFRC were also investigated [36–38]. The results approved the positive effects of reinforcing concrete with CFs. However, in recent years, many researchers have focused on the special effects of CFs in concrete, such as ice prevention [40], deicing [27,41], reinforcing pervious concrete [42], being used in repair material [43] and other special properties [44–46] that make it a special type of fiber with multiple beneficial aspects.

This chapter provides a concise review of recent advancements in CFRC as well as introduces a new sustainable and low-cost type of BBCF. A systematic study on the microstructure and elemental composition of Bitumen-based, Pitch-based, and PAN-based CFs was carried out to compare the newly introduced fiber with the previously widely used CFs. SEM was carried out to investigate the physical morphology, including surface texture of the three groups of fibers and EDX was employed to obtain the elemental spectrum of the specimens.

2.2. Carbon fibers

2.2.1. Properties

CFs possess beneficial properties that have the potential to greatly improve the behavior of concrete, particularly in terms of durability and strength. However, it is important to note that commercially available CFs are generally more expensive compared to other fiber types. These fibers exhibit high tensile strength and elastic modulus, with specific values varying depending on the type of fiber used. Another valuable characteristic of CFs is their chemical

inertness, rendering them resistant to most chemicals. CFs can be broken down into two major subcategories called PAN and pitch, which are created by different precursors and thus yield different mechanical and physical properties [47]. Apart from PAN and Pitch precursors, there are additional precursors used for CF production, such as cellulosic, silk, chitosan, and rayon. CFs can also be classified on the basis of the fiber structure and degree of crystallite orientation: ultrahigh-modulus (UHM), high-modulus (HM), intermediate-modulus (IM), high-tensile-strength (HT), and isotropic CF [48]. Table 1 shows the classification of CFs [48].

Table 1. Classification of carbon fibers

<table>
<tr><th>Carbon fiber type</th><th>Heat treatment temperature (°C)</th><th>Crystallite orientation</th><th>Long-distance order</th><th>Classification</th></tr>
<tr><td rowspan="2">Type 1 high modulus</td><td rowspan="2">> 2000</td><td rowspan="2">Mainly parallel to fiber axis</td><td rowspan="2">High</td><td>UHM</td></tr>
<tr><td>HM</td></tr>
<tr><td>Type 2 high strength</td><td>≈ 1500</td><td>Mainly parallel to fiber axis</td><td>Low</td><td>IM
HT</td></tr>
<tr><td>Type 3 isotropic</td><td>< 1500</td><td>Random</td><td>Very low</td><td>Isotropic</td></tr>
</table>

2.2.1.1. PAN fibers

Over the years, acrylic precursors have been used for CF preparation by many manufacturers. Polyacrylonitrile (PAN) is the most commonly used acrylic precursor to create CFs. Approximately 70-80% of commercially produced CFs are created from PAN polymers [49]. PAN CFs are produced by carbonizing polyacrylonitrile at high temperatures and then aligning the crystallites by stretching to create the fibers [47].

2.2.1.2. Pitch fibers

Precursors for pitch CFs have a high modulus of elasticity in comparison to PAN CFs. Although the elasticity is high, pitch CFs have poor compressive properties when compared to PAN fibers. Pitch precursors are usually a mix of polyaromatic molecules and heterocyclic compounds. Normal pitch fibers are produced by refining petroleum or the distillation of coal, which tends to be a less expensive process than producing PAN fibers [48].

2.2.1.3. Morphology

Chae et al [50] have reported that most PAN-based CFs exhibit a particulate morphology, whereas pitch-based CFs exhibit a sheet-like morphology. PAN-based CFs show higher tensile and compressive strengths than pitch-based CFs because PAN-based fibers consist

of particle-like structures and smaller crystals in comparison with the sheet-like structure and larger crystals in pitch-based fibers. However, it is important to note that reports on the morphology of CFs can vary across different research papers and depend on the specific classification of the fibers being studied. Different manufacturing processes, precursor materials, and conditions can influence the resulting morphology of CFs, leading to diverse observations in different studies. In a study by Kim et al. [51], the SEM photos of PAN film show that they are relatively flat and exhibit a dense sponge-like structure. Naito et al. [52] suggested that there is a big difference in the morphology of high and ultra-high strength PAN-based CF with high modulus pitch-based CFs. From the SEM photos, the fractured surfaces of the high and ultrahigh strength PAN-based CFs exhibit a rough, rather poorly defined granular texture with no indication of sheet-like structures, but high modulus pitch-based CFs have slightly sheet-like structures in their cross sections.

2.2.2. Carbon fibers in concrete

CFs are usually added to concrete to give it the property of self-sensing [53]. By adding CFs to concrete, the resulting electrically conducting concrete can serve as a smart structural material capable of non-destructive electrical probing for flaw monitoring [34]. There have been numerous studies that have investigated the effects of the incorporation of different types of CFs in concrete. Table 2 shows the properties of some types of CFs used in concrete.

Table 2. Carbon fiber properties in previous studies

Type	Length	Equivalent diameter	Specific gravity	Tensile strength	Elastic Modulus	Reference
	(mm)	(μm)		(Mpa)	(Gpa)	
PAN	3	18		650	35	[54]
PAN	5	7	>1.75	1950	>175	[55]
PAN	spool	-	1.6	3600	230	[56]
PAN		6.5	1.79	4000	240	[57]
PAN	spool	-	1.6	5600	276	[56]
Pitch	5.1	10	1.6	690	48	[34]
Pitch	5	10				[37]
Pitch	5	15	1.6	690		[58]
Pitch	5	15± 3	1.6	690	48	[36]
Pitch	5	7	1.78	>3000	220-240	[59]
Pitch	-	11.49	-	3200	940	[60]
Pitch	Plain weave	7	-	3530	920	[61]
Pitch	5	11.55	-	4000	935	[62]
×	5	7	1.6	2500	240	[63]
×	5	7	>1.75	1950	>175	[64]

Chen et al. [65] investigated the conductive behavior of CF cement-based composites. The influence of CF volume, size, cement-based matrix, relative humidity and curing age on the characteristics of the new composites was studied in the investigation. The results showed that the relationship between conductivity and volume fraction of CF obeys the statistical percolation theory, and the theory is applicable for the change in conductivity of a system with the volume of CF.

Shi et al [36] were one of the first researchers to investigate the effects of CF being used for traffic monitoring. They added 5 mm pitch carbon into their concrete mixtures (0.5% and 1% by weight of cement) and reported that self-monitoring concrete containing short CFs is effective for traffic monitoring and weighing in motion. The results showed that that the resistance decreases reversibly with increasing stress up to 1 MPa and is independent of speed up to 55 mph. Other researchers also approved the effects of other carbon products such as carbon black filler and carbon nanotubes to be used in traffic monitoring [66,67].

The capability of CFs to be used as thermal sensors has been reviewed in several studies [68,64,55,69]. In 1999, Mingqing et al. [68] examined the relationship between the temperature differential and thermoelectric force in CFRC. The results showed that thermoelectric force is proportional to temperature change over a wide range of temperatures, and the self-monitoring CFRC possesses high sensitivity and good repeatability. The final result revealed that CF can be used as a thermal sensor embedded in massive concrete structures.

Piezoelectric and piezoresistive properties of CFs in mortar and concrete were also studied by a few researchers. Sun et al. [64] studied the piezoelectric properties of concrete with short CFs under dynamic loading. The results revealed that the new composite can be used as a good sensor for monitoring dynamic loading. Azhari et al. [53] worked on developing a new composite with 5 mm pitch-based CFs and carbon nanotubes that enhance the electrical conductivity of concrete. The results showed that under cyclic loading, the changes in resistivity mimic the changes in applied load and material strain with high fidelity. Bontea et al. [70] classified damage in concrete in two groups of minor and major damage and studied the effects of adding short pitch CFs on the resistance of concrete. Fibers in the amounts of 0.5, 1 and 2% by weight of cement were used in concrete samples and the damage in concrete reinforced with short CFs was monitored by measurement of the DC electrical resistance in the stress direction during repeated compressive loading at increasing and decreasing stress amplitudes. A minor damage that didn’t change the compressive modulus being revealed by a partially reversible increase in resistance was resulted from the invetigation, which occurred mainly during loading, particularly at a stress above that in prior loading cycles. The results also showed that that major damage that was accompanied by a decrease in modulus was

revealed by the damage-induced resistance increase occurring in every loading cycle irrespective of the prior loading and by an irreversible increase in the baseline resistance.

During the past few years, self-heating concrete has become an attractive topic among researchers. The aim is to produce a type of concrete that can thaw the snow and ice above it. Gomiz et al. [71] studied the self-heating property of carbonaceous cement paste produced by the application of an electric current to conductive cement pastes. One of the carbonaceous materials was the 3 mm CF used in the cement paste. The results indicated that addition of carbonaceous compounds to cementitious materials will reduce the electrical resistance of the resulting material, so that application of a potential difference produces an electric current by the Joule effect, which quickly melts the ice accumulated or prevents its formation. Galao et al. [40] also conducted research on the feasibility of conductive CFRC as a self-heating material for ice formation prevention and curing in pavements. Tests were carried out in lab ambient conditions at different voltages and then specimens were put in a freezer at 15 °C. The specimens inside the freezer were exposed to different fixed voltages when reaching +5 °C for prevention of icing and when reaching the temperature inside the freezer, i.e., -15 °C, for curing of icing. The test outcome revealed that that the new type of concrete with 2% oxidized PAN CF (by weight of cement) could act as a heating element in pavements with a risk of ice formation. It also consumes a reasonable amount of energy for both anti-icing and deicing. Wu et al. [41] used three kinds of electrically conductive materials in concrete, namely steel fiber, carbon fiber, and graphite to deice concrete pavements. The results revealed that 1% volume fraction of steel fiber, 0.4% volume fraction of carbon fiber, and 4% volume fraction of graphite are the optimum percentages for deicing pavements.

2.2.3. Bitumen

Bitumen is a semi-solid material that can be produced either from certain crude oils or in nature as “natural asphalt”. Bitumen consists of a mixture of hydrocarbons of different molecular sizes containing heteroatoms like Sulphur and nitrogen as well as traces of metals like vanadium and nickel, However, the true nature of bitumen is not completely known. Recent studies on bitumen chemistry describe that bitumen is a colloidal dispersion of asphaltenes in maltenes [72]. According to SARA separation, bitumen can be classified into four groups: saturants, aromatics, resins and asphaltenes [73]. High-quality CFs can be produced from bitumen due to its composition and molecular constituents [74]. Bitumen has the potential to be utilized in the production of PAN and potentially pitch product. This can be achieved by processing cracked gas derived from bitumen. The distinctive high-asphaltene content found in oil sands bitumen makes it a particularly suitable raw material for these processes [75].

2.3. Fiber characterization

Three types of pitch, bitumen and PAN-based fibers according to Figure 2, were investigated in this study. Pitch fibers were acquired from Mitsubishi Chemical Carbon Fiber and Composites and PAN fibers were acquired from Teijin Chemicals. The properties of fibers as provided by the manufacturers are summarized in Table 3.

Table 3. Properties of fibers

Type	Equivalent diameter (μm)	Specific gravity	Tensile strength (MPa)	Elastic Modulus (GPa)
Pitch	11	2	2345	186
PAN	7	1.8	4890	227

(a) (b) (c)

Figure 2. a) pitch-based carbon fibers b) bitumen-based carbon fibers c) PAN-based carbon fibers

2.3.1. Scanning electron microscopy

Figure 3 shows the morphology of the microstructure of the three types of fibers. It is evident that both pitch-based and PAN-based fibers exhibit a textured outer surface, while the surface of the BBCF appears smoother in comparison. The presence of this rough texture can enhance mechanical anchoring within composite materials by improving the quality of the fiber/matrix interface [76]. Figure 4 shows SEM photos of the newly developed BBCF at different scales and locations. The cross-section of this fiber is circular, and the fibers are arranged in parallel to each other in a bunch. Furthermore, the thickness of fiber ranges from 10 to 15 μm. The SEM photo of the cut surface of the fiber confirms its smooth texture on the diameter.

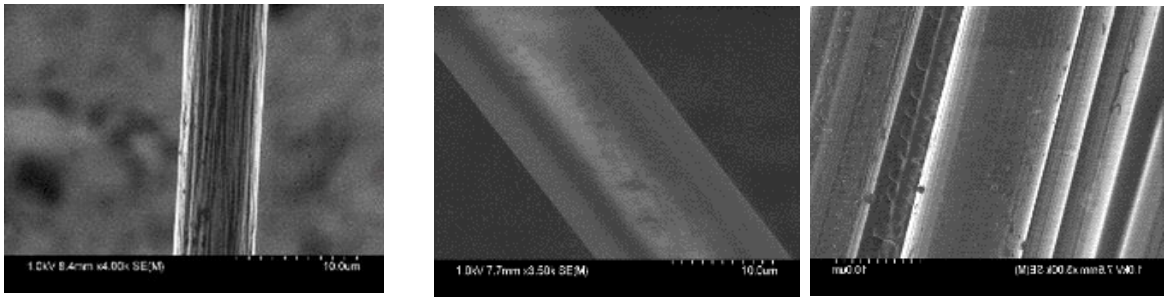

(a) (b) (c)

Figure 3. SEM photos of a) pitch-based carbon fibers b) bitumen-based carbon fibers c) PAN-based carbon fibers

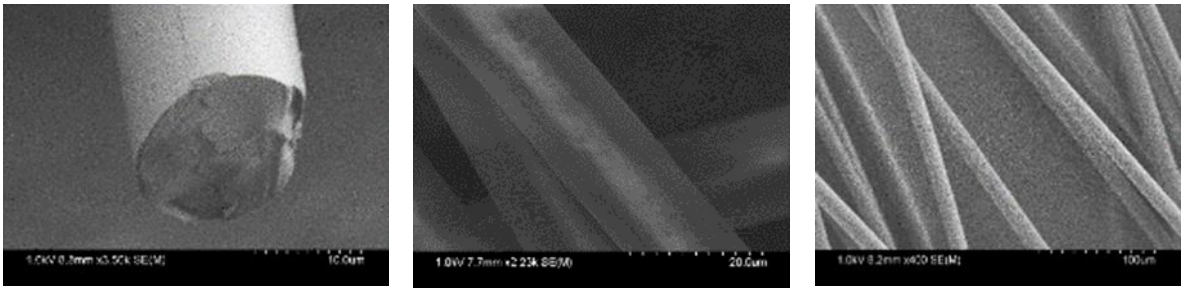

Figure 4. SEM photos of a) cross-section b) longitudinal view and c) bunch of bitumen-based carbon fibers

2.3.2. Energy dispersive x-ray

EDX was tested at least on three different points and surfaces on fibers to confirm the validity of the results. EDX results can be found in Figure 5. EDX provides information on carbon (C), Oxygen (O), Nickel (Ni), Vanadium (V), Titanium (Ti) and Sulphur (S) content of three groups of CFs. As expected, carbon is the primary component in all types of fibers, but the carbon content varies among different fibers. In the case of BBCF, the carbon content of 81% is relatively low compared to other available fibers. Moreover, BBCFs contain approximately 6% of Sulphur which necessitates further investigation and analysis of additional samples. Other types of pitch and PAN fibers didn't show any traces of Sulphur in their combination.

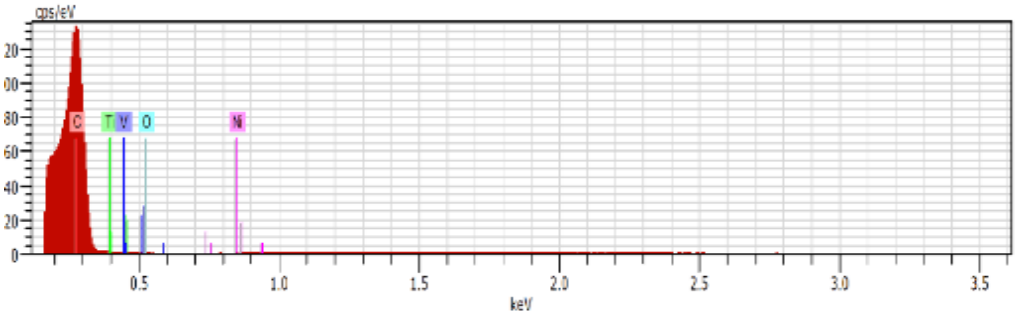

EL	AN	unn. C (wt.%)	norm. C (wt.%)	Atom C (wt.%)	Error C (%)
C	6	93.81	93.81	95.29	28.2
O	8	6.16	6.16	4.7	1.9
S	16	0	0	0	0
V	23	0	0	0	0
Ti	22	0	0	0	0
Ni	28	0.02	0.02	0	0

(a)

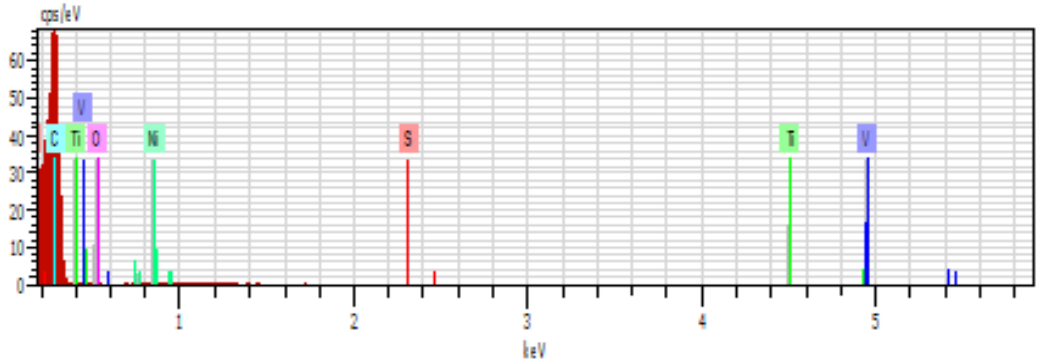

EL	AN	unn. C (wt.%)	norm. C (wt.%)	Atom C (wt.%)	Error C (%)
C	6	81.1	81.1	87.48	24.6
O	8	12.1	12.1	9.8	3.9
S	16	6.61	6.61	2.67	0.3
V	23	0.08	0.08	0.02	0
Ti	22	0.05	0.05	0.01	0
Ni	28	0.06	0.06	0.01	0

(b)

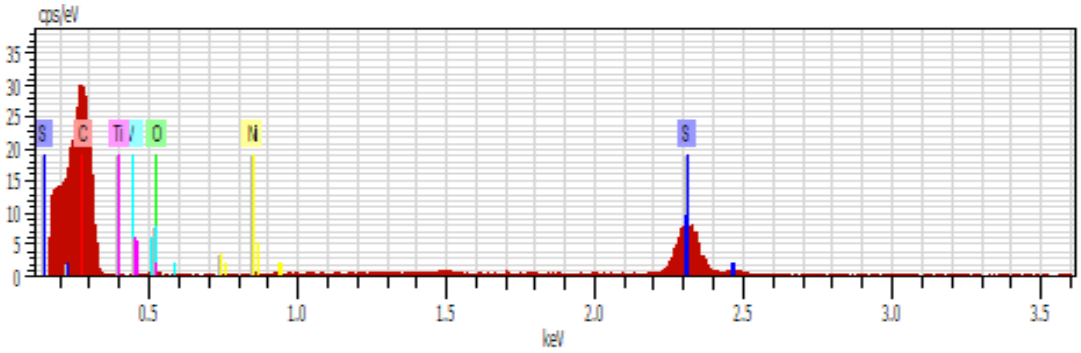

EL	AN	unn. C (wt.%)	norm. C (wt.%)	Atom C (wt.%)	Error C (%)
C	6	97.97	97.97	98.55	29.4
O	8	1.88	1.88	1.42	0.6
S	16	0	0	0	0
V	23	0	0	0	0
Ti	22	0.01	0.01	0	0
Ni	28	0.14	0.14	0.03	0.1

(c)

Figure 5. EDX results of a) pitch-based b) bitumen-based c) PAN-based carbon fiber

2.4. Alberta bitumen-based carbon fiber microstructural analysis

To conduct a more comprehensive analysis of the microstructure of CFs, a second round of analysis was performed, involving a larger number of samples. In this second round, point, area, and line scans using EDX were conducted on the BBCF. The focus was on investigating the surface, diameter, and composition of the carbon fiber.

The SEM photos of the BBCF, as shown in the Figure 6, reveal several noteworthy observations. Firstly, many of the CFs appear to be broken in the SEM images, indicating potential fragility or brittleness of BBCF. Additionally, a significant number of fibers that showed cylindrical microstructure are hollow inside. The diameter of the fibers varies considerably, ranging from 16.7 to 38.6 micrometers, indicating a wide size distribution. Furthermore, the SEM images demonstrate the presence of micropores on the surface of the BBCF, suggesting potential porosity within the fibers.

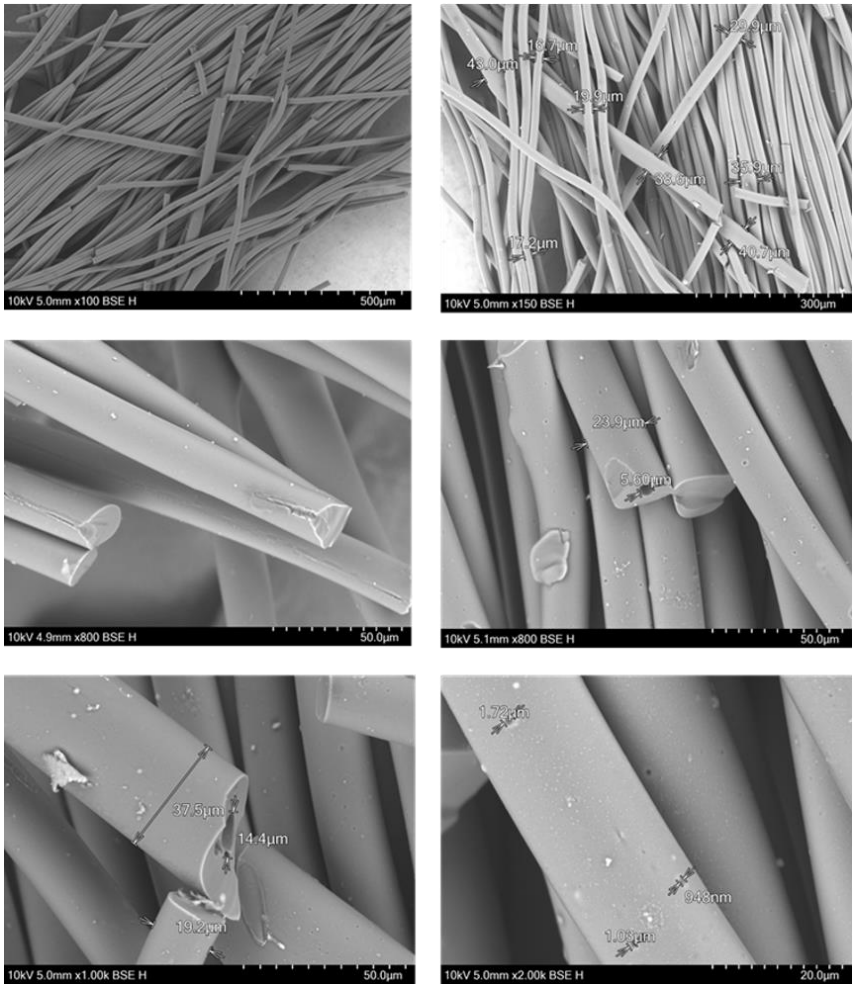

Figure 6. SEM of BBCF

Figures 7-9 show the elemental map, elemental point analysis and line scan profile of the BBCF. The results obtained from the subsequent round of EDX analysis further validate the initial findings and confirm the presence of sulphur in the BBCF.

The elemental map provides a visual representation of the distribution of different elements within the CFs, confirming the presence and concentration of sulphur in specific areas. The line scan profile offers a quantitative analysis of the elemental composition along a designated path, shows a very small sulfur peak corresponding to the BBCF samples. Additionally, the elemental point analysis focuses on specific locations to provide detailed information about the presence of around 5% sulphur on the fiber surface. By conducting this additional EDX analysis, the presence of sulphur in the BBCF is unequivocally confirmed.

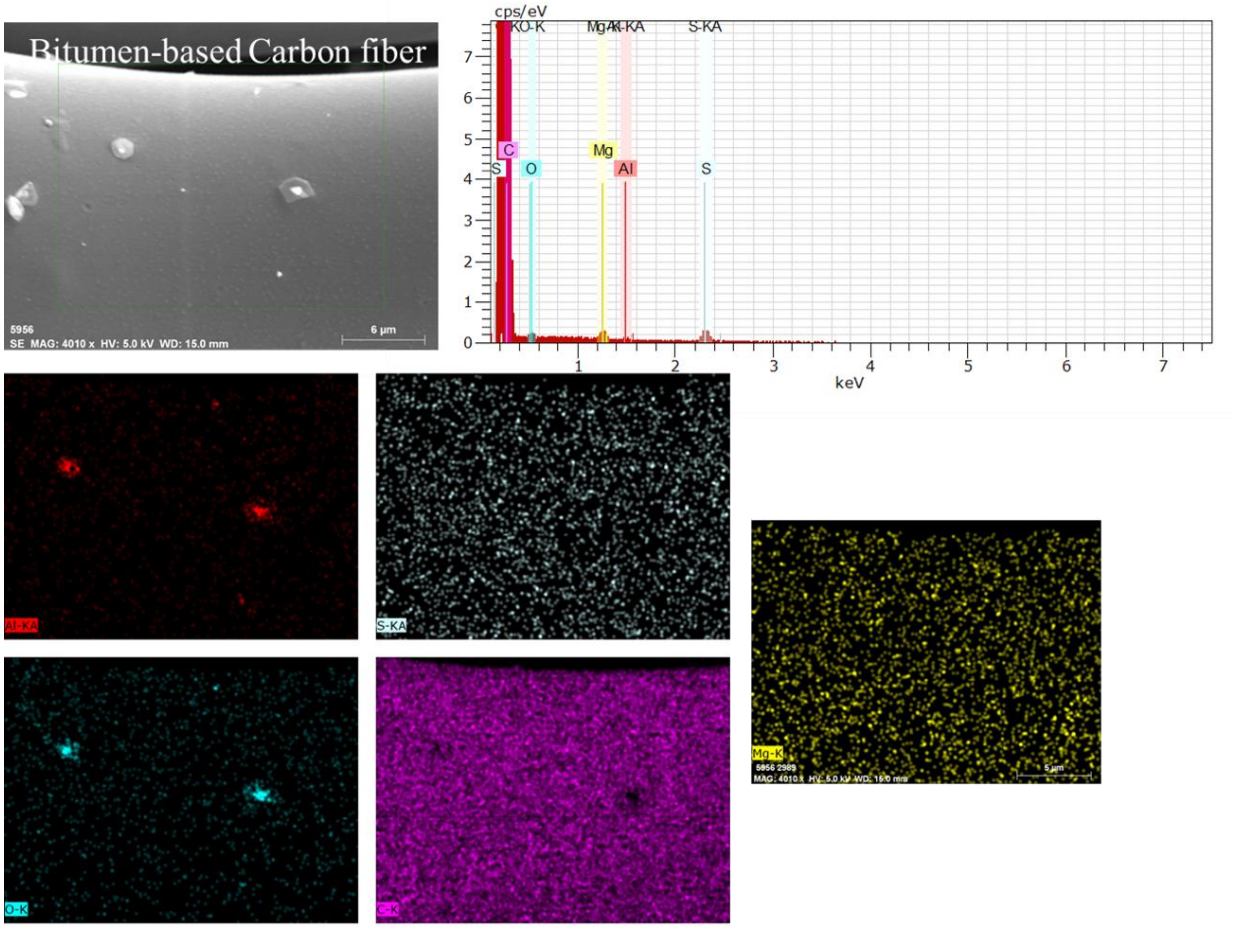

Figure 7. Elemental map of BBCF

El	AN	Series	unn. [wt.%]	C norm. [wt.%]	C Atom. [at.%]
C	6	K-series	92.74	92.74	96.86
S	16	K-series	5.58	5.58	2.18
Mg	12	K-series	1.36	1.36	0.70
O	8	K-series	0.32	0.32	0.25
Si	14	K-series	0.00	0.00	0.00
Al	13	K-series	0.00	0.00	0.00
Total:			100.00	100.00	100.00

El	AN	Series	unn. [wt.%]	C norm. [wt.%]	C Atom. [at.%]
C	6	K-series	94.11	94.11	97.49
S	16	K-series	4.70	4.70	1.82
Mg	12	K-series	0.83	0.83	0.43
O	8	K-series	0.31	0.31	0.24
Si	14	K-series	0.04	0.04	0.02
Al	13	K-series	0.00	0.00	0.00
Total:			100.00	100.00	100.00

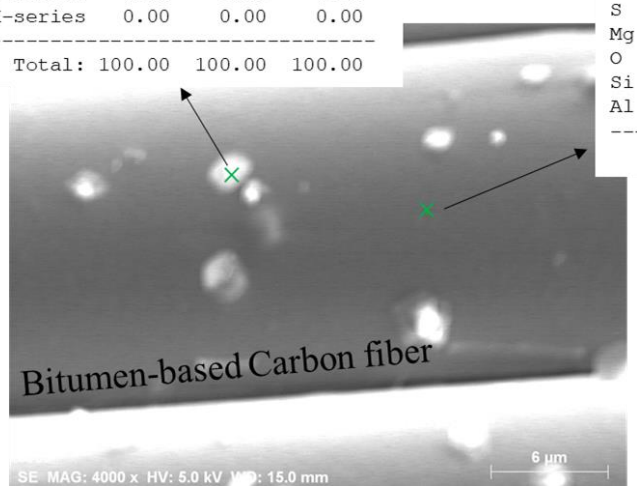

Figure 8. Elemental point analysis of BBCF

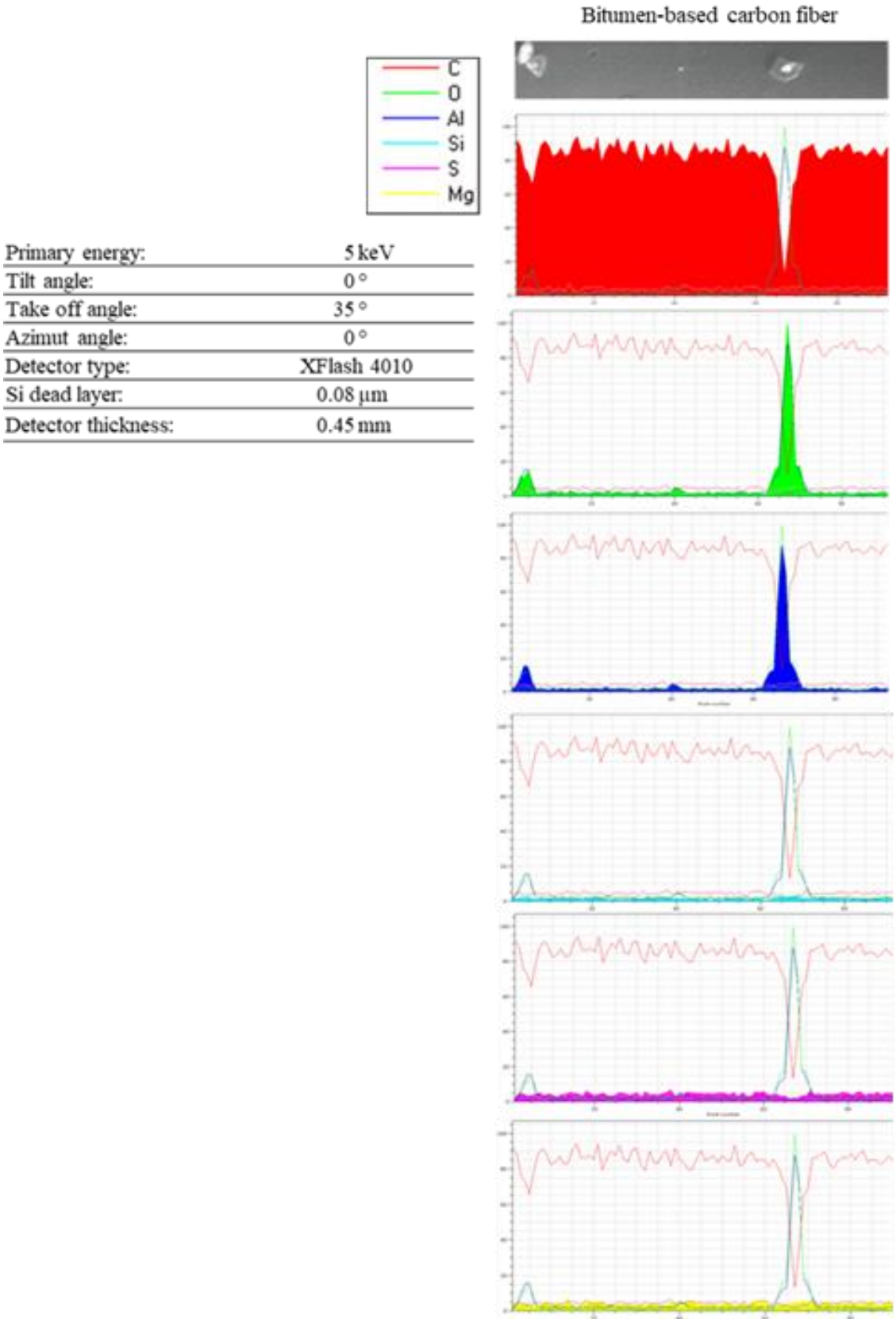

Figure 9. Line scan profile of BBCF

2.5. Conclusion

This chapter presents a review of various CFs available today that can be used for producing cementitious composites. In this chapter, the properties of a new carbon fiber extracted from bitumen were studied in order to evaluate the possibility of using it as reinforcement in cementitious materials. The following conclusions were drawn from the results of the microstructural tests of this new natural fiber.

- The study of the surface morphology by SEM revealed that the cross-section of BBCF has a circular shape similar to other fibers and the surface of it is smooth. BBCFs are in parallel to each other in bundles.
- EDX results showed around 6% of Sulphur in BBCF which necessitate the need for further confirmatory investigation.
- The BBCF exhibits notable variations in diameter, ranging from 16 to 43 micrometers. This wide range in diameter influences its mechanical and performance characteristics.
- The surface of the BBCF from Alberta is adorned with numerous small pores. These pores could play a role in influencing properties such as porosity, absorption, and interfacial interactions.
- BBCF has a different structural appearance compared to other fibers, with certain fibers showing a hollow cylindrical design while others remain solid. This variation in fiber structure can significantly influence the fiber's performance, as evidenced by fractures occurring at points where solid transitions to hollow.

Chapter 3. Effect of curing age on pull-out response of carbon fibers

Paper Title: Effect of curing age on pull-out response of carbon, steel and synthetic fiber embedded in cementitious mortar matrix.

Author(s): Maryam Monazami, Rishi Gupta

The paper has been published in a peer-reviewed journal [77] and has been subtly modified to ensure alignment with the dissertation's integrity and overall flow. The study focuses on investigating the interfacial bond properties between fiber and matrix in fiber-reinforced composites, as this bonding directly influences the mechanical behavior of the composites. The objective of the chapter is to investigate the interfacial bond properties between fiber and matrix in fiber-reinforced composites by analyzing the pull-out responses of carbon, steel, and synthetic fibers embedded in a cementitious mortar matrix at different curing ages. The study aims to evaluate fiber tensile strength, average bond strength, equivalent bond strength, and average pull-out energy, while also examining the failure modes of different fiber types. Additionally, the research aims to compare the pull-out load, bond strength, and tensile strength among the different fiber types and determine the influence of curing age on these properties. By achieving these objectives, the study enhances understanding of the fiber-matrix interface bonding behavior, contributing to the optimization and improvement of fiber-reinforced composites.

3.1. Introduction

Fibers primarily contribute to post cracking behavior of a composite by transmitting forces via fibers that bridge cracks [78]. The aforementioned transmission of forces is achieved through interfacial bonds defined as the shearing stress at the interface between the fiber and the surrounding matrix [79]. However, if the interfacial bond between the fiber and the surrounding cement matrix is weak, the fiber will slip within the surrounding matrix and cannot help preventing crack propagation. Conversely, if the bond is too strong, fibers may rupture before they can help improve the post-crack strength of the matrix [80]. Due to the effects of interfacial bond strength on post-crack behavior as well as the significant influence of the fiber-matrix ITZ on the mechanical and long-term behavior of fiber-reinforced cement composites (FRCC) [81], bond behavior in FRC is recognized as a major factor in composite action [80]. However, understanding bond characterization in FRCC is complex because of the simultaneous actions of several bond components including: 1) physical and chemical adhesion between fiber and matrix; 2) the mechanical component of bond such as in deformed, crimped, and hooked fibers; 3) fiber-to-fiber interlock; and 4) friction [82].

There are different pull-out techniques suggested by researchers to determine interfacial strength parameters in FRCC. One method involves single fibers that are pulled out of a cylindrical specimen in which the specimen was directly glued to a bottom plate [7]. Another method [79] includes embedment of a single fiber in a cement matrix block. The top end of the fiber is held by a grip, and the bottom end is attached to a linear variable differential transducer (LVDT) connected to the bench of the machine. A method proposed by Singh et al. [83] consists of pouring wet mortar in a small cylindrical mold (2-mm in diameter by 50-mm long) and putting the fiber in the matrix from the top and holding it in a slot. Another method suggested by Rato et al. [84] consists of putting each fiber in a dog-bone-shaped mold. This involves putting 25 mm embedded length on each side of a plastic separator located in the middle of the mold.

Despite a variety of pull-out techniques, calculation of interfacial bond strength between fiber and matrix and fiber pull-out energy is still one of the common approaches to determine the performance of fiber in FRCC. In recent years, considerable progress has been made in practical aspects of pull-out experiments as well as in the methods of data acquisition. However, an analysis of the force–displacement curves obtained from pull-out tests still yields useful information which characterizes fiber–matrix interfacial bond properties more adequately.

Numerous investigations have been conducted to determine fiber–matrix interfacial bond properties. Steel fibers (SF) are one of the common types of fibers used to reinforce concrete and as a result many research studies focused on bonding strength of SF in cementitious materials. Steel fibers are available in different shapes to be used in concrete. Naaman et al. [79] studied three types of steel fibers (smooth, deformed, and hooked) embedded in low, medium and high strength concrete. The pull-out test result showed that deformed fibers resisted pull-out in an oscillatory fashion, while hooked fiber resistance consistently decreased as the hook straightened as it traveled through the tunnel. Abu-Lebdeh et al. [85] reported that hooked end steel fibers showed 88-160% and 14-137% increase in the peak load and pull-out energy subsequently when they were compared to smooth steel fibers in concrete. It is also reported that hooked end steel fibers with smaller diameter show better fiber-bond behavior [86]. Other important parameters in the pull-out behavior of steel fibers such as embedment length [87], embedment inclination [88], loading rate [89], fiber distance [90], fiber coating [91] and matrix strength [85] effects have also been studied in recent years.

There is an increasing demand for other types of fibers such as synthetic macro fibers (SI) and CFs to be used in FRCC such as ground slabs and precast members [92,93]. Several studies on the synthetic fiber pull-out behavior in cement-based composites have been conducted. Straight SI were reported to show poor bonding behavior in matrix [94] and crimped-shaped SI were reported to be the optimum shape when used in concrete [95]. The

effects of embedment length and loading rate were investigated by Babafemi et al. [92], and the results showed that the pull-out strength of synthetic macro fiber is dependent on loading rate. Specifically, that a higher loading rate resulted in higher pull-out strength at all the embedment lengths.

Cement-based composites with short CF are attractive due to their high flexural strength, high toughness and low drying shrinkage in addition to their strain sensing ability [38,96,59,93,97]. CF when compared to other types of fibers are generally more expensive. However, using CFRCC as multifunctional structural elements can reduce costs and increase the durability of the composite once placed in service conditions [93]. This multifunctional composite shows superior structural functions such as enhanced mechanical strength [54,98] as well as non-structural functions such as its self-sensing ability [38, 97, 98] attributed to the excellent mechanical properties and light weight of CF. Commercially available CFs usually come in bundles, however, studies in which CF are dispersed uniformly have rarely been conducted [2]. Lu et al. [101] conducted a study on the effect of nano-SiO2 surface coating was evaluated using single CF pull-out test in which the interfacial strength of the coated CF in cement matrix is reported to be significantly higher in comparison to that of plain CF. However, to the authors knowledge, no work has been published to assess the interfacial transition zone between the cement matrix and CF bundle and as a result, further study is needed to evaluate the bond behavior of CF bundles in the cement matrix.

Although a large number of studies have been developed to investigate the effect of curing age on the pull-out behavior of steel fibers, it is still difficult to find information related to the curing age effect on CF and SI interfacial bonding. Jewell et al. [80] recently investigated the effect of ageing (1 to 56 days of curing) on bond strength of steel and polypropylene fibers (PP), and the test results revealed that low-modulus PP are best suited to resist pull-out forces at early ages of curing (<7 days), while SF have the highest bonding strength at 28 days of curing. In another study by Le et al. [102] bond strength of steel fibers in different ages and storage conditions was investigated until 120 days. The results showed that bond strength of steel fibers, cured in water for 28 days and then stored in air until 120 days increased, while the bond strength of steel fibers cured in water for 120 days decreased by time.

While there is still a perceived lack of information on pull-out behavior of CF reinforced cementitious composites and the effect of matrix aging, an experimental procedure was developed in this research to investigate and compare the effects of fiber type and curing age simultaneously. In this chapter, a series of pull-out tests were performed at different ages using the pull-out method suggested by Ratu et al. [84] in which the load and the displacement were accurately measured simultaneously. Pull-out behavior of four different fiber types (SF, SI, PAN-based CF and pitch-based CF) were investigated. The pull-out loads versus displacement, peak loads, dissipated bond energy and equivalent bond strength were

evaluated. According to the results, different failure patterns were recorded based on the fiber type. CFs experienced a sudden drop after reaching the peak load whereas, the load decrease in steel and synthetic fibers was not as abrupt. Results also confirmed that steel fibers exhibited the highest pull-out load and energy absorption capacity followed by lower values for synthetic and CFs. While monofilament of steel fiber was able to absorb 1050 N.mm, monofilament of synthetic fiber and twisted bundles of CFs could absorb 277 and 55 N.mm respectively. However, the bond strength of straight CFs was comparable to that of synthetic fiber and still lower than that of steel fiber. It was also derived from the experimental data that an increase in cement matrix age correlates to an improvement in fiber maximum pull-out load, bond strength and tensile strength. These parameters were identified and compared in all fiber types.

3.2. Experimental investigation

3.2.1. Materials and cementitious mortar

Natural river sand meeting ASTM C778 [103] was employed as fine aggregate and crushed stone was used as coarse aggregate. The gradation curve of the aggregates is presented in Figure 10. According to ASTM C136 [104], the fineness modulus of fine and coarse aggregates was 2.85 and 7.03 respectively. Quickrete Portland Cement conforming to ASTM C150 Type I [105] was used to make Cement mortar with total binder content of 811 kg/m^3 and a water-binder ratio of 0.4. The mixing process was operated in accordance with ASTM C305 [106]. The compression strength (on 5 × 5 × 5 cm cubes) and tensile strength (on dog-bone samples) of plain cement mortar at 28 days of curing was 55.8 and 4.3 MPa respectively. Hooked-end SF, STRUX® BT50 SI and 2 types of PAN and pitch-based CF from Mitsubishi chemicals were used (Figure 11) to investigate the pull-out response of fiber in cement matrix. The properties of each fiber as received from the respective suppliers and the mix design of mortar are presented in Table 4 and

Table 5 respectively.

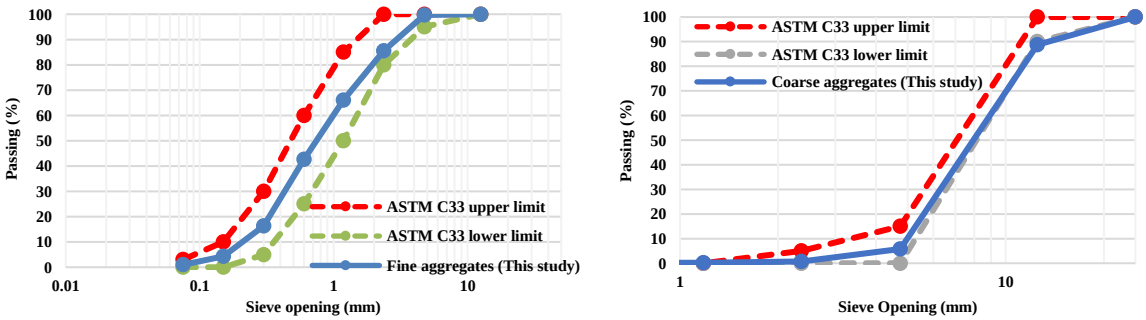

(a) (b)

Figure 10. Sieve analysis of a) fine aggregates b) coarse aggregates

(a) (b) (c) (d)

Figure 11. a) steel fiber b) synthetic fiber c) PAN-based carbon fiber d) pitch-based carbon fiber

Table 4. Physical and mechanical properties of fibers

Fiber Type	Steel	Synthetic	PAN	Pitch
Specific gravity	7.85	0.91	1.8	2
Modulus of elasticity	200 GPa	7 GPa	234 GPa	186 GPa
Tensile strength	>1100 MPa	550 MPa	4.83 GPa	2.34 GPa
Length	50 mm	50 mm	50 mm	50 mm
Nominal diameter	1mm	0.48×0.61 mm	7 μm	11 μm

Table 5. Mixture proportion of mortar mix

Material type	(kg/m^3)
Cement	811
Sand	1351
Water	324

3.2.2. Specimen preparation

Dog-bone shaped specimens were fabricated to measure the pull-out behavior of four types of fiber when embedded within the cementitious matrix. The fiber embedment lengths were 25 mm on both halves of the specimen as suggested by Ratu et al. [84]. For obtaining reliable test data, a minimum of three specimens for every mix was prepared for each test. Carbon fiber bundles were twisted in three different bundle diameters (0.5, 0.8 and 1 mm). The reason to use bundles instead of single fiber was 1) embedding one single CF (Diameter~7-11 μm) in cement mortar was impossible because the single fiber was brittle and prone to break when hit and 2) the importance of bundle behavior evaluation. Although different dispersants were introduced to ensure suitable dispersion of CFs in FRCC [107–110], the cost of these admixtures is relatively high [111], and the homogenous cement paste structure is also reported to be affected by dispersant [112]. In recent years, several alternative approaches

were introduced to disperse CF [113,114], and still a large number of studies report the presence of CF bundles in the matrix [113,115,116].

The reason to choose the aforementioned diameters was first, these values were the smallest diameter with an acceptable accuracy that we could get from the optical microscope secure of fiber breakage and second, these dimensions were comparable to SF and SI which had similar dimensions. As shown in Figure 12, an optical microscope was used to find the accurate diameter of the twisted fibers. Measurements were done on at least three points on the fiber to validate the correct diameter. Since bundles were twisted, it was assumed that cement paste could not penetrate inside the twisted fibers, and they were considered as a single fiber with an equivalent diameter equal to 0.5, 0.8 and 1 mm. Fibers were also glued together at each end of bundle, so that CFs did not disperse when put in the mold. During the preparation procedure, a single fiber or fiber bundle (for CF) was positioned inside a small hole in the middle of a thin plastic plate with 1 mm thickness (Figure 13.a, Figure 13.b). Then, half the depth of the molds was filled with mortar and the plastic plate was placed inside the matrix (Figure 13.c) such that the length of the fiber was oriented along the loading direction. The last step involved filling the rest of the mold with mortar (Figure 13.d). A summary of sample preparation steps is shown in Figure 13. Test specimens were cured at room temperature for the initial 24 ± 2 h. Then, the specimens were demolded and cured in a water bath at 23 ± 3 °C until they were tested.

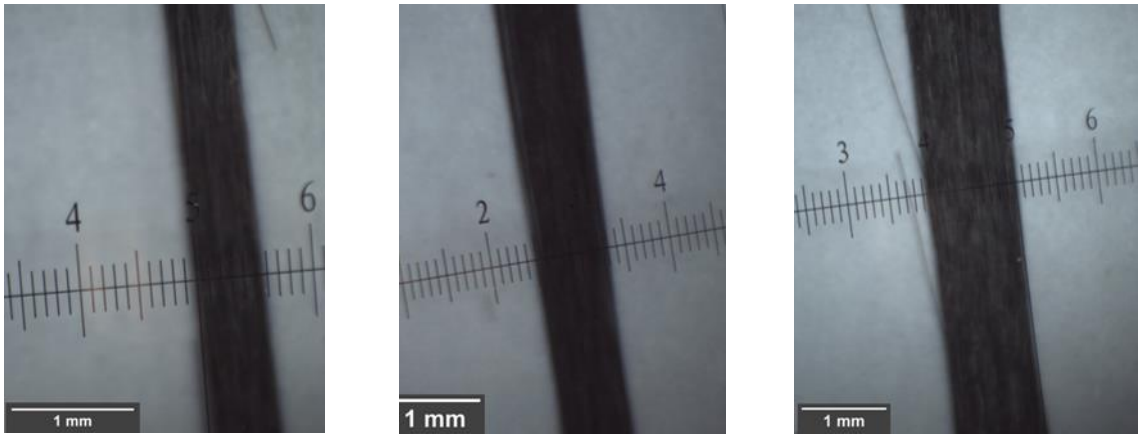

(a) (b) (c)

Figure 12. Optical microscope photos (division = 0.1 mm and D = diameter of bundle of fibers) a) D = 0.5 b) D = 0.8 c) D = 1 mm

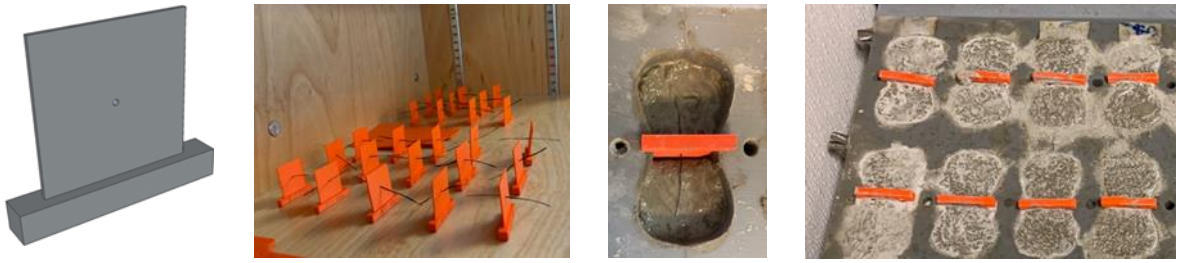

(a) (b) (c) (d)

Figure 13. Sample preparation steps a) 3D model of thin plastic plate b) 3D-printed plastic plates c) the plastic plate is placed inside the half-filled mortar d) samples ready to be demolded

3.2.3. Test setup and procedure

PASCO® Materials Testing Machine (MTM) with a load cell capacity of 7100 N (Figure 14) and a 1 mm/min crosshead loading rate was used to carry out the pull-out test. The fixture consists of identical upper and lower grips which were fixed to the test machine. During testing, the upward movement of the actuator applies a pull-out force on the upper half of the specimen. The machine is equipped with an optical encoder to measure the displacement of the sample. Force data from the load cell and displacement data from the encoder module can be recorded by a PASCO Interface with PASCO Data Acquisition Software (PASCO capstone). PASCO capstone is a data collecting software which can automatically collect and record data with different adjustable frequencies. In this experiment, data values were recorded at a frequency of 25 Hz. The optical encoder in the test machine was used to ensure no pre-load was applied to the specimen and to minimize the initial seating-based errors while sample gripping.

(a) (b) (c)

Figure 14. Pull-out test set up a) pull-out test apparatus b) MTM testing machine c) CF being pulled out.

3.3. Experimental results and discussion

The pull-out behavior of fiber is based on different factors including the physio-chemical adhesion, friction, and mechanical resistance [82]. In this test, pull-out behavior of fiber is evaluated by analyzing force-displacement curves. Similar to previous studies [117,118], pull-out force versus displacement curves are used to reflect the amount of load and total displacement of fibers being pulled out; the effect of fiber type and matrix age on the pull-out mechanism is evaluated by comparing pull-out results. All types of fibers are pulled out at 7, 14, 28 and 56 days.

According to Le et al. [102], a typical pull-out load versus slip curve for smooth steel fiber consists of the elastic stage, the partial debonding stage and the frictional stage. There is a linear elastic fiber-matrix bond in the elastic stage which is followed by a gradual separation in the adhesion between fiber and matrix which is called partial debonding phase and finally results in complete debonding. In the final stage and after debonding of the fiber, the pull-out resistance is only governed by friction [102]. Analyzing the three mentioned stages will help to get a broad insight into pull-out behavior of different types of fibers.

Different parameters can evaluate the pull-out behavior and resistance of fibers. Maximum fiber stress ($\sigma_{f,max}$) is a vital parameter to assess the performance of fibers in concrete. If the maximum fiber stress exceeds its tensile strength, the fiber will be fractured before complete pull-out. The maximum fiber stress can be calculated using Equation 1.

$$\sigma_{f,max} = \frac{P_{max}}{A_f} \quad \text{Equation 1}$$

where $\sigma_{f,max}$ is the maximum fiber stress, P_{max} is the maximum pull-out force and A_f is the cross-sectional area of fibers (in samples with CF, diameter of CF bundle is used to calculate the cross-sectional area).

Average bond strength (τ_{av}) between the fiber and the matrix is calculated using Equation 2 [119].

$$\tau_{av} = \frac{P_{max}}{\pi d_f L_e} \quad \text{Equation 2}$$

where τ_{av} is the average bond strength, d_f is the fiber diameter and $L_e$is the initial embedded length of the fiber.

Fiber pull-out energy (W_p) is the area under the pull-out force versus displacement curve up to the point where the pull-out load becomes zero; it can be calculated using Equation 3. Interface toughness of fibers is one of the most critical factors that evaluates performance of fiber and enhances the ductility of FRC. Interface toughness is defined as the mechanical energy consumed during fiber pull-out and is determined by integrating the area under the pull-out force-displacement curve.

$$W_P = \int_{S=0}^{S=L_e} P(s)ds$$ Equation 3

W_p is the fiber pull-out work and P(s) is the pull-out force at a certain slip.

Interfacial bond strength at the interface between the fiber and matrix can be evaluated by calculating equivalent bond strength (τ_{eq}) using Equation 4 (assuming shear strength is evenly distributed over the length of fiber) [120].

$$\tau_{eq} = \frac{2W_p}{\pi d_f L_e^2}$$ Equation 4

The results of maximum pull-out load (P_{max}), standard deviation of pull-out loads (SD), displacement at maximum pull-out load (Δ_{pmax}), fiber pull-out energy (W_p), maximum fiber stress ($\sigma_{f,max}$), average bond strength (τ_{av}) and equivalent bond strength (τ_{eq}) is given in Table 6 in which numbers after PA and PI represent the diameter of the twisted bundle of fiber in mm. For example, PA0.5 represents mortar mix with PAN-based CF and 0.5 mm diameter.

3.3.1. Effect of fiber type on fiber pull-out behavior

Pull-out behavior of four types of fibers was investigated. Figure 15 shows optical microscopy images of fibers after being pulled out. According to the image, after the pull-out test, cement paste was still attached to the surface of steel fiber in some areas of the surface which is proposed to be an indication of strong fiber-matrix bonding. In hooked end SF, the failure was a combination of matrix spalling and fiber-matrix debonding. However, in CF and SI, fiber-matrix debonding was the only and predominant failure in CF and SI.

Different failure modes were observed during pull-out test. In SF and SI samples, the failure mode was complete pull-out, while in CF, as it is shown in Figure 16, different failure patterns were observed including fiber fracture and fiber pull-out. The complete pull-out failure mode in SF and SI indicates that that bonding between fiber and matrix is weaker compared to the strength of the matrix or fiber [83,121]. Complete pull-out failure mode is a desirable failure mode to prevent sudden brittle failure in structures. However, the fracture failure mode reveals that the interfacial bonding is stronger than fiber tensile strength.

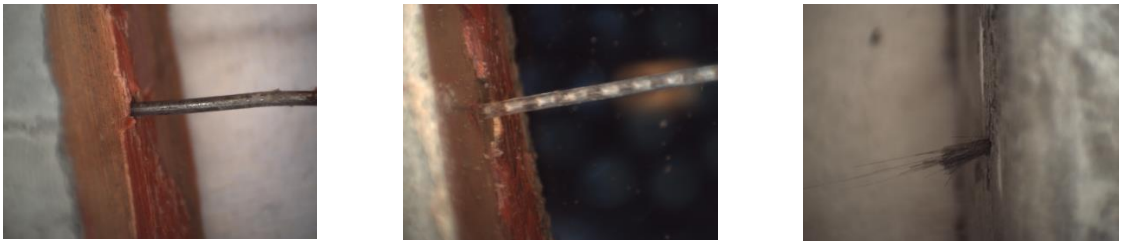

(a) (b) (c)

Figure 15. Fibers after pull-out test a) steel b) synthetic and c) carbon fiber

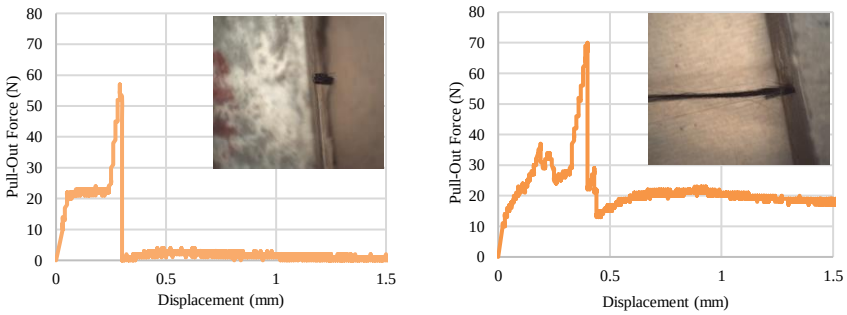

(a) (b)

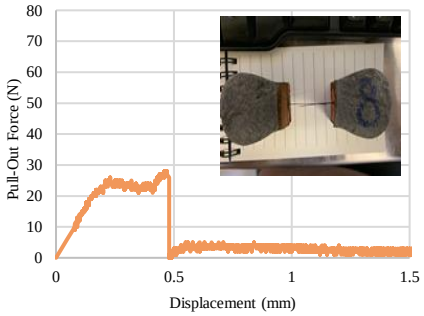

(c)

Figure 16. Different failure modes in carbon fibers a) fiber complete fracture b) fiber partial fracture c) fiber pull-out

Figure 17 is presented to show the failure pattern of different fibers. It is noteworthy to mention that each curve in the figure is a representative curve indicating a typical failure behavior of that specific fiber while being pulled out from the matrix. According to the results, the failure pattern in different fibers can be summarized as follows: In CF, a sudden drop in the pull-out load occurred after reaching the peak load. Considering the hydrophobic nature of CF, as well as the straight geometry of the fiber, the sudden drop at around 1mm of CF bundle slip is attributed to the poor interfacial bonding between the bundle and the matrix. After deboning, friction is the predominant mechanism in pull-out behavior [102] and as the slip increases, the pull-out load decreases due to the reduced friction area. However, because of the geometry of CF, the friction is much lower in CF bundles compared to SF and SI which results in lower post-crack energy absorption. In SF, the decrease in the post peak load was not as sudden as for CF similar to what was found by Nieuwoudt et al. [122]. After reaching the peak load, the increase in slip was followed by a strain softening behavior with a smooth decrease in pull-out load until anchorage of the fiber was straightened which occurred at slip of approximately 5 mm. In SI, the slope of the curve before peak load was even smoother than SF, and after reaching the peak load, a slip-hardening behavior was observed leading to

zero load at around 4.5 mm of fiber slip. The reason for slip-hardening behavior is the friction bonding which is mainly dependent on the properties of fiber rather than concrete properties [123]. Hence, fiber geometry is one of the important factors in fiber bonding behavior, and by improving the geometrical shape of fiber, the energy absorption of fibers can be enhanced significantly. Crimping fibers, for example, is an effective way of improving the post-crack behavior of SI resulting in slip-hardening behavior after the maximum pull-out force is reached.

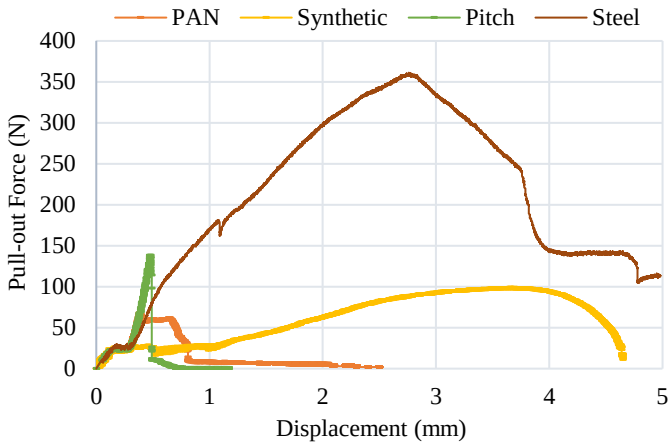

Figure 17. Failure pattern in different types of fiber

The detailed results of the pull-out test are presented in Table 6. During the preparation and testing of CF, some samples were damaged or broken due to the high vulnerability of fibers to any kind of impacts (missing values are presented by – in Table 6). These impacts were produced with sample handling, pre-test preparation, testing and also due to the matrix to matrix adherence of the two parts of the dog-bone sample. Although attempts were made to install the plastic plates in such a way that fibers were the only holders of the two parts of the briquette, still some small portion of the matrix attached to each other and needed to be broken. The load needed to break the cement matrix by the MTM was very low, but it could damage or break the bundle. Another reason for brittle behavior of CF is the high loading rate of MTM (1mm/min). The future scope of the CF pull-out test will be 1) increase in number of samples to make sure enough results will be provided in case of fiber damage 2) decrease in loading rate to avoid brittle fiber breakage 3) Fixing the divider plate inside the mold in order to make sure there is no matrix to matrix adherence.

Table 6. Summary of pull-out test results of fibers at different curing ages.

Specimen	Age (Day)	P_{max} (N)	SD	Δ_{pmax} (mm)	W_p (N.mm)	$\sigma_{f,max}$ (MPa)	τ_{av} (MPa)	τ_{eq} (MPa)
S	7	308	9.1	3.1	925	392.4	3.9	0.943
S	14	382	12.1	3.7	915	486.6	4.9	0.932
S	28	358	0.7	3.5	1050	456.1	4.6	1.070
S	56	346	71.1	3.6	1053	440.8	4.4	1.073
SI	7	106	29.1	3.6	255	353.3	1.9	0.374
SI	14	115	38.5	3.1	245	383.3	2.1	0.360
SI	28	122	25.4	3.5	277	406.7	2.2	0.407
SI	56	140	15	4.18	453	466.7	2.5	0.665
PA0.5	7	31	12.1	0.8	16	158.0	0.8	0.033
PA0.5	14	43	21.9	0.8	14	219.2	1.1	0.029
PA0.5	28	-	-	-	-	-	-	-
PA0.5	56	76	-	0.7	15	387.4	1.9	0.031
PA0.8	7	65	-	-	-	-	-	-
PA0.8	14	73	33.23	0.7	36	145.4	1.2	0.046
PA0.8	28	135	-	0.7	36	268.9	2.1	0.046
PA0.8	56	143	-	0.8	38	284.9	2.3	0.048
PA1	7	139	16.9	1.1	36	177.1	1.8	0.037
PA1	14	144	-	0.8	44	183.4	1.8	0.045
PA1	28	155	-	0.8	47	197.5	2.0	0.048
PA1	56	160	-	0.9	54	203.8	2.0	0.055
PI0.5	7	81	10.2	0.6	27	412.8	2.1	0.055
PI0.5	14	100	-	0.7	48	509.7	2.5	0.098
PI0.5	28	111	-	0.7	50	565.7	2.8	0.102
PI0.5	56	-	-	-	-	-	-	-
PI0.8	7	98	35.3	0.7	36	195.2	1.6	0.046
PI0.8	14	110	-	0.7	42	219.1	1.8	0.054
PI0.8	28	-	-	-	-	-	-	-
PI0.8	56	127	-	0.8	55	253.0	2.0	0.070
PI1	7	100	-	0.7	28	127.4	1.3	0.029
PI1	14	104	-	0.7	36	132.5	1.3	0.037
PI1	28	156	108.5	0.5	55	198.7	2.0	0.056
PI1	56	165	22	0.7	62	210.2	2.1	0.063

According to the bond strength results, SF had the highest bond strength and pull-out energy, followed by SI and then CF. According to the literature, the superior bond behavior will result in better fracture behavior [115,116]. At 28 days of curing, steel fibers were able to carry an average of 358N force, while this amount was 122, 155 and 156 N for SI, PA1 and PI1 at 28 days respectively. This means steel fiber could carry more than twice the amount of force compared to other fibers, and the other three fiber types showed comparable results in

terms of maximum pull-out force. However, for both S and SI samples, the maximum load was at 3.5 mm of slip, while for PA1 and PI1, the displacement at maximum load was 0.8 and 0.5 respectively.

Another factor to assess the performance of fiber is the amount of energy that can be absorbed by fibers. As shown in Table 6, the average fiber pull-out energy obtained was 1050, 277, 15, 36, 47, 50, 50 and 55 N.mm for S, SI, PA0.5, PA0.8, PA1, PI0.5, PI0.8 and PI1 at 28 days, respectively. The results showed the superior behavior of SF to absorb energy as well as a suitable behavior of SI and thus, in order to provide an equal reinforcement effect to a cement-based composite, a much greater amount of CF will be needed. The reason is mainly due to the fact that hooked-end steel fibers anchor at the ends and crimped fibers anchor along the length while in straight filament fibers the frictional shear stress at the interface determines the energy absorption capacity of fibers.

Figure 18 shows the tensile strength of fibers generated by force. According to the results, PI0.5 had the highest tensile strength; notably it was higher that SF and SI and thicker bundles. The increase in tensile strength with the decrease in diameter of the bundle approves the importance of fiber dispersion in order to maximize the capacity of CF. However, by comparing fiber tensile strength and energy absorption values, fibers with better tensile strength did not result in better energy absorption while fibers with better shear or bonding strength had improved energy absorption and after crack behavior. Although the tensile strength generated by force in all CF samples is lower than the fiber tensile strength, a few CFs were fractured before complete pull-out. This is mainly due to the initiation of fracture of single fibers around the bundle which are adhered to cement matrix and then the gradual breakage of inner fibers until all of fibers are fractured.

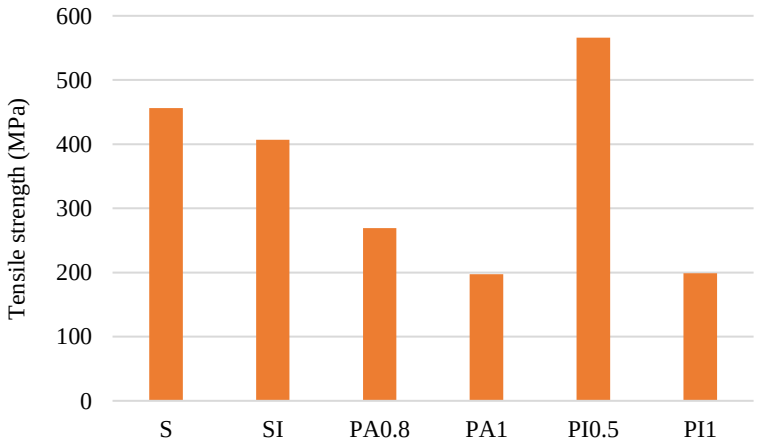

Figure 18. Average tensile strength of different fibers at 28 days of curing

3.3.2. Effect of matrix age on fiber pull-out behavior

Figure 19 shows maximum pull-out force versus matrix age of fibers. In case of the effect of matrix age, an increase in specimens curing age led to an improvement in fiber tensile strength in all fiber types except SF. The reason why SF didn't show the same pattern as in CF and SI is because of an important additional major contributor to pull-out resistance, that is, mechanical anchorage [88,102]. This means when the hooked end fiber is pulled out, a large amount of energy is needed for the fiber to become straightened, and hence the interlock between the anchorage and the matrix is one of the determining factors in pull-out behavior of fiber.

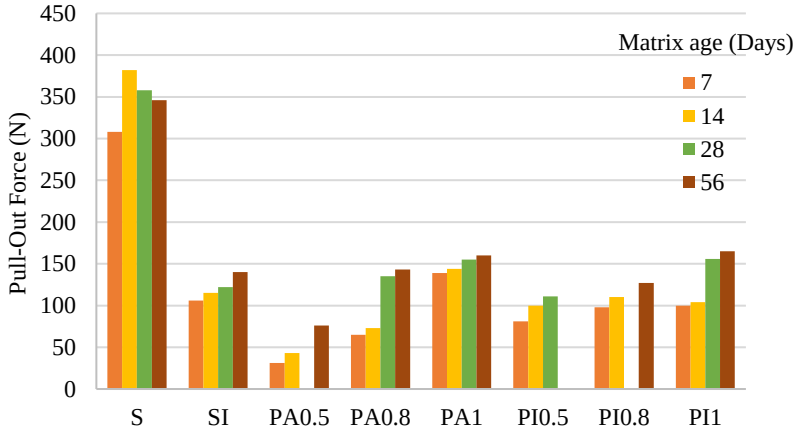

Figure 19. Pull-out behavior of fibers at different curing ages

The improvement in interfacial bond properties with an increase in curing age is mainly due to the production of hydration products especially Calcium Silicate Hydrate and development of microstructure of ITZ as the degree of hydration increases over time. For CFs, after curing for 7 days, all tests ended with the fibers being pulled out from the mortar which indicated the weak bonding between fiber and matrix at early ages. As the curing age increased to 28 and 56 days, a few fiber samples were fractured while being pulled out which indicates improvement in fiber bonding at later ages.

3.3.3. Interfacial strength

The fiber pull-out test is important since it provides information about interfacial properties of CF in the cement matrix. The pull-out force versus slip curves of various specimens is shown in Figure 20. Although the test machine was equipped with an optical encoder to minimize the gripping error, a few samples still show some pre-loading values in the pull-out force versus slip curve. These errors, which can be seen in Figure 20.a were removed during the analysis.

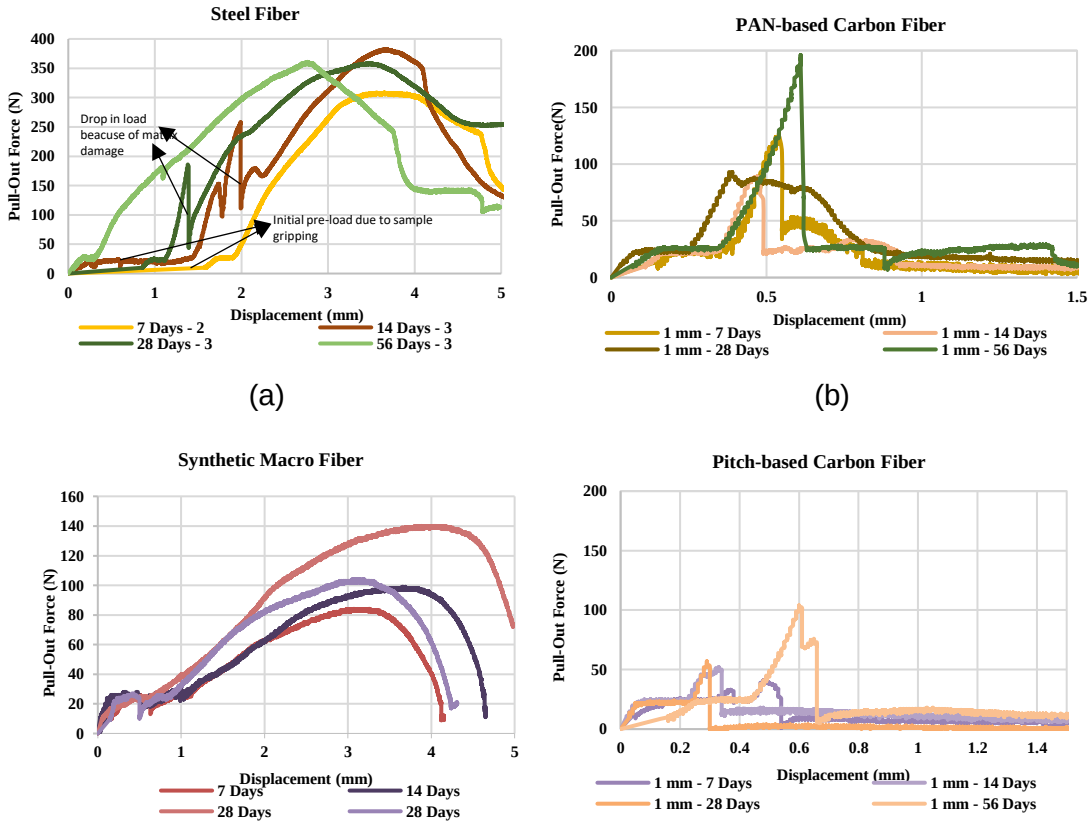

Figure 20. Pull-out force-displacement behavior of different fibers: a) SF b) PAN-based CF c) SI d) pitch-based CF

The pull-out curves revealed the characteristics of the bonding properties of each type of fiber. In CF samples, after failure of fiber (after P_{max}), the pull-out force decreased with increase in slip and no slip-hardening or slip-softening was observed which is in conformity with previous studies [101]. In synthetic macro fibers, the initial incline of the force-slip curve is linear to the point of failure and then follows a smooth decrease in the amount of force until fiber failure. In steel fibers due to the anchorage at the end of the fiber, the cement matrix will be damaged while fibers are being pulled out from the matrix and as a result several drops in load prior to final fiber failure are seen in the force-slip curve (Figure 20). Having a smooth surface is the main reason for a sudden drop in the pull-out force of CFs.

Although steel and synthetic fibers showed a much better energy absorption capacity, the bonding behavior of CFs is comparable with other fibers. Average bond strength (τ_{av}) is considered as an important factor to evaluate the ITZ quality between fiber and matrix. According to Table 6, after steel fibers, most CFs showed a comparable bond strength compared with synthetic fibers. In a few samples such as PI0.5, bond strength was reported to be higher compared to bond strength of SI. Although the effect of fiber bundle diameter on

bond strength didn't result in a particular and clear trend, it can be interpreted that as the age of samples increases, a better bonding is formed between fibers and matrix in all 4 types of fibers.

3.4. Conclusions

This study investigated the effects of fiber types as well as cement matrix age on pull-out behavior of steel, synthetic, PAN-based and pitch-based CFs embedded in the cement matrix. For this, three different twisted CF bundles with different diameters (0.5, 0.8 and 1 mm) were tested. Other fibers included a hooked-end steel fiber and a crimped synthetic macro fiber. Based on the test results obtained in this study, the following conclusions can be drawn:

- Different failure modes were recorded during pull-out test. In SF and SI samples, the failure mode was complete pull-out of fiber from cement matrix, while in CF, fiber fracture and fiber pull-out were the two failure modes observed during pull-out test. The complete pull-out failure is an indication of weaker bonding between fiber and matrix compared to the strength of the matrix or fiber. This is a desirable failure mode to prevent sudden brittle failure in structures.
- The failure pattern of fibers was investigated using pull-out force versus slip curves. In CF, after fibers reached the peak load, a sudden drop in the pull-out load occurred which was mainly due to the fast debonding between the fiber and the matrix around the fiber. In SF, the increase in slip after peak load was followed by a gradual decrease in pull-out load until the anchorage of the fiber was straightened. In SI, the decrease rate was much more significant than in SF but still smoother than CF. It is noteworthy to mention that all types of CF reached their peak load in less than 1 mm of slip, while this amount was much higher in other fiber types.
- Peak load and fiber pull-out differed significantly according to the fiber type. The highest average pull-out force of 358 N was obtained for SF while this amount was 122, 155 and 156 N for SI, PA and PI with the same diameter at 28 days respectively. For both SF and SI samples, the maximum load occurred at approximately 3.5 mm of slip, while for PA1 and PI1, the slip at maximum load was 0.8 and 0.5 mm respectively which is a main reason for much lower pull-out energy absorption capacity of CF compared to SF and SI.
- Average fiber pull-out energy obtained was 1050, 277, 15, 36, 47, 50, 50 and 55 N.mm for SF, SI, PA0.5, PA0.8, PA1, PI0.5, PI0.8 and PI1 at 28 days, respectively. The anchorage at the hook end SF is one of the main reasons for higher energy absorption, while in straight fibers such as CF, the frictional shear stress at the interface determines the energy absorption capacity of fibers.
- With an increase in cement matrix age, an improvement in fiber interfacial pull-out

properties was identified in all fiber types. However, after 28 days of curing, the increment was more gradual compared to other early curing ages. The main reason for improvement in bond behavior is development of the microstructure of ITZ as the curing age increases due to the hydration process. The fast hydration rate in early ages will result in faster microstructure improvement which is followed by denser ITZ and finally faster fiber-matrix bond improvement.

- During the preparation and testing of CF, several samples were damaged or broken due to vulnerability of fibers to any kind of impacts. These impacts were produced during sample handling, pre-test preparation, testing and also due to the matrix to matrix adherence of the two parts of the dog-bone sample. Another reason for the brittle behavior of CF was the high applied loading rate (1mm/min) used. In future experiments, it is recommended to decrease the loading rate as well as to make more samples to avoid data loss.
- Average bond strength was investigated in all four fiber types. The results showed that after SF, CF and SI showed comparable results and in some samples such as PI0.5, the bond strength value of CF was even higher than SI. The effect of fiber bundle diameter on bond strength didn’t result in a particular and clear trend.

Chapter 4. Behavior of alkali treated and fly ash-alkali treated carbon fibers

Paper Title: Comparative study of alkali treated and fly ash-alkali treated carbon fibers

Author(s): Maryam Monazami, Rishi Gupta

This paper was presented at the 2023 Canadian Society for Civil Engineering (CSCE) Conference and will be published in the conference proceedings [124], investigates the effectiveness of two fiber coating methods, namely fly ash and NaOH treatment, in improving the microstructure of the cement matrix. This paper has been subtly modified to ensure alignment with the dissertation's integrity and overall flow. The objective is to develop sustainable construction materials with enhanced mechanical and durability properties. The study utilizes fly ash as a supplementary cementitious material (SCM) to coat CFs, while NaOH treatment is employed to roughen the fiber surface and promote better adhesion between the fiber and cement matrix. The results highlight the potential of using SCM as a fiber coating to enhance the microstructure and overall performance of cement-based materials, emphasizing the importance of sustainable approaches in civil engineering.

4.1. Introduction

Cementitious composites are widely used as building materials due to their easy accessibility, low cost, easy forming, etc. However, brittleness, low tensile strength, low resistance to thermal stress, and flexibility adversely affect their durability and resilience [125]. By incorporating supporting components like fibers, concrete's mechanical properties can be improved. The bond behavior of fiber-reinforced concrete has been identified as a key element in composite behavior. The simultaneous operations of numerous bond components, such as the physical and chemical adhesion between fiber and matrix, make understanding bond characterization difficult. To evaluate the adhesion between the fiber and the matrix, a detailed examination of the microstructural and mechanical properties of a single fiber is required.

CFs have outstanding strength, stiffness, lightweight, electric conductivity, thermal conductivity, and amazing fatigue characteristics, and hence are finding wide application as the reinforcement material for composite materials, including reinforced cement and reinforced plastics [126]. However, CFs are hydrophobic, chemically inert and they have poor wettability and inherent smoothness [127]. As a result, a long-standing problem to solve is the poor interfacial interaction between the CFs and the matrix (water-based materials). The fiber-cement-based matrix interface must be specifically designed to enable acceptable interfacial

load transmission to improve the mechanical performance of the carbon-concrete composite [128–130].

Fiber surface treatment is a well-known technique for improving fiber-to-cement matrix interfacial adhesion. Surface treatments can change the fiber/concrete interaction by roughening the fiber surface and changing the surface polarity. The various surface treatments can be broadly classified as oxidation treatments and non-oxidation treatments [131]. Oxidation treatments include catalytic oxidation, chemical or electrochemical liquid-phase oxidation and gas-phase oxidation [131–133]. The non-oxidative treatments entail the deposition of more active forms of carbon, such as the extremely efficient whiskerization, the deposition of pyrolytic carbon [134,135], or the grafting of a surface modifier on the CF surface [113–114]. The efficacy of surface treatment and the adherence of fibers in concrete can be evaluated based on different measurements, including the interfacial shear strength [138], scanning electron microscopy [139] and optical microscopy [140]. Surface wettability and contact angles have also been used as approaches in adhesion testing [87–118].

In CFs, the traditional approach to reducing the surface roughness of fibers is to mechanically treat them [142]. However, mechanical treatment leaves the fiber sizing (often a polymer coating) intact, which could be detrimental to the mechanical performance of composites at higher temperatures [130]. The chemical approach often involves solvolysis, super/sub critical fluid technologies, and acid and alkali treatments. Because the procedure often provides a low-cost, straightforward, and easy-to-operate solution, acid and alkali treatments are suited for the large-scale treatment or industrial disposal of fiber composite wastes [142]. However, treating fibers with chemicals might cause fiber degradation and affect the mechanical performance of the fiber [143].

Taking into account that the degradation of fiber surfaces while chemically treated might alter the mechanical properties of fiber and that mechanically treating fibers might not be sufficient to ensure a proper bond between fibers and matrix, a new strategy for improving the microstructure of the matrix around fiber is suggested in this chapter. In the present study, a combination of mechanical and chemical treatment approaches was used to enhance the adhesion of CFs to the cement matrix. CFs were modified by alkalic oxidation followed by fly ash surface coating to produce a modified fiber with improved bonding capabilities with cement-based matrices. A comparative analysis is conducted to find which method is better for improving the adhesive properties as well as the mechanical strength of the CF. It was found that the alkali treatment weakens the mechanical strength and bonding propensity of the fiber, but the addition of the fly ash greatly compensates for the adverse effect and increases the bond strength when compared to the untreated fiber.

4.2. Experimental investigation

4.2.1. Materials

Commercially available Polyacrylonitrile (PAN)-based carbon fibers with epoxy sizing, manufactured by Teijin Cooperation, were acquired in this study. The physical appearance and chemical properties of fibers are shown in Figure 21 and Table 3. Class F fly ash according to ASTM C618 [144] was used to coat the fibers Quikrete General Use (GU) cement that agreed with CSA A3000 standard was employed as the binder [145].

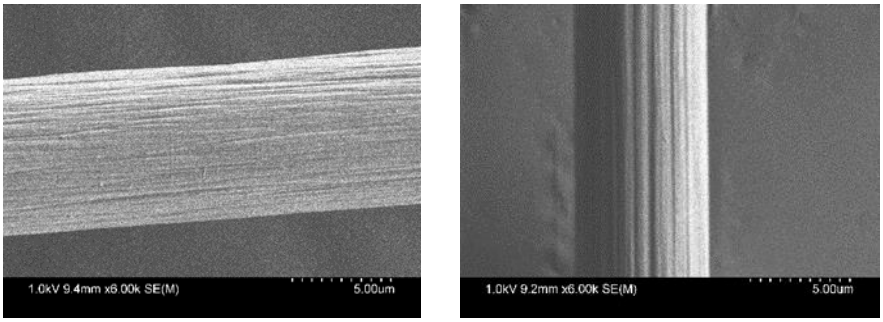

Figure 21. Scanning electron microscopy images of CFs

4.2.2. Preparation of samples

Figure 22 depicts the fiber preparation procedures. As demonstrated, a 0.5% solution of sodium hydroxide was made, after which CFs were dipped into it and allowed to soak for two hours. After that, the CFs were completely rinsed with water, and then they were allowed to dry. The following procedure involved soaking the treated CFs in a fly ash solution and allowing them to dry. Next, the 50 mm-long fiber strands were cut. Half dog-bone-shaped specimens were prepared to assess the pull-out behavior of treated CFs when placed in the cementitious matrix (Figure 22). As recommended by Ratu et al. [84], the fiber embedment lengths were 25 mm on both halves of the specimen. The cement mortar contained 1351 kg of sand and 811 kg of cement per m^3, with a water/cement ratio of 0.4.

(a) (b) (c) (d)

Figure 22. Preparation of fibers a) Magnetic Stirrer with fly ash solution b) carbon fibers soaking in NaOH solution c) carbon fibers rinsed d) carbon fibers immersed in fly ash solution.

The morphology of the coated CFs was observed using SEM on a Hitachi S-4800 FESEM machine. The fiber pull-out measurement was done on a Tinius Olsen 5ST equipment. The pull-out test was performed using Tinius Olsen 5ST machine with a load cell capacity of 5000 N (Figure 23) and a 1 mm/min crosshead loading rate. The fixture is made up of two grips, a fiber grip at the bottom and a half-dog-bone grip at the top, that are attached to the testing device. A pull-out force is applied to the briquette grip during testing by the upward movement of the actuator. Tinius Olsen's Horizon software can be connected to the machine to measure the precise displacement of the sample. To have better grip on the fiber and to prevent initial seating-based errors, the samples were placed between the sandpaper.

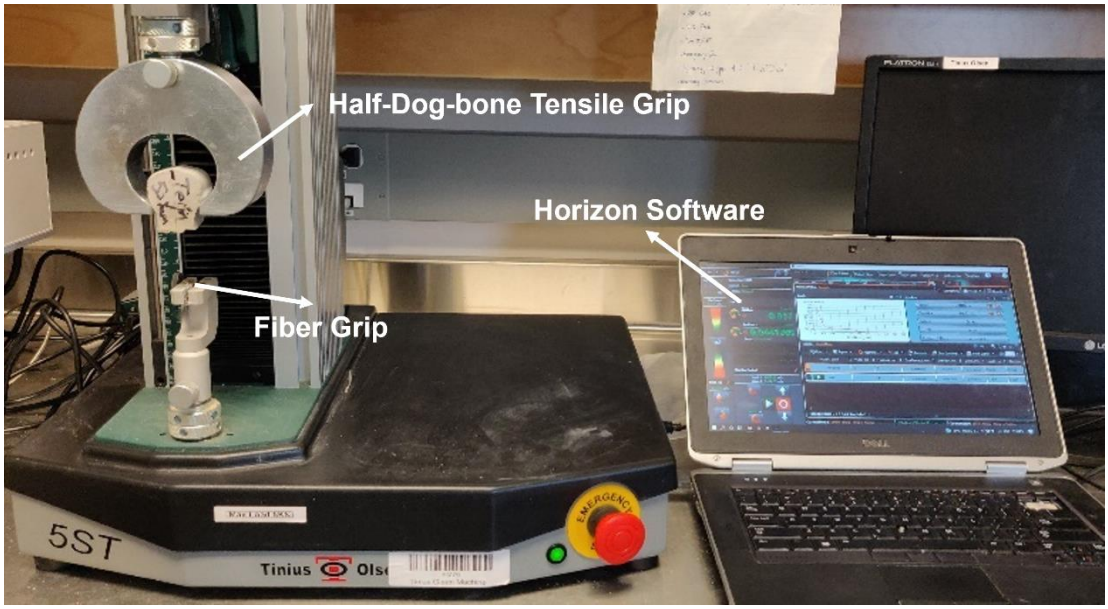

Figure 23. Fiber pull-out test set up

The sessile drop contact angle was measured with a Rame'hart Instrument Co. Tensiometer 250-U4. During the experiment, the liquid chosen was de-ionized water with a density of 0.98 g/cm^3. The testing for all the samples was conducted at 25 ºC and 65% relative humidity in a soundproof environment. The contact angles were determined by analyzing images of the droplet taken with an image quality transfer system, which is used to create fine droplets on a substrate using pulse injection equipment. The samples were suspended horizontally over the sample holder, as shown in Figure 24. Then the sample holder was

mounted on the platform of the tensiometer, and then 3 ml of water was dropped on the surface of the CF and the contact angle was measured.

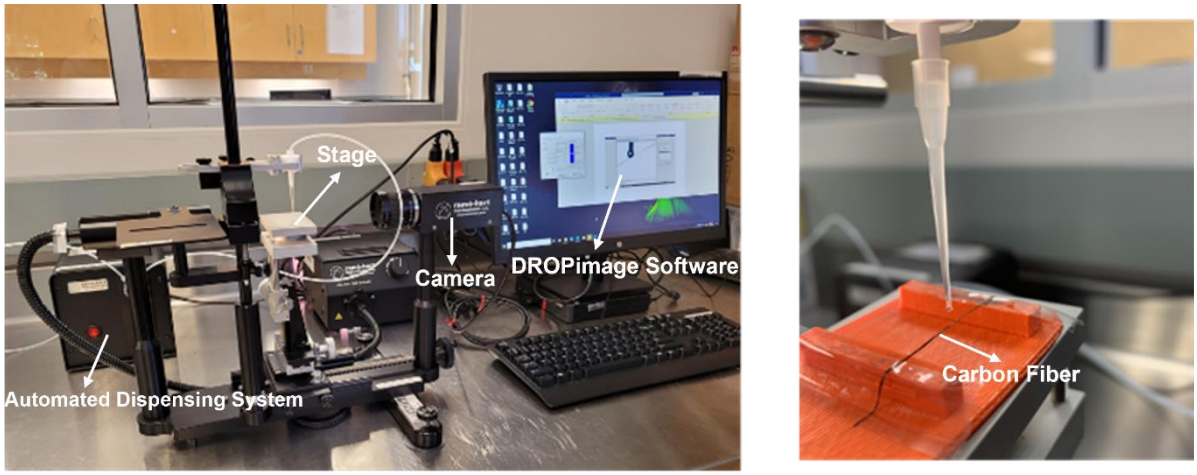

Figure 24. Fiber contact angle test set up

A four-point probe method was used to measure the resistivity of the untreated and treated CFs. In a 4-probe electrical resistivity test, one pair of probes is used for passing the current, while the other pair is utilized for voltage measurements on a separate set of electrodes. The four-probe approach produces more reliable data since contact resistance concerns are not an issue. The experimental set-up is shown in Figure 25. Silver electrodes were used to make electrical contacts. One pair of probes was used for passing the current, while a separate pair of electrodes was used for the measurement of voltage. A digital multimeter was used to measure the potential difference. The resistance is calculated by Ohm's law as given by Equation 5.

$$R = \frac{V}{I}$$ Equation 5

Where R is the electrical resistance (Ohm), V is the value of voltage (Volt) and I is the value of the applied current (Ampere). The direct current resistivity of the material is calculated with following expression:

$$\rho = \frac{RA}{L}$$ Equation 6

Where A is the cross section of the fiber bundle (m^2) and L is the length of the fiber (m)

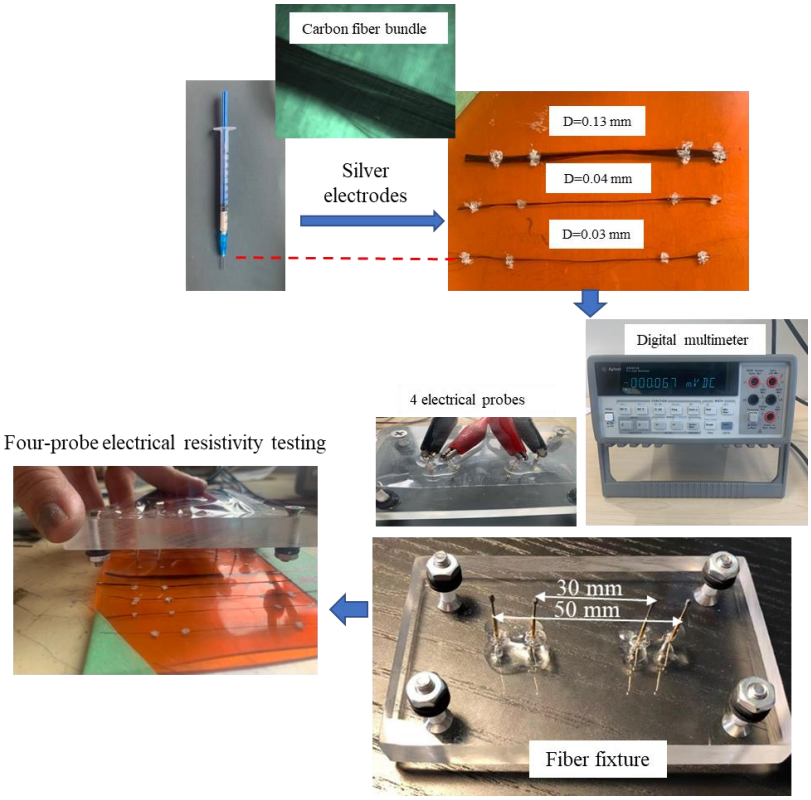

Figure 25. Electrical resistivity test set up

4.3. Results and discussion

4.3.1. Microstructure characterization of Carbon Fiber

Figure 26 shows the SEM results of the CFs. It can be seen that in samples treated with NaOH, the chemical process reduced the fiber's surface smoothness and increased its roughness. In addition, the SEM results showed that the roughness of the CFs treated with FA was further increased. After treatment, a rougher fiber surface is obtained, which is advantageous for fiber/matrix interfacial adhesion because a rougher surface promotes fiber and matrix mechanical interlocking [146]. The alkali treatment removes the sizing of the fiber, which is covering the external surface of the fiber and coating the fiber with FA will increase the rate of hydration, resulting in a higher concentration of calcium-silicate-hydrate and a lower interfacial zone thickness between the fiber and cement matrix.

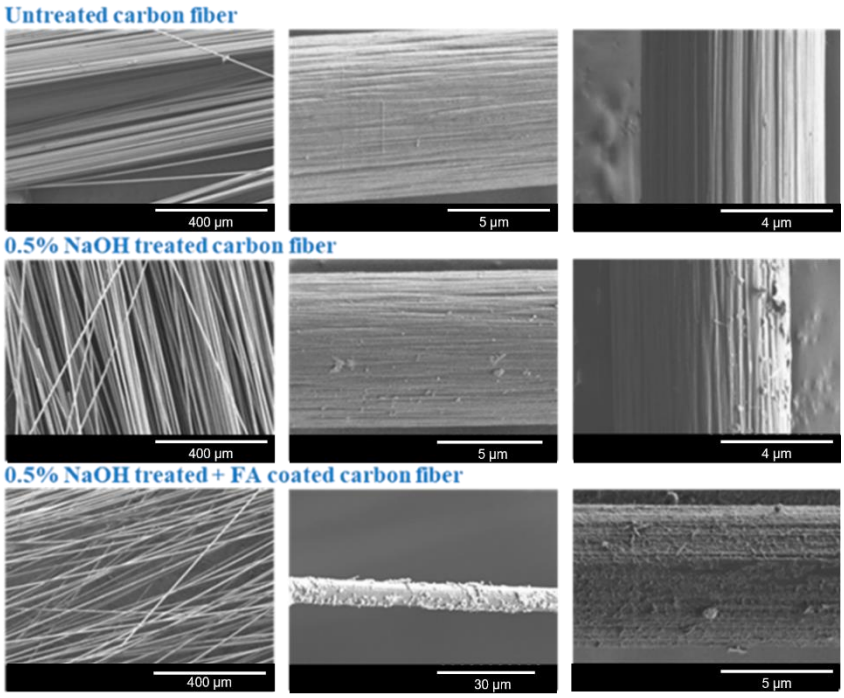

Figure 26. SEM of treated and untreated carbon fiber

4.3.2. Fiber pull-out behavior

Figure 27 shows the force-displacement behavior of fibers while being pulled out, and Table 7 shows the results for maximum pull-out load (P_{max}), standard deviation of pull-out loads (SD), displacement at maximum pull-out load (Δ_{pmax}), fiber pull-out energy (W_p), maximum fiber stress ($\sigma_{f,max}$) and equivalent bond strength (τ_{eq}). As can be observed, untreated fibers have a pull-out energy and bond strength of 5.1 N.mm and 10381 Pa, respectively, while treated fibers have a value that is substantially lower. The fiber pull-out energy and bond strength both decreased by 97.6% and 97.5%, respectively, after the alkaline treatment. This interpretation states that the alkaline treatment greatly affects the matrix's bonding activity, possibly mainly because the destructive alkaline harms the micro CFs. On the other hand, the adverse effects were eliminated when fibers were coated with FA. As depicted in Figure 27, fiber pullout, fiber breakage, and fiber debonding from the cement matrix are the three failure mechanisms that can be seen when CF is pulled out. When CFs were treated with NaOH, fiber breakage accounted for all failure processes; nevertheless, both untreated and FA-treated fibers experienced all forms of fiber breakage and fiber pullout failure. Even though FA treatment is a great method for enhancing the bonding properties, it may be necessary to switch from alkaline treatment to another less hazardous procedure.

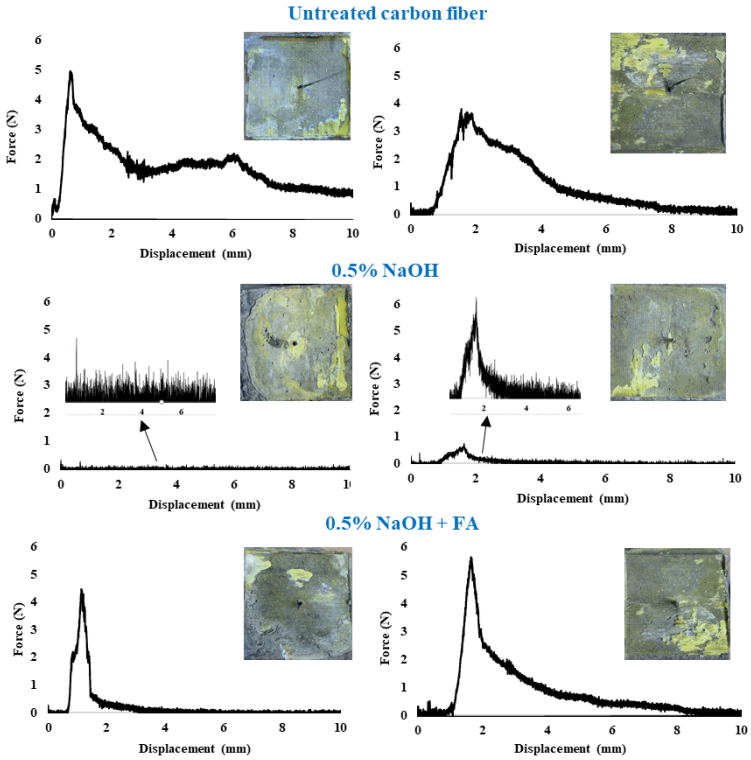

Figure 27. Force-displacement behavior of treated and untreated carbon fibers

Table 7. Summary of fiber pull-out test results

Specimen	P_{max} (N)	SD	Δp_{max} (mm)	Wp (N.mm)	$\sigma_{f,max}$ (MPa)	τ_{eq} (Pa)
Untreated carbon fiber	4.58	0.8	1.94	5.1	5.8	10381
5% NaOH treated carbon fiber	0.54	0.09	0.83	0.12	0.69	259
5% NaOH treated + FA coated carbon fiber	6.16	0.72	2.12	4.8	7.8	10825

4.3.3. Fiber contact angle

Changes of contact angle in treated and untreated CFs are shown in Figure 28. As shown in the figure, the contact angle data of untreated carbon was 134°, which suggests that the fiber-matrix adhesion is weak, which could pose a problem for carbon-fiber reinforced composites. This is mainly due to the CFs' surface morphology and properties, which can also be inferred from SEM images. The smoothness and integrity of the surface of CFs resulted in weak contact between the fiber and the cement matrix, which also could not be compensated for by treating it with NaOH. Contact angle data of NaOH treated CF and NaOH + fly ash

treated CF was 134° and 108°, respectively. It can be observed that samples treated with FA experienced a significant decrease in contact angle and the adhesion of highly hydrophobic CF was highly improved. This is an expected result because of the significant increase in the roughness of the fiber, which is also confirmed by SEM photos.

Overall, both surface-treated CFs show hydrophobicity, preventing adhesion between the fiber and the cement matrix. However, compared with the untreated CF, the contact angle decreased by 19.2%.

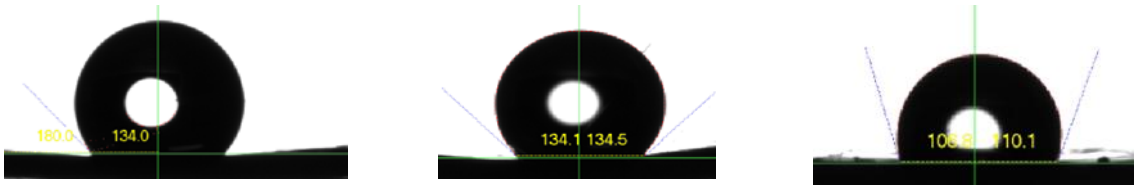

(a) (b) (c)

Figure 28. Contact angle of a) untreated carbon fiber b) NaOH treated carbon fiber c) NaOH+ fly ash treated carbon fiber.

4.3.4. Fiber electrical resistivity

CFs are commonly added to concrete to increase its composite conductivity and convert it to an electrically conductive surface. Thus, it is advantageous to research the electrical resistivity of CFs and how treatment of the fibers affects their resistivity. The change in fiber's electrical resistivity with treatment techniques is shown in Table 8. It has been demonstrated that treating CFs with NaOH effectively removes the sizing of the fiber and reduces its electrical resistivity, while treating it with NaOH and fly-ash negatively affects the fiber's resistivity. This can be due to the fact that fly-ash on its own is more resistive to electrical flow when compared to CFs.

Table 8. Electrical resistivity of untreated and treated carbon fibers

Fiber	Resistivity (μohm-m)
Untreated carbon fiber	5.3
5% NaOH treated carbon fiber	2.5
5% NaOH treated + FA coated carbon fiber	6.9

4.4. Conclusion

The overarching objective of this research was to investigate the efficacy of two fiber coating methods to discover and characterize the improvement in the microstructure of the cement matrix.

- Coating fibers with waste supplementary cementitious material (SCM) such as fly ash is approved as an efficient approach to developing a sustainable construction material

with enhanced mechanical and durability properties. The following conclusions can be drawn from the experimental results:

- The proposed NaOH treatment method is shown to have negative effects on the bonding properties of CFs. Samples with NaOH-treated CFs are reported to have lower bond strength and lower fiber pull-out toughness.
- The proposed NaOH treatment combined with the fly ash treatment provided a sufficient bond between the fiber and the matrix. This sufficient bond led to a higher bond strength and lower contact angle, as well as a rougher surface that was approved by the EDX micrographs.
- The NaOH treated CFs showed a lower electrical resistivity than the untreated CFs. However, the resistivity values of fly ash-treated CFs were comparable to those of untreated fibers.

Chapter 5. Mechanical behavior and fracture energy of carbon fiber-reinforced concrete beams and panels

Paper Title: Investigation of mechanical behavior and fracture energy of fiber-reinforced concrete beams and panels

Author(s): Maryam Monazami, Rishi Gupta

This chapter, which is a published paper in a peer reviewed journal [77] and has been subtly modified to ensure alignment with the dissertation's integrity and overall flow focuses on the quantification of CFs' role as micro-reinforcement in round panels to prevent and slow down crack formation. While CFRC has gained attention for use in pavements, previous assessments have been limited to laboratory-scale samples that do not align with the predominant failure mechanism, yield-line theory, for concrete pavements. The study investigates the effects of CF dosage and length on flowability, fiber-matrix bond, and mechanical properties, comparing them with polypropylene fiber. The findings of this chapter emphasize the potential of CFRC as a crack retarder and highlight the importance of selecting appropriate fiber types for accurate prediction of performance in concrete structures.

5.1. Introduction

Concrete slabs in Canada are commonly installed in the curb travel lane pavement at the bus stop to improve the resistance of bus pads to rutting and petroleum deterioration. However, conventional concrete is brittle with low tensile strength and strain capacity. Such unsatisfactory performance can be improved with the addition of fibers in concrete. Steel and synthetic polypropylene fibers are the two most commonly used fibers in FRC structures [147–151]. The majority of previous case studies on FRC pavements are focused on the application of steel fiber SF in concrete [152–154]. However, SFRC pavements in cold regions, such as Canada, are subjected to de-icing salts and aggressive environments where chlorides and carbonation may corrode the fibers. Additionally, fibers on exposed surfaces or fibers across crack openings will not be protected by the alkalinity of concrete and usually experience higher rate of oxidization [155]. This will negatively affect the crack bridging capacity of SF with detrimental consequences on the performance of pavement [27]. Moreover, the addition of SF with high density, leads to a significant increase in concrete weight, which limits the quantity of SF, targeted to be added into the mix.

Due to the mentioned drawbacks of SFRC pavements, PPs have been adopted in rigid pavements in recent years. Polypropylene reinforced concrete pavement (PRCP) showed advantages over the SF specially in chemical stability, lightness and workability [36]. PP are

also able to mitigate or decrease plastic and early drying shrinkage of concrete structures [149,156]. However, since it has a low young's modulus, it is not able to prevent the formation and propagation of cracks at high stress levels [157]. Polypropylene fiber is reported to be capable of being used in ejected concrete technology, which plays an important part in lining construction for tunnels [36,158]. However due to the low tensile and flexural strength, it might not be the best construction material where high stress level plays an important role such as in concrete pavements.

Over the last three decades, CFRC has found increasingly widespread applications in the construction material industry including in airports, rigid pavements, and asphalt pavements. CFRC becomes a multifunctional construction material combining the strength function with the possibility of acting as an active sensor within the structural material [157,159–162]. Adding a small portion of conductive CF is an efficient and convenient method to construct an electrically conductive pavement. CFs are also reported to be more suitable compared to SF and PP in respect to finish ability, weatherability, mixability, thermal resistance and long-term chemical stability in unstable environments [163]. Although CF are an advantageous additive material in electrically concrete pavements, the appearance of macro and micro cracks in the pavement can cut the conductive path and hence affect the electrical conductivity of the pavement. This work is novel as the existing studies on mechanical behavior and crack propagation of CFRC are mostly limited in behavior reinforced beams. Several researchers have studied the use of chopped CF as the second reinforcement of cementitious composites [164–168]. Based on the results from these studies, improved mechanical properties including flexural strength was observed [164–166].

Flexural strength is an important parameter in concrete as it involves tension on one side of the specimen and compression on the opposite side. Flexural behavior of concrete is usually evaluated using three-point or four-point bending test on beams. However, it is reported that the characteristic values determined from FRC beam tests are remarkably lower than the mean value, because of the high scatter in beam test results as well as small fracture area which is linked with a few numbers of fibers. On the other hand, it is reported that FRC mixes with low fiber volume are particularly suitable for structures with a high degree of redundancy where stress redistribution occurs [117]. It is noteworthy to mention that flexural loading is also commonly encountered by concrete structural components such as slabs flexural failure mechanism of CFRC panels in which the failure mechanism follows the yield line theory. Because of the reasons, to get more realistic experimental value, standard tests should be carried out on specimens with larger fracture areas that suggests a different specimen geometry like fiber reinforced concrete panels where a stress redistribution may also occur. As a result, it is recommended to consider a new different specimen geometry like

FRC panels [169], therefore, the behavior of the structure is dependent to the material properties including fiber properties.

While to the best knowledge of authors, the studies on the effects of CF on the flexural behavior of CFRC panels are rare. The information in this field is necessary for the selection of suitable amount, type, and length of fiber especially for pavement applications and slabs on grade. The present chapter was developed to assess concrete behavior reinforced by CF and PP mixed in different volume fractions and having different lengths with the aim of giving a useful contribution to the ongoing wider project involving the installment of a CFRC bus pad in Victoria, Canada, and its comparison to non-fibrous rigid pavement. Three different phases in this chapter include experiments conducted on fiber-reinforced cement mortar (FRCM), FRC samples, and fiber-reinforced concrete panels (FRCP). Specimens mixed with PP and CF with different volume fractions were casted, and the results were compared. Uniaxial compression tests were performed to derive compressive strength of FRCM and FRC, fibers pull-out tests were performed to evaluate fiber-matrix bond strength; center-point bending tests were conducted on specimens to obtain first crack strength and other flexural properties and using a fitted surface plot, the optimum length and concentration were obtained. To predict the behavior of FRC, composite analysis was proposed, and the predicted results were compared to that of experimental results. The final section of the work is focused on flexural behavior of round panels using yield line analysis, both from an experimental and theoretical point of view and the results were compared with beams using analysis of variance (ANOVA) model. The results showed beneficial effect of CFRC on pre-crack energy absorption, and their role as crack retarders was justified when the absorbed energy was compared to non-fibrous mixes. The residual flexural strength was also improved in beams and round panels reinforced with CFs. Using the composite theory, the experimental-to-predicted flexural strength ratios in PAN-based CFs were in the range of 1.11 to 1.34. However, the predicted strengths of mixtures with polypropylene and pitch-based CFs were significantly higher than the experimental values.

5.2. Materials and methods

5.2.1. Raw materials

River sand was employed as fine aggregate and crushed stone was used as coarse aggregate. The gradation curve of the aggregates is presented in Figure 10. General Use (GU) cement conforming to requirements of CSA A3000 standard was used as the binder [145]. PP with different fiber lengths (6, 13 and 19 mm) and 3 different types of PAN and pitch-based CFs with 6, 12 and 18 mm length were used. CF were acquired from Mitsubishi chemicals and Teijin cooperation and PP were provided from Euclid Chemicals. The physical

appearance and chemical properties of fibers are shown in Figure 29, Table 3 and Table 4. Class F fly ash according to ASTM C618 [144] was used in concrete mixes as a partial substitute of cement. High-range water reducing agent (HWRA) which meets the ASTM C494/C494 M [170] requirements for Type A water-reducing, and Type F high-range water-reducing admixtures was used to reduce water usage. Air entraining agent (AEA) was used in concrete samples to increase the amount of entrained air in samples for superior FT resistance. AEA used in this study meets the requirements of ASTM C260/260 M [171].

(a) (b) (c) (d)

Figure 29. Physical appearance of fibers a) Mitsubishi PAN-based CF b) Mitsubishi pitch-based CF c) Teijin PAN-based CF d) PP

5.2.2. Design of FRCM

23 groups of mortar mixtures with different concentrations of CF (0.5%, 1%, 2% and 3% by volume) and polypropylene fibers (0.5% and 1% by volume) with different lengths were considered to examine the effects of fiber type, length, and concentration on the behavior of cement mortar mixes. To achieve a target strength of 40 MPa, the water / binder ratio was 0.39 in all specimens. Mortar beams with the dimensions of 30 mm × 30 mm × 100 mm were designed for flexure test and 50 mm × 50 mm × 50 mm cubes were designed for compression test. Abbreviations were denoted in such a way that the first number shows the dosage of fiber, and the last number illustrates the length of the fiber. Non-fibrous mix abbreviated to CO and P, PAM, PIM, and PAT denote samples with polypropylene fiber, PAN-based Mitsubishi CF, Pitch-based Mitsubishi CF and PAN-based Teijin fiber. For example, 0.5PAM6 represents mix containing 0.5% PAN-based Mitsubishi CF with 6 mm fiber length. The mix proportions of mortar mixtures are listed in Table 9.

Table 9. Mixing proportions of cement mortar samples

Cement mortar					Concrete			
Label			Fiber		Label	Fiber		Fresh density
			(kg/m^3)	% (Vol)		(kg/m^3)	% (Vol)	(kg/m^3)
CO			0	0	CO	0	0	2620
0.5P6	0.5P13	0.5P19	4.5	0.5	1P13	9.1	1	2450
1P6	1P13	1P19	9.1	1	2P13	18.2	2	2300
0.5PAM6			9.0	0.5	1PAM6	18	1	2520
1PAM6			18.0	1	1PIM6	20	1	2480
2PAM6			36.0	2	0.5PAT18	9.5	0.5	2530
3PAM6			54.0	3	1PAT18	19	1	2410
0.5PIM6			10.0	0.5	2PAT18	38	2	2120
1PIM6			20.0	1				
2PIM6			40.0	2				
3PIM6			60.0	3				
0.5PAT6	0.5PAT12		9.5	0.5				
1PAT6	1PAT12		19.0	1				
2PAT6	2PAT12		38.0	2				
3PAT6	3PAT12		57.0	3				

Mortar: Sand: 1188 kg/m^3, Cement: 712 kg/m^3, Water: 281 kg/m^3

Concrete: Gravel: 1055 kg/m^3, Sand: 815 kg/m^3, Cement: 276 kg/m^3, fly ash:60 kg/m^3, water: 148 kg/m^3

5.2.2.1. Tests on FRCMs

Flow table test was performed on mortar samples in accordance with ASTM C1437 [172]. According to the test, the flow is the resulting increase in average base diameter of the horizontal flow measured in two perpendicular directions after lifting Abrams cone when the table is dropped 25 times in 15 s. The results, which is called flowability, is expressed as a percentage of the original base diameter. A compressive strength test was performed on cube samples at 28 days in accordance with ASTM C109 [173]. Forney mechanical testing machine equipped with the appropriate compression platens was used for the test with a loading rate of 900-1800 N/s.

Center-point flexural test was performed on beam samples at 28 days of curing according to ASTM C293 [174]. According to Equation 7, the amount of absorbed energy can be determined by integrating the area under the load-displacement curve [175]. In this research, the amount of flexural toughness was calculated at $3\delta_0$ (corresponding displacement with 3

times as high as the corresponding displacement of maximum load, δ_0). Loading rate in flexural strength tests was 1mm/min and a minimum of three specimens for every mix was prepared for each test.

$$W = \int_0^{\delta} P \, d\delta \quad \text{Equation 7}$$

Where W is the absorbed energy (mJ); P is the force (N) and δ is the displacement (mm) in the middle of the flexural sample span.

Micro-structural analysis was conducted on thin polished sections of FRCMs using scanning electron microscope (Hitachi Tabletop Scanning Electron Microscope). SEM images were used to identify changes in ITZ of fibers and cement matrix.

5.2.3. Design of FRC

Considering the workability and mechanical strength results analysis of FRCMs, a total of 8 groups of concrete mixes (CO, 1P13, 2P13, 1PAM6, 1PIM6, 0.5PAT18, 1PAT18 and 2PAT18) were chosen and designed for further investigation. Considering the positive effect of CF length and considering the size of concrete beams compared to mortar beams, it was decided to use longer fibers (Length = 18 mm) in concrete samples. All the specimens were made in accordance with ASTM C192 standard [176] . Chemical admixtures including HWRA and AEA were used to reduce water usage and increase the entrained air content as recommended in CSA A23 [119]. The samples were prepared in a drum mixer using the following mixing procedure. First, the aggregates and fibers were placed in the drum mixer and mixed for 1 minute. Then, 2/3 of mixing water with AEA were added to the mixture and mixed for another 1 minute. Fly ash was then added to the mixture and mixed for 3 minutes. Cement was gradually fed into the mixer while it was running. When the entire cement had been added, the mixer was stopped. The rest of the mix water with HRWR were added to the mixture, and the whole mixture was mixed for another 3 minutes. Table 3 shows the mix proportions of concrete samples.

Samples were removed from the molds after 24 hours and were immersed in water tanks for 28 days at a temperature of 23±2°C until the day of testing. In this phase, concrete beams with the dimensions of 100 mm × 100 mm × 400 mm were designed for flexural test and cylinders with diameter of 100 mm and height of 200 mm were designed for the compression test.

5.2.3.1. Fresh properties

The slump test on concrete was used to assess the workability of all concrete mixtures in accordance with ASTM C143 [120]. AEA was adjusted in such a way to remain the air content of concrete samples between 3-7% as suggested by CSA [119].

5.2.3.2. Compressive strength

Compressive strength test was performed on cylinder samples at 28 days in accordance with ASTM C39 [177]. The loading rate was in the range of 900 to 1800 N/s. The reported results are the average of compressive strength tests of three samples molded from a single batch of mortar and tested at the same age.

5.2.3.3. Flexural behavior of FRC

Center-point bending test through displacement control was conducted on 100 mm × 100 mm × 400 mm prismatic specimens to investigate the flexural behavior of samples as shown in Figure 30. The load was applied by universal testing machine (MTI) load cell with 250 kN maximum capacity. The load–deflection curve was obtained for each specimen tested. The deflection at the center of the specimens was measured using Two linear variable differential transformers (LVDTs) installed at the center of each side of beam using a yoke. The loading rate was set at 1 mm/min.

The flexural strength of a beam subjected to center-point bending test can be evaluated as follows:

$$f_r^{'} = \frac{3PL}{2bd^2} \qquad \text{Equation 8}$$

$f_r^{'}$ is the flexural strength (MPa), P is the ultimate load (N), L is the span of the test specimens (mm), b is the width of the test specimens (mm) and d is the height of the test specimens (mm).

Flexural toughness of samples is quantitatively calculated like cement mortar flexural toughness evaluation, and it is equal to the ratio of flexural toughness at $3\delta_0$ divided by the initial flexural toughness.

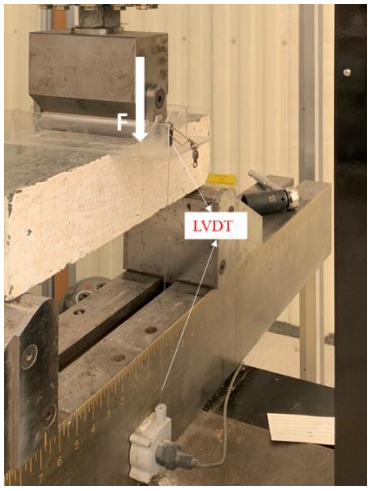

Figure 30. Center-point flexural test on beams

5.2.4. Design of FRCP

Round concrete panels were cast and tested using a 50000 kg pneumatic/hydraulic press, under single point loading following the testing arrangement and procedures of ASTM C155 [177]. The forms were first pre-oiled and levelled. An internal needle vibrator and a tamping rod were used to consolidate the concrete in the forms. The surface was screeded by racking a screed across the surface of the specimen and the extra concrete was struck off to make sure the surface is level with the sides of the form. According to the yield line theory, when a point load is applied at the center of a round panel supported on three symmetrically (120°) arranged pivots, stresses develop leading to the formation of three radial cracks (yield lines) on the opposite face and the yield lines follow a certain pattern as shown in Figure 31 [178].

Round panels shown in Figure 32, with dimensions of 75 mm in thickness and 800 mm in diameter were cast for flexural testing. Round concrete panels were demolded 24 hours after casting and kept inside wet burlaps until the day of testing. The mix proportions chosen for round panel testing were CO, 0.5PAT18 and 1PAT18 according to Table 9.

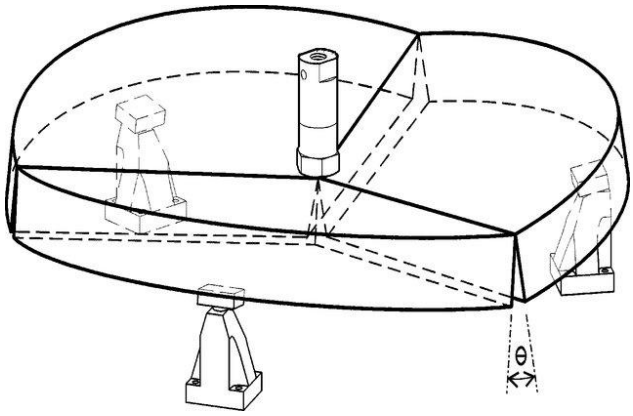

Figure 31. Failure pattern in round panels according to ASTM C1550 [174]

5.2.4.1. Flexural behavior of FRCP

According to ASTM C1550 [174], post-crack performance of round panels subject to a central-point load can be represented by the energy absorbed by the panel up to a specified central deflection. In this test method, the energy absorbed up to a specified central deflection was calculated to represent the ability of a FRCP to redistribute stress following cracking.

As it is shown in Figure 32, molded round panels of cast FRC are subjected to a central-point load while supported on three symmetrically arranged pivots. The load is applied through a hemispherical-ended steel piston advanced at a prescribed rate of displacement and. The cracks initiate from the bottom central point of the panel and gradually propagate to the edges between the supports and as the cracks widen at the center, the load resistance drops as deflections increase load-deflection values are recorded to evaluate the behavior of FRCP.

The load carried by the plate is recorded by means of a load cell and the displacement of the crosshead of the press [162].

The peak load, energy absorption and residual loads at 5, 10, 20, and 40 mm central deflection were extracted from the load-displacement curves and the peak load was used to calculate the flexural strength or Modulus of Rupture (MOR) of a panel using the following equation:

$$f_{ct} = \frac{2rP}{\sqrt{3}t_0^2 R} \qquad \text{Equation 9}$$

R is the radius of the panel = 400 mm; t_0 is the thickness of the panel = 75 mm and r is the distance from the center of the panel to the supports = 375 mm.

Analysis of variance (ANOVA) model was used to evaluate the variance between the values in flexural test of beams and panels and to determine if a statistically significant difference exists among the flexural strength measured by two different tests. ANOVA was performed with the software MATLAB©.

(a) (b) (c)

Figure 32. Round panel test set up a) pre-cracking state b) the appearance of first crack c) complete failure state.

5.3. Results and discussions

5.3.1. Fresh properties

Flowability of concrete is an important parameter that should be investigated to understand the contribution of fibers in concrete and to achieve optimum benefits from the fibers. The orientation of the fibers inside the matrix is affected by several parameters and one important factor is the flowability. Slump test is the most common empirical test for fresh concrete. Although slump test does not give any value of a rheological behavior of concrete, it can be efficient for classifying and comparing different construction materials in terms of their ability to fill-up a formwork. It was reported that the distribution and orientation of fibers, which has an important impact on bending properties of concrete, is related to the rheology of the

concrete [162]. In higher slump concrete, fibers have a satisfying mobility within the cement matrix; they can move and orient more easily under vibration. However, in concrete with lower slump values, there is a risk of formation of fiber balls and the movement of fibers is limited in the cement matrix.

The slump flow results of the fresh mortar mixtures with different fiber content, type and length are presented in Figure 33.a. The data illustrates the change of flowability of FRCMs with different variables. It is apparent that an increase of the fiber content, regardless of fiber type or length, causes a decrease in slump flow ability of samples decreases. It was observed that with the addition of more than 1% of fiber, except for 1PAM6 and 1PIM6 samples, the flowability of mortar was reduced to more than 50% and samples with 3% fibers showed 0% flowability. In polypropylene fiber-reinforced mortar (PPRM) samples, with an increase of fiber length, flowability dropped significantly. However, in carbon fiber-reinforced mortar (CFRM) samples, the flow results were not solely related to fiber length and the results didn't follow a specific trend. It was observed that for lower fiber fractions (up to 1%), fibers with higher aspect ratio showed relatively less vulnerability to changing slump values. The results can be described in such a way that for a constant volume of CF, a shorter length (with lower aspect ratio) possesses a greater number of fibers and as a result generating a higher negative effect on the slump values of fresh mortar samples. Figure 34 shows the influence of fiber content on the flow diameter of cement mortar.

Fibers also affect the workability of concrete mixes. The inclusion of fibers must be carefully optimized, and the flow characteristics of mixtures should be properly evaluated. According to the results presented in Figure 33.b, The slump values exhibited a high descending tendency up to 63% and 90% with the existing of 0.5% and 1% CF respectively, while this amount was 47% for 1% PP. The slump ranges for pavements and slab according to ACI 211.1 [179] is represented in Figure 33.b. As it can be seen, only the slump value of 1PAT18 mix falls into the range of 25–75 mm and can be classified as the proper mix for pavement and slab application.

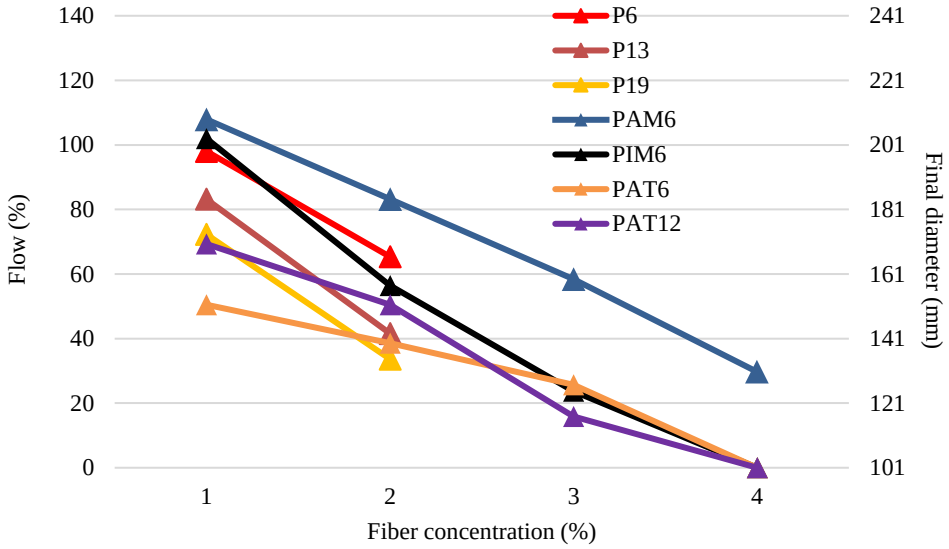

(a)

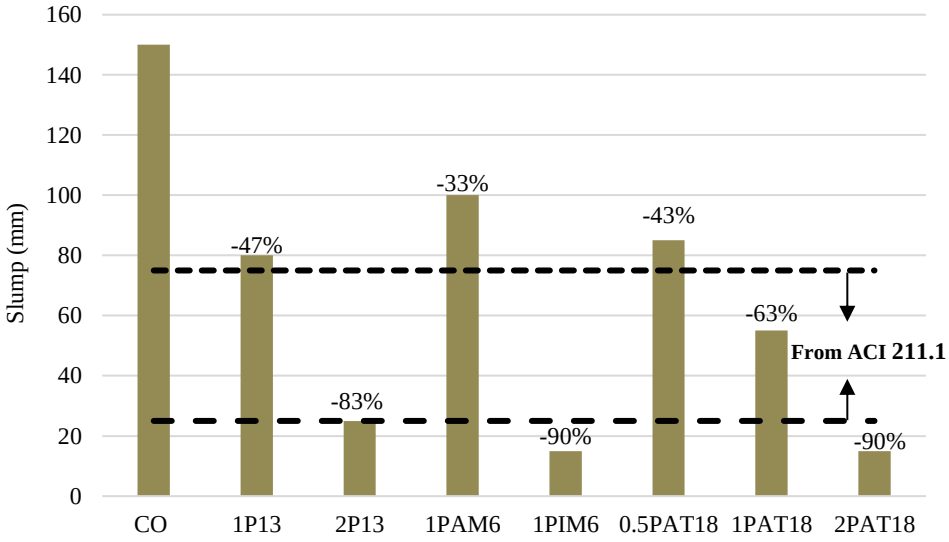

(b)

Figure 33. Flowability tests a) flow table results of cement mortar b) slump values of concrete (variation to CO shown over each bar)

(a) (b)

Figure 34. Flow table test a) NC b) P6

5.3.2. Compressive strength

5.3.2.1. Compressive strength of FRCM

Compressive strength is a major and important mechanical property of concrete, and it is considered as one of the main parameters in many design codes and standards. The compressive strengths of the mortar mixes are presented in Figure 35.a. The addition of PP in cement mortar decreased the compressive strength. In PPRMs reinforced with a volume fraction of 0.5% and 1%, the compressive strength of samples was 6.2% to 15.2% lower than that of the non-fibrous mortar (55.87 MPa). The lowest reduction was observed when 13 mm fibers were added and 1P13 samples earned strength equal to 52.4 MPa. Reduction in compressive strength of cementitious composites with PP addition was also reported in other studies [163–165]. This reduction could be mainly attributed to increased porosity due to the inclusion of PP and the existence of weak interfacial bonds between the PP and cement matrix [166] which is presented and justified in SEM photos in Figure 36. Fiber-reinforced mortar is mainly composed of 3 parts: cement paste, pores, and fibers. Investigation of changes in any of the mentioned parts is usually done by SEM micrograph. The black spaces in SEM photos are the pores inside the matrix and as it is shown in Figure 36, addition of fibers will produce a new porous phase between fiber-matrix known as ITZ. ITZ, which is only 20-40 μm in thickness, is considered as a new appearing defect in fiber-reinforced concrete [167].

Addition of CF up to 1% into cement mortar led to negligible change in compressive strength of mixtures (about ±5% difference compared to NC), except for 1PAT6 and 1PAT12 which experienced 15.0% and 12.6% strength improvement respectively. However, as the fiber content increased to more than 2%, all samples experienced notable strength loss. About 38% compressive strength reduction was reported when samples were reinforced with 3% CF. As previously mentioned, the incorporation of fibers inevitably introduces more air in the matrix due to the appearance of new porous area in fiber-matrix interface. However, in CFRM,

it is attributable that confinement of high stiffness CF compensates the drawback of increased porosity, and the increment in addition of CF from 0.5 to 1% improves the compressive strength of specimens, whose maximum compressive strength can reach 64.2 MPa.

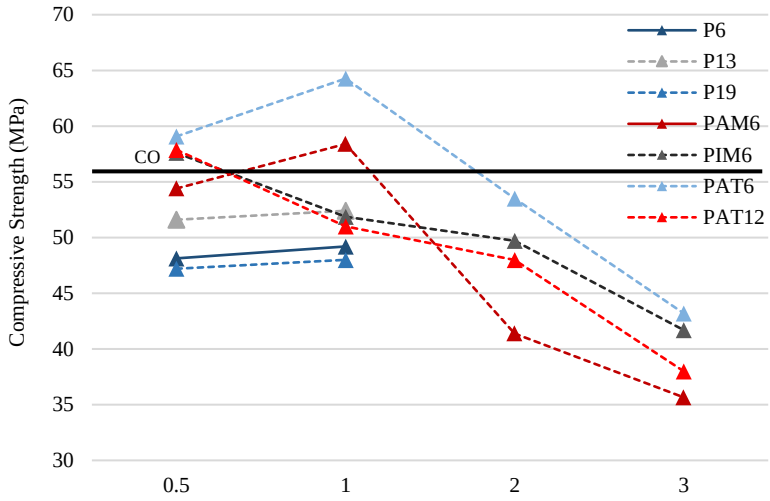

(a)

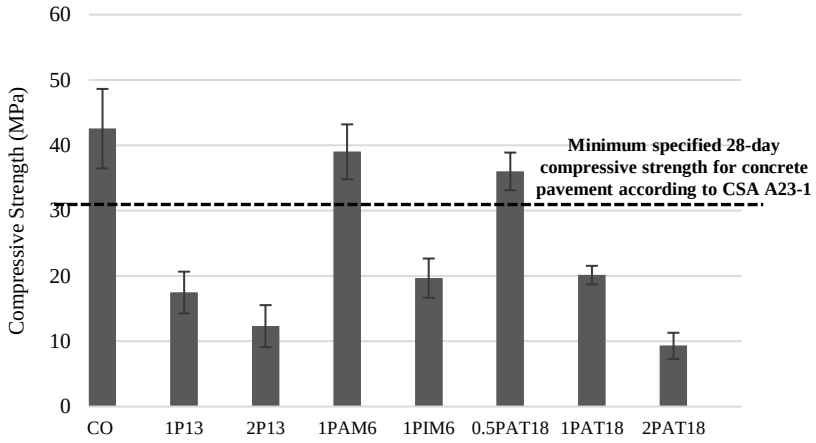

(b)

Figure 35. Compressive strength results of a) cement mortar b) concrete

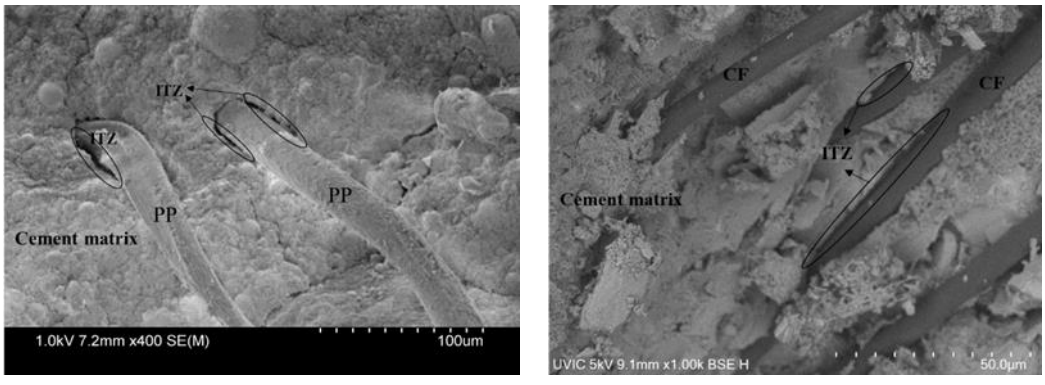

(a) (b)

Figure 36. SEM of FRCM a) PPRM b) CFRM

5.3.2.2. Compressive strength of FRC

The compressive strength results of concrete samples are presented in Figure 35.b, and the fracture patterns in tested samples are shown in Figure 37. During compression test, it was observed that non-fibrous samples failed explosively at the peak load while FRC samples failed with vertical cracks at the peak load but in a more ductile manner. In samples reinforced with fibers, the vertical cracks appeared at about 70–85% of the peak load. The results also show that the concrete mixes did not follow the same trend as in the mortar mixes. The highest compressive strength (42.5 MPa) was found in non-fibrous concrete, and the compressive strength of all samples decreased with an increase in fiber content. The least decrement was found in 1PAM6 (39.0 MPa) and 0.5PAT18 (36 MPa), which experienced approximately 4.8% and 15.2% decrease respectively in comparison with CO. On the other hand, Polypropylene fiber-reinforced concrete (PFRC) had the highest strength reduction (more than 15 MPa). Neither of the PFRCs meet the minimum strength requirement from CSA A23 [180] for any structural and non-structural applications.

According to CSA standard, the minimum specified compressive strength for non-structurally reinforced concrete exposed to chlorides and freezing and thawing such as concrete pavements and slabs is 32 MPa and among the mixes, 1PAM6 and 0.5PAT18 mixtures at 28 days surpass the threshold value of CSA to be used as slabs and pavements.

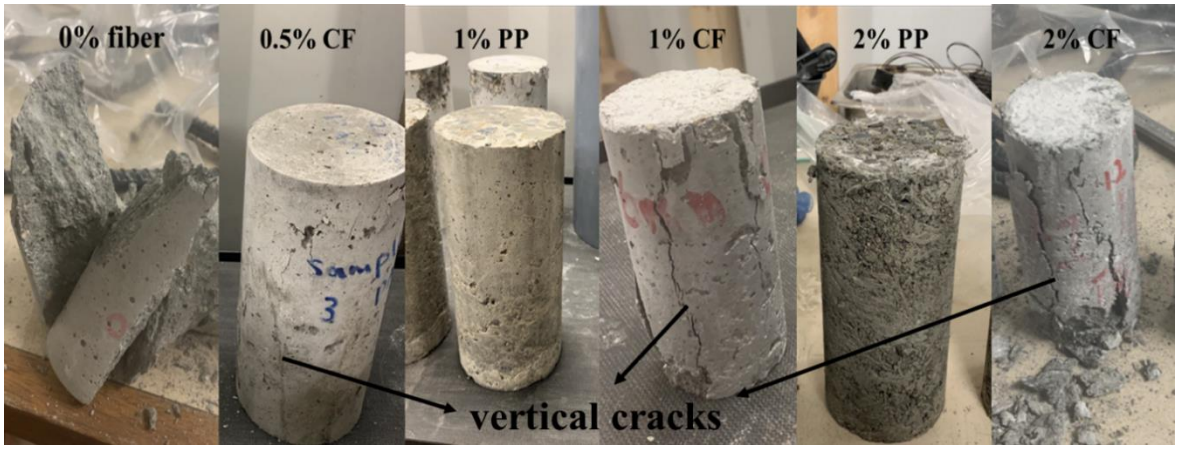

Figure 37. Fracture behavior of different samples under compression

5.3.3. Flexural properties

5.3.3.1. Modulus of rupture and flexural toughness index (I5)

The ultimate load, its corresponding displacement, the flexural strength, and pre-crack/post-crack energy absorption of all the mortar samples were obtained from the load-displacement curves, where the values are the average of three specimens. The detailed results are presented in Table 10. During the flexural test, different failure behavior was

observed among mixes. In samples reinforced with CF, fibers were able to successfully retard the crack initiation, hence absorbing more energy before reaching the peak load and in PPRM samples, fibers were able to bridge cracks and restrain propagation after the formation of cracks while non-fibrous samples failed under brittle behavior at the peak load. Representative load-displacement curves for non-fibrous, PPRM and CFRM samples are represented in Figure 38, in which the behavior is well-depicted. However, to better evaluate the effects of fibers, the absorbed energy until peak load compared to the absorbed energy after peak load, until $3\delta_0$, is plotted in Figure 39. The figure shows that the pre-crack absorbed energy rises with an increase in fiber content. However, the amount of pre-crack absorbed energy in CFRM samples is much more significant compared to that of PPRM. Comparing the results of samples with different fiber length revealed that increase in fiber length had a positive effect on the absorbed energy and samples with 12 mm long fibers have larger pre and post cracking stiffness than those with 6 mm fibers.

The flexural strength results are presented in Figure 40. According to the results, addition of PP decreased the flexural strength significantly (19.7% to 38.4% compared to CO). Two main reasons for the strength reduction of the PPRMs are as follows: First, due to deformation incompatibility of the PP and mortar materials and the presence of the ITZ between fiber and cement matrix, fibers detach from the matrix under loading, forming microcracks at the interface of the fibers and cement-matrix; second, adding fibers to concrete increases the porosity of the structure reducing the ultimate flexural strength.

On the other hand, samples reinforced with CF achieved higher ultimate load than both CO and PPRMs. This is mainly attributed to the confinement ability of micro CFs, holding and bridging microcracks in cement matrix, retarding the initiation and growth of cracks and compensating the strength reduction caused by increased porosity.

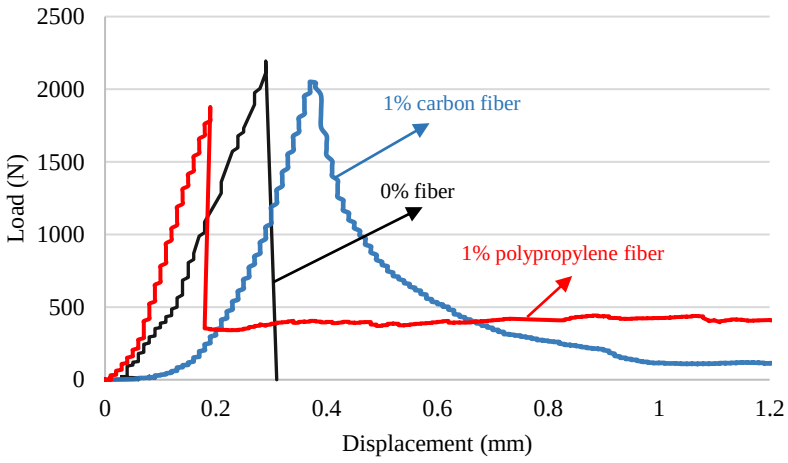

Figure 38. Load-Displacement curve in flexure

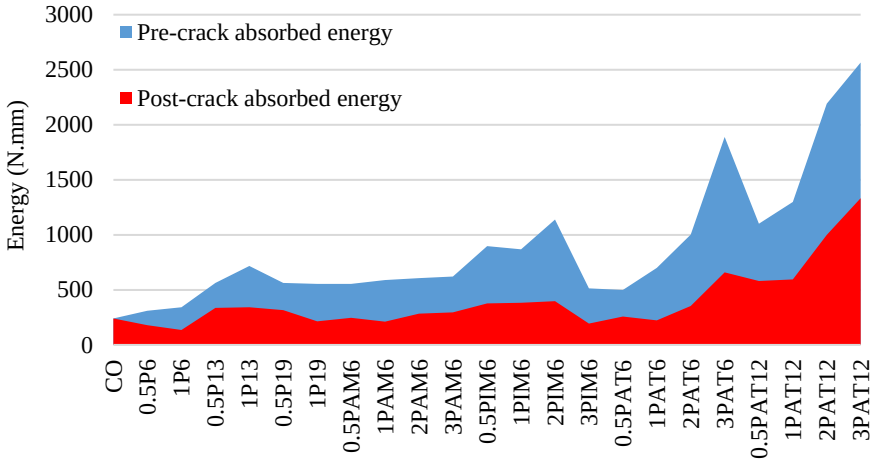

Figure 39. Pre-crack/post-crack energy absorption of cement mortar mixes

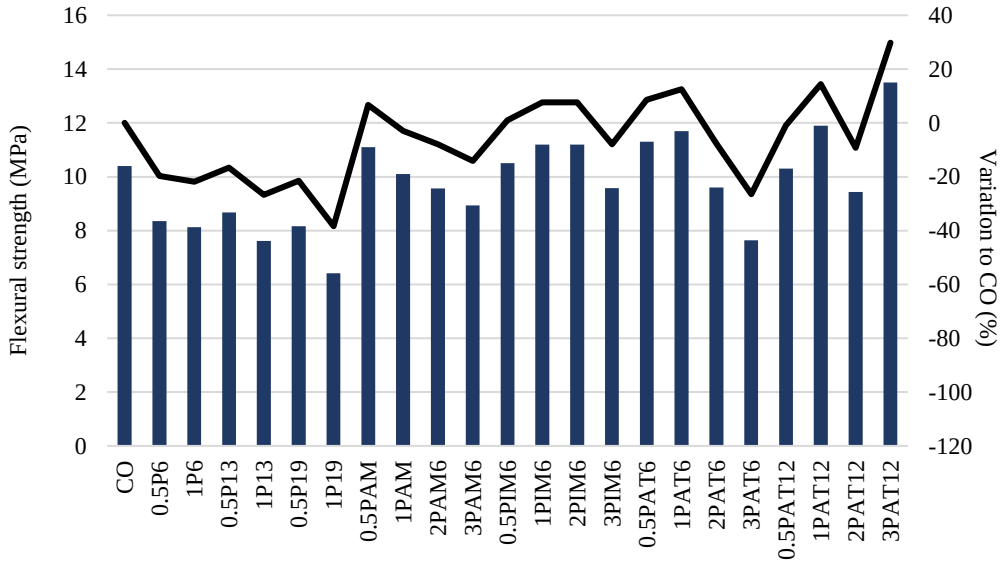

Figure 40. Flexural strength of mortar mixes

Table 10. Flexural testing results of cement mortar samples

Code	P_{MAX}	δ_0	$E_{\Delta 0}$	MR	$P_{3\delta 0}$	$f_{eq,3\delta 0}$	$E_{3\delta 0}$	I_5
	(N)	(mm)	(mJ)	(MPa)	(N)	(MPa)	(mJ)	
CO	2203	0.31	240.7	10.40	0.0	0.00	240	1.00
0.5P6	1768	0.20	178.4	8.35	334.0	1.58	309.7	1.74
1P6	1721	0.19	135.6	8.13	470.7	2.22	341	2.51
0.5P13	1836	0.29	337.0	8.67	340.5	1.61	564.4	1.67
1P13	1614	0.32	342.8	7.62	800.0	3.78	718.6	2.10
0.5P19	1727	0.39	316.4	8.16	381.5	1.80	561.9	1.78
1P19	1357	0.21	215.0	6.41	645.0	3.05	553.2	2.57
0.5PAM6	2350	0.39	245.5	11.10	75.0	0.35	555.6	2.26
1PAM6	2152	0.53	211.0	10.16	146.3	0.69	588.5	2.79
2PAM6	2027	0.55	284.0	9.57	169.0	0.80	607.5	2.14
3PAM6	1891	0.59	295.4	8.93	187.0	0.88	621.6	2.10
0.5PIM6	2229	0.41	378.3	10.53	0.0	0.00	898	2.37
1PIM6	2381	0.69	381.8	11.24	179.0	0.85	868.1	2.27
2PIM6	2388	0.53	396.2	11.28	201.0	0.95	1137.9	2.87
3PIM6	2029	0.33	194.0	9.58	133.5	0.63	513.7	2.65
0.5PAT6	2411	0.36	257.2	11.38	0.0	0.00	500	1.94
1PAT6	2496	0.33	222.3	11.79	0.0	0.00	700	3.15
2PAT6	2034	0.41	355.0	9.60	398.0	1.88	1001	2.82
3PAT6	1619	0.94	658.0	7.64	326.0	1.54	1889.3	2.87
0.5PAT12	2195	0.69	580.3	10.36	0.0	0.00	1100	1.90
1PAT12	2523	0.50	595.3	11.91	0.0	0.00	1300	2.18
2PAT12	2200	0.69	1000.0	10.39	354.3	1.67	2190.3	2.19
3PAT12	2865	1.19	1333.0	13.53	307.0	1.45	2565.5	1.92

5.3.3.2. Fiber optimization through analysis of model

To have an overall view of the effect of different types of CF on flexural behavior of FRC, a mathematical model was plotted using polynomial fitting technique. Curve fitting in MATLAB is the process of drawing a curve that has the best fit to a series of data points to find the optimum values. The fitting of the surface plot can show the behavioral complexity of the elements effective in a complex composite. It will also help to find the maximum and minimum points of the surface to find the optimum values. To find the best fitting curve that covers most of the data point, the surface quadratic polynomial fitting of experimental values on flexural strength and pre-crack/post-crack behavior of mortar samples was used and the curves are presented in Figure 41. The color scheme shows the variations in Z values and the maximum and minimum flexural strength values are clearly shown in the surface. Considering the maximum points of the surface, the optimized range for all types of CF is shown to be between 0.5% and 1%.

Pre-crack/post-crack surface shows a smooth surface, in which the effect of fiber length on improvement of pre-crack/post-crack energy absorption is well depicted in Figure 41.b and Figure 41.c. The optimum fiber dosage for both figures is reported to be between 2 and 3%. However, 12 mm long fibers show satisfactory values in all fiber dosages.

To determine the optimal concrete mix for the next phase, a comprehensive evaluation of results on fresh properties such as flowability and slump diameter, as well as mechanical characteristics including compressive strength, tensile strength, flexural strength, and energy absorption, was undertaken. The assessment also took into account the cost advantages associated with lower fiber content. After careful consideration, it can be concluded that a fiber content range of 0.5-1% is deemed the optimum percentage for FRCMs.

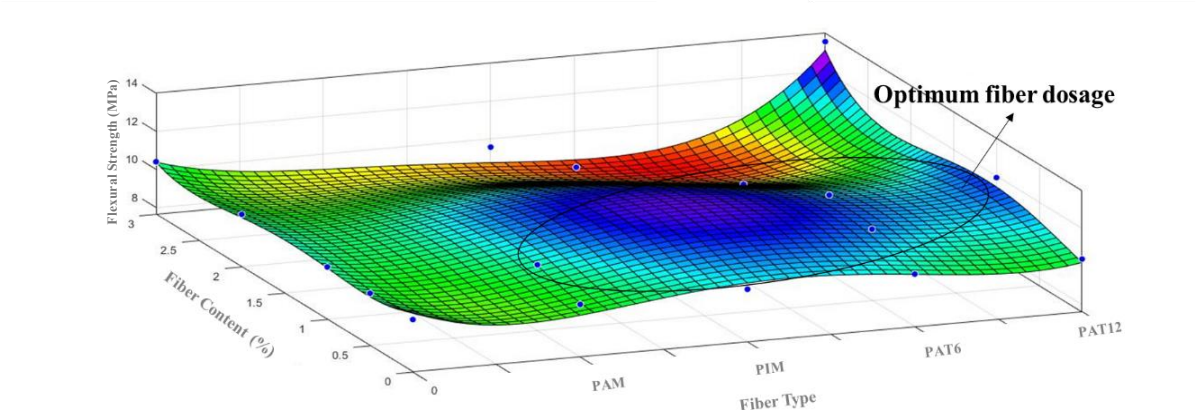

(a)

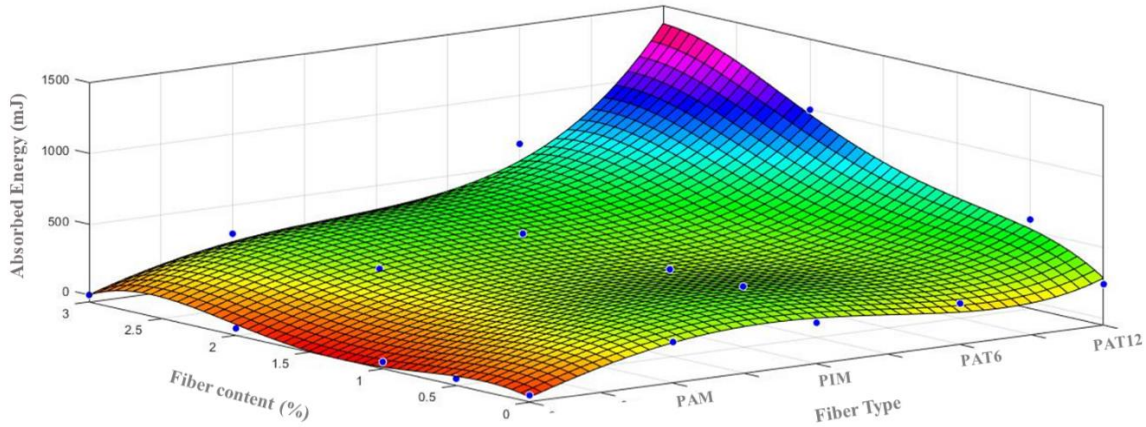

(b)

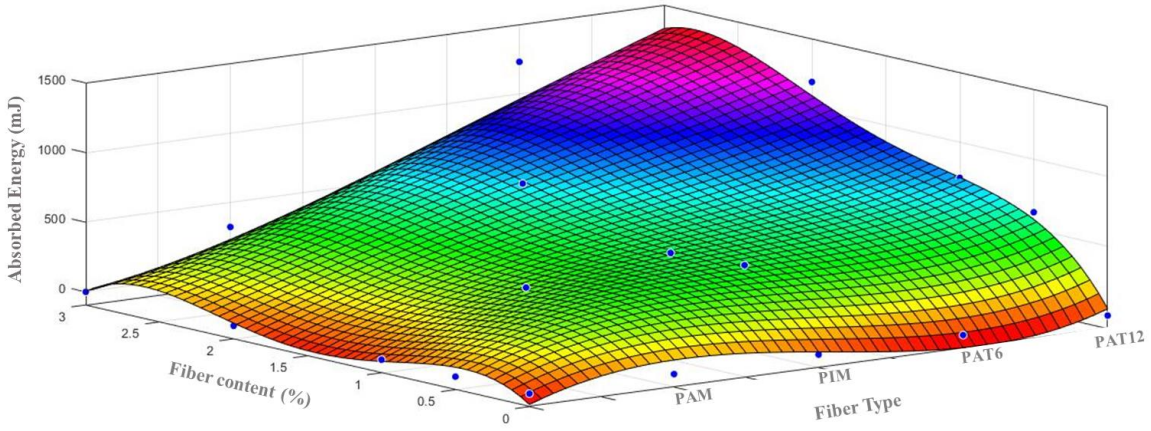

(c)

Figure 41. Surface quadratic polynomial fitting of a) flexural strength b) pre-crack absorbed energy c) post-crack absorbed energy.

5.3.3.3. Flexural behavior of concrete

According to the results given in Figure 42, the flexural strength of CFRCs is greater than that of unreinforced CO, except for 1PIM6 and PFRCs. Based on the results, the ideal strength gain is obtained from CFRCs with fiber length of 18 mm. However, in samples reinforced with 18-mm-long fibers, when the fiber content rises from 0.5% to 1%, the corresponding strength increases from 5.30 MPa to 6.84 MPa, and with the fiber content of 2%, the corresponding strength drops to 3.84 MPa. The load-displacement curves of FRC samples are plotted in Figure 43. The reason why the increased fiber contents (more than 1%) do not help increase the corresponding strength values can be explained by the interaction of the matrix-fiber structure. Since the cement matrix phase is similar in all mixes, the flexural behavior in concrete samples is dominated by the contribution of fiber in the mix. If the amount of the fiber added to the mix reaches a critical level, a weak structure surface in the interior of the formed backfill matrix will be created, thereby leading to the quicker failure of the sample subjected to bending. On the other hand, addition of fiber (more than a critical level) to concrete results in decrease in density and increase in porosity of concrete which can be considered as another main points of flexural strength reduction in CFRC. In this study, the critical level of the fiber content was experimentally found to be 1%.

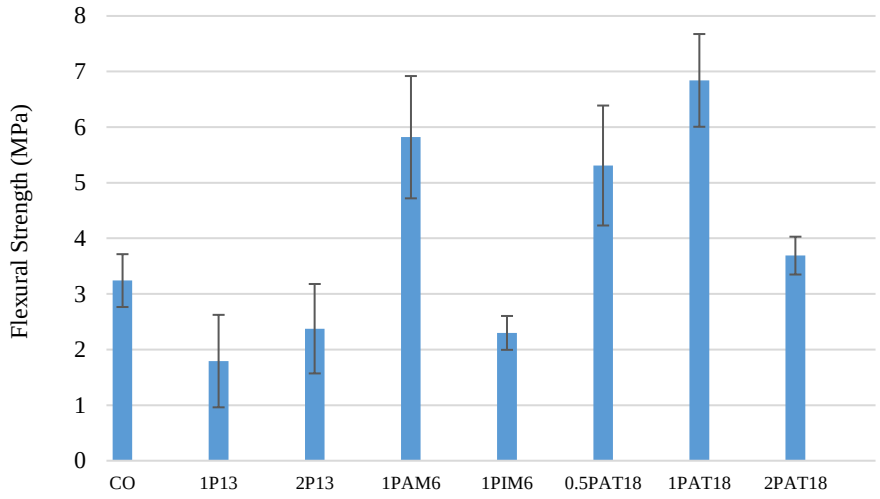

Figure 42. Flexural strength of concrete mixes

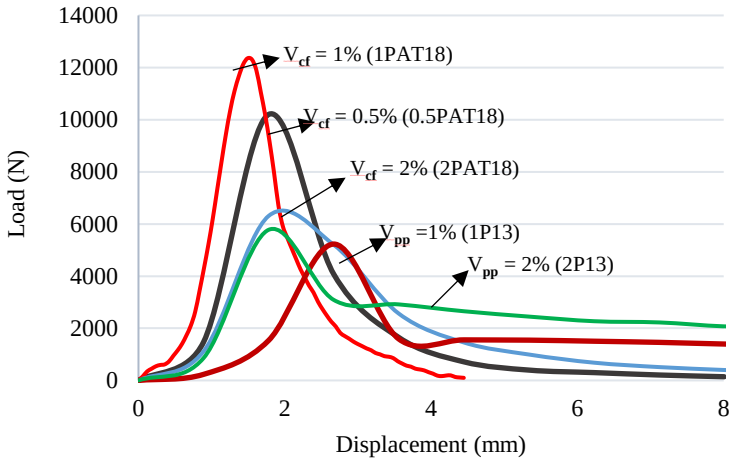

Figure 43. Load-Displacement curve of concrete mixes under flexure

5.3.3.4. Prediction of flexural strength

The flexural strength of FRC can be calculated based on the Composite Theory (CT) combined with the flexural-to-tensile strength ratio (α). In CT, tensile strength of FRC can be predicted by having the characteristics of fiber and cement matrix as well as the fiber-matrix bond strength. In this theory, it is assumed that the tensile strength of composite is a sum of tensile strength of cement matrix and fiber, and it can be calculated according to Equation 10 [168].

$$\sigma_{tc} = \sigma_{tm}(1 - V_f) + \sigma_{tf}V_f \qquad \text{Equation 10}$$

σ_{tc} is the tensile strength of fiber-reinforced composite (MPa); σ_{tm} is the tensile strength of cement mortar (MPa); V_f is fiber content by volume of the composite (unitless); σ_{tf} is the average tensile strength of the fiber (MPa).

Considering the effect of fiber orientation and length, Equation 10 can be rewritten as following:

$$\sigma_{tc} = \sigma_{tm}(1 - V_f) + \eta_l \eta_\theta \sigma_{tf} V_f \quad \text{Equation 11}$$

σ_{tf} is the tensile strength of carbon or polypropylene fiber; η_l is the length factor (unitless); η_θ is the fiber orientation factor (unitless) and can be determined by Equation 12 [117]:

$$\eta_\theta = \int_{\theta_{min}}^{\theta_{max}} p(\theta) \cos^2 \theta d\theta \quad \text{Equation 12}$$

p(θ) is the probability density distribution of fiber orientation; θ is the inclined angles of fibers to the cutting plane.

η_θ = 1 means that that all the fibers are perpendicular to the cut plane and η_θ= 0 means that all the fibers are parallel to the cut plane. The fiber orientation factor can be precisely measured using x-ray computer tomography [169], however, in literatures this factor was reported to be about 0.5-0.7 [117,168]. In this research fiber orientation was chosen 0.7 for best fitting of the results.

Length factor in fibers is highly related to the critical length of fiber. The critical length can be calculated as follows:

$$l_f^{cr} = \frac{d_f \sigma_{t\,max}}{2\tau} \quad \text{Equation 13}$$

l_f^{cr} is the critical length of fiber (mm); df is the fiber diameter (mm); τ is the bond strength between embedded fibers and cement matrix (MPa).

According to the previous studies, the length factor of fiber during flexural loading can be calculated as follows [181,182]:

$$\eta_l = 1 - \frac{l_f^{cr}}{2l_f} \text{ (if } l_f > l_f^{cr}) \quad \text{Equation 14}$$

$$\eta_l = \frac{l_f^{cr}}{2l_f} \text{ (if } l_f \leq l_f^{cr}) \quad \text{Equation 15}$$

l_f is the total fiber length.

Based on Equation 14 and 15, if fiber pullout-length is greater than the critical length, pull-out failure mode would be observed, and Eq. 12 can be used. Otherwise, Equation 15 will be used in the case of rupture failure of fiber.

The relationship between the tensile strength of fiber (σ_{tf}) and fiber critical length for failure is presented in Equation 16.

$$\sigma_{tf} = \frac{2l_f^{cr}}{d_f}\tau$$ Equation 16

Therefore, considering η_θ= 0.7, Equation 11 can be finally derived to calculate the tensile strength of the fiber reinforced concrete.

$$\sigma_{tc} = \sigma_{tm}(1 - V_f) + \frac{l_f}{2d_f}\tau V_f$$ Equation 17

Having the tensile strength of composite and assuming that a linear relationship exists between flexural strength (σ_{fc}) and tensile strength (σ_{tc}) of fiber reinforced cement-based composites [181], flexural strength can be calculated according to the following:

$$\sigma_{fc} = \alpha\sigma_{tc}$$ Equation 18

α is a coefficient (unitless), which usually equals to 2.0 [181,182], however, based on the preliminary results of cement mortar mixes and average of the calculated value (Figure 44), α was considered 2 in samples reinforced with PP and 2.6 in samples reinforced with CF.

The predicted and experimental flexural strengths of samples are summarized in Table 11. The experimental to predicted flexural strength for CFRC mixtures made with 1% PAN-based CF ranged from 1.11 to 1.34, suggesting good prediction results. However, the predicted values for PFRC are significantly greater than the values obtained from experiment. The reason why experimental results are significantly lower is mainly due to the higher porosity of samples.

Table 11. Comparison of the predicted and experimental flexural strengths

Code	Flexural strength (MPa)		Experimental to predicted flexural strength
	Experimental	Predicted	
1P13	1.79	5.02	0.36
2P13	2.37	6.81	0.35
1PAM6	5.81	4.34	1.34
1PIM6	2.29	3.82	0.6
0.5PAT18	5.30	4.55	1.16
1PAT18	6.84	6.14	1.11
2PAT18	3.68	8.51	0.43

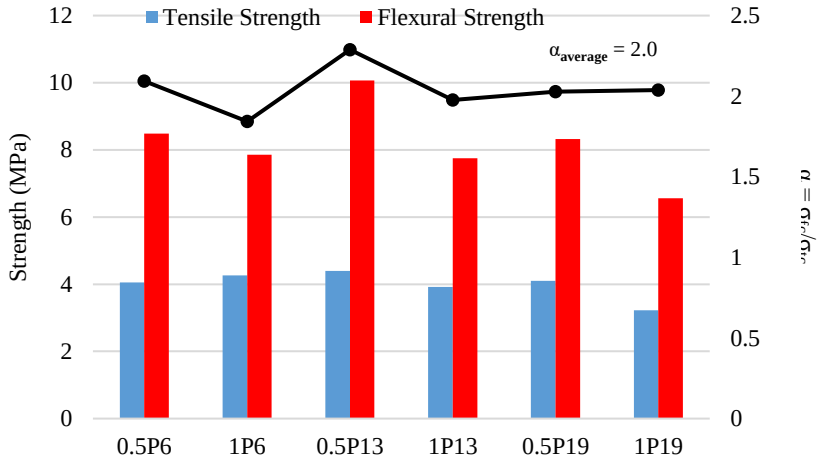

(a)

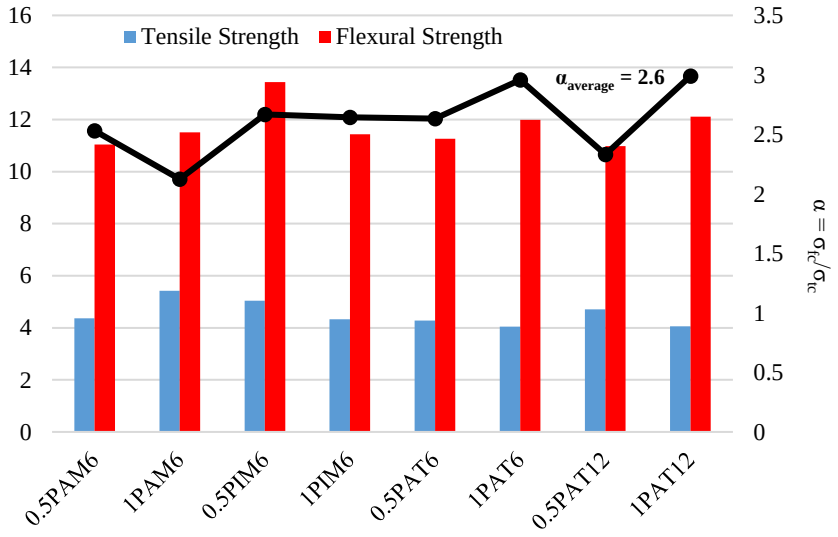

(b)

Figure 44. Variation of tensile strength vs flexural strength in a) PPRM b) CFRM

5.3.4. Flexural behavior of round panels

The yield line analysis method provides an upper limit estimate of the maximum ultimate resistance of a slab for an assumed mode of failure. The slab is assumed to fail by deflecting until plastic hinges (yield lines). Yield lines subdivide the slab into parts that rotate about the hinges until maximum deflection or failure occurs. The yield line theory developed by Johansen in 1972, is a practical method to provide an upper bound solution for the collapse load of a structure and can help obtain the flexural strength from the panels [183]. Based on the flexure behavior of concrete slabs, yield lines could be either symmetrical or non-symmetrical. Figure 45 Shows the fracture pattern of CO, 0.5PAT18 and 1PAT18 panels. During the testing, it was observed that all non-fibrous sample failed in a symmetrical yield

line pattern, while FRC panel experienced a non-symmetrical pattern. The behavior of round panels was evaluated under bending and the results can be found in Figure 46. The influence of the increase in fiber content from 0.5% to 1% is compared in the figure. The results show that 1% fiber content presents a stronger post-cracking response than the 0.5% fiber content, while 0.5% CF showed slightly higher ultimate strength.

The ultimate load, its corresponding displacement, the displacement at the failure, the flexural strength and the absorbed energy at 5, 10, 15 and 20 mm displacement were obtained through load-displacement curves, where the values are the average of three specimens. The detailed results are presented in Table 12. According to the results, it was observed that the ultimate deflection in CO sample was 20.6 mm, while this amount was equal to 114.7 mm and 158 mm in 0.5PAT18 and 1PAT18 respectively. 0.5PAT18 showed a comparable flexural strength compared to non-fibrous panel, while the strength of 1PAT18 was reduced to more than 20%. 1% CF in panels result in better performance in post-crack stage and panels were able to absorb an average of 158J energy compared to 114J and 20.6J in 0.5PAT18 and CO respectively. According to Table 8, absorbed energy values in CO did not fit in the minimum and maximum energy absorption given by ASTM C1550 [174], while the energy absorbed in 0.5PAT18 (in 5mm deflection) and 1PAT18 (in 5 and 10 mm deflection) samples fit in the energy absorption range suggested by the ASTM standard.

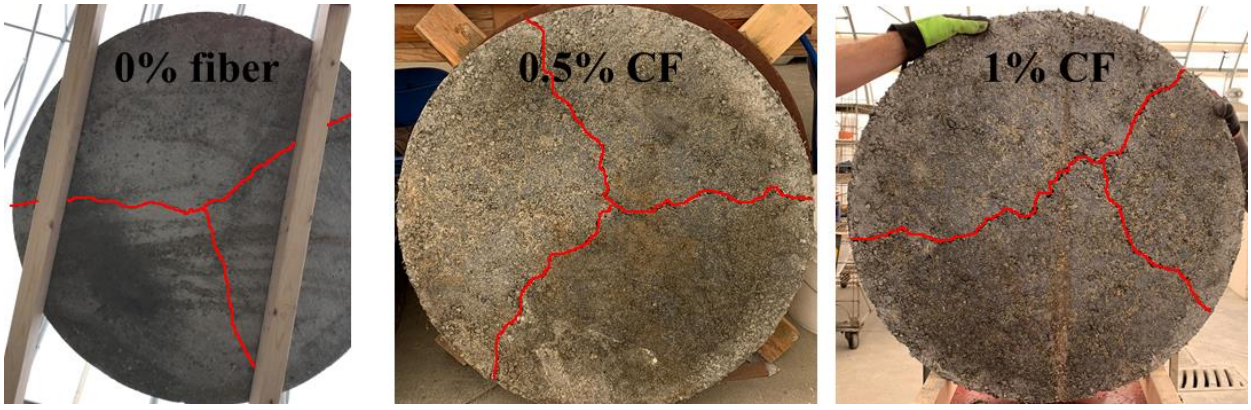

(a) (b) (c)

Figure 45. Fracture pattern of round panels a) CO b) 0.5PAT18 c) 1PAT18

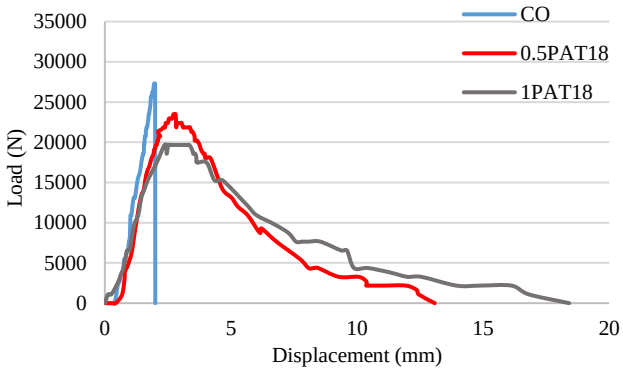

(a)

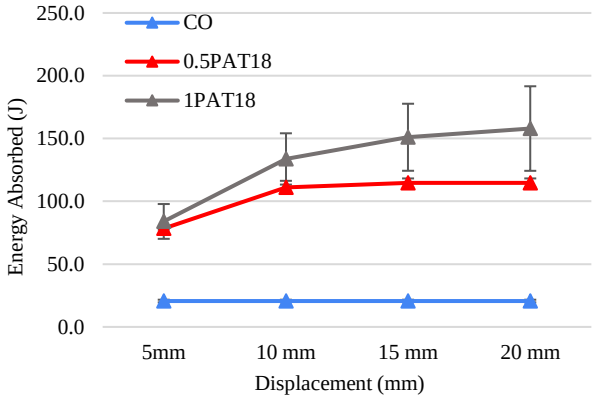

(b)

Figure 46. Round panel test results a) representative load-displacement curves of round panels under bending b) energy absorption of panels at certain displacements

Table 12. Summary of flexural behavior of round panels

Label	Peak load	δ_{peak}	δ_{max}	MOR	Energy (J)				Residual Load (N)			
	(N)	(mm)	(mm)	(MPa)	5 mm	10 mm	15 mm	20 mm	5 mm	10 mm	15 mm	20 mm
CO	26218.5	1.7	1.7	5.04	20.6	20.6	20.6	20.6	0	0	0	0
0.5PAT18	25940.5	3.2	13.0	4.99	78.4	111.1	114.7	114.7	13653	2730	0	0
1PAT18	20206.0	3.8	19.2	3.88	84.0	133.8	151.0	158.0	16929	6007	2730	546

Table 13. Minimum and maximum values of energy absorption in C1550 round panel specimens [174]

Deflection (mm)	Minimum energy (J)	Maximum energy (J)
5	61	136
10	121	200
15	195	343
20	236	473

5.3.5. Correlation between beams and panels flexural behavior

Round panels and beams were cast from the same batch of concrete; hence the flexural behavior of the beam samples and round panels is expected to be closely related. The relation between flexural strength in beams and panels is presented in Figure 47. It can be observed that the values from CO round panels did not show much difference compared to those from beams. On the contrary, in fiber-reinforced samples, the results of round panel were lower (up to 41%) compared to the beam samples. The results are mainly due to the different methodology used in beams and panel testing. In center point testing, the specimens are forced to crack at a given location (middle third), hence the crack does not necessarily open at the section with low strength material, however, when round panels are subjected to bending, yield lines follow the weakest sections. Although different methods including addition of superplasticizer, proper mixing procedure and using tamping rod and internal vibrator to consolidate the concrete samples were employed to ensure the uniform distribution of fibers, in samples with more that critical content of CF (1% and more), the fiber balling phenomenon was inevitable [184] and as a result, as shown in Figure 45, it was observed that the yield lines in several panels develop over an unsymmetrical pattern. On the other hand, round panels have a much larger crack area and as a result, they are expected to show a lower variance compared to beam samples. Figure 47 shows the spread of values in two different bending tests on each mix design, and as confirmed by the results, flexural strength values in panels have lower variance compared to beam samples.

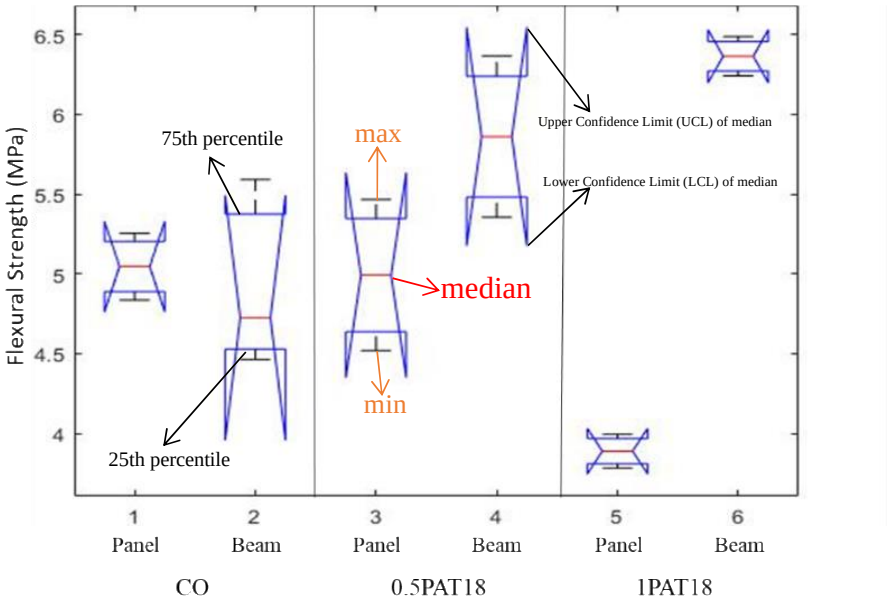

Figure 47. Analysis of variance on beams and round panels

5.4. Conclusions

The various types of fibers that can improve the performance of cementitious materials (including mortar and concrete) by decreasing crack initiation and propagation rate are discussed in this chapter. The experimental performance of polypropylene and CF reinforced mortar and concrete are evaluated to assess the efficacy of fibers on the rate of cracking in different samples. Non-fibrous samples are used as reference and the fresh (workability) and mechanical properties of fiber-reinforced samples are compared to them. The following conclusions can be drawn from the completed work:

- With an increase in fiber content, regardless of fiber type or length, the slump flow ability of cement mortar decreases. However, with more than 1% fiber, the flowability was reduced to more than 50%, and with 3% fibers, samples showed 0% flowability. Fiber length was reported to have a negative effect on the flowability of FRCM.
- Concrete slump values exhibited a remarkable loss as 0.5% and 1% CF decreased slump value up to 63% and 90% respectively. 1PAT18 was the only mix where the slump value was within the range of 25–75 mm, which can be classified as the proper mix for pavement and slab application.
- The compressive strength of PPRMs with volume fraction of 0.5% and 1% was 6.2% to 15.2% lower compared to non-fibrous concrete specimens. However, in CFRMs addition of fiber up to 1% led to a negligible ±5% change in compressive strength of mixes and as the CF content increased to 3%, all samples experienced a notable strength loss up to -38%. The reason behind this observation could be an increase in porosity and appearance of ITZ between fibers and cement matrix.
- In FRC, the highest compressive strength (~42 MPa) was found in non-fibrous concrete and the compressive strength of all samples decreased with an increase in fiber content. The least decrement was found in 1PAM and 0.5PAT, which experienced approximately 4.8% and 15.2% strength reduction respectively and the highest decrements was in PFRCs with more than 15 MPa strength reduction. The mechanical strength of FRC is closely related to the existence of porosity in the composite. With the inclusion of fibers, the porosity within FRC tends to increase, leading to a reduction in mechanical properties, notably compressive strength. Neither of the PFRCs meet the minimum strength requirement from CSA for any structural and non-structural applications.
- The flexural strength results showed that addition of PP decreased the flexural strength significantly (-19.7% to -38.4% compared to non-fibrous samples), which is mainly due to the deformation compatibility between fiber and cement matrix and presence of ITZ. However, CFRMs achieved higher ultimate load than both NC and PPRM samples. This was mainly due to the confinement ability of micro CF holding and bridging microcracks in

cement matrix.

- During flexural testing, CFRMs were able to successfully retard the crack initiation, hence increasing the pre-crack energy and in PPRM samples, fibers were able to bridge cracks and restrain crack propagation, while non-fibrous samples experienced brittle failure. Increase in fiber length had a positive effect on the pre-crack/post-crack absorbed energy.
- The quadratic polynomial fitting of a surface was used to show the optimum fiber dosage and length using the available information on the flexural strength. Considering the maximum points of the surface, the optimized range for flexural strength of CFRMs was shown to be between 0.5% and 1%. However, the optimum fiber dosage for pre-crack/post-crack energy absorption is reported to be 2% to 3%.
- Based on flexural strength results, the strength of FRCs is greater than that of non-reinforced concrete, except for 1PIM6 and PFRCs. Fiber length was reported to have a positive effect on flexural strength and the critical level of the fiber content was experimentally found to be 1%. Flexural strengths of concrete samples were predicted using the composite theory. The experimental to predicted flexural strength for CFRCs reinforced with PAN-based CF ranged from 1.11 to 1.34, suggesting good corroboration with predicted results. On the other hand, the predicted values for PFRCs are significantly higher than the experimental values which is mainly due to the higher porosity of samples.
- Analysis of Variance between flexural behavior of beams and panels showed that CO round panels didn't show significant variation when compared to those from beams. On the contrary, in FRCP, the results of round panel were up to 41% lower compared to the beam samples. The difference is mainly due to the different methodology used in beams and panel testing.

Chapter 6. Cement matrix deterioration after freeze-thaw exposure in electrically conductive carbon fiber-reinforced concrete

Paper Title: Analyzing concrete deterioration after freeze-thaw exposure in electrically conductive carbon fiber-reinforced concrete using non-destructive evaluation methods.

Author(s): Maryam Monazami, Rishi Gupta

This chapter, which is a submitted research paper in a peer-reviewed journal aims to analyze the bond-deterioration process during FT exposure in electrically conductive CFRC utilizing non-destructive methods. The focus is on understanding the effects of FT cycles on the bond strength between CFs and the concrete matrix. NDTs are employed to assess the bond condition without causing damage to the specimens. The study seeks to gain insights into the deterioration mechanism and behavior of CFRC under FT conditions, which is crucial for evaluating the long-term performance and durability of CFRC structures in cold regions. By analyzing the bond characteristics using non-destructive methods, this research contributes to a better understanding of the behavior of CFRC and provides valuable information for the development and optimization of CFRC mixtures for enhanced durability in freezing environments.

6.1. Introduction

In 2018, road accidents in Canada resulted in the tragic loss of 1,759 lives, with an additional 23,872 individuals being hospitalized due to severe injuries. The transportation sector incurred significant costs, ranking second highest at $3.6 billion in relation to these injuries. Among the various contributing factors, the presence of snow-covered roads and snowy conditions emerged as the primary cause of these accidents [185]. Data from the traffic accident information system (TAIS) supports this, indicating that accidents tend to increase during the winter season due to the detrimental effects of snow. Snow reduces the pavement's roughness and decreases the friction between tires and the road surface [186].

In order to address the hazardous effects of snow and ice on streets, researchers have been investigating various strategies and techniques to effectively managing icing and de-icing on roads. While mechanical snow removal is the most common method used, it is both time-consuming and expensive. Although mechanical snow removal is the conventional approach, it has drawbacks such as being time-consuming and costly. Additionally, snowplows often leave behind a thin layer of snow that necessitates further removal efforts [187]. Synthetic materials have been introduced to support the de-icing process, but some of

these substances have been found to cause considerable damage to infrastructure and the environment [188,189].

The harmful effects of snow on road pavements are attributed to the behavior and response of concrete under freezing conditions. The damage caused by freezing and thawing cycles in concrete can be explained by two established theories: the hydraulic pressure theory and the osmotic theory. According to the hydraulic pressure theory, the expansion of water during freezing exerts pressure on the pore walls or surrounding unfrozen water, leading to the formation of microcracks [190]. Conversely, the osmotic theory suggests that the difference in water vapor pressure between large and small pores causes water to be forced into smaller pores through osmosis, potentially resulting in microcracking if the tensile strength of the pore walls is exceeded [191].

Concrete contains air voids, categorized into three types based on their size: pores larger than 5 μm, capillary holes ranging from 5 nm to 5 μm, and gel pores smaller than 5 nm. [192]. During freezing, the larger open pores within the concrete experience expanding pressure as water transitions into ice, causing a volume increase. If this pressure surpasses the concrete's tensile strength, microcracks may develop, compromising the structural integrity of the pavement [193].

The presence of capillary voids, and gel pores contributes greatly to the damage caused by freezing and thawing cycles. Capillary holes permit water to enter the concrete and are consistent with hydraulic pressure theory [190]. When water freezes and swells within these capillary holes, it exerts pressure on the surrounding pore walls, causing microcracks and deterioration. The osmotic theory is connected with gel pores, which are smaller in size. Because these small pores have lower water vapor pressure than bigger pores, water migrates towards them via osmosis. This migration increases pore pressure and may exceed the tensile strength of the pore walls, leading to the formation of microcracks and further concrete degradation [10].

To enhance frost resistance and prevent micro-cracking, the use of fibers as reinforcements in concrete has been widely advocated [194,195]. Numerous studies investigated the durability and mechanical characteristics of cementitious composites reinforced with various types or amounts of fiber [196–199]. Dong et al. [197] studied the effect of polyethylene and steel fiber on the FT behavior of FRC. The results showed that due to the high compactness of concrete, the relative dynamic modulus of elasticity of FRCs are unaffected by hundreds of FT cycles. Ren et al. [151] studied the effect of adding polypropylene fibers in concrete and resulted that PP fiber was a good option to increase the concrete’s resistance to frost. The effect of adding Basalt fiber in concrete was investigated by Li et al. [198] and a significant improvement in mechanical behavior and mass loss when the amount of fiber increased in the concrete was reported. Jute fibers are also reported to

improve the dynamic modulus of elasticity of concrete and concrete with jute fibers were reported to sustain freezing and thawing cycles better than normal concrete [199].

Furthermore, beyond the use of standard fibers, there is an intriguing path for further improving concrete performance in colder locations. While the use of electrically conductive CF in concrete-related technologies has been thoroughly researched and published in a variety of applications [27,71,187,200], there is currently a research gap in the freezing and thawing behavior of electrically conductive composites. A comprehensive and in-depth analysis is necessary to adequately analyze the appropriateness and possible benefits of using CFs in concrete for places prone to cold weather conditions.

The significance of this chapter lies in its comprehensive exploration of the performance of electrically conductive composites under freezing and thawing cycles, utilizing a set of non-destructive evaluation (NDE) techniques. By studying how these composites behave during FT cycles and assessing their structural integrity using NDE methods, the research provides crucial insights into their durability and performance in colder climates. The results showed that after 300 freeze-thaw cycles, all the test results clearly indicated that the FT cycles significantly affected the properties of CFRC. The damage to the concrete increased with higher fiber concentrations. The optimal fiber dosage was determined to be 0.5%, which generally exhibited the best performance in terms of dynamic modulus of elasticity and mass loss, while effectively preserving the structural integrity under repeated freezing and thawing.

6.2. Experimental investigation

6.2.1. Materials

The aggregates' gradation curve is depicted in Figure 10. The Teijin Cooperation provided PAN-based CFs with 18 mm length. Digital microscope and SEM images of CFs are shown in Figure 48. In this study, 5 groups of concrete mixtures with different concentrations of CF (0%, 0.5%, 1%, 2% and 3% by volume) were considered to examine the effects of fiber on the FT behavior of CFRC. To enhance the concrete's resistance to degradation caused by FT cycles, a target air content between 5% to 8% was maintained for all mixes. The concrete mix design is provided in

Table 14. To ensure accuracy, three specimens are tested for each test, and the average value is reported. Abbreviations were denoted in such a way that the first number shows the dosage of fiber, and the last number illustrates the length of the fiber. Non-fibrous mix abbreviated as CO.

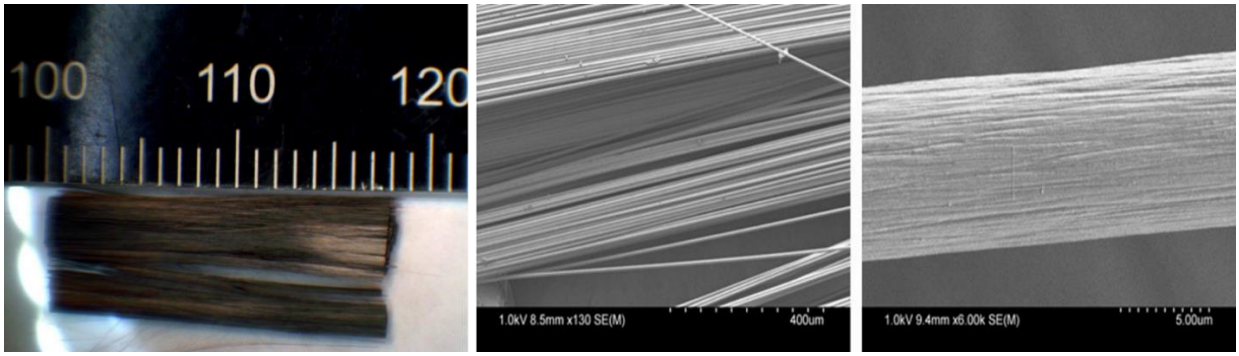

(a) (b) (c)

Figure 48. Images of a) digital microscope, b & c) SEM of PAN-based carbon fibers

Table 14. Mix designs of five different CFRC mixes

Mix	Fiber		Gravel	Sand	Cement	Fly ash	Water
	(kg/m^3)	%	(kg/m^3)	(kg/m^3)	(kg/m^3)	(kg/m^3)	(kg/m^3)
CO	0	0	1055	815	276	60	148
0.5CFT18	9	0.5	1055	815	276	60	148
1CFT18	19.0	1	1055	815	276	60	148
2CFT18	39.0	2	1055	815	276	60	148
3CFT18	48.0	3	1055	815	276	60	148

6.3. Methods and equipment

6.3.1. Preliminary mechanical tests

Cylindrical samples were subjected to a 28-day compression strength test as per ASTM C39 [201]. The loading speed ranged between 900 and 1800 N/s. The results presented are the average of three samples that were molded from the same batch of concrete and evaluated at the same age. To examine the flexural behavior of materials, center-point bending tests were performed on prismatic specimens of 100 x 100 x 400 mm in accordance with ASTM C293 [202]. A universal testing machine from Measurement Technology Inc (MTI) with a maximum load capacity of 225 kN was employed to apply the load. The load was applied using a load cell at a speed of 1 mm/min. Two linear variable differential transformers (LVDTs) were mounted at the center of each sample. The amount of absorbed energy was determined by integrating the area under the load-displacement curve [175]. The amount of flexural toughness was calculated at $3\delta_0$ (corresponding displacement with 3 times as high as the corresponding displacement of the maximum load, δ_0).

6.3.2. Freeze-thaw cyclic test

The experiments were carried out in a Humboldt HC-3186S4F freeze-thaw chamber (Figure 49). The test, which involved rapid freezing and thawing in water, was carried out in

accordance with ASTM C666 [203] standard. Each FT cycle consisted of rapidly freezing and thawing the specimens in water. The temperature of the specimens was reduced from +4.4 °C to -17.8 °C and then raised from -17.8 °C back to 4.4 °C. This temperature change occurred over approximately 3.5 hours. It is worth noting that the freezing and thawing times were roughly equal within a single FT cycle. At regular intervals, specifically every 30 cycles of FT, the machine was halted. Nondestructive testing (NDT) methods were employed to evaluate the behavior of the samples. These NDTs were performed on specimens in the saturated surface dry (SSD) condition at room temperature. The testing process continued until 300 cycles of FT were completed.

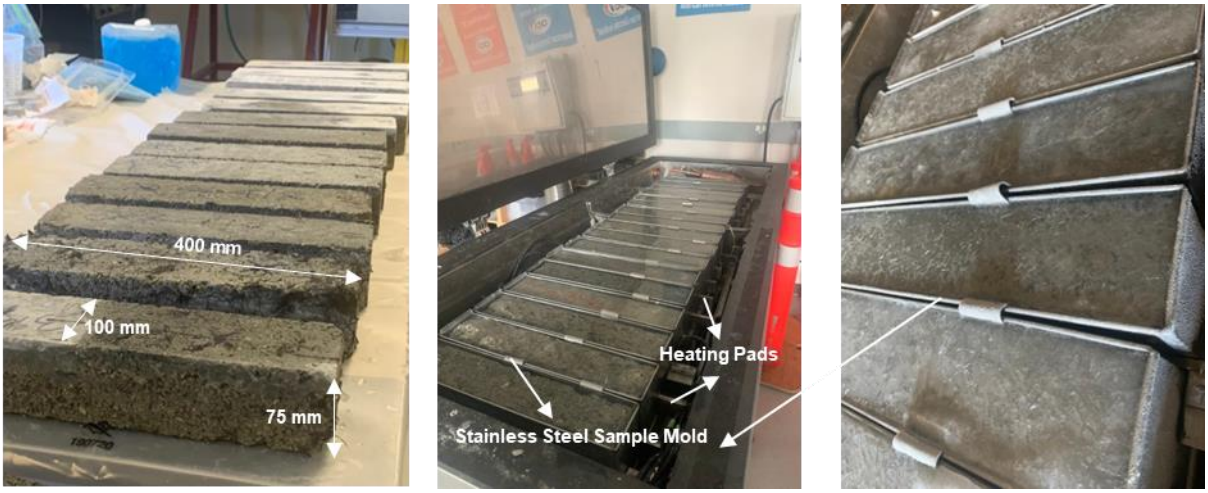

Figure 49. Freeze-thaw test setup

6.3.3. Mass loss

When concrete is subjected to repeated FT cycles, the water traps within its pores can freeze and expand. As mentioned earlier, this expansion exerts internal pressure on the concrete, leading to microcracks and damage. Upon thawing, the water within these cracks can refreeze during subsequent cycles, causing further deterioration and expansion. This cyclic process can result in the spalling of surface mortar and a reduction in the overall mass of the concrete. To quantify the extent of mass loss and evaluate the concrete's frost resistance, the mass loss ratio (ΔM) is commonly utilized. The formula to calculate the mass loss ratio is as follows:

$$\Delta M_n = \frac{M_n - M_0}{M_n} \qquad \text{Equation 19}$$

ΔM_n is mass loss ratio after n FT cycles (%); M_n is mass of sample after n FT cycles and M_0 is mass of sample at 0 FT cycle.

6.3.4. Resonant frequency test

As with the compressive strength of concrete, the dynamic modulus of elasticity is one of the most significant features illustrating mechanical performance [204]. ASTM C215 [205], specifies a procedure for determining the dynamic elastic modulus of cementitious materials using the resonant frequency of prismatic specimens. As indicated in Figure 50, the process involves attaching a PCB Piezotronics 353B15 accelerometer near the top of the specimen and striking the specimen's center with a hammer to measure the transverse frequency. The resonant frequency data, captured by the accelerometer and recorded using an Olson Instruments RTG-1 Resonance Test Gauge, is used in equations 2 and 3 to calculate the dynamic elastic modulus. This test method provides valuable information on the material's elastic behavior under dynamic loading conditions.

$$E_d = CM_n^2 \qquad \text{Equation 20}$$

E_d is dynamic modulus of elasticity (Pa); C is dimensional factors of the specimen; M is mass of the specimen (kg); and n is fundamental transverse frequency (Hz).

$$P_c = \left(\frac{(E_d)_n}{(E_d)_0}\right) 100 \qquad \text{Equation 21}$$

P_c is relative dynamic modulus of elasticity after n cycles of freezing and thawing (%); $(E_d)_n$ is dynamic modulus of elasticity after n cycles of freezing and thawing; and $(E_d)_0$ = initial dynamic modulus of elasticity at 0 cycles of freezing and thawing.

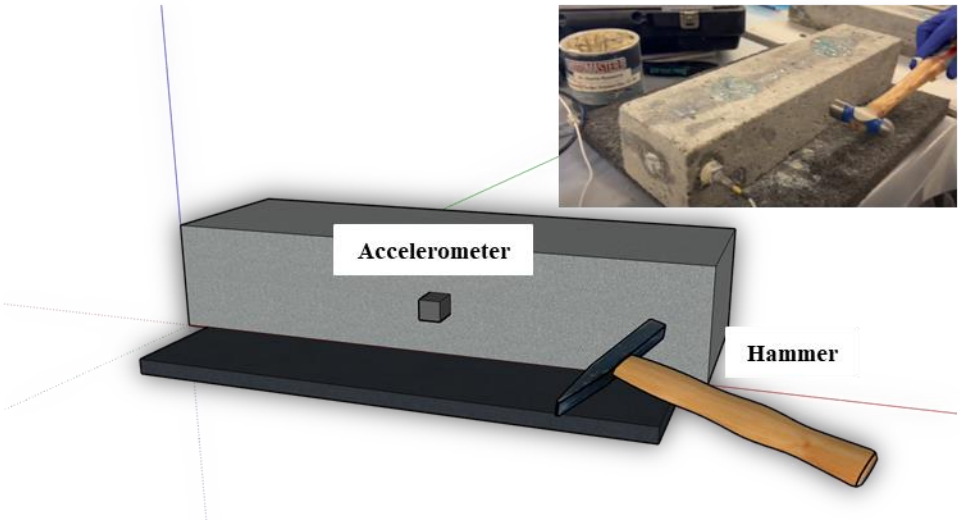

Figure 50. Resonant frequency test

6.3.5. Ultrasonic pulse velocity test

The ultrasonic pulse velocity (UPV) method is a NDT technique used to measure the speed of an ultrasonic pulse in a material, such as concrete. It is a practical method for assessing

the quality of concrete because the pulse velocity is primarily influenced by the elastic properties of the material and not its geometry [206]. The density and elastic qualities of the material affect how quickly these waves go through solid materials. The UPV test measures the speed at which ultrasonic pulses propagate through the material. The test setup consists of an emitter that emits ultrasonic pulses, a receiver that receives the pulses, and a device that displays the time it takes the pulses to travel between the emitter and the receiver (Figure 51). The portable Proceq Pundit UPV tester with a frequency of 54 kHz was used in this test. Three beams from each mixture were tested, and the average UPV values were calculated under Saturated Surface Dry (SSD) condition. The following equation can be used to calculate the pulse velocity in accordance with ASTM C597 [207].

$$V = \frac{L}{t} \quad \text{Equation 22}$$

V is the pulse velocity (m/s), L is path length (m) and t is transit time (s)

Equation 5 provides the relationship between UPV and dynamic modulus of elasticity [208]:

$$E_d = \rho V^2 \frac{(1+\mu)(1-2\mu)}{(1-\mu)} \quad \text{Equation 23}$$

E_d is dynamic modulus of elasticity (DMOE) (Pa); μ is dynamic Poisson's ratio; ρ is concrete density (kg/m^3); and V is pulse velocity (m/s).

For the calculation of DMOE, the Poisson's ratio of concrete is assumed to be 0.2 [209,210].

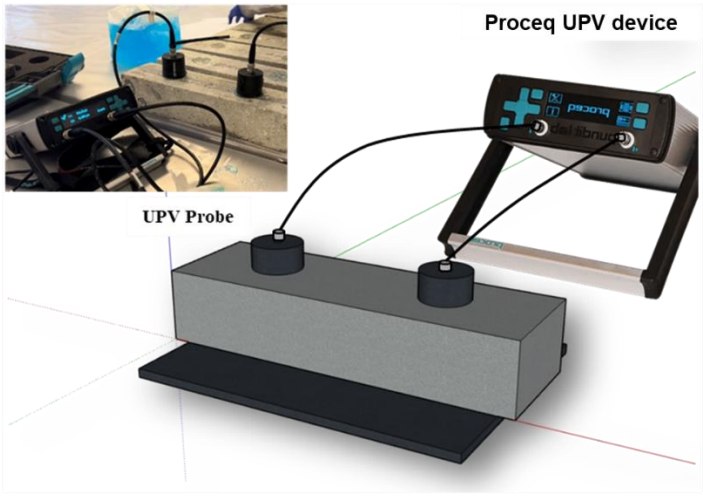

Figure 51. Ultrasonic pulse velocity test

6.3.6. Infrared (IR) thermography technique

Another NDT used to determine the extent and depth of flaws in concrete specimens is infrared thermography. There are two alternative IR thermography testing procedures depending on the source of the heat. The active technique, which uses an external thermal stimulation, induces the necessary heat flow condition on the concrete under investigation.

The passive strategy, a popular method for monitoring the health of infrastructure, relies on solar heating and fluctuations in the surrounding temperature [211]. During the day, the light both directly and indirectly warms the concrete by increasing the surrounding temperature. Heat is absorbed by concrete, which then begins to radiate energy. the surface area above any subsurface delamination resists heat transfer and warms up more quickly. This can be seen on IR images as a ”hot spot” on the concrete surface. The region of sound concrete, however, loses heat at a slower pace than delaminated sections at night when the ambient temperature typically drops. Thus, subsurface delamination shows up on thermal IR imaging as” cold spot” on the concrete surface [212]. In this study, the FLIR E60, a high-resolution thermal camera with 25 x 19-degree field of view and thermal imaging at 320 x 240 pixels, was employed. The camera settings were adjusted to enable it to capture infrared (IR) images under controlled laboratory conditions. Features and specifications of the camera is summarized in Table 15.

Table 15. Features and specifications of the FLIR camera

Items	Parameters
IR camera resolution	320 x 240 pixels
IR FOV	25°
IR spectral range	7.5 - 13 µm
IR temperature range	-20° to 650° C
Visible camera resolution	2048 x 1536
Image Fusion	Yes, MSX

6.3.7. Hammer percussion

ASTM D4580 describes [213] a number of common techniques for acoustically probing concrete to find delamination, including the hammer percussion (HP) technique. The hammer percussion method as shown in Figure 52 involves striking concrete samples with a hammer to cause an acoustic disturbance, and recording the resulting acoustic response with a microphone [214]. The acoustic signal can be further analyzed to extract valuable information such as resonance frequencies. In this particular study, the specimens were positioned on a sponge rubber pad and struck using a steel ball hammer weighing 56.7 g. The resulting sound response was captured using a recording setup consisting of an audio recorder and a pair of microphones. Specifically, a Polsen OLM-20 Dual Omni directional Lavalier Microphone was used as the microphone, while a Zoom H1 digital voice recorder with a maximum sampling rate of 96 kHz and 24-bit depth was utilized. The Zoom H1 recorder's 24-bit analog-to-digital conversion capability ensures precise data acquisition during post-production analysis.

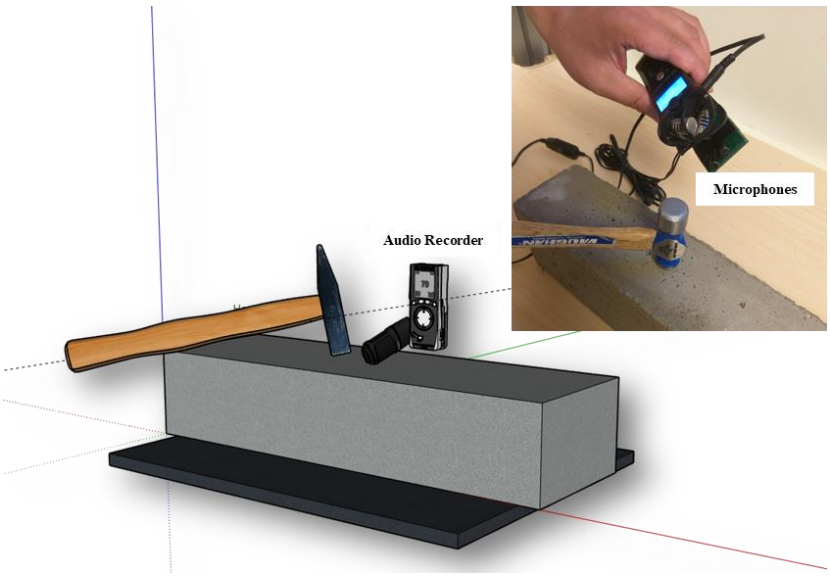

Figure 52. Hammer percussion test

6.4. Results and discussion

6.4.1. Compressive strength

The average initial compressive strength and flexural characteristics of samples (flexural strength, initial energy absorption and toughness index-I_5) are displayed in Table 16. It is important to note that in cylindrical samples with 3% CF, it was difficult to grind or cap the samples because of their extremely low strength and presence of large voids, which caused the samples to break during the grinding process and even during handling. It can be seen that the compressive strength of all samples dropped as the amount of CF increased. The minimum specified compressive strength required by CSA A23 [180] standards for non-structurally reinforced concrete exposed to chlorides and freezing and thawing, such as concrete pavements and slabs, is 32 MPa. As a result, for this application, the maximum permissible amount of CF that can be added to concrete while preserving its initial mechanical properties is 0.5%. This limited addition of CF is necessary to ensure that the strength values of the concrete remain within the range recommended by CSA standards.

Figure 53 shows the crack patterns of samples after failure in compression test. It was seen that CO samples exhibited a few macro vertical cracks and experiences a brittle failure, while all samples reinforced with CF failed in a ductile mode with a number of thinner cracks.

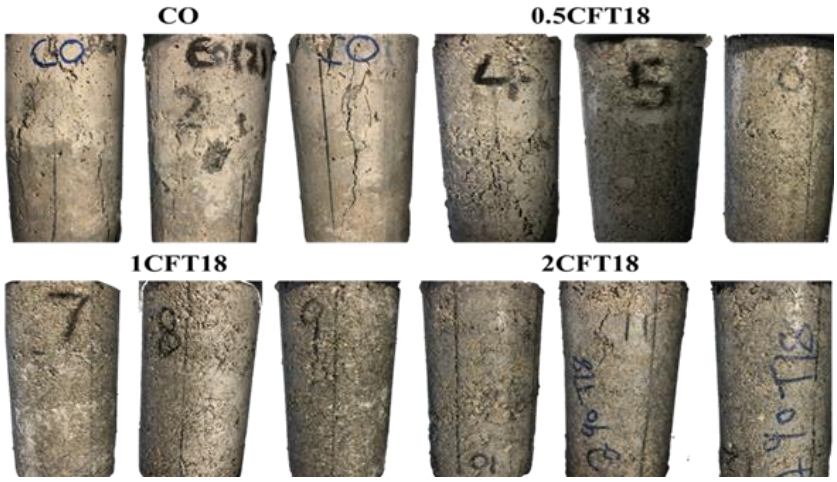

Figure 53. Fracture pattern of concrete samples after compression test

6.4.2. Flexural properties

To further investigate the impact of CF addition in concrete, the flexural strength of the samples was evaluated. Flexural properties of samples were investigated at two stages (one before the start of FT test and secondly after FT test completion). Table 16 displays the flexural properties of the samples at 0 and 300 FT cycles. The results at 0 FT cycle demonstrate that the flexural strength of samples (also known as the modulus of rupture, or MOR), dropped as the concentration of CF increased, following a similar trend to that of compressive strength. However, the inclusion of CF (up to 2%) greatly improved the pre-crack and post-crack characteristics. 0.5CFT18, 1CFT18 and 2CFT18 absorbed 162, 184 and 135% more energy respectively before the failure of beams which is a significant improvement also has been confirmed in previous study by the authors [77]. According to Table 16, the specimens reinforced with 1% CF exhibited the most favorable energy absorption and post-crack behavior, specifically in terms of initial absorbed energy. These specimens demonstrated a toughness index (I5) of 3.94, indicating their ability to absorb energy even after cracking has occurred. In contrast, the samples without any fiber reinforcement had a toughness index of 1.02 indicating a lack of post-crack energy absorption capability. The other fiber-reinforced samples showed toughness values of 2.88, 3.94, and 6.5 for the 0.5CFT18, 1CFT18, and 3CFT18 specimens, respectively. These results suggest that increasing the CF content generally leads to improved post-crack behavior and higher energy absorption capacity, with the 2% CF sample demonstrating the best performance in this regard. It is noteworthy to mention that even though the sample with 3% CF had the highest I_5 value, the low values of MR and initial energy absorption indicate that this high I_5 value is not representative of actual improved performance.

Table 16. Average compression and flexure properties of samples

Label	0 FT cycle						300 FT cycles		
	Compressive strength		Modulus of rupture	SD	$E_{initial}$	I_5	Modulus of rupture	SD	Reduction
	(MPa)	SD	(MPa)		(N.mm)		(MPa)		%
CO	46.76	2.67	9.24	0.4	765.5	1.02	8.35	0.62	9.63
0.5CFT18	31.12	1.27	8.65	0.01	2010.67	2.88	7.82	0.79	9.6
1CFT18	16.8	1.29	5.91	0.99	2180.5	3.94	5.35	0.23	9.48
2CFT18	7.56	1.59	3.65	0.63	1805	5.75	1.67	0.52	54.25
3CFT18	x	x	1.59	0.17	826.5	6.5	0.7	0.14	55.97

Furthermore, a significant disparity in strength between specimens becomes evident following 300 cycles of FT exposure. As observed in Table 16, the flexural strength of CO beams and beams with 0.5% and 1% CF exhibited a reduction of approximately 9% after 300 FT cycles. In contrast, the beams containing 2% and 3% CF experienced a drastic decrease in flexural strength, showing a remarkable reduction of nearly 55%.

The higher dosage of CFs in the concrete leads to the development of increased voids and gaps within the concrete matrix. These voids and gaps provide pathways for water to penetrate into the concrete, exacerbating the damage caused during FT cycles. As a result, the concrete becomes more porous, and larger cracks form, compromising its structural integrity.

6.4.3. Mass loss

The surface condition of representative samples of different mixes after being subjected to a total of 300 FT cycles is shown in Figure 54 and the mass loss of the samples at each FT cycle is shown in Figure 55. According to Figure 55, there are two primary stages in the mass loss curves: a gradual decline stage and a rapid drop stage. During the initial 60 FT cycles, the mass loss remained consistently low across all samples. However, beyond this threshold, the rate of mass loss notably increased, particularly in samples with higher fiber volumes. The shift from gradual to accelerated concrete damage happens due to crack formation during FT cycles. This is intensified when water and other expanding materials occupy existing pores and new cracks. Exceeding the concrete's tensile strength causes cracks, allowing moisture and harmful substances to penetrate deeper. Water exacerbates expansion and contraction during FT cycles, accelerating crack growth and damage. The presence of additional CFs, coupled with an increase in the number and width of cracks, leads to increased porosity and greater retention of water within the samples. The mass loss increases significantly when the pores and newly formed microcracks interconnect, creating pathways that facilitate the easy movement of water through the concrete sample. Furthermore, the findings regarding mass

loss were consistent with the visual observations. Samples containing 3% fibers not only exhibited visible surface deterioration after 300 FT cycles but also experienced a mass loss exceeding 1%. This is while no bulk damage was observed in specimens with 0% and 0.5% in long term, as seen by the almost constant mass with FT cycles.

The equation derived from the mass loss data enables the estimation of mass loss percentages with a high level of accuracy for samples with up to 2% of CF.

$\Delta M_n = -0.0011C + 0.0229$ Equation 24

Where ΔM_n is mass loss (%) and C is FT cycles.

Figure 54. Scaling of samples at different FT cycles

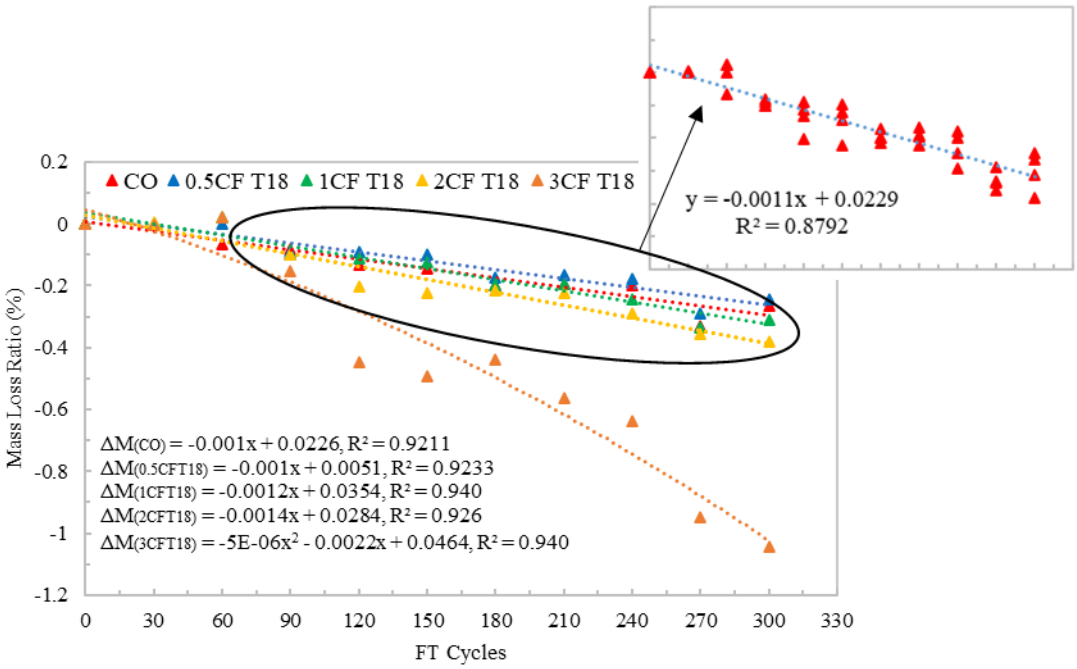

Figure 55. Mass loss of all samples at different FT cycles

6.4.4. Dynamic modulus of elasticity

An essential characteristic that shows the interior damage brought on by freezing and thawing is the dynamic elastic modulus [215]. To calculate the dynamic modulus of elasticity (DMOE) in concrete, stress wave and ultrasonic techniques have become highly common [216]. In the sections that follow, the dynamic modulus of representative samples will be determined using UPV, RFT, and HP techniques, and the results will be compared.

6.4.5. Ultrasonic pulse velocity

The propagation velocity of ultrasonic longitudinal stress waves (P-wave) through concrete in UPV test can be related to composite components used in concrete, such as cement, aggregate, and fiber type, aggregate-cement ratio and water-cement ratio [217]. Because the only difference between the five groups of samples is the amount of CF, the presence of fibers can be considered as the only cause of differences in UPV at each FT cycle. Figure 56 shows that adding CF to concrete lowered the velocity, which is caused by the addition of CF, which makes the matrix more porous. It should be mentioned that determining the UPV in concrete is an indirect testing method to learn more about the material's permeability and pore structure and the test is usually paired with other NDTs to get a more accurate prediction [214,218–220]. As a result, this study also looks at various NDTs to provide more conclusive and complete conclusions regarding the effects of employing CF in concrete.

The five sets of concrete specimens (CO, 0.5CFT18, 1CFT18, 2CFT18, and 3CFT18) had initial ultrasonic velocities of 6657, 6623, 5105, 4227 and 3329 m/s respectively. As it is shown in Figure 7, For CO and 0.5CFT18 samples, the change in velocity was more gradual, but for the other three groups, the fall in velocity was more abrupt as the number of FT cycles increased. For each set of specimens, the fitting curves with the highest coefficient of determination (R2) are presented as dashed lines. It is demonstrated that the polynomial fitting has the maximum reliability proposing that the equations can be used to predict UPV variations over time.

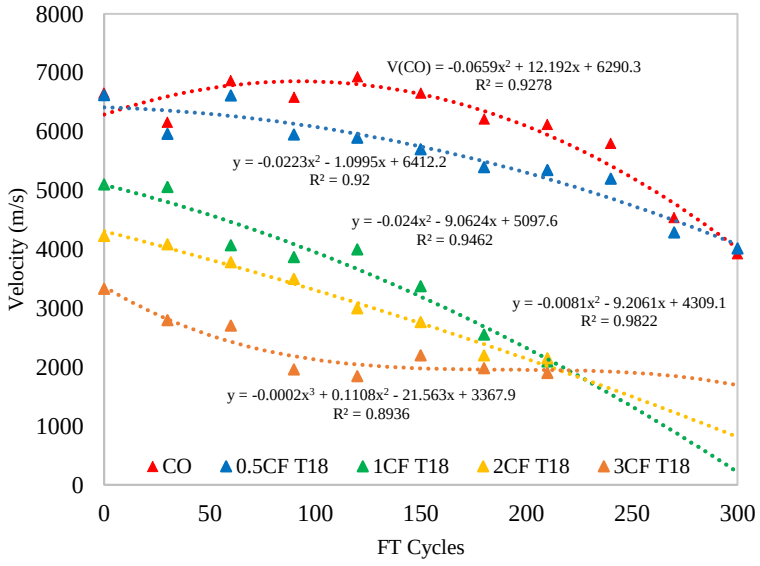

Figure 56. Ultrasonic pulse velocity variations at different FT cycles

Figure 57 shows the relation between the dynamic modulus of elasticity and FT cycles. As can be observed, the variations in the DMOE of the five groups of concrete specimens that underwent FT cycles exhibited patterns that were comparable to those of the ultrasonic pulse

velocity under FT cycles. Polynomial fitting which demonstrated a satisfactory reliability threshold, was the best fitting curve that described the variability of DMOE. As shown in Figure 57, in CO and 0.5CFT18, the DMOE of frozen-thawed concrete showed a slow declining stage and a quickly declining stage. The main reason is because during the early stages of the FT cycle, degradation occurs mostly on the concrete surface due to the dense pore structure in CO and 0.5CFT18, and the relative dynamic elasticity modulus gradually declines. On the other hand, the damage to the samples is further aggravated by the addition of CF above 0.5%, which also results in additional pores being created inside the concrete. Due to the increased porosity of such concrete, water can enter the interior and cause microcracks beginning with the early FT cycles, significantly decreasing the dynamic elasticity modulus.

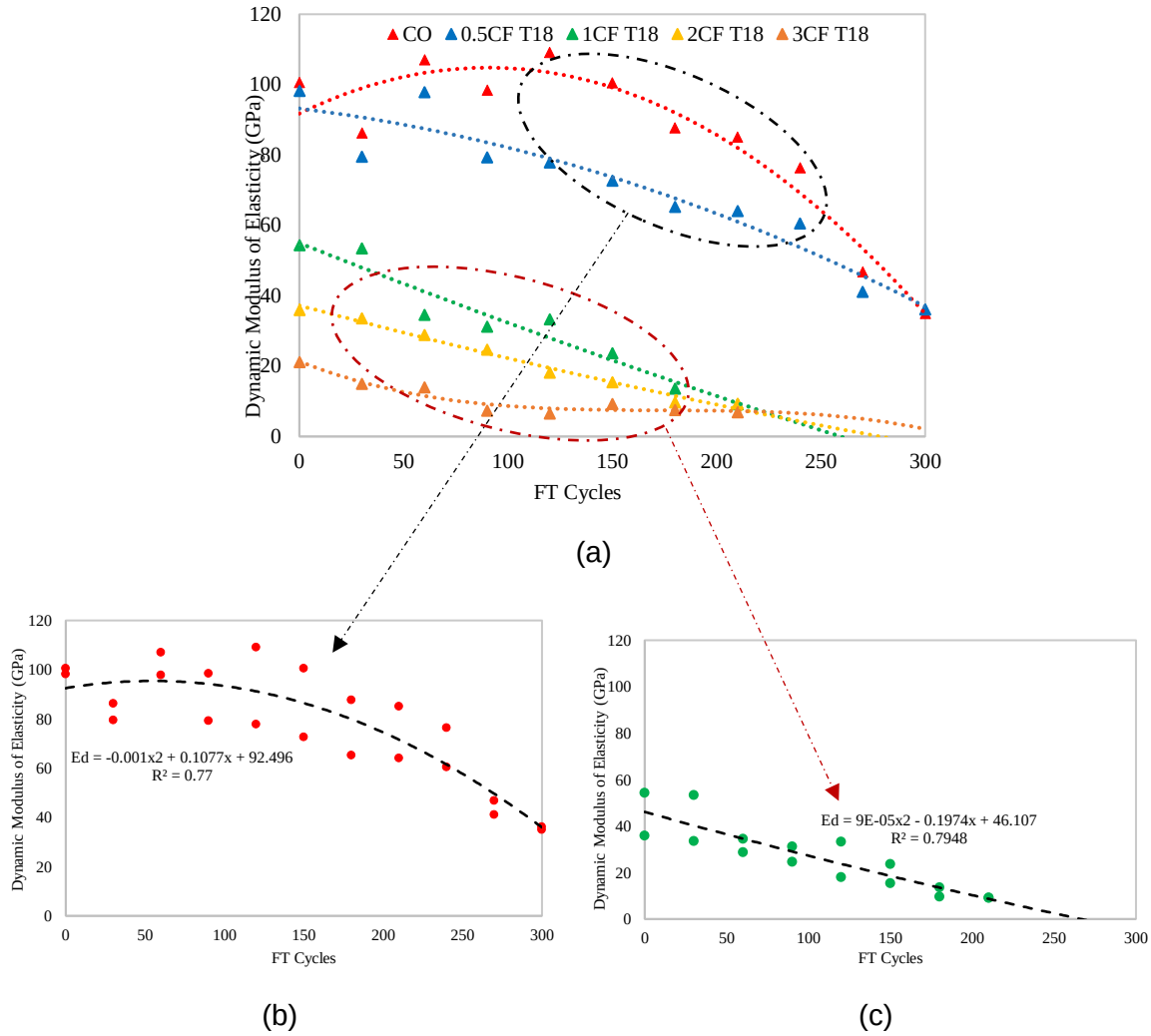

Figure 57. (a) DMOE variations at different FT cycles derived from UPV results (b) equation to predict DMOE for CF≤1% and (c) equation to predict DMOE for CF>1%

To predict the DMOE with acceptable precision based on the obtained data, it is necessary to categorize the behavior of the samples under FT cycles into two distinct groups. The first group consists of samples with CF content less than 1%, while the second group includes samples with CF content ranging from 1% to 2%. The equations are as following:

If CF≤1%

$$E_d = -0.001C^2 + 0.1077C + 92.49 \quad (R^2 = 0.77)$$ Equation 25

If CF>1

$$E_d = 0.00009C^2 - 0.1974C + 46.107 \quad (R^2 = 0.79)$$ Equation 26

Where E_d is the dynamic modulus of elasticity (GPa) and C is the FT cycles

6.4.6. Resonant frequency

The fundamental bending, longitudinal, and torsional modes of vibration of a beam can be properly represented with a closed-form expression. If only the 1-D motion of it is considered [119]. This approximation is the foundation of the approach for calculating dynamic elastic constants from vibration frequencies described in ASTM C215 [159]. According to the standard, the concrete beam was struck with a hammer at various points to stimulate the three primary vibration modes (longitudinal, transverse, and torsional). The mechanical vibrations picked up by the sensor are then converted into time-domain signals, which are then turned into spectrum by a Fast Fourier Transform (FFT) method.

Based on the position and strength of the peak in the frequency-domain spectrum, the frequency of each fundamental vibration mode can be calculated [120]. Using either the longitudinal or transverse fundamental frequency, young's modulus of the samples can be determined [159]. However, it was found that the transverse mode was preferable since the peak of the longitudinal fundamental vibration mode was relatively gentle, making the peak position easily impacted by noise and leading to a more subjective assessment [221]. As a result, only the transverse frequency was utilized for the dynamic modulus investigation in this chapter.

Figure 58 shows the relative dynamic modulus of elasticity values and the dynamic modulus of elasticity for all samples at various FT cycles. Samples with 0.5% CF had comparable results to non-reinforced ones. According to Figure 58.a, there is a definite trend showing that the dynamic modulus decreases exponentially as fibers concentration increases. According per ASTM C666 [158], the test should continue until the beam has gone through 300 cycles or, if earlier, until its relative DMOE reaches 60% of the initial modulus. Hence, a 60% drop in DMOE can be regarded as a beam failure. Considering what was recently stated,

all samples with 1, 2, and 3% of CF failed before 60 FT cycles, however those with 0.5% fiber were able to endure 300 FT with a minimal decline in DMOE.

Although CO and 0.5PAT18 greatly outperformed other samples in both UPV and RFT tests, the findings of the comparison between the two test results were inconsistent in terms of the trend for DMOE. It is demonstrated that in UPV test, the DMOE decreases proportionally as the FT cycle increases, however in RFT test, the DMOE difference was only negligible until 300 FT cycles in both CO and 0.5PAT18 samples. It was also shown that the DMOE results did not have similar magnitudes. In comparison to RFT results, it was claimed that UPV exhibited substantially higher values.

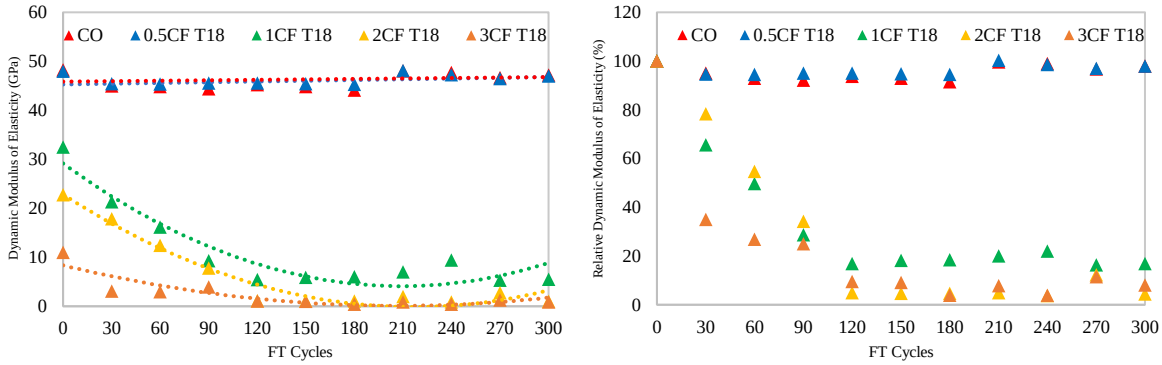

(a) (b)

Figure 58. Dynamic properties at different FT cycles derived from RFT results

6.4.7. Hammer percussion

Dynamic properties of CO and CFRC samples are shown in Figure 59. The results demonstrate that the 0.5CFT18 and CO samples exhibited the least reduction in DMOE, with decreases of 15% and 10% respectively after 300 FT cycles. These findings suggest that samples containing 0.5% CF are the most resilient to the detrimental effects of FT cycles.
The relative dynamic elasticity modulus showed distinct patterns for different samples. For CO and 0.5CFT18, the decrease in DMOE followed a linear trend, indicating a gradual and consistent decline in their dynamic elasticity modulus as the FT cycles progressed. On the other hand, the behavior of the remaining samples (1CFT18, 2CFT18, and 3CFT18) followed a polynomial fitting curve, suggesting a more complex and non-linear relationship between the FT cycles and their dynamic properties.

After 60 FT cycles, samples with 1% and 2% of CF experienced a dramatic reduction in the relative dynamic elasticity modulus, surpassing a 60% loss. This considerable decrease indicates severe damage to the specimens, compromising their dynamic properties and structural integrity. Visual inspection further confirmed the impaired condition of these samples, corroborating the detrimental effects of FT cycles on their overall performance.

Despite having a very low initial DMOE value in 3CFT18 samples, indicating a structurally weak sample from the beginning, its dynamic properties deteriorated rapidly. As early as 30 FT cycles, the relative dynamic elasticity modulus began to fall dramatically. This emphasizes the poor structural quality of the 3% CF sample, which rendered it highly susceptible to the negative impact of FT cycles. Visual inspection also confirmed the compromised structural integrity of the specimen.

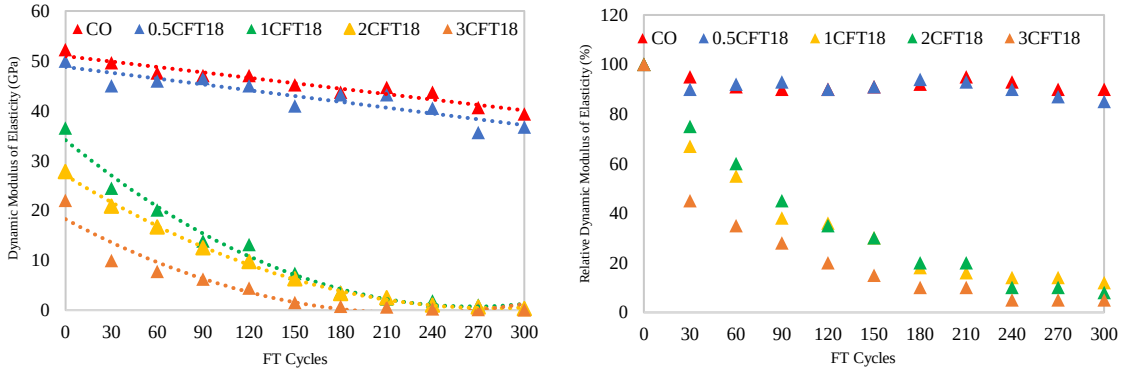

Figure 59. Dynamic properties of samples at different FT cycles derived from HP results

6.4.8. Infrared imaging

Figure 60 shows infrared images of samples at 0 and 120 FT cycles. At 0 FT cycle, the CO sample exhibits the most uniform temperature distribution among all the samples. This suggests a relatively consistent homogeneity in the CO sample, indicating a more uniform structure. The 0.5% CF sample exhibits void areas before the start of FT testing, these voids were visible in the infrared images, and indicated the presence of pores within the material. However, after undergoing 120 FT cycles, the infrared images of the 0.5CFT18 sample remain intact. This suggests that the structural integrity of the 0.5CFT18 sample has been maintained, despite the presence of voids. In contrast, the CO sample shows some observable deterioration parts on its surface. The degradation amount of CO and 0.5CFT18 at 120 FT cycles were comparable according to the FLIR photos.

The high porosity of the 3CFT18 samples was already confirmed from previous tests. The infrared images in Figure 60 further confirm the presence of a porous structure in those samples. The infrared images provide visual evidence of the porous nature of the 3CFT18 samples, with the increased porosity becoming more apparent as the cyclic FT loading progresses. These findings suggest that the 0.5CFT18 sample may possess superior characteristics that contribute to the highest resistance to FT damage.

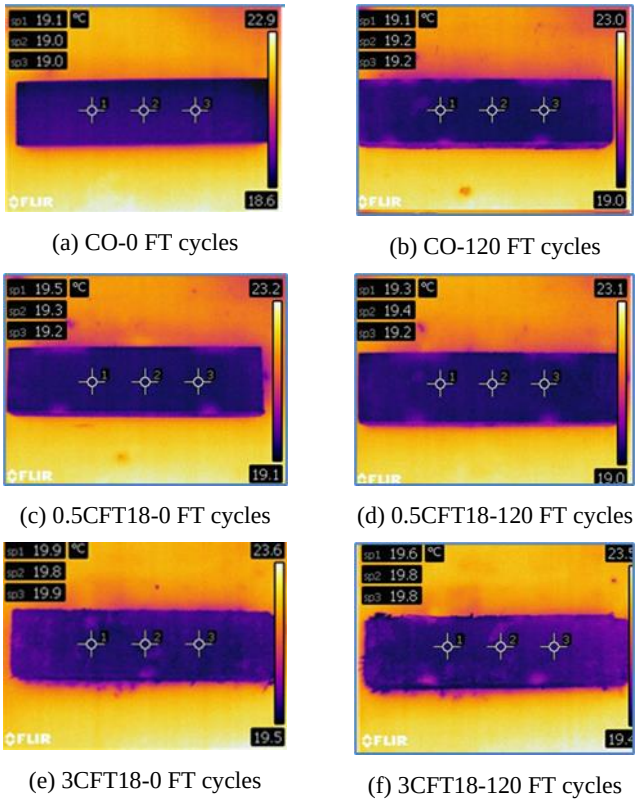

(a) CO-0 FT cycles (b) CO-120 FT cycles

(c) 0.5CFT18-0 FT cycles (d) 0.5CFT18-120 FT cycles

(e) 3CFT18-0 FT cycles (f) 3CFT18-120 FT cycles

Figure 60. Infrared images of samples at 0 and 120 FT cycles

6.5. Result agreement

A comparative analysis was conducted to assess the reliability of three testing methods, UPV, RF, and HP, in evaluating the dynamic modulus of elasticity (DMOE) of concrete specimens subjected to FT cycles. The main objective was to determine if the test results from these non-destructive testing (NDT) methods could be correlated and indicate their suitability for testing FT concrete specimens.

To evaluate the agreement between the testing methods, Figure 61 presents a summary of the DMOE achieved in UPV, RF, and HP tests. Each sample at every FT cycle is represented by three values corresponding to each NDT method. The analysis of the data has yielded interesting findings.

- In the UPV test, initial UPV values ranged from 6657 m/s (CO) to 3329 m/s (3CFT18). The velocity decline was gradual for CO and 0.5% CF samples but more abrupt for higher CF concentrations, as FT cycles increased. The addition of CF above 1% resulted in a decrease in UPV, indicating increased porosity & permeability due to CF presence. UPV provided indirect information about permeability and pore structure, but additional NDT methods were necessary for accurate predictions. Polynomial fitting was found to

be the most reliable method for predicting UPV variations over time.

- The DMOE obtained from the RF test showed a similar trend to UPV under FT cycles. CO and 0.5% CF samples exhibited a slow declining stage followed by a rapid decline due to degradation and increased porosity with higher dosage of CF addition. The DMOE difference was only negligible until 300 FT cycles in both CO and 0.5PAT18 samples, as observed in the experimental data. For higher CF addition, the periodic freezing and thawing decreased the dynamic elastic modulus of concrete, with the loss rate stabilizing after more FT cycles.

- In the HP test, CO and 0.5% CF samples showed the least reduction in DMOE after 300 FT cycles. A linear decline was observed in DMOE, while higher CF concentrations showed a non-linear relationship with FT cycles. Samples with 1% and 2% CF experienced a drastic reduction in DMOE after 60 FT cycles, indicating severe damage. The 3% CF sample had low initial DMOE and deteriorated rapidly, suggesting poor structural quality.

The samples with 0% and 0.5% CF content demonstrated the highest consistency among the three tests. This indicates that the results obtained from UPV, RF, and HP tests for these samples did not align well. However, the HP and RF test results showed strong agreement with each other in nearly all samples, suggesting a significant correlation between these two testing methods.

There can be discrepancies in the test results obtained from the UPV test compared to the HP and RF tests. These disparities arise due to the distinct physical principles and mechanisms underlying each of these testing methods.

- The UPV test involves measuring the propagation velocity of ultrasonic longitudinal stress waves through the concrete specimens, relying on ultrasound penetration to evaluate the dynamic properties of the material. It provides valuable information about the speed of sound wave transmission, which can be correlated with the DMOE of the concrete [222].

- On the other hand, the HP and RF tests operate under impact loading conditions. In the HP test, a hammer strikes the concrete surface, while in the RF test, the concrete beam is stimulated to vibrate in its fundamental modes. The resulting mechanical vibrations are analyzed to determine the resonant frequencies, which can be associated with the DMOE of the concrete [223].

In conclusion, there can be disparities in the test results obtained from the UPV, HP, and RF tests due to the different physical principles underlying these methods. UPV relies on

ultrasound penetration, while HP and RF tests operate under impact loading conditions. The comparison of the HP and RF methods provides insights into their agreement and suitability for evaluating the DMOE of concrete specimens subjected to FT cycles. The observed similarities suggest a consistent and reliable assessment of the DMOE using these methods.

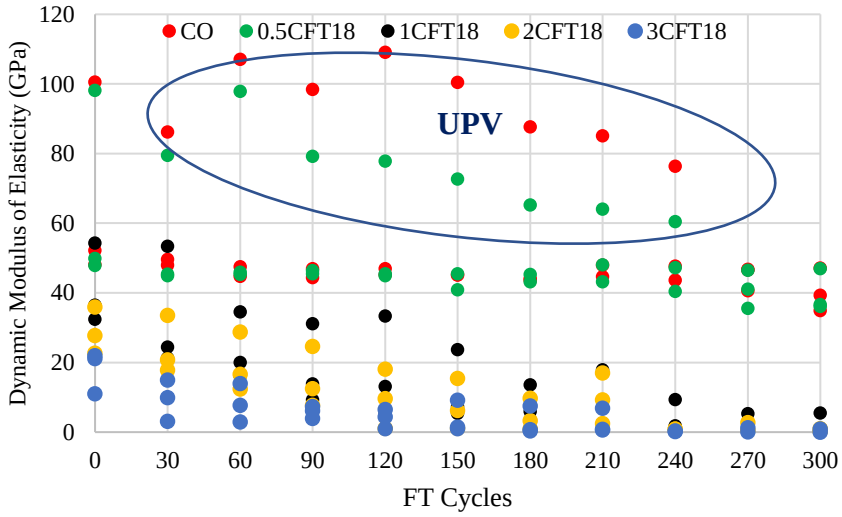

Figure 61. Summary of the DMOE derived from UPV, RF, and HP tests

6.6. Conclusion

This study examines the effects of CFs on both the dynamic and static mechanical characteristics of concrete, aiming to enhance the performance of frost-resistant concrete through the use of discrete CFs. The experimental results and analysis presented in this chapter provide valuable insights into the mechanical and durability properties of CFRC subjected to FT cycles. The preliminary mechanical tests revealed that the compressive strength and flexural strength of the CFRC samples decreased with an increase in CF content. However, the inclusion of CF improved the pre-crack and post-crack behavior of the samples, as indicated by the increased energy absorption and toughness index (I_5) values. The 1% CF content was found to be the most favorable in terms of energy absorption and post-crack behavior.

Based on the results and discussions presented, the following conclusions can be drawn from this study:

- The compressive strength of the samples decreased as the amount of CF increased. The amount of CF to maintain the initial mechanical properties was around 0.5%. Samples with 3% CF exhibited extremely low strength and large voids.

- Mass loss of the samples increased significantly with higher fiber volumes, particularly after 60 FT cycles. The mass loss measurements demonstrated that the CFRC samples experienced accelerated deterioration during FT cycles, especially at higher CF volumes.

The presence of CF led to increased porosity and water retention, resulting in the formation and propagation of cracks, which facilitated the movement of water through the concrete. The 3% CF sample exhibited visible surface deterioration and significant mass loss after 300 FT cycles, indicating its vulnerability to FT damage.

- The DMOE analysis using UPV and RFT revealed that CF addition negatively affected the DMOE of the CFRC samples. The DMOE decreased exponentially with increasing CF content, and the samples with 1% to 3% CF failed before reaching 60 FT cycles. However, the 0.5% CF sample demonstrated superior durability, enduring 300 FT cycles with minimal decline in DMOE. Concrete, being inherently brittle, experiences microcrack development under cyclic loading. However, the introduction of fibers to concrete introduces fiber/matrix debonding, which occurs during repetitive expansion and contraction of water within concrete pores. This phenomenon ultimately leads to energy loss and is one of the main cause of the decrease in DMOE. Concrete samples with lower fiber volume fractions exhibited a lesser reduction in DMOE.
- Hammer percussion tests further confirmed the accepted resistance of the 0.5% CF sample, showing the least reduction in DMOE after 300 FT cycles compared to other CFRC samples. The relative dynamic elasticity modulus exhibited different patterns for different samples, with linear decline for CO and 0.5% CF samples and polynomial decline for higher CF contents.
- Infrared imaging provided visual evidence of the porous nature of the CFRC samples, with the 0.5% CF sample demonstrating superior resistance to FT damage compared to other CFRC samples.

In summary, this chapter demonstrated that the addition of CF influenced the mechanical properties of concrete, including compressive strength, flexural strength, post-crack behavior, energy absorption, and dynamic modulus of elasticity. It emphasized the importance of carefully selecting the CF content to maintain desired concrete performance and comply with standards. The 0.5% CF content was found to be the most optimal in terms of balancing mechanical performance and durability. These findings can guide the design and application of CFRC in concrete structures exposed to FT cycles, providing valuable insights for ensuring long-term performance and durability.

Chapter 7. Performance of carbon fiber-reinforced pavement with embedded sensors using destructive and non-destructive testing

Paper Title: Evaluating performance of carbon fiber-reinforced pavement with embedded sensors using destructive and non-destructive testing

Author(s): Maryam Monazami, Ashutosh Sharma, Rishi Gupta

This research paper which is published in a peer reviewed journal [218] evaluates the performance of a CFRC bus pad compared to a normal concrete bus pad. The paper has minor modification to ensure alignment with the dissertation's integrity and overall flow. Real-time monitoring using embedded sensors such as temperature and humidity sensors, thermocouples, strain gauges, and piezoelectric patches was conducted during the construction of both pavements. These findings highlight the improved performance of CFRC in terms of crack resistance and indicate the potential of embedded sensors for monitoring and assessing the condition of concrete pavements.

7.1. Introduction

Infrastructure deterioration is an inevitable process, and aggressive environmental conditions in the entire North American subcontinent proliferate the intensity of degradation. In a 2019 Canadian Infrastructure Report Card developed by the Federal of Canadian Municipalities (FCM), it has been established that long-term investments are urgently required to address the critical infrastructure needs of Canada. Nearly 40% of roads and bridges are rated as fair, poor, or very poor, and nearly 80% are over 20 years old [224].

More than 15 million Canadians use public transit such as buses to get to work [225] and an estimate of 142.7 million passenger trips were recorded in November 2015. Public transit roads are generally developed using asphalt, which is often the most suitable material. Bus stops are subjected to sudden braking and acceleration of buses and asphalt pavement tends to develop waves or ripples (distortion of asphalt) under the weight of the bus (axle loads). As a result, cracks are formed in the asphalt that very often enlarge into potholes. This is usually obviated by constructing bus pads made of concrete to safely accommodate the weight of buses. Concrete Bus Pads (CBP), commonly found at bus stops are the most durable portion of the road surface.

However, concrete’s vulnerability and constant exposure to aggressive environments in Canada causes CBPs to deteriorate faster than stated, aggrandizing repair cost [226]. It has been reported that crack width movements are generally larger at the top surface of concrete pavement, and crack width movements vary across the depth due to varying temperatures.

Further, it was also suggested that crack width movements increase with a decrease in longitudinal steel ratio [227]. In another study [228], it was found that the geometry of the concrete slab significantly influences the potential for longitudinal cracking, especially when the traffic is composed of more tandem and tridem axles. It has been reported that temperature during the construction and curing of concrete slabs greatly influences the cracking [229]. In general, deterioration in CBPs is related to higher tensile stresses than its tensile strength and is usually due to concrete shrinkage, temperature changes in concrete, traffic loads, low humidity, wind, etc.

Figure 62 shows the deterioration of the pavement with time. Phase A corresponds to the slow progression of deterioration of the concrete pavement, restricted to the top surface. During this phase, deterioration remains a function of the quality of construction, materials used, design mix, and the routine maintenance regime. This is followed by phase B, wherein deterioration is accelerated and makes inroads across the depth of the concrete pavement. In phase C, the surface of the pavement is completely cracked, and damage continues to increase significantly. It should be noted that repair and rehabilitation can only be done until phase C. In phase D, the pavement is significantly damaged. Although the pavement can still last for some more years, it requires replacement for safe transit applications. With each passing phase, the cost of repairs and maintenance also rises exponentially.

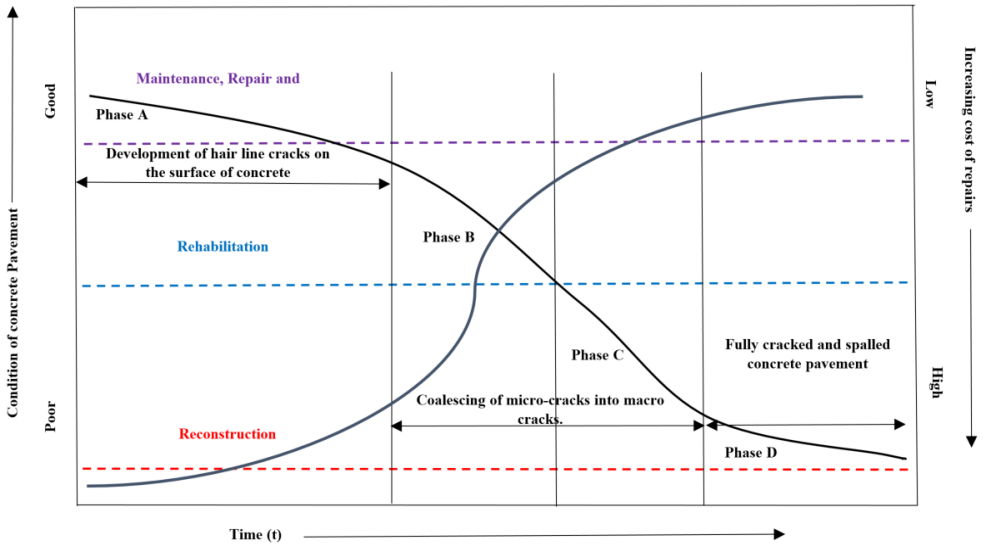

Figure 62. Deterioration of pavement with time [230]

The increased service life of the pavement implies that the condition of the pavement should remain in phase A for a longer duration. This can only be done by successfully preventing the microcracks from developing in the concrete. The prime focus of this study is

to increase the service life of the bus pad by limiting the cracking during the initial phase and as a result, prolonging phase A of the deterioration curve.

By the principle of adhesion and interfacial bond, e.g., the anchor effect of interlocked fibers, fibers can improve the mechanical strength characteristics and post-crack toughness of the composite [138]. The randomly oriented fibers can effectively prevent the extension and propagation of internal micro-cracks.

The primary study on CFRCC was conducted in 1973 [231], wherein superior mechanical properties of PAN-based CFRCC were reported. Owing to their high modulus, it has been proposed that CFs can significantly reduce plastic shrinkage cracking [38,232], improve thermal resistance, weather ability, and chemical stability in aggressive environments [38]. Although various studies investigated the effect of CFs in concrete, most are limited to laboratory tests, and, to the best knowledge of the authors, there are only few studies that have reported the field applications of CFs especially in concrete bus pads. As a result, to gain further insight into the development and field performance of CFRC pavements, a thorough evaluation of the behaviour of pavement is required.

There are several NDT techniques that are currently being employed in the condition assessment field. These techniques include surface hardness methods such as Schmidt hammer [233], resonant frequency tests (by vibration or by impact) [234], maturity methods [235], ultrasonic pulse velocity methods [236], impact echo methods [237] and many more methods that are mainly employed to determine the quality and integrity of concrete without affecting its functions [238]. A set of NDTs is usually operated on the whole pavement in the first phase. After the data interpretation, locations with potential deficiencies will be identified and such points receive a more in-depth study with potential material extraction. The approach used in this chapter was created to fill a gap in the literature by conducting a number of non-destructive field tests and subsequently analyzing the data to gain a thorough knowledge of carbon-fiber-reinforced pavements with the aim of designing a crack-free concrete bus pad. A set of sensors were used in both pavements to monitor the temperature, humidity, and strain variations and a performance-based comparison between the CFRC bus pad and a normal concrete bus pad have been investigated. When compared to normal concrete bus pads, which have electrical resistivities of roughly 30 kΩ-cm, CFRC bus pads showed extremely low electrical resistivity. Schmidt hammer and UPV both revealed degradation in the normal concrete bus pad in comparison to the CFRC bus pad. Several clusters of very low UPV values were observed in the location of bus pad cracks. The lesser values in the CFRC bus pad are indicative of the scatter in the wave energy due to the presence of CFs.

7.2. Materials and methodology

7.2.1. Selection of carbon fibers

Three different fiber types with varying lengths, material characteristics, and sources were obtained during the early phase of this investigation. Mitsubishi Chemicals supplied PAN-based and pitch-based CFs, while Teijin Cooperation supplied another set of PAN-based CFs. Initially, limited quantities of fibers were obtained for testing lab-based mortar and concrete samples. Teijin fibers with longer lengths performed better during the early testing of carbon fiber-based composites.

7.2.2. Selection of site

With the help of local authorities at Saanich municipality and BC Transit, a local survey of bus pads in the Saanich municipality was done by the research team. Finally, a site at the University of Victoria bus exchange was identified that included a series of four bus pads. Out of the four bus pads, permission to replace three of them was sought. The plan of the slabs, the construction details of the pavement, and the Google map of the bus pad's location are presented in Figure 63. Abbreviations were denoted in such a way that bus pad #1 is abbreviated to B_{N-1}, bus pad #2 is abbreviated to B_{N-2S}, and bus pad #3 is abbreviated to B_{CF-S} (letter N, S, CF applies to Normal concrete, Sensor, and CF). Figure 64 shows the deteriorated bus pads selected for this study.

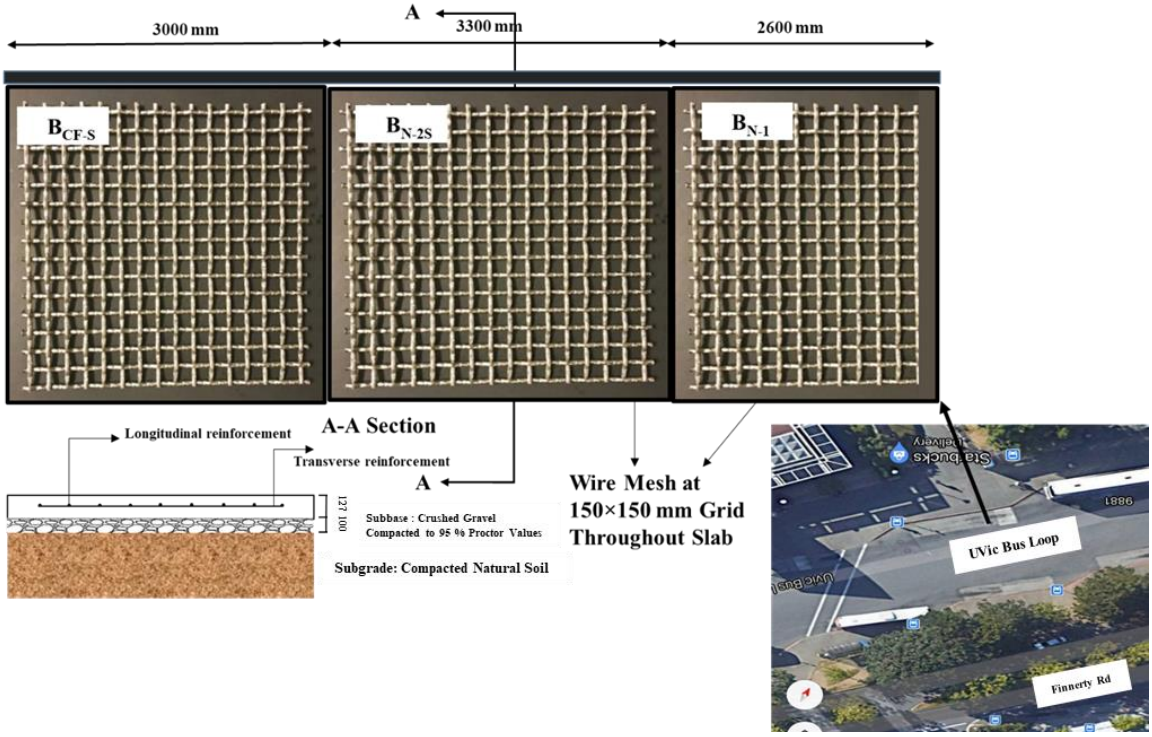

Figure 63. Details of the pavement and the construction site

(a) (b) (c)

Figure 64. Pre-exising condition of bus pads (a) B_{N-1} (b) B_{N-2S} (c) B_{CF-S}

7.2.2.1. Image analysis on pre-existing bus pads

Before replacing the bus pads, the condition assessment of existing bus pads was conducted. Image analysis was performed using ImageJ software to quantify the antecedent damage in the deteriorated bus pads. Figure 65 shows the different images of the bus pads that were analyzed to evaluate the total crack area, crack area fraction, maximum crack width, and average crack width for all bus pads were calculated. Table 17 shows detailed results of image analysis of the pavements. Bus pad #2 had the worst condition regarding the highest crack area and bus pad #1 was the worst pavement in regard to the highest average crack width. Further, it should be noted that all the bus pads were in phase D of the 'pavement condition curve'.

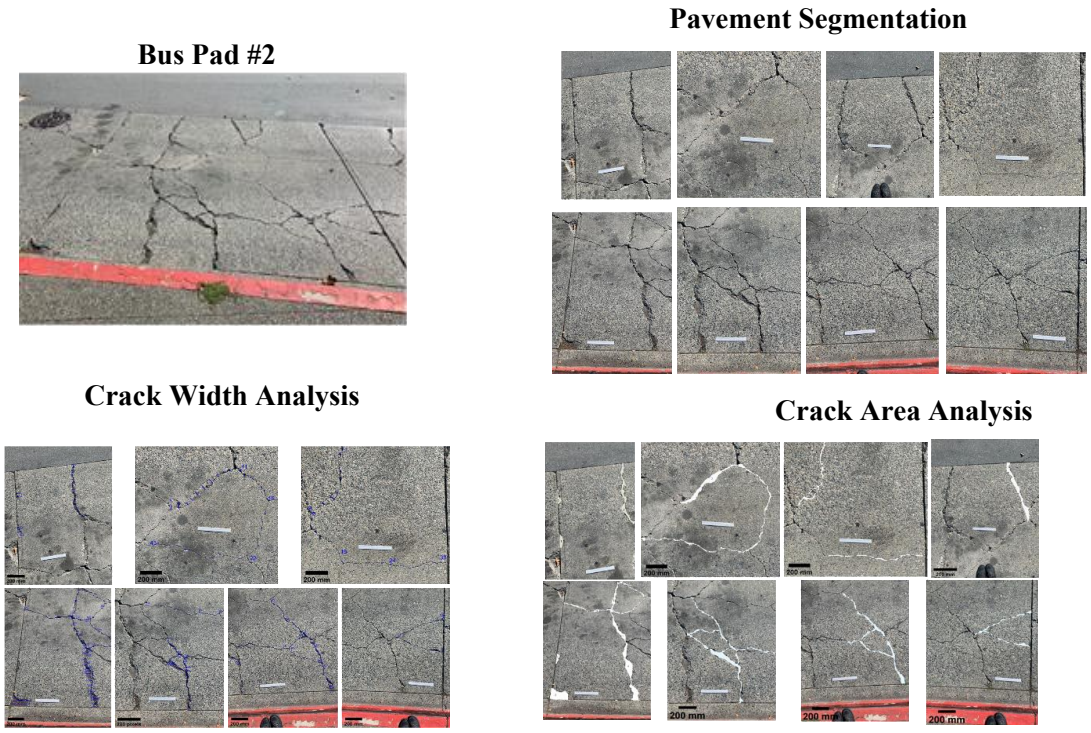

Figure 65. Image analysis of pre-existing bus pad

Table 17. Crack analysis of existing bus pads

Code	Crack Area	Crack Area/Pavement Area	Maximum Crack Width	Average Crack Width
	(mm^2)	(%)	(mm)	(mm)
B_{N-1}	150246	2.33	253	35.53
B_{N-2S}	301796	3.05	219	14.41
B_{CF-S}	101203	1.12	65	17.70

7.2.3. Site development

7.2.3.1. Excavation of the existing bus pads

In order to implement real bus pad construction practices available in Victoria, a local contractor was hired for undertaking all stages of the project including excavation, sub-base compaction, reinforcement installation, concrete mixing, and pouring. Excavation of deteriorated bus pads was done two days before the concrete pouring. According to BC Transit Infrastructure Design Guidelines [239], the concrete bus pad thickness should be designed as follows: 225 mm for Portland cement concrete, 150 mm for base coarse, and 300 mm for sub-base coarse. However, the constructed bus pad consisted of a 125-mm thick layer of concrete. Upon excavation, a thin wire mesh was laid on the bed of the pad. Figure 66 shows the excavated bus pad site.

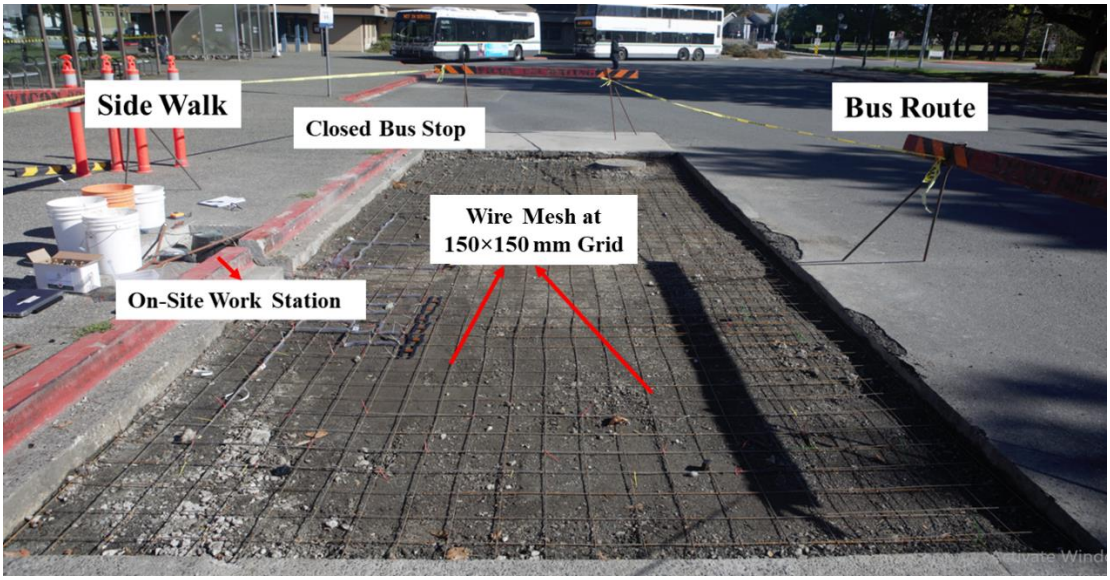

Figure 66. Excavated bus pad site

7.2.3.2. Installation of sensors

The construction of the bus pads was scheduled two days after the excavation work was completed. This was done primarily for of the installation of different types of sensors. After the excavation was complete, a complete survey of the excavated bus pad was conducted and the actual depth at multiple points was noted (as shown in Figure 67). Out of the three excavated bus pads, two of them (BN2 and BCF) were selected for the embedment of sensors. The sensors were installed inside the bus pads with a dual objective: 1) to monitor the deterioration of BN2 and BCF, with time; 2) to monitor the behavior of the bus pads under different volumes of traffic. To achieve the objectives, a series of wireless temperature and humidity sensors, thermocouples, strain gauges, and piezo patches were installed in the bus pad. Furthermore, an on-site workstation was also developed on the curb wherein all the wires coming from both the bus pads were laid. This was developed to be able to access data at the site while the bus pad was open to traffic. Figure 67 shows the location of different sensors inside the bus pad. The sensors used are given in the figure and described in the following sub-sections.

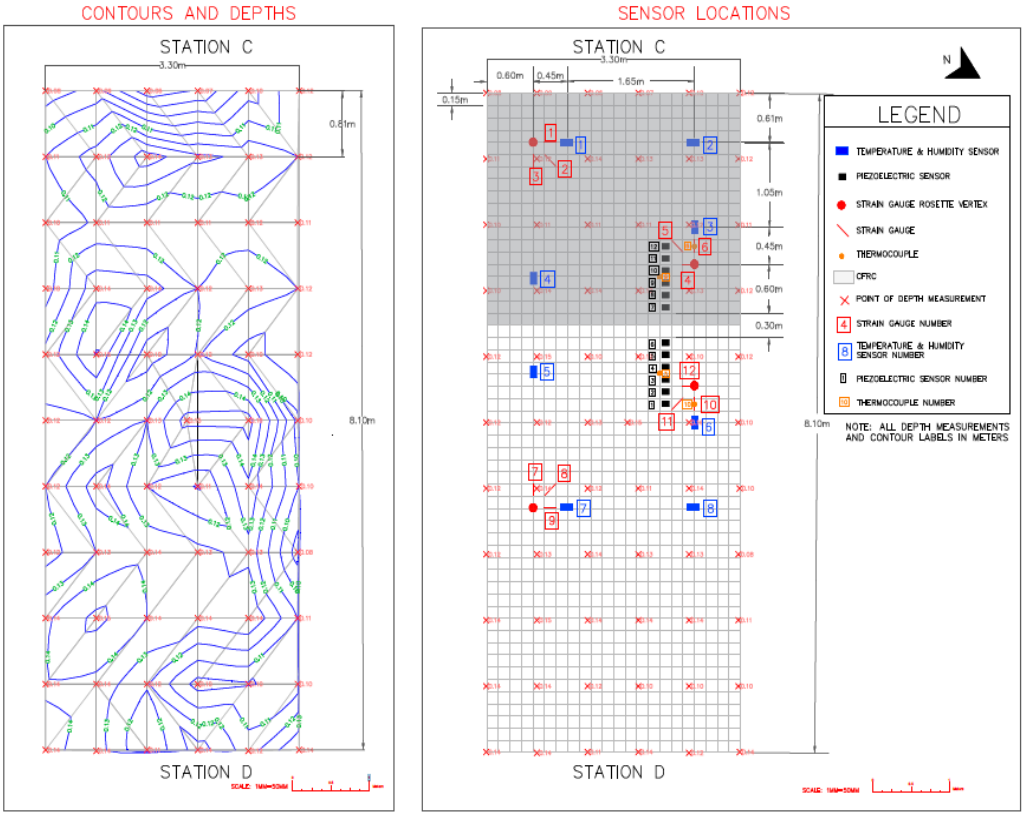

Figure 67. The layout of bus pads and sensor location

7.2.3.2.1. Temperature and relative humidity sensors

A series of BlueRockTM sensors for measuring temperature and relative humidity were procured from Giatec Scientific. These sensors can map the temperature and humidity of in-

place concrete from fresh to hardened stages. Using the BlueRockTM mobile app, real-time variations in the concrete's internal humidity can be studied. A total of 5 BlueRockTM sensors were tied to the wire mesh at different locations (as shown in Figure 68), inside $B_{N\text{-}2S}$ and $B_{CF\text{-}S}$ as well. In addition to BlueRockTM sensors, two thermocouples (Type WENK-01), with a diameter of 0.3 mm were also embedded inside each bus pad for continuous monitoring. A NI-data logger was employed to acquire data from the thermocouples. Figure 68 shows the details of the location of the sensors.

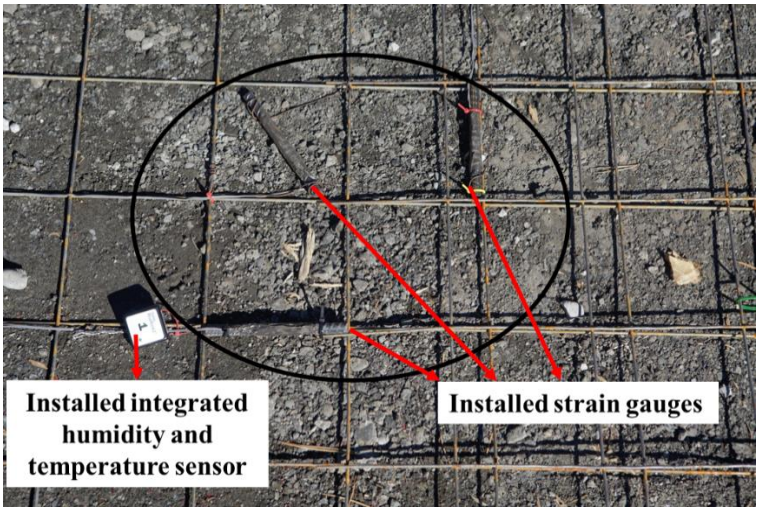

Figure 68. Installed sensors and strain gauges

7.2.3.2.2. Strain gauges

The bus pads were also instrumented with strain gages, deployed in rosettes at different locations. A set of concrete materials using pre-wired strain gauges from Tokyo Sokki Kenkyujo Co. were acquired to monitor the displacement of the slabs. The strain gauges had thin stainless-steel backings to avoid the penetration of moisture from the reverse sides. The strain gauges had moisture proofing over-coating and integral lead wire in addition to the stainless-steel backing. These strain gauges are intended for long-term measurement of concrete structures, consisting of a 10-mm-long gauge with 118 ± 0.5 Ω gauge resistance. Each strain gauge was wired with a 3-m-long lead wire with a resistance of 0.32 Ω/m. Each strain gauge was mounted on a #3 rebar with a length of 100 mm, and the rebar was loosely tied to the embedded wire mesh. The strain gauge had an error in recording thermal strains to the order of 11×10-6/C. Preliminary frequent visits to the bus pad enabled researchers to find the expected locations of the wheel loads and hence, three strain gauges were installed orthogonally (forming a rosette) at each designated location. This was done to obtain the strains in all directions The detailed location of strain gauges is shown in Figure 67. It should be noted that each thermocouple was deployed close to the strain rosette to enable any required temperature correction. A National Instruments Data Acquisition system (DAQ) was

used to read the values of strain gauges. Figure 68 shows the details regarding the installation of strain gauges and BlueRockTM sensor.

7.2.3.2.3. Piezoelectric patches

A piezoelectric patch is a thin flexible commercially manufactured piezo ceramic transducer that works on the principle of converting electrical signals to stress waves and vice-versa. When a high input voltage is applied to a piezoelectric patch, it creates a mechanical strain that excites the host structure. A piezoelectric patch that generates stress waves within a host structure is called an 'actuator', and the patch that receives these stress waves is called a 'sensor'. Piezoelectric patches can be embedded in a concrete structure for early detection of damage by evaluating various phenomena occurring within the concrete.

To further quantify the behavior of bus pads subjected to aggressive environmental conditions in addition to the busloads, monitoring of bus pads using piezoelectric patches was also implemented. Two sets of piezoelectric patches were embedded in an array form in B_{N-2S} and B_{CF-S}, as shown in Figure 69. An array of 6 piezoelectric patches were embedded in B_{N-2S} with a spacing of 150 mm between consecutive patches. At a gap of 300 mm from the last piezoelectric patch in B_{N-2S}, another array of 6 piezoelectric patches with the same spacing were embedded in B_{CF-S}. The piezoelectric patches were secured with tape to the grid to hold them in the correct location when the concrete was poured. The wires from the electrical contacts of piezoelectric patches were secured to the grid, protected by transparent ducts, and guided through the curb to the separate compartments. These compartments, as shown in Figure 69, installed within the sidewalk allowed the monitoring of B_{N-2S} and B_{CF-S} over time. The concrete signatures recorded by piezoelectric sensors at different time intervals can be linked with induced damage such as progressive cracking. It should be noted that the study using Piezo patches is still ongoing and will be reported in the subsequent papers.

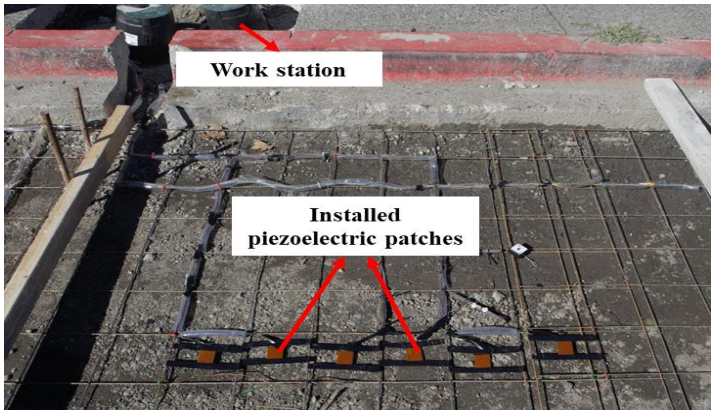

Figure 69. Installed piezoelectric patches

7.2.4. Design mix and placing of concrete.

The estimated amount of concrete required for three bus pads and several molds for lab testing of concrete was more than 6 cubic meters and therefore, the concrete was supplied by a local ready-mix concrete producer. A local contractor was hired to bring a truck of dry concrete to the site. The concrete ordered had a target strength of 30 MPa and an air content of 5-8%. The maximum size of aggregates used was 12 mm and a slump of 80 mm was desired. It should be noted that properties of fresh concrete such as slump value, air content, bulk density, etc. were evaluated on-site as per ASTM C143 [221] and ASTM C231 [240] at the time of construction of bus pads.

In a truck mixer with a capacity of 10 m^3, dry concrete was mixed with water at a w/c ratio of 0.5. The appropriate amount of CF was packaged in 5 kilogram water-soluble bags. The concrete mixing and placing procedure followed in the concrete plant and at the job site was as follows:

1- A few hours before concrete pouring, the sensors were cleaned, and their connectivity to the workstation was checked.

2- With the arrival of the drum mixer, quality control on concrete including two sets of slump test and air meter test was operated. The weather temperature was reported to be 10˚C.

3- The normal concrete was poured in the first 2 slabs, spread manually, consolidated by a vibrating screed, and finished. Six 100 × 100 × 200 mm cylinders, six 100 × 100 × 400 mm beams, two 75×75×800 mm panels were taken from the plain concrete in the field. Then the mixer was stopped.

4- The fibers were incrementally added to the concrete truck. Considering the optimum amount of 0.5%-1% from the experimental results, and by calculation of the amount of poured concrete, a sufficient amount of CF was added to the mixer in order to meet the targeted fiber dosage. The volume of fiber added into the concrete turned out to be 0.55% which is in accordance with the optimum experimentally obtained dosage. To assess the uniform dispersion of fibers in concrete, three cylinders were filled with fresh CFRC and were taken to the laboratory for further investigation. The concrete was washed away, and fibers were sieved from cement paste. The fibers were then oven-dried and weighed. A fiber volume fraction of V_f = 0.58%, 0.54% and 0.59% was calculated from each cylinder. This confirmed the approximate uniform distribution of CFs over the entire bus pad.

5- A carbon-fiber-reinforced bus pad was then screeded and finished. It should be noted that during the screeding of BCF-S, agglomerated fibers were found on the surface of the slab. Figure 70 shows the finished bus pads constructed with normal concrete and CFRC.

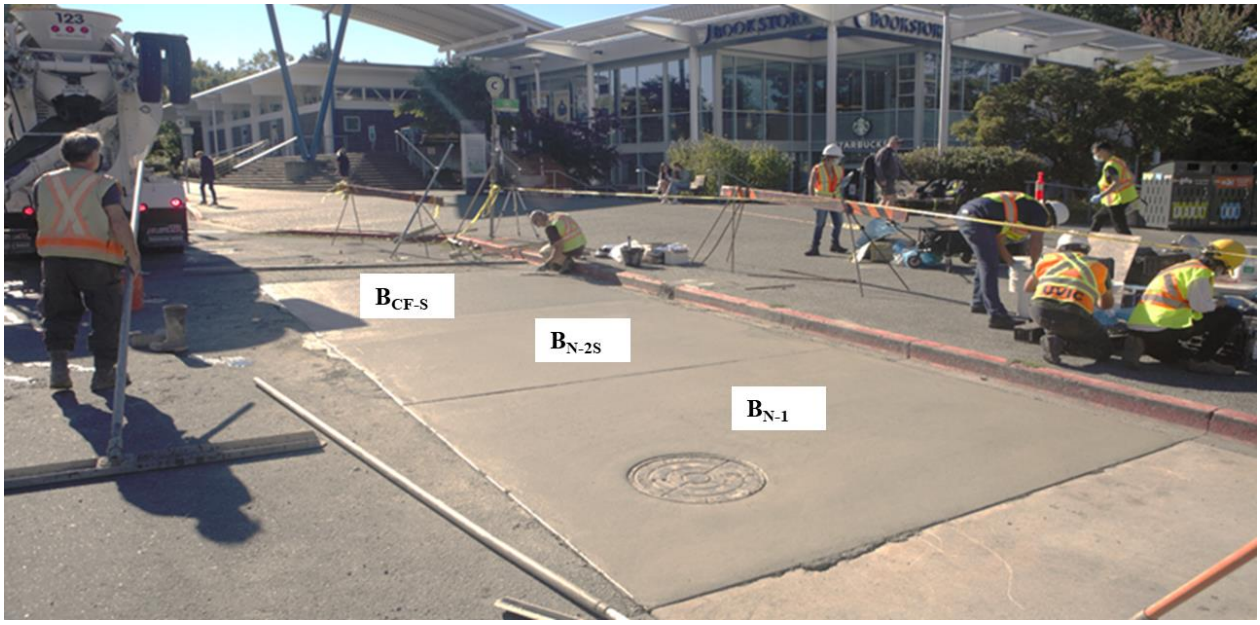

Figure 70. Finished bus pads

7.3. Results and discussions

7.3.1. Laboratory-based tests on concrete

7.3.1.1. Destructive tests

In order to evaluate the quality of concrete placed at the site for the construction of bus pads, 6 beams, 6 cubes, 6 cylinders, and 2 round panels for each mix were cast and cured for 28 days. Table 18 gives the details of the samples. It should be noted that samples were subjected to dry curing at ambient temperature to simulate the real conditions experienced at the bus pad site in the laboratory. Later, the samples were tested under compression using a compressive testing machine. The average 28-day compressive strength obtained for cylinders made with normal concrete was 20 MPa and for those of CFRC cylinders was 18 MPa (loss of 15%). The results indicate that the addition of fibers slightly decreased the compressive strength of concrete mainly due to the workability reduction. Considering the preliminary tests, the reduction rate in bus pad samples is in good correlation from those obtained in the lab, wherein a decrease up to 16 % in compressive strength was seen at 0.5 % fiber volume.

The peak load, its corresponding displacement, the Modulus of Rupture (MOR), pre-crack/post-crack flexural toughness, and the absorbed energy at certain deflection (2.5 mm and 5 mm) of beams and round panels were obtained through the load-displacement curve. The detailed results are presented in Table 18. According to the results, the influence of the incorporation of CFs on the flexural behavior of concrete is more distinct than on compressive strength. A 26% increase in flexural strength of CFRC beams was observed during flexural

testing, while the improvement in the round panel was negligible. The strength improvement in beams is mainly due to the confinement ability of CFs in flexure, holding, and bridging microcracks and as a result, retarding the initiation and growth of cracks and compensating the strength reduction caused by low workability. However, the difference between the results of beams and round panels is mainly due to the different methodology used in the two tests. In the center-point bending test, the specimens are forced to crack at a given location, hence the crack does not necessarily open at the section with low strength material. However, when round panels are subjected to bending, yield lines follow the weakest sections. In concrete panels reinforced with 18 mm fibers, it is hard to avoid fiber balling and get uniform distribution throughout the concrete mix and as a result, the weak section cab is either at the location of fiber balling or at the location where the fiber reinforcement is not sufficient, hence showing a similar MOR compared to CO.

Table 18. Summary of flexural behavior of beams and round panels

Sample geometry	Label	Peak load (N)	δ_{peak} (mm)	δ_{max} (mm)	MOR (N.mm)	Energy (J)			
						δ = 2.5 mm	δ = 5 mm	Pre-crack	Post-crack
Beam	CO	6938	1.27	1.65	3.64	2.8	2.8	2.65	0.14
	CFRC	8750	2.13	5.5	4.59	5.61	6.07	4.97	1.11
Round panel	CO	20774	2.14	2.4	4.00	24.61	24.61	23.23	1.38
	CFRC	21000	2.7	5.1	4.04	22.85	40.04	26.53	13.51

Figure 71 compares the post-crack energy absorption of samples. It should be noted that although the peak load for CFRC beam samples is reported to be greater than that of the CO beams, there is minimal improvement in the post-crack behavior of the beams while the red area (post-crack absorbed energy) is quite large in round panels. The obtained results are mainly owed to the fact that larger fracture areas, with a much higher number of fibers, are involved in round panel testing, and therefore, the behavior of the structure is highly dependent on the material properties including the crack bridging effect of CF.

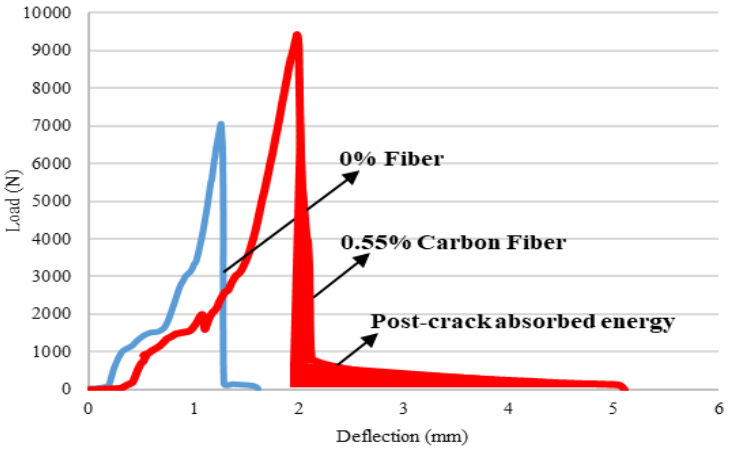

(a)

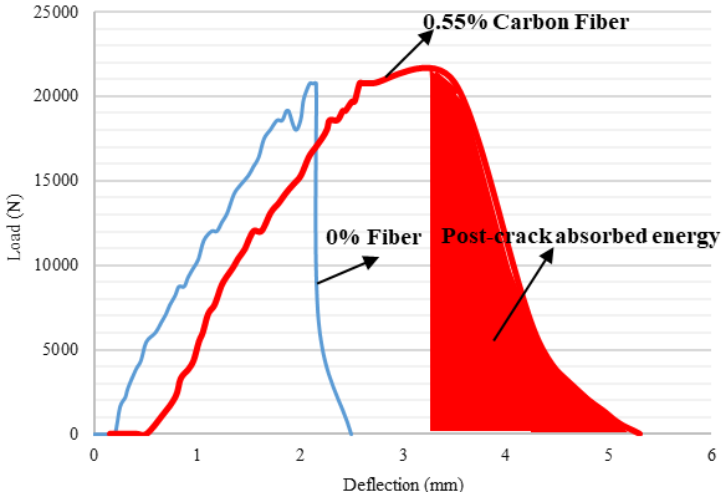

(b)

Figure 71. Load-displacement behavior of CO and CFRC under flexure a) beams b) round panel

7.3.2. Structural health monitoring of bus pads

Using several NDT techniques, the performance of the pavements was monitored from the first hours to 28 days after concrete placement. Figure 72 shows the non-destructive techniques applied in this study.

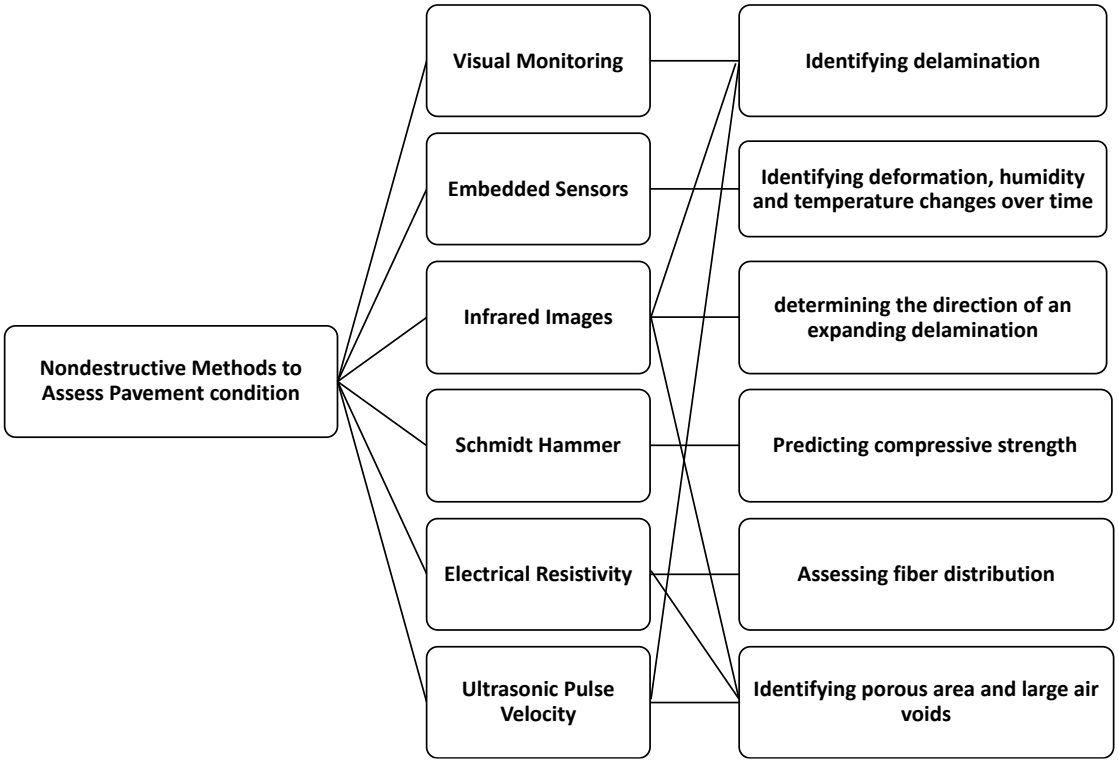

Figure 72. NDTs used to assess pavement condition.

7.3.2.1. Visual monitoring of bus pads

After construction, the bus pads were closed to traffic for 7 days to allow the concrete to gain strength. The research team regularly monitored the constructed bus pads for any sign of cracking. After the bus pad was opened to traffic, the research team conducted visual monitoring twice a day and a FLIR camera was used to monitor the temperature variation at different locations. This was done to find the potential locations of crack initiation and to track the development of cracks or any other signs of deterioration in the bus pads. Initially, in BCF-S bus pad, small chunks of agglomerated CFs beneath the top layer of concrete were visible at some. Once the bus pad was opened, it was found that fibers from these areas started coming out due to the abrasion of the surface. However, no cracks were observed in the B_{CF-S} bus pad. On the contrary, both B_{N-1} and B_{N-2S} started developing very thin hairline cracks immediately 7 days after casting. The first cracks which initiated in the middle of the slab is mainly attributed to the combined loading and curling effects and therefore the midspan experienced the maximum deflection [241]. Figure 73 shows the condition of three bus pads after 28 days of construction. It can be observed that cracks have only slightly widened after 28 days of casting. Thermal imaging photos (using FLIR camera) of B_{C-1}, $_{BC-2S}$, and B_{CF-S} are presented in Figure 74. In the figure, it is easy to see the delaminated areas (lower temperature on the cracks) and the temperature gradient on the pavement which make it possible to determine the direction of an expanding delaminated region [242]. It was also observed that the CFRC bus pad had a uniform temperature variation with a slightly lower

internal temperature compared to the other bus pads which is mainly due to the high electrical conductivity of the fibers.

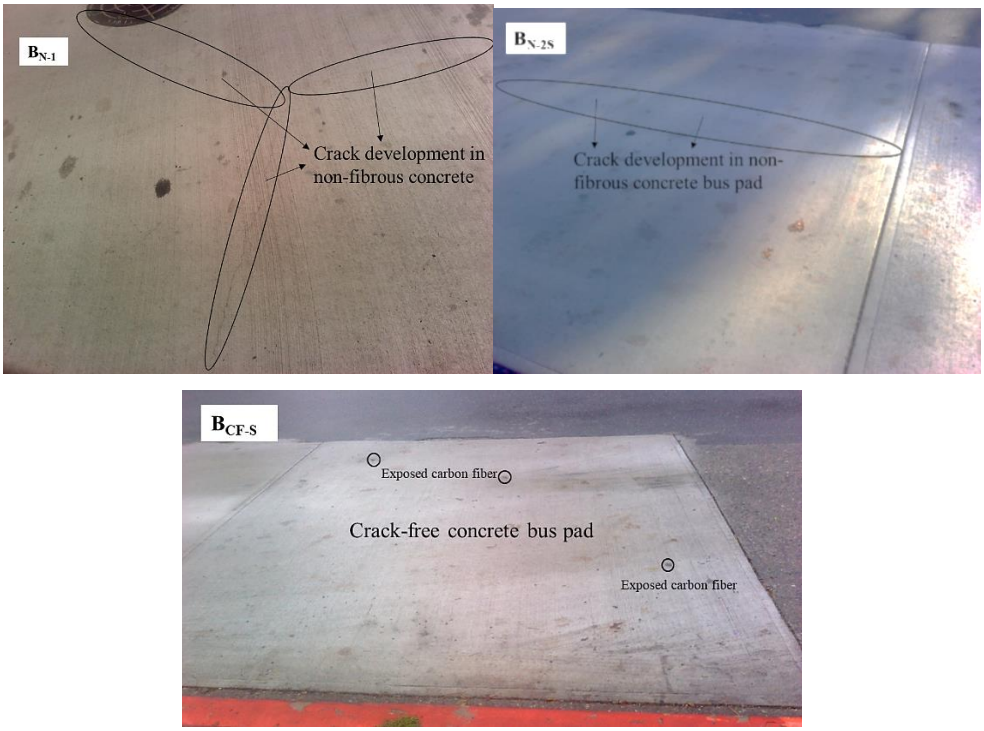

Figure 73. Condition assessment of bus pads at 28 days

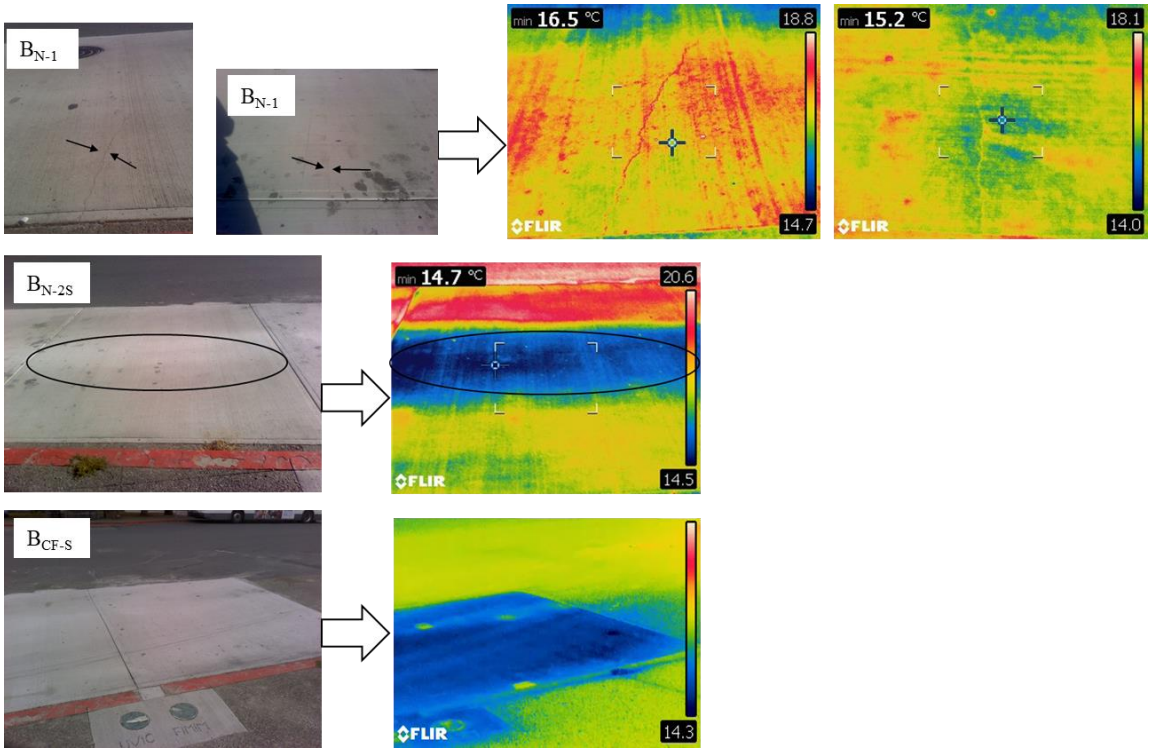

Figure 74. Thermal photos of bus pads

7.3.2.2. Temperature and humidity monitoring of bus pads

Monitoring the temperature and humidity of concrete provides useful information about the strength gain and maturity of concrete as well as the progress of deterioration mechanisms in the structure. Temperature and humidity data were logged from wireless sensors every eight hours. The logged data was stored on the sensors automatically which was downloaded every day via Bluetooth through the BlueRock™ app. After the construction was completed, the data was logged immediately, and it was found that the wireless sensors embedded in the BCF-S were not able to transmit the data via Bluetooth. This can most probably be attributed to the interference in the Bluetooth signal by the presence of CFs in the matrix. Fortunately, the thermocouples that were installed for providing temperature corrections to the strain gauge readings were able to record any temperature changes inside the concrete. Figure 75 shows the variation of data obtained from temperature sensors that were embedded in $B_{N\text{-}2S}$. From the graphs, it can be seen that the temperature variation (based on data from sensors and thermocouples) for the first 30 days in $B_{N\text{-}2S}$ is similar to $B_{CF\text{-}S}$. Temperature variation is primarily a function of the process of hydration, inside the concrete. Additionally, the rate of moisture evaporation which leads to shrinkage and therefore shrinkage strains, inducing cracking in concrete, is a function of air temperature, relative humidity, concrete temperature, and wind velocity [243]. Figure 75 also represents the variation of temperature based on the data obtained from thermocouples embedded in $B_{CF\text{-}S}$. From the graphs, the trends of temperature change with time are identical for both the normal concrete bus pad ($B_{N\text{-}2S}$) and carbon-fiber-reinforced concrete bus pad ($B_{CF\text{-}S}$). It should be noted that the temperature variation exhibited in both the bus pads is in coherence with the standard temperature variation for concrete. Since embedded BlueRock™ sensors in the $B_{CF\text{-}S}$ bus pad did not work, the humidity-based data is not discussed in this chapter.

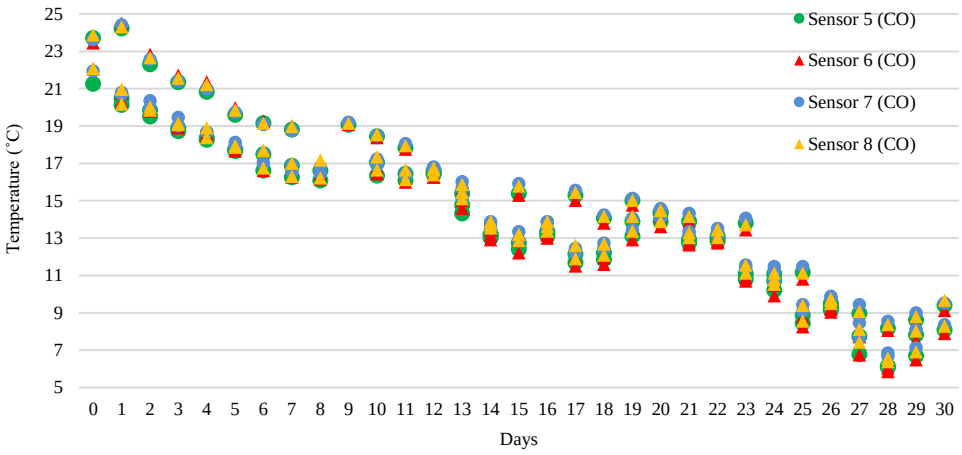

(a)

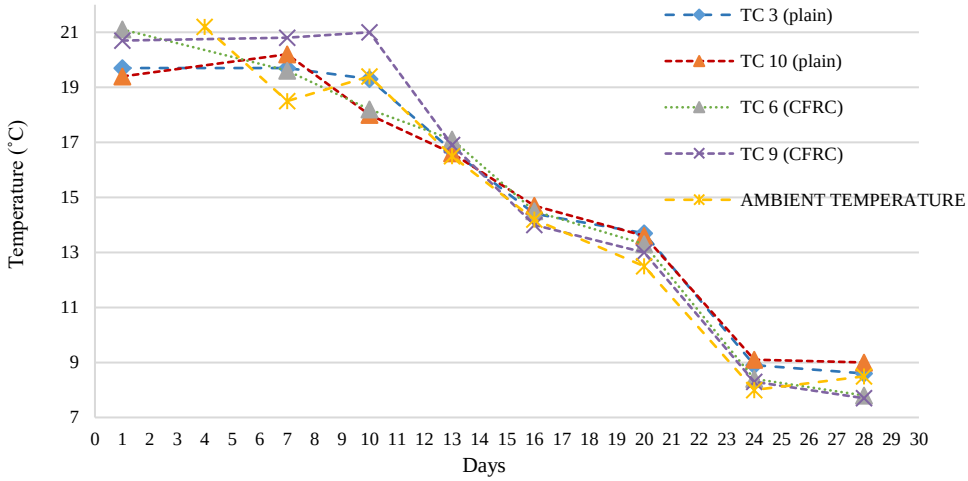

(b)

Figure 75. Temperature variation from a) wireless sensors b) thermocouples

7.3.2.3. Strain gauge measurements of bus pads

Initial strain results can be viewed in Figure 76. It can be observed that the graphs do not conform to a distinct trend. Rather than fluctuating within a limited range, the values appear to primarily consist of what would be considered outliers, readings exceeding the expected limits for strain measured in experimental work, typically -0.005 to +0.005 [244]. The strain readings additionally do not conform to either compressive or tensile values, but rather fluctuate between the two strain types. This pattern is observed in gauges 1, 5, 6, 9, 10, 11, and 12, and is therefore not specific to one concrete type. Further investigation will be conducted to determine the cause of inconsistent compression and tension values, as the gauges would be expected to record either only tension or compression only based on their positions in the slab.

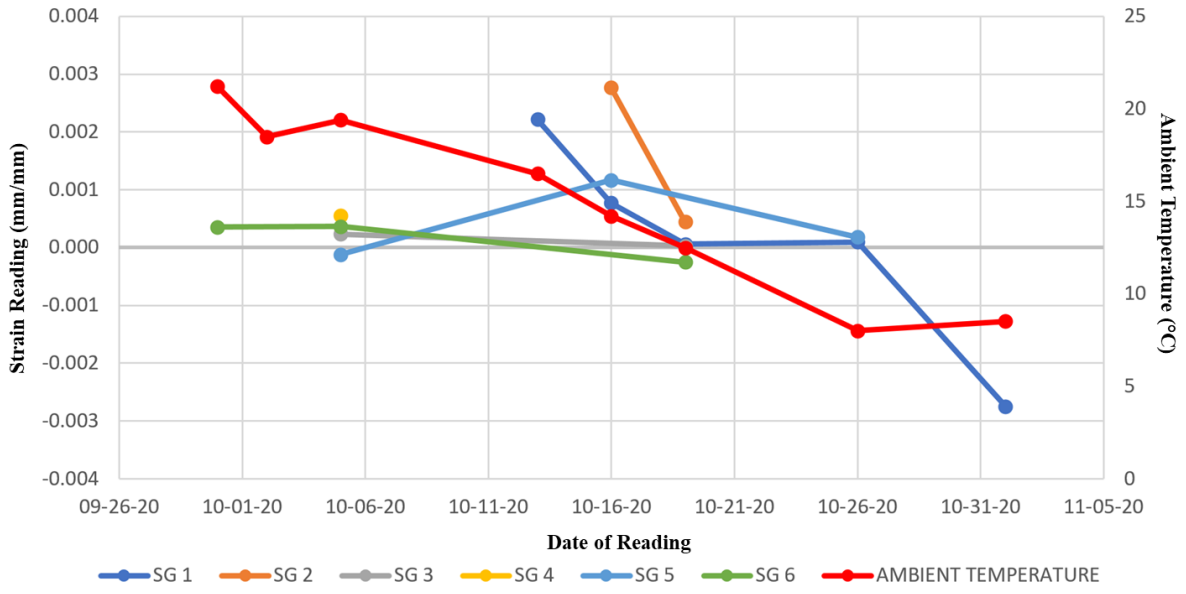

(a)

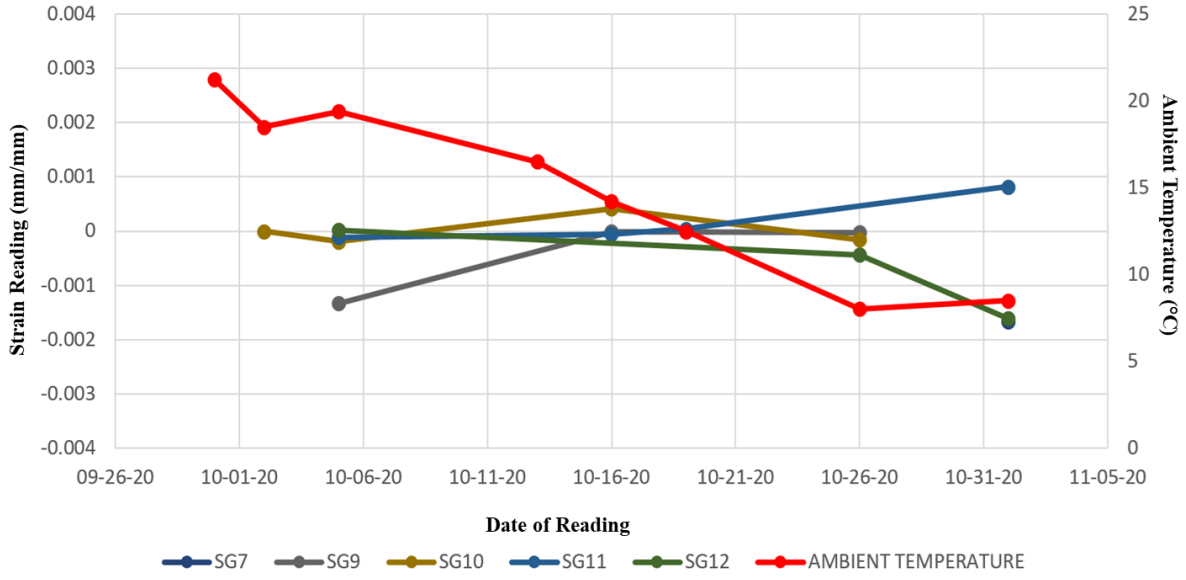

(b)

Figure 76. Strain gauge data after temperature corrections a) $B_{N\text{-}2S}$ b) $B_{CF\text{-}S}$

7.3.2.4. Health monitoring of bus pads at 28 days of casting

After 28 days of construction, permission was granted from BC Transit to close the bus pad to traffic for 5 days, to conduct testing. In addition to regular temperature, humidity, strain gauge, and piezo measurements, three more tests were conducted including Schmidt hammer, Electrical Resistivity (ER), and Ultrasonic Pulse Velocity (UPV) tests. Figure 77 shows how the gridlines were drawn on concrete bus pads for NDTs.

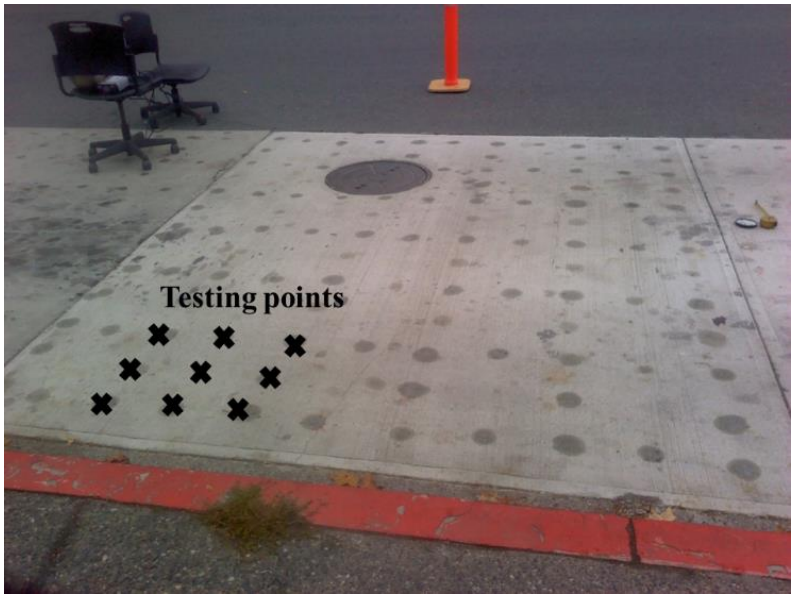

Figure 77. NDT at 25 cm × 25 cm grids on bus pad

7.3.2.4.1. Schmidt hammer testing

A rebound hammer is a low-cost method employed to assess the quality of concrete near the surface and to estimate the strength of concrete based on the rebound number. As the rebound hammer test can evaluate the condition of concrete up to a depth of 3 cm effectively [245], it was expected that the rebound hammer test would be able to provide valuable insights.

To evaluate the condition of the bus pad subjected to traffic load, an N-type Schmidt hammer test was conducted as per ASTM C805 [246] for all the bus pads. The three bus pads were divided into grids of 50 cm × 50 cm for the rebound number test and 25 cm × 25 cm for UPV and electrical resistivity tests. The calibration of the rebound hammer was done on an anvil before and after testing. The rebound hammer values were then converted into the corresponding compressive strength values using the chart provided by the manufacturer. The values of compressive strength at different impact points taken by rebound hammer are plotted in Figure 78. It can be observed that in B_{N-1} and B_{N-2S}, the average compressive strength is 24 MPa, and for the CFRC bus pad, the average compressive strength is equal to 21 MPa. It should be noted that the rebound hammer predicted compressive strength is in good correlation with those of the samples tested in the lab. It was also observed that the strength values in the center of each slab are higher compared to the concrete placed at the corners. The rebound hammer values were successfully able to differentiate between the material characteristic of plain concrete and fiber-reinforced concrete. The addition of the fibers to the concrete does increase its porosity at this largely affects its surface hardness and hence, impacts the rebound hammer values.

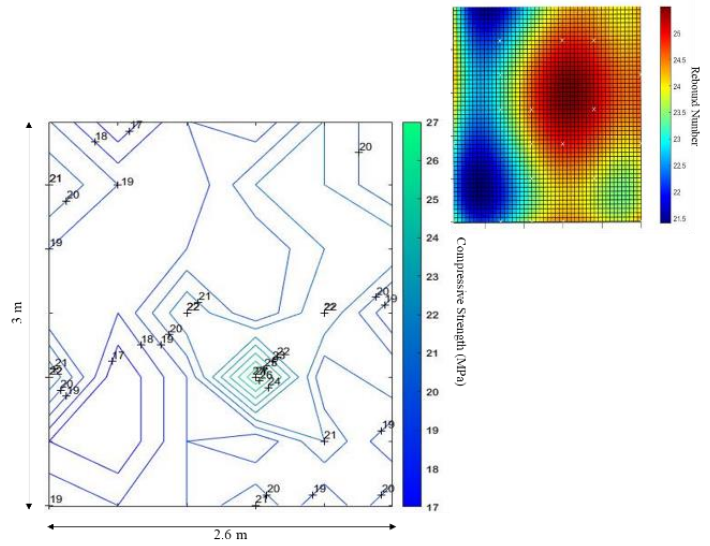

(a)

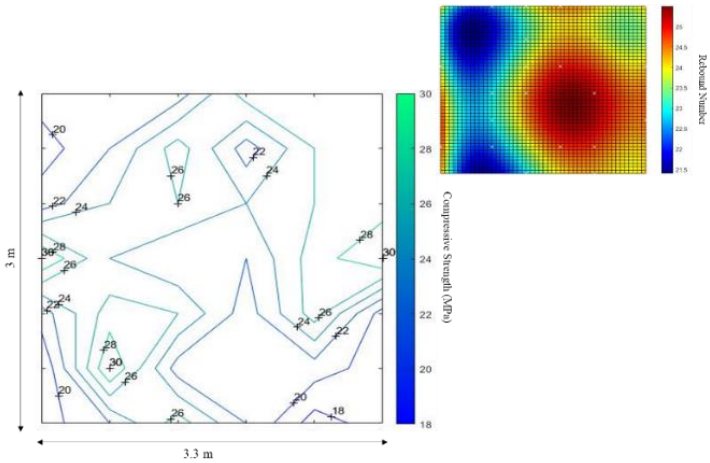

(b)

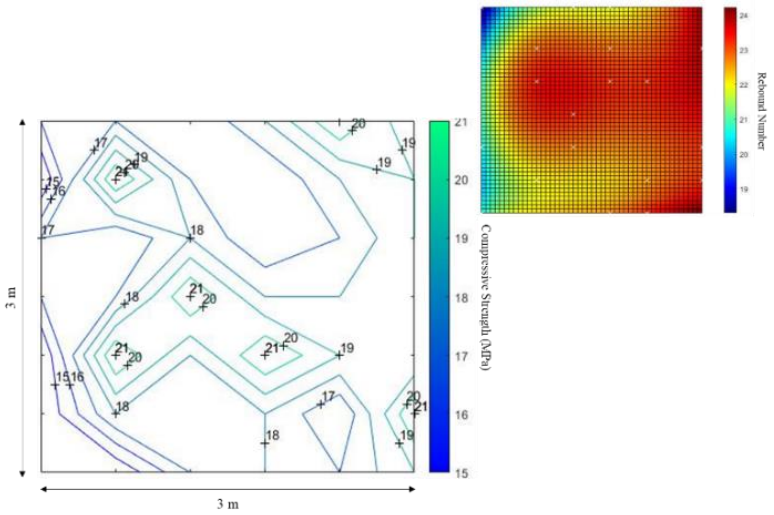

(c)

Figure 78. Variation of the Rebound number and compressive strength of bus pads a) B_{N-1} b) B_{N-2S} c) B_{CF-S}

7.3.2.4.2. Electrical resistivity

In general, there are three phases of plain concrete at 28 days [39]: 1) liquid phase with pores containing solutions of water; 2) solid phase including cementitious products of hydration and aggregates; 3) vapor phase with pores filled with air. Both the solid phase and vapor phase have high values of electrical resistivity ranging from 1011 Ω-cm to 1019 Ω-cm and hence they act as insulators. The liquid phase has considerably lower values of resistivity of the order of 5 to 100 Ω-cm and therefore acts as the conductors. Overall, the plain concrete is not electrically conductive with the electrical resistivity of oven-dried concrete at around 105 Ω-cm [247]. Several correlations have been reported that confirm the relationship between the transport parameters of concrete and the durability of concrete. Ion transport through the concrete microstructure controls the durability of concrete. This highlights the importance of electrical resistivity as it defines the ability of concrete to withstand the transport of charged ions in its microstructure. Therefore, the electrical resistivity data can signify the vulnerability of concrete to deterioration as lower values will indicate the easy transfer of ions, which in turn increases the risk of corrosion of the embedded rebar.

The electrical resistivity evaluation of the bus pad utilized the Wenner probe technique, with four equally spaced linear electrodes. All the bus pads were divided into grids of size 25 cm × 25 cm. Readings were taken on the same day (within one hour) to ensure the moisture condition of all slabs was consistent. The electrical resistivity was measured and plotted as a map presented in Figure 79 . From the figure, in the B_{N-1} and B_{N-2S} bus pads, electrical resistivity ranges up to 30 kΩ-cm. This confirms the existence of the liquid phase inside the concrete as the testing was conducted only 28 days after construction. The electrical resistivity map also confirms the effect of cracks (presented as zone 1, 2, 3, 4, 5, and 6 on the map) on the resistivity of concrete as the resistivity value is much lower in these areas compared to areas with no cracks.

On the other hand, the electrical resistivity values for the CFRC were negligible. As CFs are electrically conductive, the electrical resistivity of the overall composite was significantly decreased [27,248]. The uniform low value of electrical resistivity is attributable to the acceptable fiber network formation in the pavement. This further suggests that the measurement of electrical resistivity is not a suitable measure of durability for CFRC. Figure 79 also confirms the uniform distribution of CFs in the bus pad as the recorded values of electrical resistivity at all points were nearly negligible. However, this also indicates the effectiveness of a small V_f in reducing the resistivity of a CFRC slab, which could be useful in the future in designing self-sensing properties of CFRC.

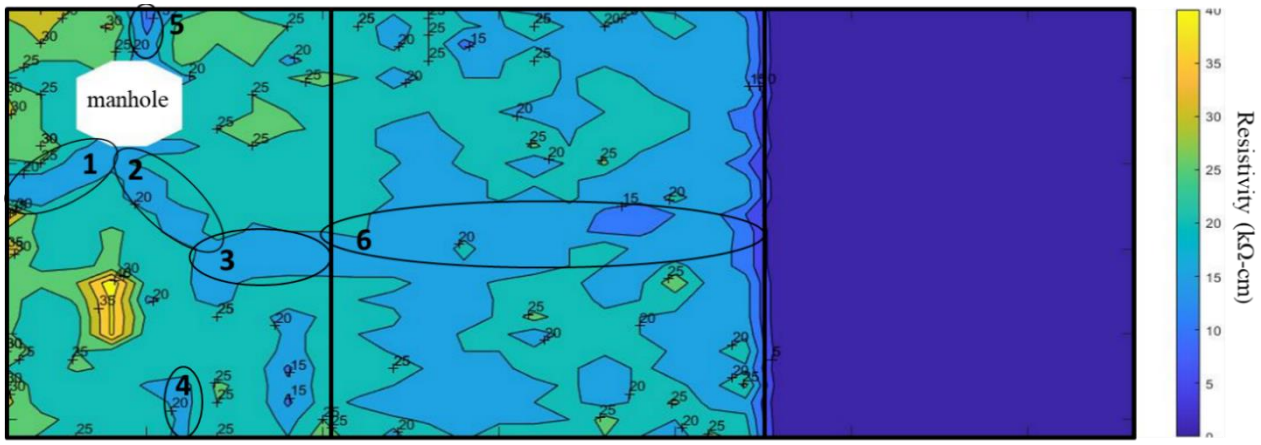

(a) (b) (c)

Figure 79. Variation of the Electrical resistivity of concrete across the bus pad a) B_{N-1} b) B_{N-2S} c) B_{CF-S}

7.3.2.4.3. Ultrasonic pulse velocity testing

Elastic waves in concrete are generally influenced by their mechanical characteristics, and ultrasonic pulse velocity utilizes this principle to estimate elastic stiffness and other strength-related properties. In any material, ultrasonic waves depend on the density of the material and other elastic properties. Hence, for a material such as concrete with a known density, well-defined ultrasonic signals can be used to estimate the modulus of the concrete and estimate the strength of the concrete.

For testing the concrete bus pads, the Proceq Pundit Lab UPV test instrument was used, with transducers of diameter 50 mm with a maximum frequency of 54 kHz. The UPV testing was conducted as per ASTM C597 [207]. All bus pads were divided into grids of size 25 cm × 25 cm. This implies that the maximum distance between each transducer was 25 cm. All the acquired data was plotted as shown in Figure 80. Several clusters of very low wave velocities can be seen in both B_{N-1} and B_{N-2S}, marked as zone 1, 2, 3, 4, 5, and 6 in Figure 80. It should be noted that the marked zones represent cracked areas in the bus pad as observed during the visual inspection of the pads (Figure 73). For both the B_{N-2S} and B_{CF-S} bus pads, the UPV values vary from 3 to 4.5 km/sec which indicates a good quality of concrete. The inclusion of fibers reduced the rate of UPV penetration into the mixtures, which is consistent with literatures [249,250]. The lesser values in BCF-S also indicate the scatter in the wave energy due to the presence of CFs. Further, the wave velocity is somewhat constant for the entire bus pad, which also indicates good fiber dispersion in the B_{CF-S} bus pad.

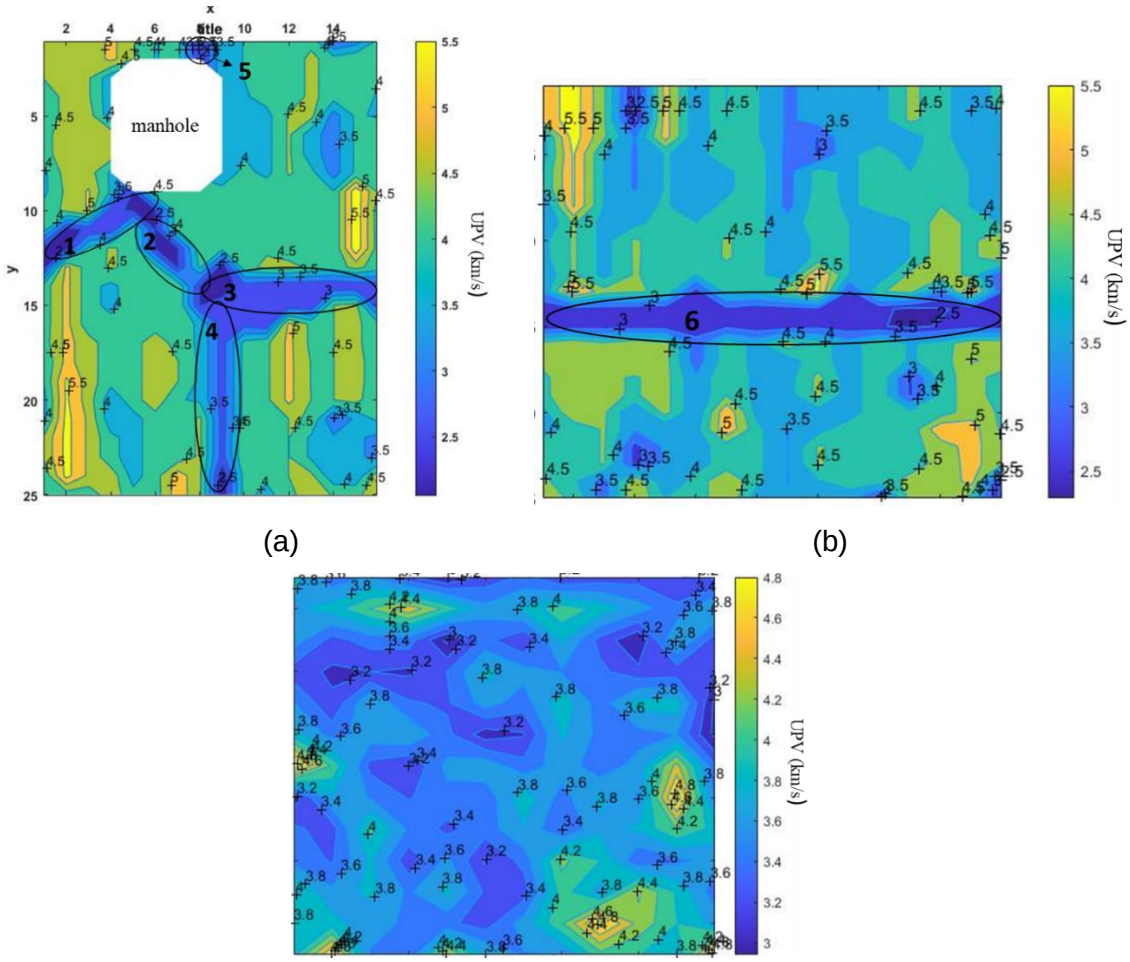

(a) (b)

(c)

Figure 80. Variation of the UPV of concrete across the bus pad (a) B_{N-1} (b) B_{N-2S} (c) B_{CF-S}

7.4. Conclusions

This chapter employs the real-time evaluation of CFRC for the purpose of its usage in the construction of a bus pad. Further, the bus pads were equipped with several sensing modules such as temperature sensors, thermocouples, strain gauges, and piezo patches. The data from these embedded sensors were regularly acquired and monitored. In addition to that, several other NDT techniques were employed at 28 days after construction of the bus pad such as Schmidt hammer, electrical resistivity, and ultrasonic pulse velocity. The following conclusions are drawn from the entire study:

- According to the DT performed on concrete beams and round panels, the influence of the incorporation of CF on the flexural behavior of concrete is reported to be more distinct when compared to the compressive strength. Samples with 0.5% and 1% fiber content among the examined CFRMs and CFRCs are more efficient since they exhibit the greatest improvements in most of the mechanical parameters compared to conventional concrete. According to the quadric polynomial fitted surface models, it has been demonstrated that the best fiber dosage for absorbing energy is between 2%

and 3% of the total fiber content.

- Flexural testing on sample taken from the site revealed a 26% increase in the flexural strength of CFRC beams, compared to a negligible improvement in the round panel. CFs' capacity to retain and bridge microcracks in flexure, which delays the initiation and propagation of cracks is primarily responsible for the strength improvement in beams.
- During visual observation, in the B_{CF-S} bus pad, small chunks of exposed CF were visible, and it was found that fibers from these areas started coming out due to the abrasion of the surface of the bus pad. However, no cracks were observed in the B_{CF-S} bus pad, while both B_{N-1} and B_{N-2S} developed very thin hairline cracks in the middle of the slab mainly due to the combined stress and curling effects.
- From the graphs derived from the thermocouples, the trends of temperature change with time were the same for B_{N-2S} and B_{CF-S}, and the temperature variation exhibited in both the bus pads is identical and in coherence with the standard temperature variation for concrete.
- According to the Schmidt hammer test results, the average values for compressive strength were reported to be 24 MPa for B_{N-1} and B_{N-2S} and 21 MPa for B_{CF-S}. It was also found that the strength values in the middle were higher than those in the corners. It should be noted that the rebound hammer predicted compressive strength is in a good correlation with those of the samples tested in the lab.
- The value of electrical resistivity in B_{N-1} and B_{N-2S} ranges up to 30 kΩ-cm, which confirms the existence of the liquid phase inside the concrete as the testing was conducted only 28 days after construction. The electrical resistivity values for the B_{CF-S} were negligible. CF is electrically conductive and the addition of CF in concrete significantly reduces the electrical resistivity of the overall composite. According to the results, the electrical resistivity of B_{CF-S} has a uniformly low value, which can be attributed to the pavement's acceptable formation of a fiber network and an acceptable fiber distribution.
- Several clusters of very low UPV values were observed in the location of bus pad cracks. For both the B_{N-2S} and B_{CF-S} bus pads, the UPV values varied from 3 to 4.5 km/sec which indicates good quality of concrete. The lesser values in BCF-S are indicative of the scatter in the wave energy due to the presence of CFs.
- Based on the DT and NDT results, the CFRC bus pad is a conductive pavement likely to be effective in controlling the rate of crack initiation in the pavement. CFRC with a very low electrical resistivity can be used as a self-sensing construction material, able to sense and record internal deficiencies in the bus pad.

7.5. Authorship contribution statement

Maryam Monazami: Conceptualization, Investigation, Methodology, Investigation, Software Analysis, Writing.

Ashutosh Sharma: Methodology, Resources, Sensor procurement, review and editing.

Rishi Gupta: Review, Methodology, Supervision, Resources

Chapter 8. Concluding remarks and key findings

This dissertation has investigated the application of CFs in CFRCC, yielding valuable knowledge about their microstructural properties, mechanical and durability behaviour, and performance characteristics. While each chapter concludes with a thorough conclusion, the following provides the dissertation's findings along with supplementary explanations and information.

1. Microstructural properties: The comprehensive microstructural analysis of different CF types along with introducing a new type of BBCF offers a valuable resource for researchers and engineers and provides clear understanding of the characteristics of the CFs and potential applications of different CFs. The following research outcomes were resulted from microstructural analysis:

- EDX analysis indicated the presence of approximately **6% sulfur content** in BBCF. Such high sulfur content renders the BBCF unsuitable for utilization in concrete applications.
- The surface of the BBCF displays **numerous small pores**. These impact cement matrix characteristics like porosity, absorption capability, and interactions at ITZ.
- The **geometry of the BBCF** differ from those of conventional fibers. BBCF possess a **hollow cylindrical structure**, while others have solid cylinder shape. This structural variation significantly influences the fiber's performance, this can be seen by the presence of fractures at points where the transition from solid to hollow cylinder is seen.

2. Bonding Properties: The research findings shed light on the bonding properties between CFs and the cement matrix. The study identifies the influence of various factors on fiber-matrix interaction, such as **fiber type**, **surface morphology** and **curing age**. Following research remarks were derived form the research results:

- The improvement in **bond behavior** is related to the microstructure of ITZ. The **rapid hydration at the initial stages** speeds up microstructure enhancement, causing a **denser ITZ and ultimately fastening the improvement of the bond** between the fiber and matrix.
- Different fibers showed different bonding properties. The **highest average pull-out force**, reaching 358 N, was recorded for **SF**. The pull-out forces for SI, PAN-based CF, and pitch-based CF were measured at 122 N, 155 N, and 156 N respectively.
- The **anchorage at the hook end SF** is one of the main reasons for higher energy absorption, while in straight fibers such as CF, the frictional shear stress at the interface

determines the energy absorption capacity of fibers.

3. Coating Methods: The **use of supplementary cementitious materials** as coating material for CFs highlights their potential to enhance the microstructure and durability of the cement matrix. The research demonstrates the effectiveness of these coating methods in improving the bond strength and overall performance of CFRC. Below are the summarized research outcomes:

- The utilization of the proposed **NaOH treatment** method exhibited **adverse effects** on the bonding properties of CFs and fibers subjected to NaOH treatment showed reduced bond strength and diminished fiber pull-out toughness.
- **Combining the NaOH treatment with fly ash coating** led to increased bond strength (10825 Pa), **decreased contact angle** (~ 110), and a rougher surface texture, which was confirmed through SEM images.
- **NaOH-treated** CFs demonstrated **lower electrical resistivity** (2.5 µohm.m compared to 5.3 µohm.m) in comparison to untreated CFs. Conversely, the electrical resistivity values of **fly ash-treated** CFs were comparable to those of untreated fibers (6.9 µohm.m).

4. Optimal Fiber Dosage: Based on the experimental and predicted results and considering the mathematical model, CFRCs are likely to be effective in **controlling the rate of crack initiation** and **propagation** in concrete. The following items summarizes the results obtained in each mechanical testing:

- CFRMs demonstrated **higher ultimate load** compared to both NC and PPRM samples. This can be primarily attributed to the micro CFs' capacity to confine and bridge microcracks within the cement matrix.
- Among the investigated CFRCs, 0.5% and 1% CFRC is likely to be more effective because of the **highest improvement** in most of the investigated mechanical properties compared to PFRCs and non-fibrous concrete.
- Using composite theory, the range of **experimental to predicted flexural strength** was between 1.11 and 1.34 for CFRC. This range indicates a **favorable agreement** between the experimental and predicted outcomes.
- Taking factors such as **cost** and **workability** into account, it is recommended that an **optimal percentage of 0.5%** CF be utilized for **slab** and **pavement** applications.

5. Yield Line Theory: Fracture pattern of round panels under flexure showed that non-fibrous panels failed in a **symmetrical yield line pattern**, while FRC panels experienced a **non-symmetrical pattern**. In flexural testing, it was observed that the ultimate deflection was 20.6 mm, 114.7 mm, and 158 mm in CO, 0.5PAT18 and 1PAT18 respectively. Samples with 0.5% CF showed a comparable flexural strength value compared to non-fibrous panel, while the strength of 1PAT18 was reduced by more than 20%. **1% CF** in panels result in better performance in **post-crack stage** compared to 0.5PAT18 and CO respectively.

6. Freeze-thaw Resistance: The research comprehensively assessed the FT resistance of CFRC under rigorous FT cycles. The findings unequivocally demonstrated the exceptional durability of CFRC specimens containing 0.5% CFs. The following points were derived from analyzing the FT results:

- The trend of **mass loss** indicates an **accelerated deterioration** in CFRC samples exposed to FT cycles, especially in those with higher CF volume. This can be attributed primarily to the inclusion of additional CFs, along with an increased appearance and width of cracks, leading to high porosity and easier water retention within the specimens. Noticeable mass loss becomes more significant when pores and newly formed **microcracks connect**, creating pathways that enhance the **water movement** through the concrete sample. The derived equation from the mass loss data enables accurate estimation of mass loss percentages with a noteworthy level of accuracy.
- the CFRC samples with 0.5% CF exhibited **minimal signs of deterioration**, including negligible cracking, surface degradation, or loss of mechanical properties.
- The **DMOE** showed a notable exponential decrease as the CF content was raised. Following 60 FT cycles, specimens containing 1% and 2% CF encountered a significant drop in the **relative DMOE**, exceeding a 60% loss. This significant reduction points towards extensive damage of the specimens, undermining both their dynamic characteristics and structural integrity.
- **Infrared imaging** provided visual confirmation of the porous characteristics within CO and CFRC samples. The CO sample showed the most **even temperature** distribution among all samples, implying a relatively uniform structure and homogeneity. The 0.5% CF sample initially displays void areas before FT testing. However, after 120 FT cycles, the 0.5CFT18 sample's infrared images remain intact, suggesting **maintained structural integrity** despite voids.

The aforementioned results validate the suitability of CFRC with 0.5% CF content for applications in cold regions, where FT cycles pose significant challenges to the durability of concrete structures.

7. Real-Time Evaluation and Infrastructure health Monitoring: The implementation of **embedded sensors** and **real-time evaluation techniques** in the research study facilitated the continuous monitoring and assessment of the constructed pavement over time. The CF-reinforced pavement exhibited **no visible cracks** indicating the effectiveness of CF in preventing crack formation. In contrast, the pavement sample without fiber reinforcement developed **hairline cracks** in less than a month after construction. These results underscore the **significant role of CF** in enhancing the crack resistance and long-term performance of concrete pavements. The utilization of CF in pavement construction can effectively mitigate crack initiation and propagation, ensuring a more durable and resilient pavement structure.

- The **strain values** in pavements appear to primarily consist of what would be considered outliers, readings exceeding the expected limits for strain measured in experimental work, typically -0.005 to +0.005.
- Using **thermal camera**, it is easy to see the delaminated areas (lower temperature on the cracks) and the temperature gradient on the pavement which make it possible to determine the **direction of an expanding delaminated region**. It was also observed that the CFRC bus pad had a uniform temperature variation with a slightly lower internal temperature (~14 °C) compared to the other bus pads (~18 °C) which is mainly due to the high electrical conductivity of the fibers.

8. Non-Destructive Evaluation Techniques: The use of non-destructive assessment techniques, such as Schmidt hammer tests and electrical resistivity measurements, in the research study offers valuable insights into the condition and performance of carbon fiber-reinforced pavement when compared to traditional concrete pavement. The research findings **address a gap** in understanding the mechanical behavior of pavement reinforced with CF. The following summary outlines the key observations:

- The $B_{CF\text{-}S}$ bus pad didn't show any cracks on the surface. On the other hand, non-reinforced concrete bus pad started getting hairline cracks just 7 days after being made. These first cracks, which appeared in the middle of the pavement are mainly due to combined **thermal** and **traffic loading** effects.
- The **Schmidt hammer** test results indicate that the average compressive strength is 24 MPa for both non-reinforced bus pads. On the other hand, the CFRC bus pad demonstrates an average compressive strength of 21 MPa. This reduction in compressive strength primarily stems from the formation of an ITZ following the introduction of fibers and thus, an associated rise in porosity.
- In the $B_{N\text{-}1}$ and $B_{N\text{-}2S}$ bus pads, the **electrical resistivity** reaches up to 30 kΩ-cm,

confirming the presence of a liquid phase within the concrete. The electrical resistivity map of pavement also demonstrates that cracks significantly lower the resistivity in these areas compared to crack-free regions. Conversely, CFRC exhibits **very low electrical resistivity** (non-detectable by the electrical resistivity probe) due to the conductive nature of CFs. These fibers effectively decrease the composite's overall electrical resistivity. The consistent low electrical resistivity is attributed to the well-distributed fiber network in the pavement.

- Non-reinforced pavements show clusters of very low **ultrasound wave velocities**, corresponding to the cracked areas observed visually in the bus pad. For both $B_{N\text{-}2S}$ and $B_{CF\text{-}S}$ bus pads, the UPV values range from 3 to 4.5 km/sec, indicating high-quality concrete. However, the addition of fibers reduces the rate of UPV penetration. The slightly lower values in $B_{CF\text{-}S}$ reflect wave energy scattering due to CF presence. Additionally, the consistent wave velocity across the bus pad suggests well-dispersed fibers in $B_{CF\text{-}S}$.

Overall, NDE techniques highlight the excellent performance of CFRC pavement, indicating its potential for long-lasting durability.

Chapter 9. Recommendation for future work

The research conducted in this dissertation has covered various microstructural and mechanical aspects of CFRC and its potential applications. However, the following areas present opportunities for further exploration and advancement in the field:

1. **Enhanced BBCF Development**: To improve the mechanical properties and application versatility of BBCF, future research could focus on refining the manufacturing process. Investigating methods to reduce fragility, hollowness, and achieving a more consistent diameter could lead to more effective and reliable CFRC components for construction and other industries.

2. **Innovative Coating Materials and Techniques**: Exploring alternative coating materials that enhance the bond strength between CFs and the concrete matrix is essential. Special attention could be directed towards conductive coatings, which not only enhance bonding but also introduce electrical conductivity to the composite. Researching various coating techniques could lead to optimized application methods for improved performance.

3. **Synergistic Effects of Conductive Materials**: Investigating the synergistic effects of combining different conductive materials in concrete offers potential advancements in both electrical conductivity and overall performance. This area requires a systematic study of compatibility and interactions between various conductive materials, with the goal of finding optimal combinations that maximize conductivity without compromising the concrete's structural integrity.

4. **Corrosion Resistance of CFRC Structures**: Further research is needed to comprehensively understand the impact of CFs on the corrosion resistance of reinforced concrete structures. This involves evaluating how CFs influence corrosion initiation and propagation. A detailed exploration of the durability of CFRC in corrosive environments will contribute to its effective application in such settings.

5. **Fatigue Life Assessment:** Analyze the fatigue life of CFRC specimens under different loading conditions. Determine the number of loading cycles required for failure or the development of critical damage. Compare these results with fatigue data from traditional concrete materials to assess the potential benefits of CFRC in terms of extended service life. During fatigue testing, the changes in mechanical properties of CFRC, such as toughness, strength, and crack propagation can be analyzed.

Validation between the findings from laboratory fatigue testing and real-world case studies or field data can be done to assess the consistency of laboratory results with practical performance.

6. **Seismic Performance**: Research is needed to investigate CFRC's performance in seismic-resistant designs. Composite response to lateral forces, its energy dissipation capacity, and its ability to prevent brittle failure modes during earthquakes can be investigated and the results be compared with traditional concrete.

7. **Repair and Strengthening**: CFRC's potential for repairing and strengthening existing structures needs to be explored. Its effectiveness in enhancing the load-carrying capacity and extending the service life of deteriorated or under-designed elements could be assessed.

8. **Cold Climate Suitability Assessment**: The feasibility of using CFRC in cold climates like Alberta, where temperature fluctuations, FT cycles, and de-icing agents pose unique challenges to traditional concrete materials needs to be investigated. CFRC performance under these conditions in terms of durability, resistance to cracking, and maintenance requirement can be investigated. A case study of CFRC application in a cold environment like Alberta not only enriches the diversity of research but also provides valuable insights for practical implementation. The findings from this case study can contribute to the broader body of knowledge on CFRC's adaptability and performance across different climatic conditions.

9. **Life Cycle Assessments and Sustainability Analysis**: Conducting life cycle assessments and life cycle cost analysis to compare CFRC pavement with conventional concrete pavement would provide a holistic understanding of its environmental and economic benefits. Life cycle analysis would quantify the long-term sustainability and economic viability of CFRC in construction projects, helping decision-making processes for infrastructure development. Life cycle cost analysis evaluates factors such as initial costs, maintenance expenses, and expected service life to determine the economic viability of CFRC in various applications.

10. **Environmental Impact**: The potential reduction in maintenance and repair requirements offered by CFRC in cold climates can be evaluated considering the implications for environmental sustainability, including decreased use of de-icing agents, reduced energy consumption for maintenance, and longer service life of infrastructure.

In conclusion, the research presented in this thesis opens the door to a multitude of exciting research avenues. Exploring these future directions can contribute significantly to advancing the understanding, applicability, and sustainability of CFRC and its various applications.

References

[1] Kalpana M, Tayu A. Light weight steel fibre reinforced concrete: A review. Mater Today Proc 2020;22:884–6. https://doi.org/10.1016/j.matpr.2019.11.095.

[2] Wang Z, Ma G, Ma Z, Zhang Y. Flexural behavior of carbon fiber-reinforced concrete beams under impact loading. Cem Concr Compos 2021;118:103910. https://doi.org/10.1016/j.cemconcomp.2020.103910.

[3] Chen P-W, Chung D. Concrete reinforced with up to 0.2 vol% of short carbon fibres. Composites 1993;24:33–52.

[4] Qian C, Stroeven P. Fracture properties of concrete reinforced with steel–polypropylene hybrid fibres. Cem Concr Compos 2000;22:343–51. https://doi.org/10.1016/S0958-9465(00)00033-0.

[5] Swamy RN. Fibre Reinforced Cement and Concrete: Proceedings of the Fourth RILEM International Symposium. CRC Press; 1992.

[6] Fibre-Reinforced Concrete for Industrial Construction – a Fracture Mechanics Approach to Material Testing and Structural Analysis - ProQuest n.d. https://www.proquest.com/openview/7a7e65856cef4d56ca5207426f6c9532/1?pq-origsite=gscholar&cbl=18750&diss=y (accessed July 1, 2023).

[7] Markovich I, Van Mier J, Walraven J. Single fiber pullout from hybrid fiber reinforced concrete. HERON Vol 46 3 2001 2001.

[8] Frank E, Hermanutz F, Buchmeiser MR. Carbon Fibers: Precursors, Manufacturing, and Properties. Macromol Mater Eng 2012;297:493–501. https://doi.org/10.1002/mame.201100406.

[9] Yan H, Lu C, Jing D, Chang C, Liu N, Hou X. Recycling of carbon fibers in epoxy resin composites using supercritical 1-propanol. New Carbon Mater 2016;31:46–54. https://doi.org/10.1016/S1872-5805(16)60004-5.

[10] Ding R, Wu H, Thunga M, Bowler N, Kessler MR. Processing and characterization of low-cost electrospun carbon fibers from organosolv lignin/polyacrylonitrile blends. Carbon 2016;100:126–36. https://doi.org/10.1016/j.carbon.2015.12.078.

[11] Hassan MF, Sabri MA, Fazal H, Hafeez A, Shezad N, Hussain M. Recent trends in activated carbon fibers production from various precursors and applications—A comparative review. J Anal Appl Pyrolysis 2020;145:104715. https://doi.org/10.1016/j.jaap.2019.104715.

[12] Natali M, Rallini M, Torre L, Puglia D. High Temperature Composites From Renewable Resources: A Perspective on Current Technological Challenges for the Manufacturing of Non-Oil Based High Char Yield Matrices and Carbon Fibers. Front Mater 2022;9.

[13] Bengtsson A, Bengtsson J, Jedvert K, Kakkonen M, Tanhuanpää O, Brännvall E, et al. Continuous Stabilization and Carbonization of a Lignin–Cellulose Precursor to Carbon Fiber. ACS Omega 2022;7:16793–802. https://doi.org/10.1021/acsomega.2c01806.

[14] Harzallah S, Chabaat M, Saidani M, Moussaoui M. Numerical investigation of the seismic vulnerability of bridge piers strengthened with steel fibre reinforced concrete (SFRC) and carbon fibre composites (CFC). Case Stud Constr Mater 2022;17:e01235. https://doi.org/10.1016/j.cscm.2022.e01235.

[15] Navaratnam S, Selvaranjan K, Jayasooriya D, Rajeev P, Sanjayan J. Applications of natural and synthetic fiber reinforced polymer in infrastructure: A suitability assessment. J Build Eng 2023;66:105835. https://doi.org/10.1016/j.jobe.2023.105835.

[16] Türkmen ÖS, De Vries BT, Wijte SNM, Vermeltfoort AT. In-plane behaviour of clay brick masonry wallettes retrofitted with single-sided fabric-reinforced cementitious matrix and deep mounted carbon fibre strips. Bull Earthq Eng 2020;18:725–65. https://doi.org/10.1007/s10518-019-00596-2.

[17] Fagone M, Ranocchiai G, Rotunno T, Grande E. Predictive Capability of a Finite Element Micro-Mechanical Model for Masonry Elements Reinforced Using CFRP. Key Eng Mater 2022;916:186–92. https://doi.org/10.4028/p-jco79d.

[18] Hu JY, Zhang SS, Chen E, Li WG. A review on corrosion detection and protection of existing reinforced concrete (RC) structures. Constr Build Mater 2022;325:126718. https://doi.org/10.1016/j.conbuildmat.2022.126718.
[19] Golias E, Zapris AG, Kytinou VK, Kalogeropoulos GI, Chalioris CE, Karayannis CG. Effectiveness of the Novel Rehabilitation Method of Seismically Damaged RC Joints Using C-FRP Ropes and Comparison with Widely Applied Method Using C-FRP Sheets—Experimental Investigation. Sustainability 2021;13:6454. https://doi.org/10.3390/su13116454.
[20] Efficiency of Carbon Fiber Composite Structural Systems for Tall Buildings: A Parametric Simulation Based Framework for Finite Element Analysis - ProQuest n.d. https://www.proquest.com/openview/a27f23844b2f69e507925c9b952a7ef1/1?pq-origsite=gscholar&cbl=18750&diss=y (accessed August 13, 2023).
[21] Materials | Free Full-Text | Advanced Carbon Reinforced Concrete Technologies for Façade Elements of Nearly Zero-Energy Buildings n.d. https://www.mdpi.com/1996-1944/15/4/1619 (accessed August 13, 2023).
[22] Paterson J, Mitchell D. Seismic Retrofit of Shear Walls with Headed Bars and Carbon Fiber Wrap. J Struct Eng 2003;129:606–14. https://doi.org/10.1061/(ASCE)0733-9445(2003)129:5(606).
[23] Seismic Retrofit of Lap Splices in Nonductile Square Columns Using Carbon Fiber-Reinforced Jackets - ProQuest n.d. https://www.proquest.com/openview/99023dcbb457dd008a683c86cf79605a/1?pq-origsite=gscholar&cbl=36963 (accessed August 13, 2023).
[24] Rahman ML, Malakooti A, Ceylan H, Kim S, Taylor PC. A review of electrically conductive concrete heated pavement system technology: From the laboratory to the full-scale implementation. Constr Build Mater 2022;329:127139. https://doi.org/10.1016/j.conbuildmat.2022.127139.
[25] Maleki P, Iranpour B, Shafabakhsh G. Investigation of de-icing of roads with conductive concrete pavement containing carbon fibre-reinforced polymer (CFRP). Int J Pavement Eng 2019;20:682–90. https://doi.org/10.1080/10298436.2017.1326235.
[26] Rahman ML, Malakooti A, Ceylan H, Kim S, Taylor PC. Identifying the best mixing procedure practice for ready-mix concrete plant production of carbon fibre reinforced electrically conductive concrete. Int J Pavement Eng 2023;24:2225119. https://doi.org/10.1080/10298436.2023.2225119.
[27] Sassani A, Arabzadeh A, Ceylan H, Kim S, Sadati SS, Gopalakrishnan K, et al. Carbon fiber-based electrically conductive concrete for salt-free deicing of pavements. J Clean Prod 2018;203:799–809.
[28] Notani MA, Arabzadeh A, Ceylan H, Kim S, Gopalakrishnan K. Effect of Carbon-Fiber Properties on Volumetrics and Ohmic Heating of Electrically Conductive Asphalt Concrete. J Mater Civ Eng 2019;31:04019200. https://doi.org/10.1061/(ASCE)MT.1943-5533.0002868.
[29] Monazami M, Gupta R. Microscale characteristics of new Bitumen-Based Carbon Fibers. 2nd Int Conf New Horiz Green Civ Eng Conf n.d.
[30] ACI PRC-544.4-18: Guide to Design with Fiber-Reinforced Concrete n.d. https://www.concrete.org/store/productdetail.aspx?ItemID=544418&Language=English&Units=US_AND_METRIC (accessed July 16, 2023).
[31] Ohama Y. Carbon-cement composites. Carbon 1989;27:729–37. https://doi.org/10.1016/0008-6223(89)90206-6.
[32] Ohama Y, Amano M, Endo M. Properties of Carbon Fiber Reinforced Cement With Silica Fume. Concr Int 1985;7:58–62.
[33] Banthia N. Fiber-reinforced Cements and Concretes. Can J Civ Eng 2001;28:879.
[34] Chen P-W, Chung DD. Carbon fiber reinforced concrete for smart structures capable of non-destructive flaw detection. Smart Mater Struct 1993;2:22.
[35] Chen P-W, Chung D. Concrete as a new strain/stress sensor. Compos Part B Eng 1996;27:11–23.

[36] Shi Z-Q, Chung DDL. Carbon fiber-reinforced concrete for traffic monitoring and weighing in motion. Cem Concr Res 1999;29:435–9. https://doi.org/10.1016/S0008-8846(98)00204-X.
[37] Fu X, Chung D. Self-monitoring of fatigue damage in carbon fiber reinforced cement. Cem Concr Res 1996;26:15–20.
[38] Chen P-W, Chung DDL. Low-drying-shrinkage concrete containing carbon fibers. Compos Part B Eng 1996;27:269–74. https://doi.org/10.1016/1359-8368(95)00020-8.
[39] Chung DDL. Cement reinforced with short carbon fibers: a multifunctional material. Compos Part B Eng 2000;31:511–26. https://doi.org/10.1016/S1359-8368(99)00071-2.
[40] Galao O, Bañón L, Baeza FJ, Carmona J, Garcés P. Highly conductive carbon fiber reinforced concrete for icing prevention and curing. Materials 2016;9:281.
[41] Wu J, Liu J, Yang F. Three-phase composite conductive concrete for pavement deicing. Constr Build Mater 2015;75:129–35.
[42] Rangelov M, Nassiri S, Haselbach L, Englund K. Using carbon fiber composites for reinforcing pervious concrete. Constr Build Mater 2016;126:875–85.
[43] Karzad AS, Toubat SA, Maalej M, Estephane P. Repair of reinforced concrete beams using carbon fiber reinforced polymer. MATEC Web Conf 2017;120:01008. https://doi.org/10.1051/matecconf/201712001008.
[44] Tanyildizi H. Prediction of the strength properties of carbon fiber-reinforced lightweight concrete exposed to the high temperature using artificial neural network and support vector machine. Adv Civ Eng 2018;2018:1–10.
[45] Song W, Yin J. Hybrid effect evaluation of steel fiber and carbon fiber on the performance of the fiber reinforced concrete. Materials 2016;9:704.
[46] Jeon E-B, Ahn S, Lee I-G, Koh H-I, Park J, Kim H-S. Investigation of mechanical/dynamic properties of carbon fiber reinforced polymer concrete for low noise railway slab. Compos Struct 2015;134:27–35.
[47] 544.1R 96 PDF | PDF | Concrete | Reinforced Concrete. Scribd n.d. https://www.scribd.com/document/367321644/544-1R-96-pdf (accessed June 18, 2023).
[48] Jin F-L, Park S-J. Preparation and characterization of carbon fiber-reinforced thermosetting composites: a review. Carbon Lett 2015;16:67–77.
[49] Donnet J-B, Bansal RC. Carbon fibers. Crc Press; 1998.
[50] Chae HG, Minus ML, Kumar S. Oriented and exfoliated single wall carbon nanotubes in polyacrylonitrile. Polymer 2006;47:3494–504.
[51] Kim SS, Lee J. Antibacterial activity of polyacrylonitrile–chitosan electrospun nanofibers. Carbohydr Polym 2014;102:231–7.
[52] Naito K, Tanaka Y, Yang J-M, Kagawa Y. Tensile properties of ultrahigh strength PAN-based, ultrahigh modulus pitch-based and high ductility pitch-based carbon fibers. Carbon 2008;46:189–95.
[53] Azhari F, Banthia N. Cement-based sensors with carbon fibers and carbon nanotubes for piezoresistive sensing. Cem Concr Compos 2012;34:866–73.
[54] Ivorra S, Garcés P, Catalá G, Andión LG, Zornoza E. Effect of silica fume particle size on mechanical properties of short carbon fiber reinforced concrete. Mater Des 2010;31:1553–8.
[55] Sun M, Li Z, Mao Q, Shen D. Thermoelectric percolation phenomena in carbon fiber-reinforced concrete. Cem Concr Res 1998;28:1707–12.
[56] Chae HG, Newcomb BA, Gulgunje PV, Liu Y, Gupta KK, Kamath MG, et al. High strength and high modulus carbon fibers. Carbon 2015;93:81–7.
[57] Wang W, Wu S, Dai H. Fatigue behavior and life prediction of carbon fiber reinforced concrete under cyclic flexural loading. Mater Sci Eng A 2006;434:347–51.
[58] Aydin AC. Self compactability of high volume hybrid fiber reinforced concrete. Constr Build Mater 2007;21:1149–54.
[59] Chen B, Liu J. Damage in carbon fiber-reinforced concrete, monitored by both electrical resistance measurement and acoustic emission analysis. Constr Build Mater 2008;22:2196–201.

[60] Naito K, Tanaka Y, Yang J, Kagawa Y. Flexural Properties of PAN-and Pitch-Based Carbon Fibers. J Am Ceram Soc 2009;92:186–92.
[61] Reimer T, Petkov I, Koch D, Frieß M, Dellin C. Fabrication and Characterization of C/C-SiC Material Made with Pitch-Based Carbon Fibers. Process Prop Adv Ceram Compos VII Ceram Trans Vol 252 2015:277–93.
[62] Naito K. Stress analysis and fracture toughness of notched polyacrylonitrile (PAN)-based and pitch-based single carbon fibers. Carbon 2018;126:346–59.
[63] Yao W, Li J, Wu K. Mechanical properties of hybrid fiber-reinforced concrete at low fiber volume fraction. Cem Concr Res 2003;33:27–30.
[64] Sun M, Liu Q, Li Z, Hu Y. A study of piezoelectric properties of carbon fiber reinforced concrete and plain cement paste during dynamic loading. Cem Concr Res 2000;30:1593–5.
[65] Chen B, Wu K, Yao W. Conductivity of carbon fiber reinforced cement-based composites. Cem Concr Compos 2004;26:291–7.
[66] Han B, Yu X, Kwon E. A self-sensing carbon nanotube/cement composite for traffic monitoring. Nanotechnology 2009;20:445501.
[67] Monteiro A, Loredo A, Costa P, Oeser M, Cachim P. A pressure-sensitive carbon black cement composite for traffic monitoring. Constr Build Mater 2017;154:1079–86.
[68] Mingqing S, Zhuoqiu L, Qizhao M, Darong S. A study on thermal self-monitoring of carbon fiber reinforced concrete. Cem Concr Res 1999;29:769–71.
[69] Bahar D, Salih Y. Thermoelectric behavior of carbon fiber reinforced lightweight concrete with mineral admixtures. New Carbon Mater 2008;23:21–4.
[70] Bontea D-M, Chung D, Lee G. Damage in carbon fiber-reinforced concrete, monitored by electrical resistance measurement. Cem Concr Res 2000;30:651–9.
[71] Gomis J, Galao O, Gomis V, Zornoza E, Garcés P. Self-heating and deicing conductive cement. Experimental study and modeling. Constr Build Mater 2015;75:442–9.
[72] Redelius P. Solubility parameters and bitumen. Fuel 2000;79:27–35.
[73] Altgelt K, Jewell D, Latham D, Selucky M. Separation schemes. Chromatogr. Pet. Anal., Marcel Dekker New York, NY; 1979, p. 185–214.
[74] Page not found. Alta Innov n.d. https://albertainnovates.ca/wpcontent/uploads/2018/04/BBC-Report-1.pdf (accessed June 18, 2023).
[75] Page not found. Alta Innov n.d. https://albertainnovates.ca/wpcontent/uploads/2018/04/BBC%20-%20Report%202.pdf (accessed June 18, 2023).
[76] Maache M, Bezazi A, Amroune S, Scarpa F, Dufresne A. Characterization of a novel natural cellulosic fiber from Juncus effusus L. Carbohydr Polym 2017;171:163–72.
[77] Monazami M, Gupta R. Investigation of mechanical behavior and fracture energy of fiber-reinforced concrete beams and panels. Cem Concr Compos 2022;133:104656. https://doi.org/10.1016/j.cemconcomp.2022.104656.
[78] Lin Z, Li VC. Crack bridging in fiber reinforced cementitious composites with slip-hardening interfaces. J Mech Phys Solids 1997;45:763–87.
[79] Naaman AE, Namur GG, Alwan JM, Najm HS. Fiber pullout and bond slip. I: Analytical study. J Struct Eng 1991;117:2769–90.
[80] Jewell RB, Mahboub KC, Robl TL, Bathke AC. Interfacial bond between reinforcing fibers and calcium sulfoaluminate cements: Fiber pullout characteristics. ACI Mater J 2015;112:39.
[81] Bentur A, Alexander M. A review of the work of the RILEM TC 159-ETC: Engineering of the interfacial transition zone in cementitious composites. Mater Struct 2000;33:82–7.
[82] Naaman AE, Najm H. Bond-slip mechanisms of steel fibers in concrete. Mater J 1991;88:135–45.
[83] Singh S, Shukla A, Brown R. Pullout behavior of polypropylene fibers from cementitious matrix. Cem Concr Res 2004;34:1919–25.
[84] Ratu RN. Development of polypropylene fiber as concrete reinforcing fiber 2016.

[85] Abu-Lebdeh T, Hamoush S, Heard W, Zornig B. Effect of matrix strength on pullout behavior of steel fiber reinforced very-high strength concrete composites. Constr Build Mater 2011;25:39–46.
[86] Qi J, Wu Z, Ma ZJ, Wang J. Pullout behavior of straight and hooked-end steel fibers in UHPC matrix with various embedded angles. Constr Build Mater 2018;191:764–74.
[87] Kim B-J, Yi C, Ahn Y. Effect of embedment length on pullout behavior of amorphous steel fiber in Portland cement composites. Constr Build Mater 2017;143:83–91.
[88] Tai Y-S, El-Tawil S. High loading-rate pullout behavior of inclined deformed steel fibers embedded in ultra-high performance concrete. Constr Build Mater 2017;148:204–18.
[89] Kim DJ, El-Tawil S, Naaman AE. Loading rate effect on pullout behavior of deformed steel fibers. ACI Mater J 2008;105:576.
[90] Kim J-J, Yoo D-Y. Effects of fiber shape and distance on the pullout behavior of steel fibers embedded in ultra-high-performance concrete. Cem Concr Compos 2019;103:213–23.
[91] Pi Z, Xiao H, Du J, Liu M, Li H. Interfacial microstructure and bond strength of nano-SiO2-coated steel fibers in cement matrix. Cem Concr Compos 2019;103:1–10.
[92] Babafemi AJ, Boshoff WP. Pull-out response of macro synthetic fibre from concrete matrix: Effect of loading rate and embedment length. Constr Build Mater 2017;135:590–9.
[93] Donnini J, Bellezze T, Corinaldesi V. Mechanical, electrical and self-sensing properties of cementitious mortars containing short carbon fibers. J Build Eng 2018;20:8–14.
[94] Won J-P, Lim D-H, Park C-G. Bond behaviour and flexural performance of structural synthetic fibre-reinforced concrete. Mag Concr Res 2006;58:401–10.
[95] Oh BH, Kim JC, Choi YC. Fracture behavior of concrete members reinforced with structural synthetic fibers. Eng Fract Mech 2007;74:243–57. https://doi.org/10.1016/j.engfracmech.2006.01.032.
[96] Azhari F, Banthia N. Carbon fiber-reinforced cementitious composites for tensile strain sensing. ACI Mater J 2017;114:129.
[97] Sassani A, Ceylan H, Kim S, Gopalakrishnan K, Arabzadeh A, Taylor PC. Influence of mix design variables on engineering properties of carbon fiber-modified electrically conductive concrete. Constr Build Mater 2017;152:168–81.
[98] Inn JJ. Conference Venue 2018.
[99] Micheli D, Vricella A, Pastore R, Delfini A, Morles RB, Marchetti M, et al. Electromagnetic properties of carbon nanotube reinforced concrete composites for frequency selective shielding structures. Constr Build Mater 2017;131:267–77.
[100] Yıldırım G, Sarwary MH, Al-Dahawi A, Öztürk O, Anıl Ö, Şahmaran M. Piezoresistive behavior of CF-and CNT-based reinforced concrete beams subjected to static flexural loading: Shear failure investigation. Constr Build Mater 2018;168:266–79.
[101] Lu M, Xiao H, Liu M, Li X, Li H, Sun L. Improved interfacial strength of SiO2 coated carbon fiber in cement matrix. Cem Concr Compos 2018;91:21–8.
[102] Le HV, Moon D, Kim DJ. Effects of ageing and storage conditions on the interfacial bond strength of steel fibers in mortars. Constr Build Mater 2018;170:129–41.
[103] C01 Committee. Specification for Standard Sand. ASTM International; n.d. https://doi.org/10.1520/C0778-17.
[104] ASTM. ASTM C136/C136M-19, Standard Test Method for Sieve Analysis of Fine and Coarse Aggregates 2019.
[105] ASTM C150/C150M-20. Standard specification for Portland cement. Tech Rep ASTM Int West Conshohocken PA 2020.
[106] Astm C. 305, Standard practice for mechanical mixing of hydraulic cement pastes and mortars of plastic consistency. ASTM Int 1999.
[107] Cao J, Chung D. Carbon fiber reinforced cement mortar improved by using acrylic dispersion as an admixture. Cem Concr Res 2001;31:1633–7.
[108] Chen P-W, Fu X, Chung D. Microstructural and mechanical effects of latex, methylcellulose, and silica fume on carbon fiber reinforced cement. Mater J 1997;94:147–55.

[109] Fu X, Lu W, Chung D. Ozone treatment of carbon fiber for reinforcing cement. Carbon 1998;36:1337–45.
[110] Chuang W, Geng-sheng J, Bing-liang L, Lei P, Ying F, Ni G, et al. Dispersion of carbon fibers and conductivity of carbon fiber-reinforced cement-based composites. Ceram Int 2017;43:15122–32.
[111] Chung D. Dispersion of short fibers in cement. J Mater Civ Eng 2005;17:379–83.
[112] Muhua T, Roy DM. An investigation of the effect of organic solvent on the rheological properties and hydration of cement paste. Cem Concr Res 1987;17:983–94.
[113] Gao J, Wang Z, Zhang T, Zhou L. Dispersion of carbon fibers in cement-based composites with different mixing methods. Constr Build Mater 2017;134:220–7.
[114] Wang H, Gao X, Wang R. The influence of rheological parameters of cement paste on the dispersion of carbon nanofibers and self-sensing performance. Constr Build Mater 2017;134:673–83.
[115] Bhosale A, Rasheed MA, Prakash SS, Raju G. A study on the efficiency of steel vs. synthetic vs. hybrid fibers on fracture behavior of concrete in flexure using acoustic emission. Constr Build Mater 2019;199:256–68.
[116] Deng Z, Li J. Mechanical behaviors of concrete combined with steel and synthetic macro-fibers. Int J Phys Sci 2006;1:57–66.
[117] Wu Z, Khayat KH, Shi C. How do fiber shape and matrix composition affect fiber pullout behavior and flexural properties of UHPC? Cem Concr Compos 2018;90:193–201.
[118] Bhutta A, Farooq M, Zanotti C, Banthia N. Pull-out behavior of different fibers in geopolymer mortars: effects of alkaline solution concentration and curing. Mater Struct 2017;50:1–13.
[119] Kanda T, Li VC. Interface property and apparent strength of high-strength hydrophilic fiber in cement matrix. J Mater Civ Eng 1998;10:5–13.
[120] Kim DJ, El-Tawil S, Naaman AE. Correlation between single fiber pullout and tensile response of FRC composites with high strength steel fibers, 2007, p. 67–76.
[121] Richardson A. Bond characteristics of structural polypropylene fibres in concrete with regard to post-crack strength and durable design. Struct Surv 2005;23:210–30.
[122] Nieuwoudt PD, Boshoff WP. Time-dependent pull-out behaviour of hooked-end steel fibres in concrete. Cem Concr Compos 2017;79:133–47.
[123] Nanni A, Bakis C, Boothby T. Test methods for FRP-concrete systems subjected to mechanical loads: State of the art review. J Reinf Plast Compos 1995;14:524–58.
[124] Monazami M, Gupta R. Comparative study of alkali treated and fly ash-alkali treated carbon fibers. 2023 Can Soc Civ Eng CSCE Conf-Springer Proc n.d.
[125] Garg M, Azarsa P, Gupta R. Self-healing potential and post-cracking tensile behavior of polypropylene fiber-reinforced cementitious composites. J Compos Sci 2021;5:122.
[126] Tiwari S, Bijwe J. Surface treatment of carbon fibers-a review. Procedia Technol 2014;14:505–12.
[127] An F, Lu C, Li Y, Guo J, Lu X, Lu H, et al. Preparation and characterization of carbon nanotube-hybridized carbon fiber to reinforce epoxy composite. Mater Des 2012;33:197–202.
[128] Servinis L, Beggs KM, Scheffler C, Wölfel E, Randall JD, Gengenbach TR, et al. Electrochemical surface modification of carbon fibres by grafting of amine, carboxylic and lipophilic amide groups. Carbon 2017;118:393–403.
[129] Fitzer E, Geigl K-H, Hüttner W, Weiss R. Chemical interactions between the carbon fibre surface and epoxy resins. Carbon 1980;18:389–93.
[130] Li H, Liebscher M, Ranjbarian M, Hempel S, Tzounis L, Schröfl C, et al. Electrochemical modification of carbon fiber yarns in cementitious pore solution for an enhanced interaction towards concrete matrices. Appl Surf Sci 2019;487:52–8.
[131] Chand S. Review carbon fibers for composites. J Mater Sci 2000;35:1303–13.
[132] Ibarra L, Macias A, Palma E. Stress-Strain and stress relaxation in oxidated short carbon fiber-thermoplastic elastomer composites. J Appl Polym Sci 1996;61:2447–54.

[133] Jiang J, Yao X, Xu C, Su Y, Zhou L, Deng C. Influence of electrochemical oxidation of carbon fiber on the mechanical properties of carbon fiber/graphene oxide/epoxy composites. Compos Part Appl Sci Manuf 2017;95:248–56.
[134] Xu G, Saavedra J, Jarosz A. Transactions of non ferrous metals society of China, Transactions of Nonferrous Metals Society of China; 2011, p. 5–10.
[135] Araki H, Noda T, Suzuki H, Abe F, Okada M. Effect of pyrocarbon pre-coating on the mechanical properties of CVI carbon fiber/SiC composites. J Nucl Sci Technol 1995;32:369–71.
[136] Anna Z, Xuqin W, Shijin L. J. East China Univ. Sci Tech 1994;20:485.
[137] Zhang R, Gao B, Ma Q, Zhang J, Cui H, Liu L. Directly grafting graphene oxide onto carbon fiber and the effect on the mechanical properties of carbon fiber composites. Mater Des 2016;93:364–9.
[138] Monazami M, Gupta R. Effect of Curing Age on Pull-Out Response of Carbon, Steel, and Synthetic Fiber Embedded in Cementitious Mortar Matrix. J Mater Civ Eng 2022;34:04022275.
[139] Santos AG, Rincón JM, Romero M, Talero R. Characterization of a polypropylene fibered cement composite using ESEM, FESEM and mechanical testing. Constr Build Mater 2005;19:396–403.
[140] Bentur A, Mindess S, Vondran G. Bonding in polypropylene fibre reinforced concretes. Int J Cem Compos Lightweight Concr 1989;11:153–8. https://doi.org/10.1016/0262-5075(89)90087-0.
[141] Park J-M, Kim P-G, Jang J-H, Wang Z, Hwang B-S, DeVries KL. Interfacial evaluation and durability of modified Jute fibers/polypropylene (PP) composites using micromechanical test and acoustic emission. Compos Part B Eng 2008;39:1042–61.
[142] Wang Y, Zhang S, Luo D, Shi X. Effect of chemically modified recycled carbon fiber composite on the mechanical properties of cementitious mortar. Compos Part B Eng 2019;173:106853.
[143] Kabir M, Wang H, Lau K, Cardona F. Chemical treatments on plant-based natural fibre reinforced polymer composites: An overview. Compos Part B Eng 2012;43:2883–92.
[144] ASTM A. ASTM C618-19 Standard Specification for Coal Fly Ash and Raw or Calcined Natural Pozzolan for Use in Concrete. ASTM Int West Conshohocken PA 2018.
[145] Canadian Standards Association. CSA A3000-13 Cementitious Materials Compendium. CSA Group Mississauga Ont 2013.
[146] Yan L, Chouw N, Huang L, Kasal B. Effect of alkali treatment on microstructure and mechanical properties of coir fibres, coir fibre reinforced-polymer composites and reinforced-cementitious composites. Constr Build Mater 2016;112:168–82.
[147] Alhozaimy AM, Soroushian P, Mirza F. Mechanical properties of polypropylene fiber reinforced concrete and the effects of pozzolanic materials. Cem Concr Compos 1996;18:85–92. https://doi.org/10.1016/0958-9465(95)00003-8.
[148] Banthia N, Gupta R. Influence of polypropylene fiber geometry on plastic shrinkage cracking in concrete. Cem Concr Res 2006;36:1263–7.
[149] Abbass W, Khan MI, Mourad S. Evaluation of mechanical properties of steel fiber reinforced concrete with different strengths of concrete. Constr Build Mater 2018;168:556–69.
[150] Chen Y, Cen G, Cui Y. Comparative analysis on the anti-wheel impact performance of steel fiber and reticular polypropylene synthetic fiber reinforced airport pavement concrete under elevated temperature aging environment. Constr Build Mater 2018;192:818–35.
[151] Rao R, Fu J, Chan Y, Tuan CY, Liu C. Steel fiber confined graphite concrete for pavement deicing. Compos Part B Eng 2018;155:187–96.
[152] Frazão C, Camões A, Barros J, Gonçalves D. Durability of steel fiber reinforced self-compacting concrete. Constr Build Mater 2015;80:155–66.
[153] Toutanji HA. Properties of polypropylene fiber reinforced silica fume expansive-cement concrete. Constr Build Mater 1999;13:171–7.

[154] Qian C, Stroeven P. Development of hybrid polypropylene-steel fibre-reinforced concrete. Cem Concr Res 2000;30:63–9.
[155] Behfarnia K, Behravan A. Application of high performance polypropylene fibers in concrete lining of water tunnels. Mater Des 2014;55:274–9.
[156] Han B, Ou J. Embedded piezoresistive cement-based stress/strain sensor. Sens Actuators Phys 2007;138:294–8.
[157] Guo Z, Zhuang C, Li Z, Chen Y. Mechanical properties of carbon fiber reinforced concrete (CFRC) after exposure to high temperatures. Compos Struct 2021;256:113072.
[158] Mastali M, Dalvand A, Sattarifard A. The impact resistance and mechanical properties of the reinforced self-compacting concrete incorporating recycled CFRP fiber with different lengths and dosages. Compos Part B Eng 2017;112:74–92.
[159] Deng Z. The fracture and fatigue performance in flexure of carbon fiber reinforced concrete. Cem Concr Compos 2005;27:131–40.
[160] Xiong B, Wang Z, Wang C, Xiong Y, Cai C. Effects of short carbon fiber content on microstructure and mechanical property of short carbon fiber reinforced Nb/Nb5Si3 composites. Intermetallics 2019;106:59–64.
[161] Minelli F, Plizzari G. Derivation of a simplified stress–crack width law for Fiber Reinforced Concrete through a revised round panel test. Cem Concr Compos 2015;58:95–104.
[162] Boulekbache B, Hamrat M, Chemrouk M, Amziane S. Flowability of fibre-reinforced concrete and its effect on the mechanical properties of the material. Constr Build Mater 2010;24:1664–71.
[163] Yousefieh N, Joshaghani A, Hajibandeh E, Shekarchi M. Influence of fibers on drying shrinkage in restrained concrete. Constr Build Mater 2017;148:833–45.
[164] Mohammadhosseini H, Awal AA, Yatim JBM. The impact resistance and mechanical properties of concrete reinforced with waste polypropylene carpet fibres. Constr Build Mater 2017;100:147–57.
[165] Abaeian R, Behbahani HP, Moslem SJ. Effects of high temperatures on mechanical behavior of high strength concrete reinforced with high performance synthetic macro polypropylene (HPP) fibres. Constr Build Mater 2018;165:631–8.
[166] Karahan O, Atiş CD. The durability properties of polypropylene fiber reinforced fly ash concrete. Mater Des 2011;32:1044–9.
[167] Swamy R, Mangat P. The interfacial bond stress in steel fiber cement composites. Cem Concr Res 1976;6:641–9.
[168] Abrishambaf A, Pimentel M, Nunes S. Influence of fibre orientation on the tensile behaviour of ultra-high performance fibre reinforced cementitious composites. Cem Concr Res 2017;97:28–40.
[169] Mu R, Li H, Qing L, Lin J, Zhao Q. Aligning steel fibers in cement mortar using electro-magnetic field. Constr Build Mater 2017;131:309–16.
[170] ASTM C. 494. Standard Specification for Chemical Admixtures for Concrete 1999.
[171] ASTM. Standard specification for air-entraining admixtures for concrete. ASTM C 260 2010.
[172] Astm C. 1437, Standard test method for flow of hydraulic cement mortar. West Conshohocken PA Am Soc Test Mater ASTM Int 2001.
[173] C01 Committee. Test Method for Compressive Strength of Hydraulic Cement Mortars (Using 2-in. or [50mm] Cube Specimens). ASTM International; n.d. https://doi.org/10.1520/C0109_C0109M-21.
[174] C1550 Standard Test Method for Flexural Toughness of Fiber Reinforced Concrete (Using Centrally Loaded Round Panel) n.d. https://www.astm.org/c1550-20.html (accessed June 25, 2023).
[175] Tahmouresi B, Koushkbaghi M, Monazami M, Abbasi MT, Nemati P. Experimental and statistical analysis of hybrid-fiber-reinforced recycled aggregate concrete. Comput Concr Int J 2019;24:193–206.

[176] American Society for Testing and Materials. Committee C-09 on Concrete and Concrete Aggregates. Standard test method for flexural performance of fiber-reinforced concrete (using beam with third-point loading). ASTM International; 2013.
[177] ASTM C143 / C143M - 20 Standard Test Method for Slump of Hydraulic-Cement Concrete n.d. https://www.astm.org/Standards/C143 (accessed April 7, 2021).
[178] Dupont D, Vandewalle L. Comparison between the round plate test and the RILEM 3-point bending test, RILEM, Bagneux, France; 2004, p. 101–10.
[179] Dixon DE, Prestrera JR, Burg G, Chairman SA, Abdun-Nur EA, Barton SG, et al. Standard practice for selecting proportions for normal, heavyweight, and mass concrete (ACI 211.1-91). Farmington Hills ACI 1991.
[180] CSA A. 23.1: Concrete Materials and Methods of Concrete Construction. Can Stand Assoc Tor 2009.
[181] Han B, Dong S, Ou J, Zhang C, Wang Y, Yu X, et al. Microstructure related mechanical behaviors of short-cut super-fine stainless wire reinforced reactive powder concrete. Mater Des 2016;96:16–26.
[182] Krenchel H. Fibre reinforcement; theoretical and practical investigations of the elasticity and strength of fibre-reinforced materials 1964.
[183] Hossain M, Awal AA. Experimental validation of a theoretical model for flexural modulus of elasticity of thin cement composite. Constr Build Mater 2011;25:1460–5.
[184] Li J, Niu J, Wan C, Liu X, Jin Z. Comparison of flexural property between high performance polypropylene fiber reinforced lightweight aggregate concrete and steel fiber reinforced lightweight aggregate concrete. Constr Build Mater 2017;157:729–36.
[185] Costs by cause of injury – Parachute n.d. https://parachute.ca/en/professional-resource/cost-of-injury-in-canada/costs-by-cause-of-injury/ (accessed June 21, 2023).
[186] Meng X, Li P, Hu Y, Song F, Ma J. Recognition of Road Surface by Low-THz Frequencies. ArXiv E-Prints 2021:arXiv-2102.
[187] Sassani A, Ceylan H, Kim S, Arabzadeh A, Taylor PC, Gopalakrishnan K. Development of carbon fiber-modified electrically conductive concrete for implementation in Des Moines International Airport. Case Stud Constr Mater 2018;8:277–91.
[188] Chung D. Materials for thermal conduction. Appl Therm Eng 2001;21:1593–605.
[189] Farnam Y, Dick S, Wiese A, Davis J, Bentz D, Weiss J. The influence of calcium chloride deicing salt on phase changes and damage development in cementitious materials. Cem Concr Compos 2015;64:1–15.
[190] Alexander M, Bentur A, Mindess S. Durability of Concrete: Design and Construction. CRC Press; 2017.
[191] Effect of Cryo-Suction and Air Void Transition Layer on Hydraulic Pressure of Freezing Concrete - ProQuest n.d. https://www.proquest.com/openview/e96ab51fd0c685edfa603f8dce464139/1?pq-origsite=gscholar&cbl=37076 (accessed July 2, 2023).
[192] Zhang P, Wittmann FH, Vogel M, Müller HS, Zhao T. Influence of freeze-thaw cycles on capillary absorption and chloride penetration into concrete. Cem Concr Res 2017;100:60–7.
[193] Wang R, Hu Z, Li Y, Wang K, Zhang H. Review on the deterioration and approaches to enhance the durability of concrete in the freeze–thaw environment. Constr Build Mater 2022;321:126371.
[194] Tiberti G, Minelli F, Plizzari G. Cracking behavior in reinforced concrete members with steel fibers: A comprehensive experimental study. Cem Concr Res 2015;68:24–34.
[195] Yun H-D, Kim S-W, Lee Y-O, Rokugo K. Tensile behavior of synthetic fiber-reinforced strain-hardening cement-based composite (SHCC) after freezing and thawing exposure. Cold Reg Sci Technol 2011;67:49–57.
[196] Nam J, Kim G, Lee B, Hasegawa R, Hama Y. Frost resistance of polyvinyl alcohol fiber and polypropylene fiber reinforced cementitious composites under freeze thaw cycling. Compos Part B Eng 2016;90:241–50.

[197] Dong F, Wang H, Yu J, Liu K, Guo Z, Duan X, et al. Effect of freeze–thaw cycling on mechanical properties of polyethylene fiber and steel fiber reinforced concrete. Constr Build Mater 2021;295:123427.
[198] Li W, Liu H, Zhu B, Lyu X, Gao X, Liang C. Mechanical Properties and Freeze–Thaw Durability of Basalt Fiber Reactive Powder Concrete. Appl Sci 2020;10:5682.
[199] Affan M, Ali M. Experimental investigation on mechanical properties of jute fiber reinforced concrete under freeze-thaw conditions for pavement applications. Constr Build Mater 2022;323:126599.
[200] Sassani A, Arabzadeh A, Ceylan H, Kim S, Gopalakrishnan K, Taylor P. Factorial study on electrically conductive concrete mix design for heated pavement systems 2017.
[201] ASTM C. Standard test method for compressive strength of hydraulic cement mortars (Using 2-in. or [50-mm] cube specimens). Am Soc Test Mater 2002.
[202] ASTM ASA. C293/C293M-16: Standard Test Method for Flexural Strength of Concrete (Using Simple Beam with Center-Point Loading), ASTM; 2008.
[203] Standard A. C666-97: Standard Test Method for Resistance of Concrete to Rapid Freezing and Thawing. Annu Book ASTM Stand 2000;4.
[204] Carrillo J, Ramirez J, Lizarazo-Marriaga J. Modulus of elasticity and Poisson's ratio of fiber-reinforced concrete in Colombia from ultrasonic pulse velocities. J Build Eng 2019;23:18–26. https://doi.org/10.1016/j.jobe.2019.01.016.
[205] Standard A. C215. Standard Test Method for Fundamental Transverse, Longitudinal, and Torsional Resonant Frequencies of Concrete Specimens. ASTM Stand 2019:1–7.
[206] Kewalramani MA, Gupta R. Concrete compressive strength prediction using ultrasonic pulse velocity through artificial neural networks. Autom Constr 2006;15:374–9.
[207] Astm C. 597, Standard test method for pulse velocity through concrete. ASTM Int West Conshohocken PA 2009.
[208] Saremi SG, Goulias DG, Akhter AA. Non-Destructive Testing in Quality Assurance of Concrete for Assessing Production Uniformity. Transp Res Rec 2023;2677:1259–75.
[209] Neville A. Properties of concrete (vol. 4): Longman london 1995.
[210] Shariq M, Prasad J, Masood A. Studies in ultrasonic pulse velocity of concrete containing GGBFS. Constr Build Mater 2013;40:944–50.
[211] Robert M. Science behind thermography-thermal infrared sensing for diagnostics and control. J Thermosense 1982;371:2–9.
[212] Washer G, Fenwick R, Nelson S, Rumbayan R. Guidelines for thermographic inspection of concrete bridge components in shaded conditions. Transp Res Rec 2013;2360:13–20.
[213] Standard A. D4580: Standard Practice for Measuring Delaminations in Concrete Bridge Decks by Sounding, ed. West Conshohocken PA ASTM Int 2012.
[214] Wang B, Gupta R. Analyzing bond-deterioration during freeze-thaw exposure in cement-based repairs using non-destructive methods. Cem Concr Compos 2021;115:103830.
[215] Yan W, Wu Z, Niu F, Wan T, Zheng H. Study on the service life prediction of freeze–thaw damaged concrete with high permeability and inorganic crystal waterproof agent additions based on ultrasonic velocity. Constr Build Mater 2020;259:120405.
[216] Chauhan S, Sethy A. Differences in dynamic modulus of elasticity determined by three vibration methods and their relationship with static modulus of elasticity. Maderas Cienc Tecnol 2016;18:373–82.
[217] Kaushik S, Jaisingh L, Jaisingh M. Ultrasonic testing of concrete 2012.
[218] Monazami M, Sharma A, Gupta R. Evaluating performance of carbon fiber-reinforced pavement with embedded sensors using destructive and non-destructive testing. Case Stud Constr Mater 2022;17:e01460.
[219] Li L, Cao M. Influence of calcium carbonate whisker and polyvinyl alcohol-steel hybrid fiber on ultrasonic velocity and resonant frequency of cementitious composites. Constr Build Mater 2018;188:737–46.

[220] Mao Z, Zhang J, Ma Q, Du G, Li Y, Yang X. Performance evaluation of fiber-reinforced reactive powder concrete exposed to high temperature combining nondestructive test. J Build Eng 2022;61:105266.
[221] ASTM C143 / C143M - 20 Standard Test Method for Slump of Hydraulic-Cement Concrete n.d. https://www.astm.org/Standards/C143 (accessed April 7, 2021).
[222] Ndagi A, Umar AA, Hejazi F, Jaafar MS. Non-destructive assessment of concrete deterioration by ultrasonic pulse velocity: A review. IOP Conf Ser Earth Environ Sci 2019;357:012015. https://doi.org/10.1088/1755-1315/357/1/012015.
[223] Adham El-Newihy. Application of Impact Resonance Method for Evaluation of the Dynamic Elastic Properties of Polypropylene Fiber Reinforced Concrete 2013.
[224] Municipal Roads - The Canadian Infrastructure Report Card n.d. http://canadianinfrastructure.ca/en/municipal-roads.html (accessed June 21, 2023).
[225] Government of Canada SC. Commuting to work during COVID-19 2020. https://www150.statcan.gc.ca/n1/pub/45-28-0001/2020001/article/00069-eng.htm (accessed January 4, 2021).
[226] Tiznobaik M, Bassuoni MT. A Test Protocol for Evaluating Absorption of Joints in Concrete Pavements. J Test Eval 2017;46:20160297. https://doi.org/10.1520/JTE20160297.
[227] Oh HJ, Cho YK, Kim S-M. Experimental evaluation of crack width movement of continuously reinforced concrete pavement under environmental load. Constr Build Mater 2017;137:85–95. https://doi.org/10.1016/j.conbuildmat.2017.01.080.
[228] Xiao DX, Wu Z. Longitudinal cracking of jointed plain concrete pavements in Louisiana: Field investigation and numerical simulation. Int J Pavement Res Technol 2018;11:417–26. https://doi.org/10.1016/j.ijprt.2018.07.004.
[229] Liu J, Zhao D, Shen J, Zhang Y. Comparative Study on Crack and Factor of Continuously Reinforced Concrete Pavement in the Tunnel and Outside. Procedia - Soc Behav Sci 2013;96:98–103. https://doi.org/10.1016/j.sbspro.2013.08.014.
[230] Caminos: un nuevo enfoque para la gestión y conservación de redes viales | Digital Repository | Economic Commission for Latin America and the Caribbean n.d. https://repositorio.cepal.org/handle/11362/30314 (accessed January 4, 2021).
[231] Ali MA, Majumdar AJ, Rayment DL. Carbon fibre reinforcement of cement. Cem Concr Res 1972;2:201–12. https://doi.org/10.1016/0008-8846(72)90042-7.
[232] Wongtanakitcharoen T, Naaman AE. Unrestrained early age shrinkage of concrete with polypropylene, PVA, and carbon fibers. Mater Struct 2007;40:289–300. https://doi.org/10.1617/s11527-006-9106-z.
[233] Elrazek MA, Shafy Gamal YA. The Reliable Concrete Compression Strength Assessment by SCHMIDT Hammer for Different Concrete Grades. IOP Conf Ser Mater Sci Eng 2021;1171:012004. https://doi.org/10.1088/1757-899X/1171/1/012004.
[234] Evaluation of Elastic Properties of Fiber-Reinforced Concrete Using Fundamental Resonance Frequencies. ACI Mater J 2021;118. https://doi.org/10.14359/51730420.
[235] Nandhini K, Karthikeyan J. The early-age prediction of concrete strength using maturity models: a review. J Build Pathol Rehabil 2021;6:7. https://doi.org/10.1007/s41024-020-00102-1.
[236] Diaferio M, Vitti M. Correlation Curves to Characterize Concrete Strength by Means of UPV Tests. In: Abdel Wahab M, editor. Proc. 1st Int. Conf. Struct. Damage Model. Assess., vol. 110, Singapore: Springer Singapore; 2021, p. 209–18. https://doi.org/10.1007/978-981-15-9121-1_16.
[237] Scherr JF, Grosse CU. Delamination detection on a concrete bridge deck using impact echo scanning. Struct Concr 2021;22:806–12. https://doi.org/10.1002/suco.202000415.
[238] J. Helal, M. Sofi, Mendis P. Non-Destructive Testing of Concrete: A Review of Methods. Electron J Struct Eng 2015;14:97–105. https://doi.org/10.56748/ejse.141931.
[239] BC Transit - Planning Standards and Guidelines | Transit Future | BC Transit n.d. https://bctransit.com/kamloops/transit-future/corporate-infrastructure-initiatives/design-guidelines (accessed July 16, 2023).

[240] ASTM: 231, Standard Test Method for Air Content of... - Google Scholar n.d. https://scholar.google.com/scholar_lookup?hl=en&publication_year=2009b&author=ASTM&title=ASTM+C231%3A+Standard+test+method+for+air+content+of+freshly+mixed+concrete+by+the+pressure+method (accessed July 16, 2023).
[241] Goulias DG, Kim H, Schwartz CW. Evaluation of In Situ Pavement Material Properties and Behavior through Field Instrumentation and Load Testing. J Transp Eng 2011;137:466–73. https://doi.org/10.1061/(ASCE)TE.1943-5436.0000231.
[242] Merkle D, Reiterer A. Evaluation of thermography-based automated delamination and cavity detection in concrete bridges. In: Beyerer J, Heizmann M, editors. Autom. Vis. Insp. Mach. Vis. IV, Online Only, Germany: SPIE; 2021, p. 4. https://doi.org/10.1117/12.2592303.
[243] Qin Y, Li M, Li Y, Ma W, Xu Z, Chai J, et al. Effects of nylon fiber and nylon fiber fabric on the permeability of cracked concrete. Constr Build Mater 2021;274:121786. https://doi.org/10.1016/j.conbuildmat.2020.121786.
[244] Agilent | Agilent History Timeline - 2000s 2015. https://www.agilent.com/about/companyinfo/history/timeline_2000s.html (accessed July 16, 2023).
[245] Breysse D, Martínez-Fernández JL. Assessing concrete strength with rebound hammer: review of key issues and ideas for more reliable conclusions. Mater Struct 2014;47:1589–604. https://doi.org/10.1617/s11527-013-0139-9.
[246] ASTM C. 805, Standard test method for rebound number of hardened concrete. ASTM Int West Conshohocken PA USA 2008.
[247] Nie L, Xu J, Luo X, Chen H, Chang S, Wang T, et al. Study of aramid and carbon fibers on the tensile properties of early strength cement mortar. IOP Conf Ser Earth Environ Sci 2019;267:032009. https://doi.org/10.1088/1755-1315/267/3/032009.
[248] Li C, Ge H, Sun D, Zhou X. Novel conductive wearing course using a graphite, carbon fiber, and epoxy resin mixture for active de-icing of asphalt concrete pavement. Mater Struct 2021;54:48. https://doi.org/10.1617/s11527-021-01628-7.
[249] Adesina A, Bastani A, Heydariha JZ, Das S, Lawn D. Performance of basalt fibre-reinforced concrete for pavement and flooring applications. Innov Infrastruct Solut 2020;5:103. https://doi.org/10.1007/s41062-020-00359-y.
[250] School of Civil Engineering, College of Engineering, Universiti Teknologi MARA (UiTM), Shah Alam, Selangor, 40450, MALAYSIA, Zulkifli NI, Alisibramulisi A, School of Civil Engineering, College of Engineering, Universiti Teknologi MARA (UiTM), Shah Alam, Selangor, 40450, MALAYSIA, Institute for Infrastructure Engineering and Sustainable Management (IIESM), Universiti Teknologi MARA (UiTM), Shah Alam, Selangor, 40450, MALAYSIA, Saari N, et al. Experimental Investigation of Ultrasonic Pulse Velocity (UPV) Test Specimen in Assessing the Strength of Steel Fiber Reinforced Concrete Structure. J Adv Ind Technol Appl 2021;02. https://doi.org/10.30880/jaita.2021.02.02.004.